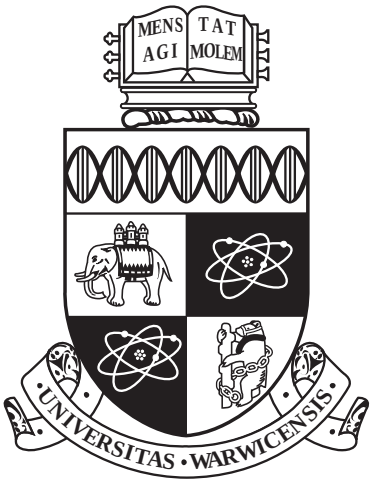

The Gaseous component to planetary debris discs at white dwarfs

by

Christopher James Manser

Thesis

Submitted to the University of Warwick

for the degree of

Doctor of Philosophy

Physics Astronomy department

November 2018

THE UNIVERSITY OF
WARWICK

Contents

List of Tables

List of Figures

Acknowledgments

I would first like to thank my supervisor Boris Gänsicke, who has given me the amazing opportunity to pursue a career in science. His support, encouragement, and guidance has made me the scientist I am today.

Thank you everyone who works, or has worked as part of the Warwick Astronomy group, who have made the department a fun, welcoming, and sometimes very distracting place to work. Special shoutouts to: Mark, who has taught me a substantial amount of coding through osmosis. Nicola, for showing me the most important feature of emacs. Matt ($\times 2$), Greg, Ryan and Tom for 1/20 chances of awesomeness. Odette and Pol, who shared my enthusiasm for puzzles. And Crisp club, who shared my enthusiasm for crisps.

My thanks to friends, inside, outside, and pre-dating the Warwick Astronomy group. For the games, the laughs, the adventures, and, most importantly, the support. In particular, thanks to Chris Goddard, for lunchtime discussions, and Henry Powell, for playing more Huskar than any person should.

An enormous thanks to my partner, Elena, who has given me her support over the last two years.

Lastly, but certainly not least, I would like to thank my family: My Mum, Dad, brothers, sister and sister-in-laws, my nieces and nephews, my aunts, uncles, cousins and nan. Thank you for giving me years of encouragement and having faith in me.

Declarations

I submit this thesis to the University of Warwick graduate school for the degree of Doctor of Philosophy. This thesis has been composed by myself and has not been submitted for a degree at another University.

An appreciable quantity of thesis includes material from published/submitted papers written by myself which are detailed below:

- Manser et al. (2016a), *Doppler imaging of the planetary debris disc at the white dwarf SDSS J122859.93+104032.9*. Chapter 4 makes use of material from this work.
- Manser et al. (2016b), *Another one grinds the dust: variability of the planetary debris disc at the white dwarf SDSS J104341.53+085558.2*. Chapter 3 includes material from this publication.
- Manser et al. (submitted to Science 2018), *A planetesimal found orbiting within the debris disc surrounding a white dwarf star*. Chapter 5 includes material from this recently submitted paper to Science. While not yet published, this paper is included in this list in the event that it is accepted before the assessment of the Thesis.

In addition, the introduction and conclusions make use of material from all three of these papers. Chapter 6 is based on work that will be submitted as a paper soon.

The work presented herein was carried out by myself with these exceptions:

- Atmospheric models to determine the temperature, $\log g$, and abundances of SDSS J1228+1040 and SDSS J1043+0845 were calculated by Detlev Koester.
- Case 3 described in Section 4.6 of Chapter 4 was performed by Dimitri Veras.

- The research contained within Chapter 5 involved collaboration with a number of people due to the novelty of the observations: (i) The observations described in Section 5.2 were reduced by Mark Hollands and Paula Izquierdo. (ii) The analysis of the best fitting period described in Section 5.3.2 was performed by Boris Gänsicke. (iii) Sections 5.4.2 & 5.4.3 were written by Wladimir Lyra to increase the confidence of the hypothesis of a body orbiting within the debris disc. (iv) Calculations within Section 5.6.1 were performed by myself along with Siegfried Eggl and Alexander Mustill.

Abstract

Via the spectroscopic detection of metal contamination of white dwarf photospheres, it has been well established that 25 – 50 % of these stars host remnant planetary systems. This pollution arises from the accretion of disrupted planetesimals, and the majority of metal-enhanced white dwarfs are actively accreting from a debris disc.

These discs are detected in the form of an infrared excess at 1 – 3 % of white dwarfs, and a subset host a co-orbiting gaseous component. In this Thesis, I analyse the morphological evolution of the gaseous emission from debris discs around two white dwarfs, including the prototypical gas disc host SDSS J122859.93+104032.9 (SDSS J1228+1040) which shows variability on short (hourly) and long (yearly) timescales. Long-term monitoring of the emission profiles from gaseous debris discs reveals that the majority of them share this seemingly-periodic, morphological evolution. For SDSS J1228+1040, I could model the variable emission profiles remarkably well by the precession of a fixed, asymmetric intensity pattern in the disc, and I produced the first image of a gaseous debris disc using the method of Doppler tomography. I suggest that the variability of the other gas discs is also generated by fixed intensity patterns in the discs that precess.

Motivated by the detection of the long-term variability of gaseous debris discs, I collected short-cadence spectroscopy of the emission from the debris disc around SDSS J1228+1040 to probe for orbital timescale ($\simeq$ hours) variability. I detected clear, periodic variability in the Ca II emission lines on a $\simeq 2$ hr period, which I interpret as the signature of a planetesimal orbiting within the debris disc. I ruled out other likely scenarios, and I hypothesise that the planetesimal generates the gas we observe, as well as inducing the long- and short-term variability.

Finally, using a spectroscopic sample of white dwarfs from the Sloan Digital Sky Survey, I calculated the fraction of white dwarfs that host a detectable gaseous debris disc as $0.06 \pm ^{0.03}_{0.02}$ per cent. This occurrence rate can be combined with the fraction of white dwarfs that host a dusty disc (1 – 3 %) to find that only 1 – 10 % of these systems have an observable gaseous component. Determining an occurrence rate using the number of known gas (7) and dust ($\simeq 38$) discs results in a value up to an order of magnitude larger ($\simeq 18$ %) than the one I have calculated, and is due to observational bias.

My research has shown that while variability of gaseous debris discs is common, appearing on time-scales of decades, months and hours, their prevalence is not. From the results of my work, I hypothesise that these discs are tracers for the presence of close-in planetesimals. Future observations to identify additional gaseous debris discs, as well as characterising their long- and short-term variability will allow this hypothesis to be tested.

Chapter 1

Introduction

The solar system is the archetypal planetary system which humans have studied for millennia. The structure of the solar system out to Saturn is shown in Figure 1.1 a, and is familiar to most if not all astronomers. However, as the solar system ages the Sun will undergo a destructive evolution, increasing in radius and engulfing some of the close-in terrestrial planets, as well as ejecting $\simeq 50\,\%$ of its mass, causing orbits of the bodies in the solar systems to widen by a factor $\simeq 2$ (Figure 1.1 b). The Sun will eventually become a white dwarf (Figure 1.1 c), and it is expected that the solar system will (for the most part) survive this transition (Duncan and Lissauer, 1998; Villaver and Livio, 2007, 2009), ending up as a remnant planetary system. Such remnant planetary systems have been discovered around white dwarfs, via the detection of dusty and gaseous debris discs and photospheric metal contamination (Figure 1.1 d, Zuckerman and Becklin 1987; Rocchetto et al. 2015; Farihi 2016).

In this chapter, I will provide a brief overview on the formation of a white dwarf using the solar system as an example. While the configuration of the solar system does not appear to be common among planetary systems, the physics discussed in this chapter applies to the majority of planetary systems. I will also give an introduction to the relevant white dwarf physics, exo-planetary systems, and the evidence we have obtained so far for remnant planetary systems around white dwarfs.

1.1 The future of the solar system

The Sun is a G2 star that is about half way through its $\simeq 10\,\mathrm{Gyr}$ lifetime on the main sequence (Carroll and Ostlie, 2006). A main sequence star steadily fuses hydrogen into helium via the proton-proton (PP) chain or the carbon-nitrogen-oxygen (CNO) cycle and is in hydrostatic equilibrium, where the thermal pressure from nuclear fusion balances gravity. The evolution of the Sun can be represented on a Hertzsprung-Russell diagram (developed independently by Ejnar Hertzsprung in 1911 and Henry Norris Russell in 1913) shown in Figure 1.2. This valuable tool allows the study of a population of stars as a whole, or to depict how the temperature and luminosity of a given object will appear and evolve over time (see Section 2.1.1).

The Sun will continue its life on the main-sequence for $\simeq 5\,\mathrm{Gyr}$, slowly increasing in radius and temperature until the core is sufficiently depleted of hydrogen, at which point the Sun will begin to fuse hydrogen in a shell around the now helium dominated core and enter the sub-giant phase. The hydrogen-burning shell produces additional helium which feeds the core, and this phase lasts until the Sun's helium core can no longer support itself, at which pount it will contract and become electron degenerate. This transition occurs as no two electrons (or fermions) can occupy the same quantum state (Pauli, 1925). At high

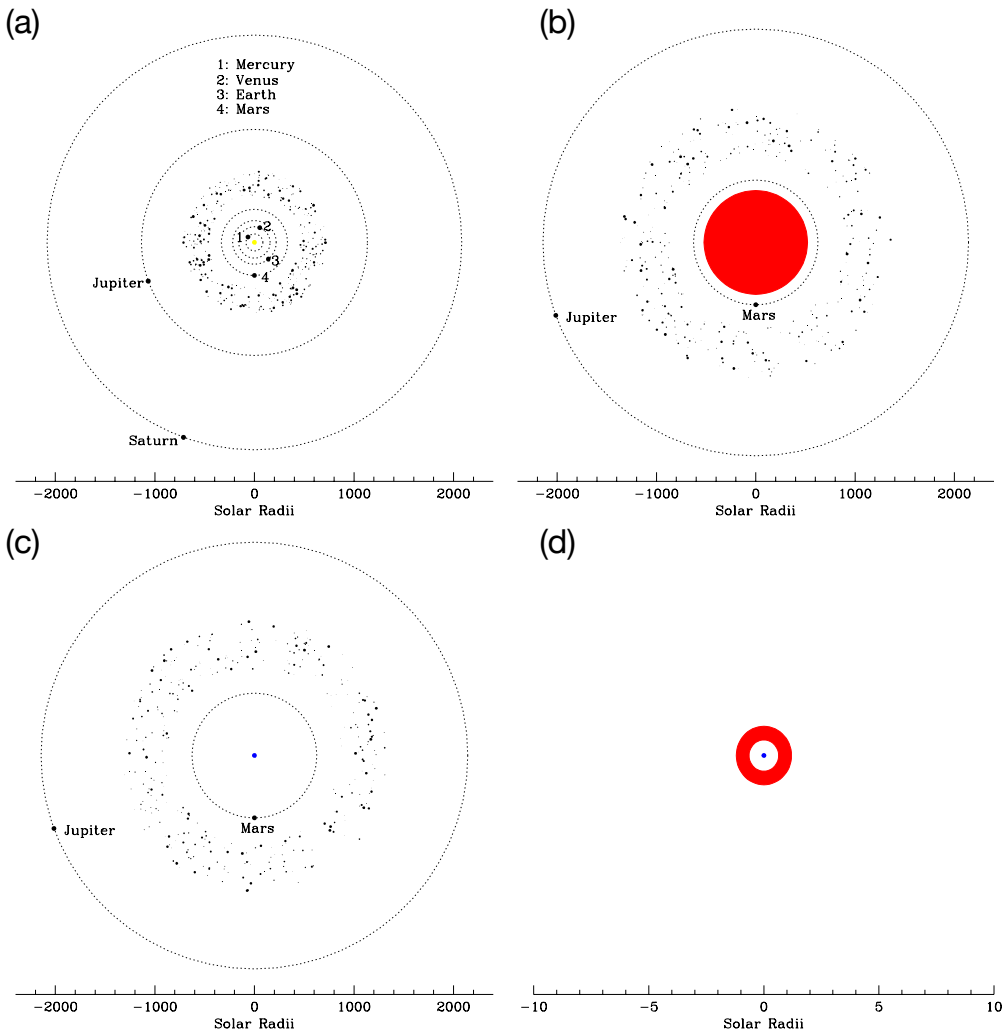

Figure 1.1: The evolution of the solar system from the current day into its final phase as a white dwarf, reproduced with permission from Boris Gänsicke. (a) The solar system as it is today, with the planets orbiting the Sun shown out to Saturn. The orbital distances are given in terms of Solar radii. (b) The solar system around 5 Gyrs from now. Once the Sun does not have enough hydrogen in the core to fuse, it will expand into a red giant consuming Mercury, Venus, and possibly Earth, and start losing its outer envelope into space. This mass loss will cause the orbits of the outer planets and the asteroid belt to expand. (c) The solar system after 5 Gyr from now. After the giant phases, the Sun will eventually lose all of its outer envelope and shrink into a white dwarf, with most of the planets surviving, but on orbits further out than their initial configuration in (a). (d) A planetary debris disc around the future Sun, that is now a white dwarf. A planetesimal from the asteroid belt could be perturbed by Jupiter (Veras et al., 2014b), putting it onto a highly eccentric orbit that would pass close to the white dwarf. If it enters the tidal disruption radius, the planetesimal will be torn apart and form a debris disc.

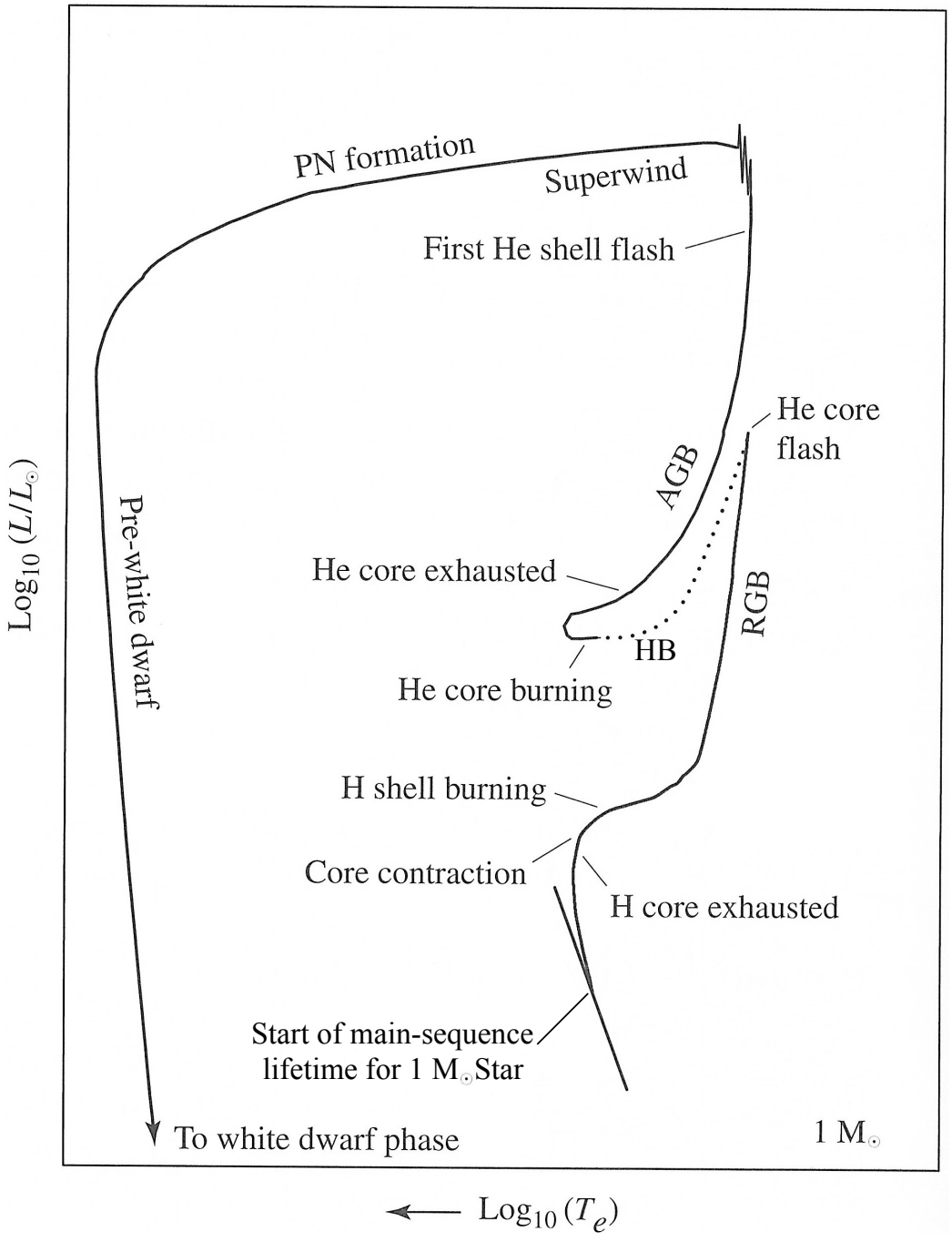

Figure 1.2: Hertzsprung-Russell diagram depicting the evolution of the brightness and temperature of a 1 $M_\odot$ star, e.g. the Sun. Adapted from Carroll and Ostlie (2006).

densities, the lowest energy states are all filled, and electrons have to occupy higher states, creating an effective pressure. The contraction of the core causes the hydrogen-burning shell to move inwards, increasing its temperature, which has the effect of increasing the Sun's radius and reducing its effective temperature making it appear more red, and marks the beginning of the red-giant branch (RGB, see Figure 1.2) phase.

The RGB phase continues, with the Sun increasing in radius and reducing in temperature until the degenerate core reaches the Schönberg-Chandrasekhar Limit (Schönberg and Chandrasekhar, 1942), which is defined as the maximum fraction of a star's mass that can be core material without collapsing under the load. Above this mass, the core can no longer support the material above it, and the core contracts and increases in temperature dramatically to the point at which the helium can fuse. As the temperature in degenerate matter does not have any effect on the pressure, fusion of helium rapidly spreads throughout the core, and can release energy up to 10^{11} times the luminosity of the Sun in larger stars (Carroll and Ostlie, 2006). This energy release only lasts for a few seconds (and most of the energy goes into lifting the degeneracy of the core), and is called a 'helium flash'. From this point, the degeneracy in the core is lifted and it expands, and the outer layers of the Sun will contract and increase in effective temperature while continuing to fuse helium in the core along the horizontal branch (HB, see Figure 1.2).

This phase continues until the helium in the core is depleted, having been converted into carbon and oxygen, and the core contracts again. This leads to a thick shell undergoing helium fusion around the carbon-oxygen core, and roughly marks the beginning the asymptotic giant branch (AGB, see Figure 1.2) phase. The continued contraction of the core leads to more intense helium fusion, which causes the hydrogen burning shell to expand, and results in a temporary cessation of hydrogen fusion. As the star evolves, the helium shell will eventually run out of fuel, and the hydrogen shell will reignite and begin fusing again, generating helium which collects in the helium shell. The mass of the helium shell will continue to increase until the boundary between the helium shell and the carbon-oxygen core becomes degenerate, and another helium flash is initiated, driving out the hydrogen burning shell and causing it to cease fusion. Fusion of helium will stop, and the hydrogen shell will recover to once again feed the helium shell. The Sun will undergo several helium flashes (also known as thermal pulses) before it leaves the AGB phase.

As mentioned above, the Sun will lose mass during the AGB phase, and this mass loss accelerates over time (Carroll and Ostlie, 2006). The lost mass is ejected into the surrounding space, eventually producing a planetary nebula. All that will be left of the Sun is its carbon-oxygen core with a mass $M \simeq 0.5\,\mathrm{M}_{\odot}$ and a thin layer of envelope material, the composition of which depends on when the last helium flash occurs. If the final helium flash occurs during the AGB phase, the envelope will contain hydrogen and helium. However, if

the flash happens after the AGB phase, the residual hydrogen is burnt, and the envelope will be almost entirely helium. The core will be initially extremely hot and as it cools, becomes a white dwarf.

1.2 White dwarfs

The majority of stars in the Universe will end their lives as white dwarfs. The cores of these stellar remnants no longer undergo fusion and are held up by electron degeneracy pressure (the same pressure that will hold up the inert helium core of the Sun when it leaves the main sequence) and are therefore very dense, compact objects. The mass distribution of white dwarfs is shown in Fig. 1.3 (Tremblay et al., 2011), which has a mean value of $0.6\,M_{\odot}$. White dwarfs have a radius close to that of the Earth ($\simeq 0.01\,R_{\odot}$), which along with their mass, results in surface gravities many orders of magnitude greater than main-sequence stars ($\log g \simeq 8$, Fig. 1.3).

Due to their high surface gravities, the atmospheres of white dwarfs are highly stratified, with heavier elements sinking out of the atmosphere and the lighter elements floating to the surface (Fontaine and Michaud, 1979; Koester, 2009). Fig. 1.4 shows the internal structure of two white dwarfs, where roughly 99 - 99.99 % of the total mass is contained within the degenerate carbon-oxygen core, leaving the remaining 1 - 0.01 % of the total mass to be within the envelope.

1.2.1 Classes of white dwarfs

The atmospheres of the majority of white dwarfs consist of hydrogen and/or helium, the two lightest elements. Hydrogen in a white dwarf atmosphere can be detected via Balmer absorption lines in the optical spectrum resulting from electrons in the energy level $n = 2$ absorbing photons and transitioning to a quantum number state, $n \geq 3$. Helium can be detected by absorption profiles in a spectrum generated by both its neutral (He I) and singly ionised states (He II), although the presence of either are dependent on the temperature of the white dwarf. As the composition of the atmosphere of a white dwarf is best determined spectroscopically, a spectral classification system was defined by Sion et al. (1983), which is presented in Table 1.1 (Koester, 2013).

The two dominant classes of white dwarfs are DAs and DBs, where only Balmer and He I absorption lines are present in the spectrum respectively, but nothing else. The four other main classes are (i) DCs, which show no spectral features apart from the continuum flux, (ii) DOs, which display He II absorption lines, (iii) DZs, which have only absorption lines from metals, and (iv) DQs, which show either atomic or molecular carbon features. These classifications can also be used in conjunction with one another, e.g. a white dwarf

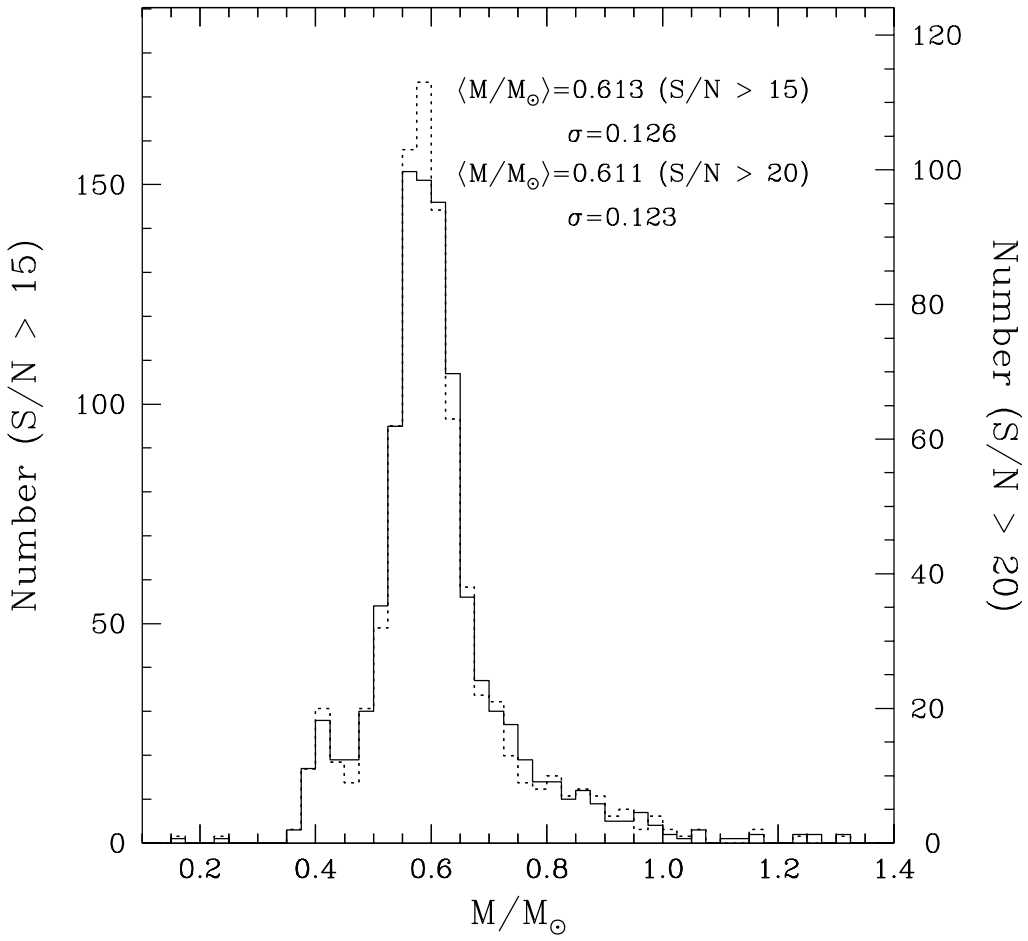

Figure 1.3: The distributions of masses for a sample of DA white dwarfs with effective temperatures 13000 K $\leq T_{\rm eff} \leq$ 40000 K in the Sloan Digital Sky Survey for two cutoffs; S/N > 15 (solid) and S/N > 20 (dashed, scaled to match the former). The mean and standard deviation for each distribution given. Reproduced from Tremblay et al. (2011).

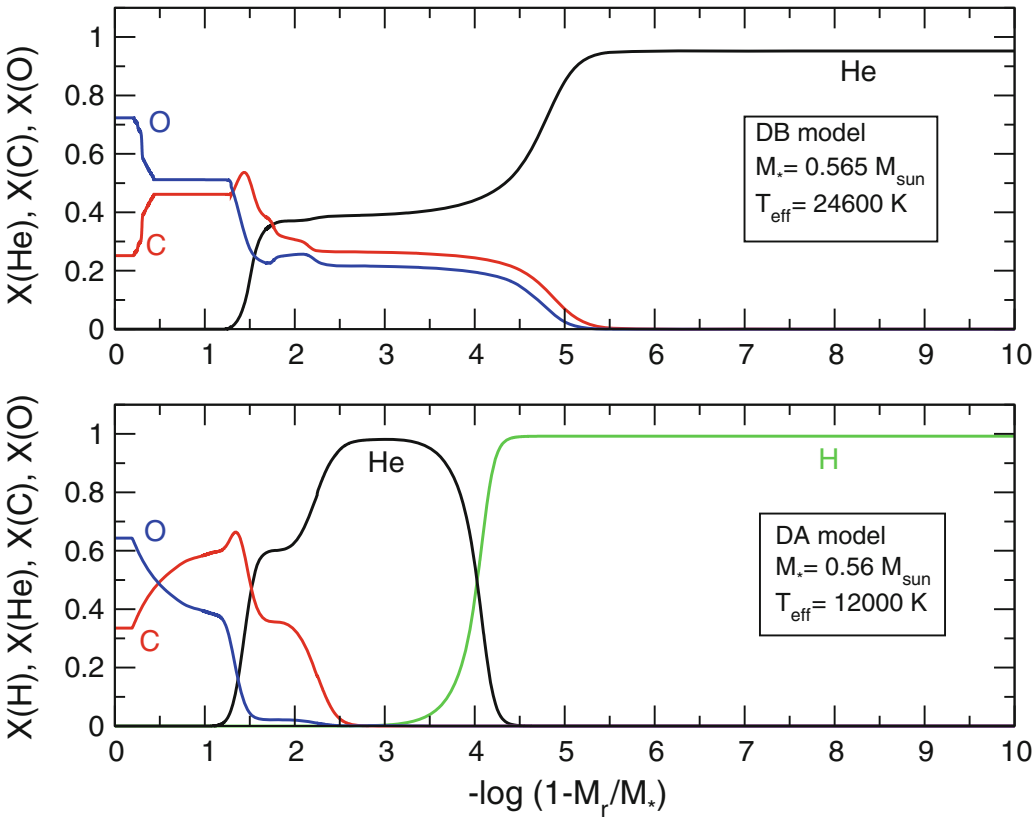

Figure 1.4: The internal structure of two white dwarfs with helium (He, top) and hydrogen (H, bottom) dominated envelopes. The letter X represents the relative fraction of the various elements. The x-axis is the logarithm of the fractional mass depth, with the core to the left, and the surface to the right. Reproduced from Althaus et al. (2010).

that has hydrogen, He I, and metal absorption features in its spectrum would be labelled a DABZ white dwarf. There are additional identifiers described in Table 1.1 which are only added to a classification, e.g. a DA white dwarf that shows Zeeman splitting of the Balmer lines due to the presence of a magnetic field would be labelled a DAH. Sample spectra for some of the possible combinations of the spectral classifiers are shown in Figure 1.5.

Table 1.1: Definition of white dwarf spectral classes. The symbols from "P" to "V" are appended onto a primary designation. Reproduced from Koester (2013).

Classification	Description
DA	Only Balmer lines present; no He I or metals
DB	He I present, no H or metals
DC	Continuous spectrum, no lines deeper than 5 % in any part of the electromagnetic spectrum
DO	He II strong; He I or H present
DZ	Metal lines only; no H or He lines
DQ	Carbon features, either atomic or molecular in any part of the electromagnetic spectrum
P	Magnetic white dwarfs with detected polarization
H	Magnetic white dwarfs with Zeeman splitting in the spectra
X	Peculiar or unclassifiable spectrum
E	Emission lines are present
?	Uncertain assigned classification; a colon (:) may also be used
V	Optional symbol to denote variability

1.2.2 Radiative and convective atmospheres

The transport of energy in the envelope of a white dwarf (and most stars) is performed by either radiative transfer or convection, and the convective regions in the envelope of typical DA and DB white dwarfs are shown in Fig. 1.6. The onset of convection is defined by the Schwarzschild criterion, and if present will dominate over radiative transfer (Koester, 2013). Convection is highly efficient in stars, and material present in a convection zone is considered to be homogeneously mixed. This will act against the diffusion of elements through the atmosphere of a white dwarf due to gravitational settling. At low temperatures ($T_{\rm eff} \leq 40000$ K), radiation pressure has a negligible effect on the diffusion of the majority of metals (Koester, 2013), however above this, the radiation field can be strong enough to slow, or even prevent the diffusion of metals in the atmosphere of a white dwarf, a process called radiative levitation. This effect is also dependent on the element being levitated, e.g. Si will be kept in the atmosphere of a white dwarf via radiative levitation down to

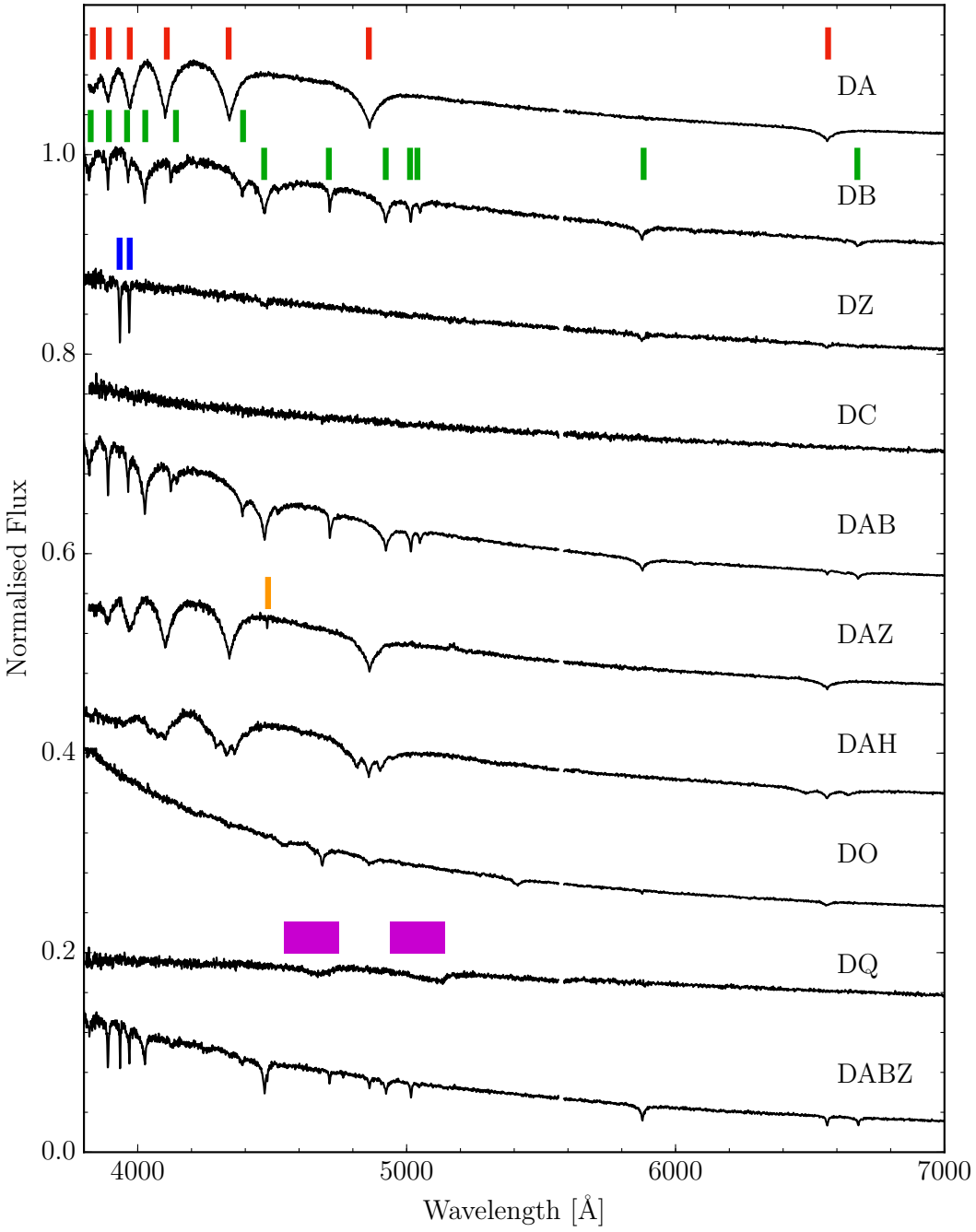

Figure 1.5: A set of ten white dwarf spectra from the Sloan Digital Sky Survey that showcase the variety in spectral features and the corresponding classifications. Strong lines of H (red), He (green), Ca (blue), Mg (orange), and C (purple) are identified.

$T_{\rm eff} \simeq 17000$ K (Chayer and Dupuis, 2010; Dupuis et al., 2010; Chayer, 2014). If Si is used to determine the overall accretion rate from planetary debris excluding radiative levitation, derived accretion rates will be erroneously higher than when calculated using a model that combines accretion, diffusion, and radiative levitation. Understanding the diffusion time-scales of material sinking out of the atmosphere of white dwarfs is crucial in determining the atmosphere's composition.

1.2.3 Diffusion time-scales

If metals are accreted by the white dwarf, they will be remain in the atmosphere for some time before diffusing out and becoming unobservable. Diffusion time-scales differ by a factor of a few between the most commonly accreted elements, but by orders of magnitude depending on the type of atmosphere (hydrogen-dominated DAs vs helium-dominated non-DAs), and the temperature of the white dwarf (Paquette et al. 1986; Koester 2009; Wyatt et al. 2014, see also Fig. 1.7). This large difference in diffusion time-scales is mainly due to whether the atmosphere is radiative or convective, and how deep the convective region is. If convection is present, the diffusion time-scale at the bottom of the convection zone (which can extend below the atmosphere, see Figure 1.6), dominates the diffusion process.

The metal pollution (DxZ) of white dwarf atmospheres is thought to primarily come from the accretion of planetary bodies (Zuckerman et al., 2003, 2010; Koester et al., 2014), and I briefly overview the detection of exo-planetary systems in the next section.

1.3 Exo-planetary systems

The first confirmed exo-planetary system, PSR 1257+12, was identified by Wolszczan and Frail (1992). The host star is a millisecond pulsar, a rapidly spinning neutron star that emits radio pulses during every rotation cycle of the star. Deviations from a constant spin period were found at this system, which was interpreted as perturbations from three planetary bodies in orbit around the pulsar. It is thought that these planets are 'second generation' planets, having formed after the pulsar progenitor exploded in a core-collapse supernova (which also removed the companion star that spun up the pulsar).

However, PSR 1257+12 is a peculiarity, and it was not until three years later when Mayor and Queloz (1995) discovered the first exo-planet around a Sun-like (or main-sequence) star, 51 Pegasi. The planet in this system is Jupiter-sized, but orbits the host star with a semi-major axis of $\simeq 0.05$ AU, putting it well within the orbit of Mercury at 0.39 AU (Carroll and Ostlie, 2006).

Currently $\simeq 3000$ exoplanets[1] have been discovered using primarily two detection

[1]Number taken from the exoplanet orbit database, http://exoplanets.org/, on 21 - 09 - 2017, (Han et al., 2014)

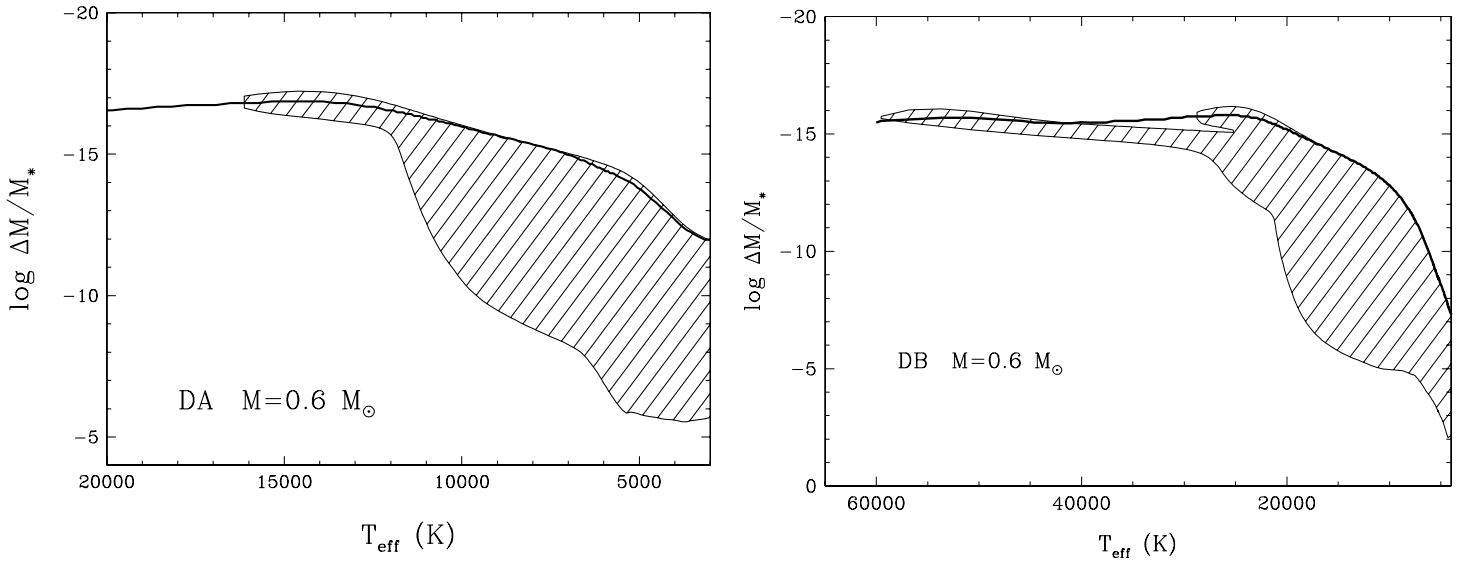

Figure 1.6: Location of the hydrogen and helium convection zones as a function of effective temperature $T_{\rm eff}$ in a $0.6\,{\rm M}_{\odot}$ DA (left) and DB (right) white dwarf respectively. The y-axis expresses on a logarithmic scale the mass fraction ΔM above a certain point with respect to the total mass of the star M_*. The thick solid line indicates the location of the photosphere. Reproduced from Dufour et al. (2007) and Bergeron et al. (2011).

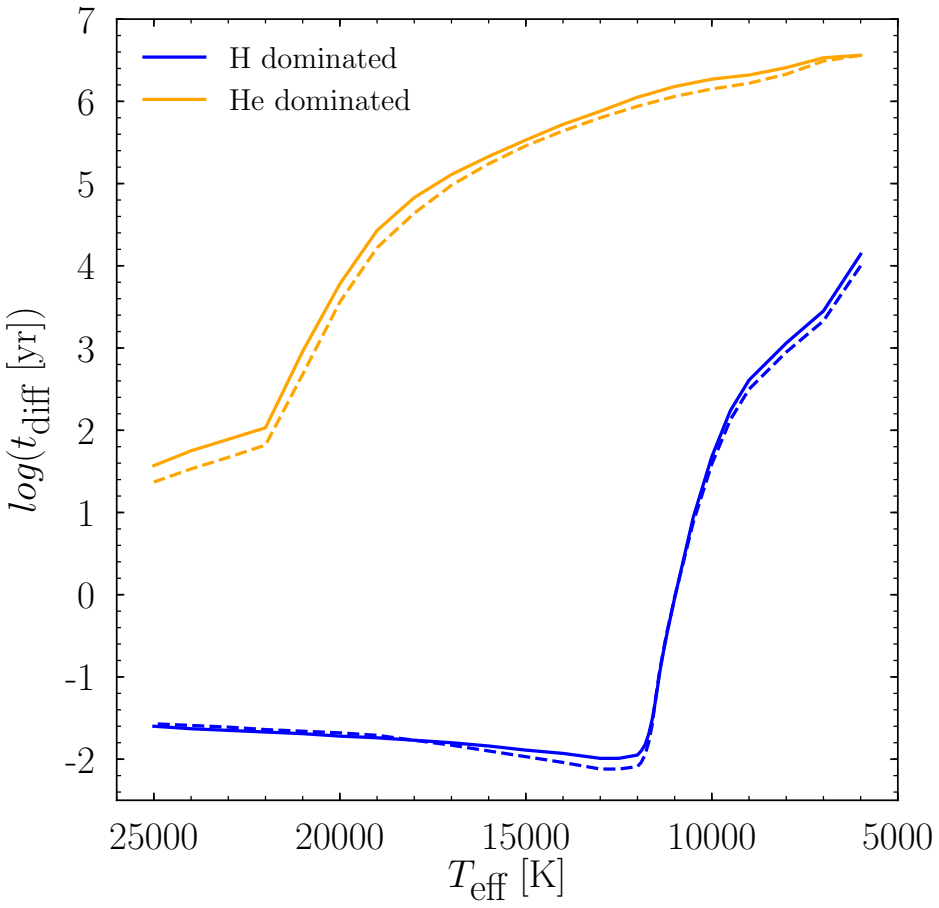

Figure 1.7: The diffusion (or sinking) timescales of Ca (solid) and Fe (dashed) as a function of effective temperature for DA (blue) and Non-DA (orange) white dwarfs. Data used to generate the figure was obtained from Koester (2009).

methods; radial velocity variations of the host star (Mayor and Queloz, 1995), and transits of a planet in front of its host star (Charbonneau et al., 2000), which are both described below.

1.3.1 The radial velocity method

A planet-star system can be viewed as a binary, where both bodies will orbit around their centre of mass. The planet will have a velocity several orders of magnitude larger than that of the host star, but will be orders of magnitude fainter and is usually undetectable, and therefore the much smaller radial velocity 'wobble' of the host star is used to indirectly determine the presence of a planet. However, the host star's radial velocity is difficult to detect as it is usually no larger than $\simeq 500\,\mathrm{m\,s^{-1}}$ (see Fig. 1.8 for an example radial velocity curve of the star 51 Peg). Starting from Kepler's third law (Kepler, 1619), one can calculate the mass of a single planet on a circular orbit around a star as

$$M_\mathrm{p} \sin i = \left(\frac{{M_*}^2 P \, {v_{*,\mathrm{o}}}^3}{2\pi G} \right)^{\frac{1}{3}}, \tag{1.1}$$

given the orbital period, P, of the planet and star, the inclination, i, of the orbit with respect to Earth, and the mass, M_*, and observed velocity, $v_{*,\mathrm{o}}$, of the host star. The inclination is usually unknown, and $M_\mathrm{p} \sin i$ is therefore a lower limit on the mass of the planet. A constraint on the inclination can be given if the planet is also transiting its host star, as this significantly tightens the range of possible inclinations.

1.3.2 The transit method

The transit method is so far the most successful technique used to detect exo-planets, thanks to wide field telescopes such as SuperWASP (Pollacco et al., 2006), NGTS (Wheatley et al., 2018), *Kepler* (Borucki et al., 2010), and *TESS* (Ricker et al., 2015), being able to observe very large numbers of stars. An example lightcurve produced by a planet transiting its host star is given in Fig. 1.9 (Charbonneau et al., 2000). Using the transiting method, one can determine the radius of a planet, R_p simply as

$$R_\mathrm{p} = \left(\frac{\Delta f}{f} {R_*}^2 \right)^{\frac{1}{2}}, \tag{1.2}$$

where f is the flux from the host star with radius, R_*, and Δf is the change in flux during the transit. Equation 1.2 relies on the stellar disc being of uniform brightness, and that the planet does not emit any flux.

The probability that a planet with radius R_p, on an orbit with semi-major axis a,

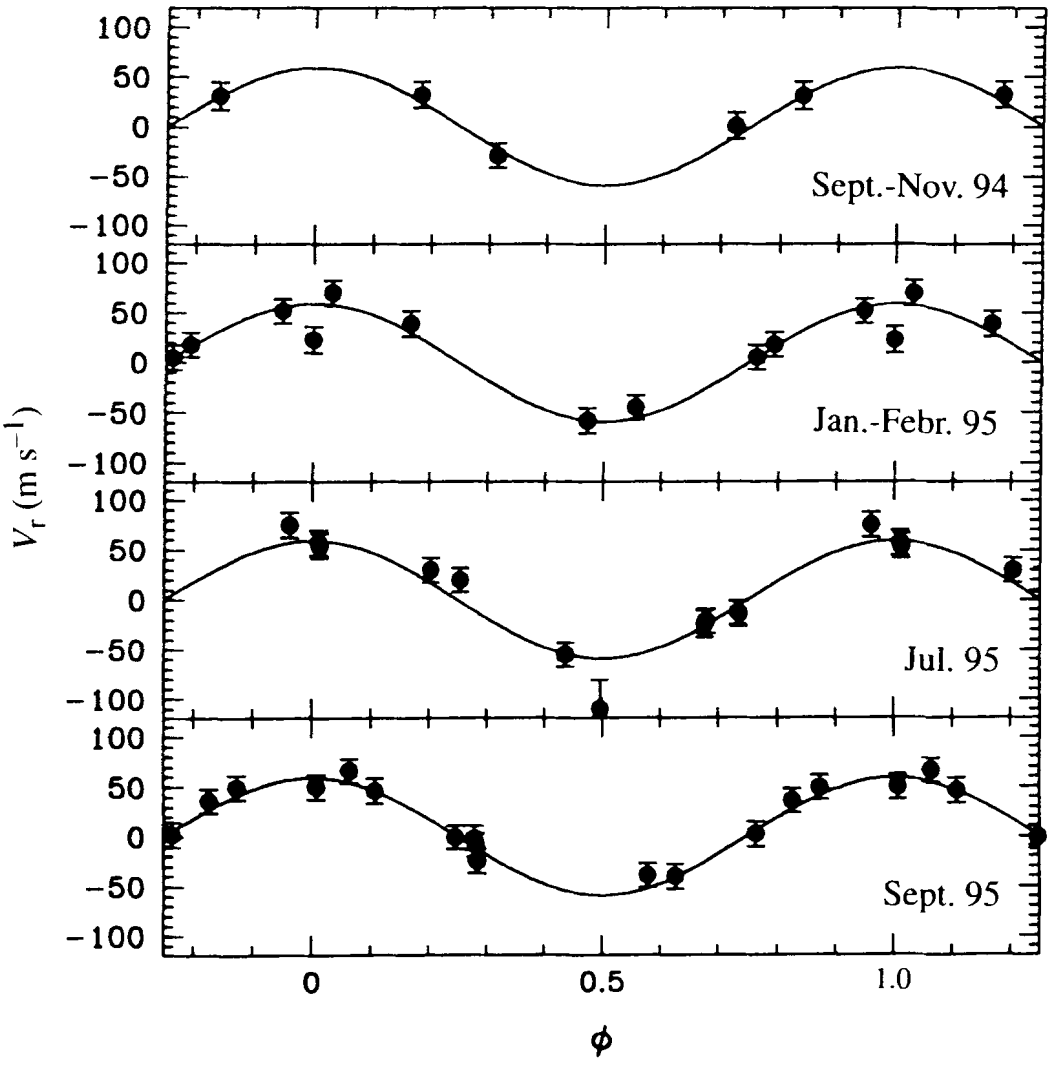

Figure 1.8: The radial velocity measurements of the star 51 Peg, showing clear sinusoidal variations due to a planetary companion. The half-amplitude of the variations is $\simeq 60\,\mathrm{m\,s^{-1}}$. Reproduced from Mayor and Queloz (1995).

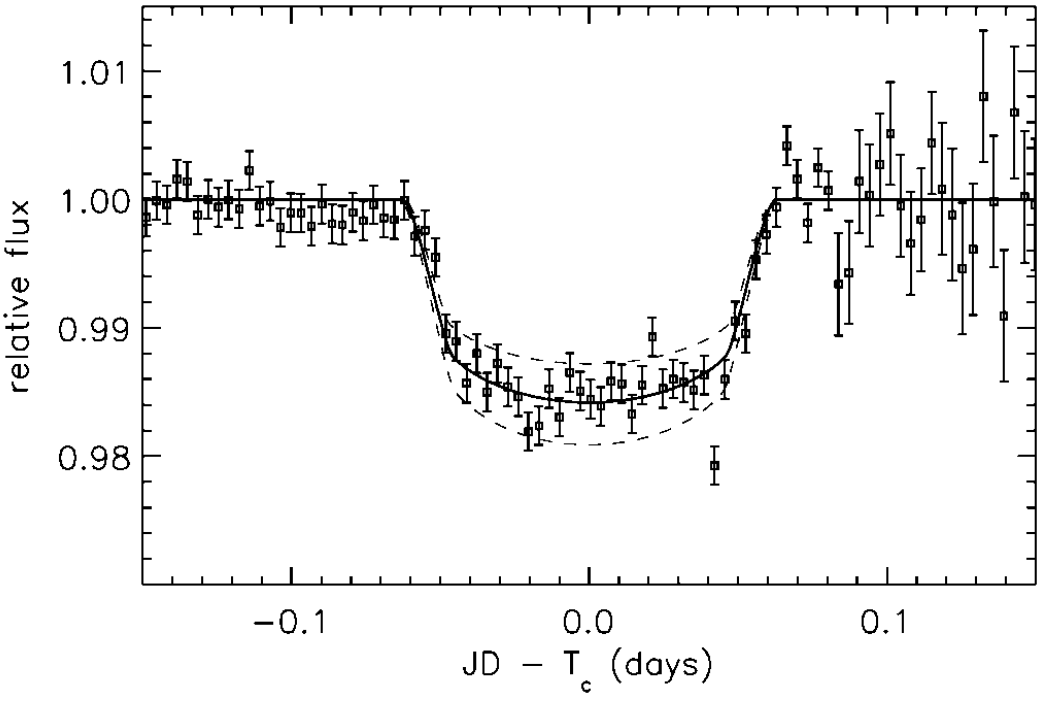

Figure 1.9: The transit of a hot Juipter around the host star HD 209458. Each point is binned over 5 mins of data, which covers two nights of observations. Reproduced from Charbonneau et al. (2000).

will transit a host star of radius R_*, is given by Haswell (2010):

$$\text{geometric transit probability} = \frac{R_\mathrm{p} + R_*}{a} \simeq \frac{R_*}{a}, \tag{1.3}$$

where the simplification relies on $R_\mathrm{p} \ll R_*$

1.3.3 The structure and composition of a exoplanets

If a planet is observed using both the transit and radial velocity methods, we can measure its radius, as well as its mass (a transiting planet system is highly inclined with $i \simeq 90$) and hence the density of the planet can be calculated. Using this information, models for the bulk structure of the planet can be computed, and some examples are shown in Figure 1.10. However, with only an average density moreoever with large uncertainties, many of these models are degenerate, and planets can span a range of possible different compositions. An example of this is GJ 1132 b in Fig. 1.10 (Berta-Thompson et al., 2015), spanning multiple model tracks.

In the solar system, the masses and radii of the planets are known to a high precision (Fig. 1.11), and the degeneracy between models based on an average density can be lifted by abundance measurements of samples collected in-situ and from meteorites (McDonough, 2000; Nimmo and Tanaka, 2005; Nittler et al., 2017). This kind of analysis is currently not possible for exo-planetary systems, however the composition of rocky exo-planetary material can be studied by investigating the accretion of planetesimals by metal-polluted white dwarfs (DxZs, see Section 1.2).

1.4 Planetary systems around white dwarfs

It is now well established that around 25 - 50 % of white dwarfs are polluted by planetary material, via spectroscopic observations detecting metallic absorption lines in white dwarf atmospheres (Jura, 2003; Zuckerman et al., 2003, 2010; Koester et al., 2014). The first such system was discovered more than 100 years ago, via the observation of the white dwarf vMa2 by van Maanen (Fig. 1.12, van Maanen 1917; Farihi 2016). This was also the first detection of a planetary system around another astronomical object, although the origin of the metallic absorption features was only realised over 80 years later.

To pollute a white dwarf, planetary material in the form of asteroids or comets needs to enter the tidal disruption radius of the white dwarf. This radius is defined as the point at which a planetesimal will be ripped apart due to the extreme gravity of the stellar remnant, and the canonical value for a rocky body is usually taken as $\simeq 1\,\mathrm{R}_\odot$ (Veras et al., 2014b, 2017). Figure 1.1 c depicts the solar system at a stage where the Sun has become a white

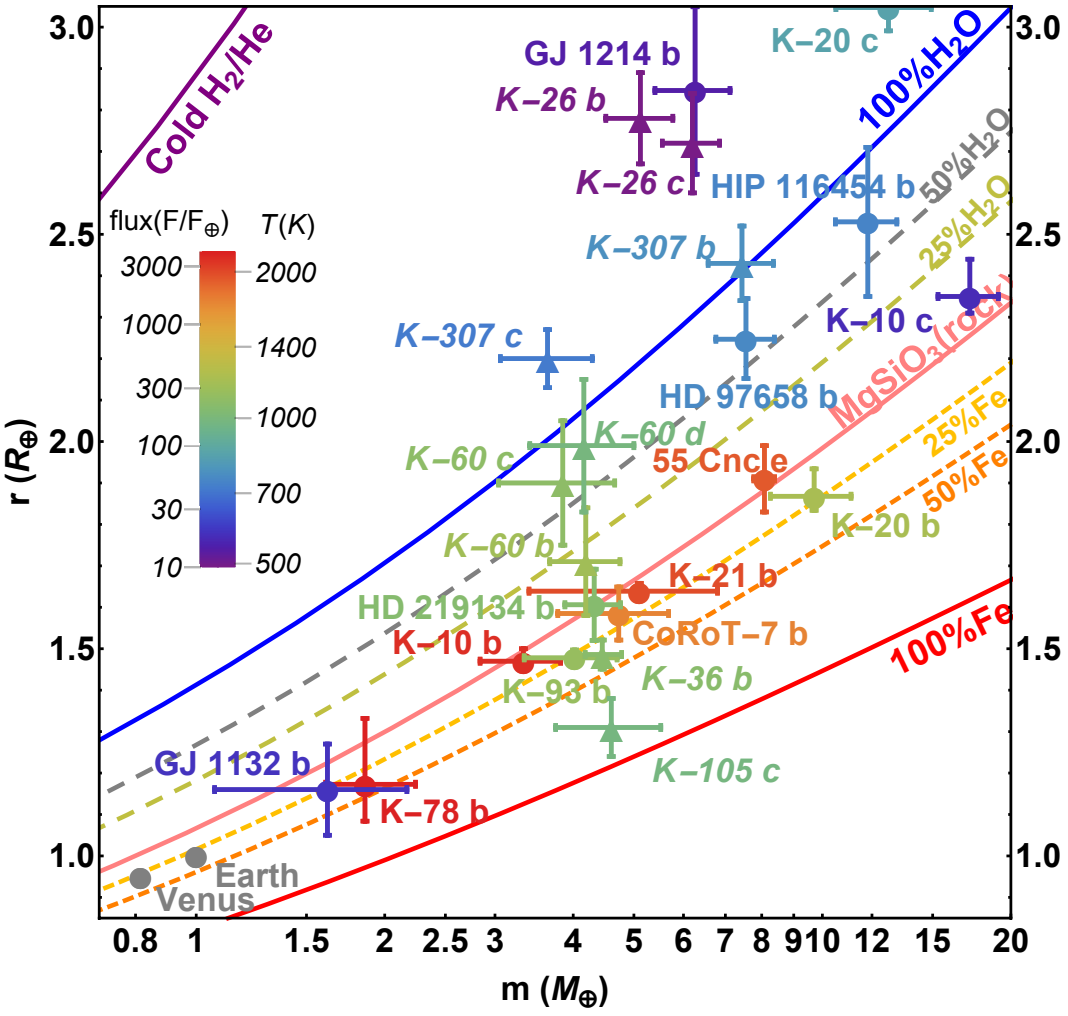

Figure 1.10: The mass-radius relation for low mass planets with different compositions along with measurements of several transiting planets. Obtained from https://www.cfa.harvard.edu/~lzeng/planetmodels.html on 20 - 09 - 2017 (Zeng et al., 2016; López-Morales et al., 2016).

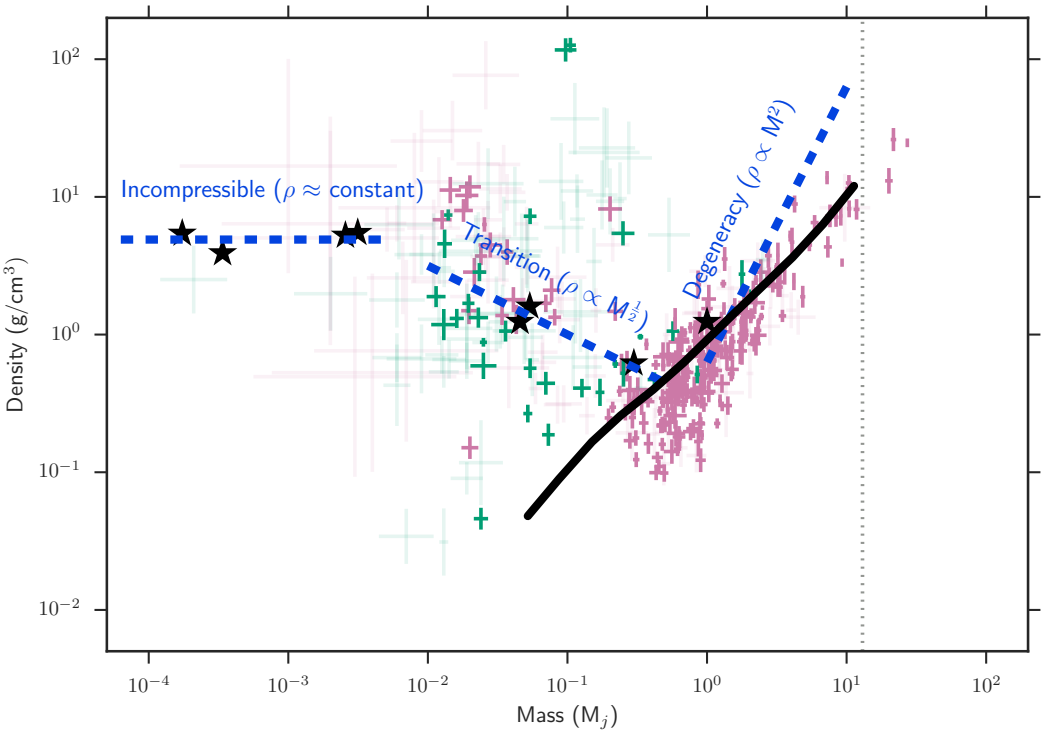

Figure 1.11: The mass-density relation for the currently known exoplanets. Planets with masses measured from radial velocity are in pink, from TTV's with green, and the eight solar system planets are labeled as black stars. In this plot the points with fractional density errors of greater than 30% have been faded to place more emphasis on the well characterized sample. The dotted grey line signifies the 13 M_J cutoff commonly used to define a planet. Blue dashed lines mark broad trends in the data. The thick black line are the model results of Fortney et al. (2007), for a coreless H/He planet on a 0.045 AU orbit around a Sun-like star. Figure and caption reproduced from Louden (2016).

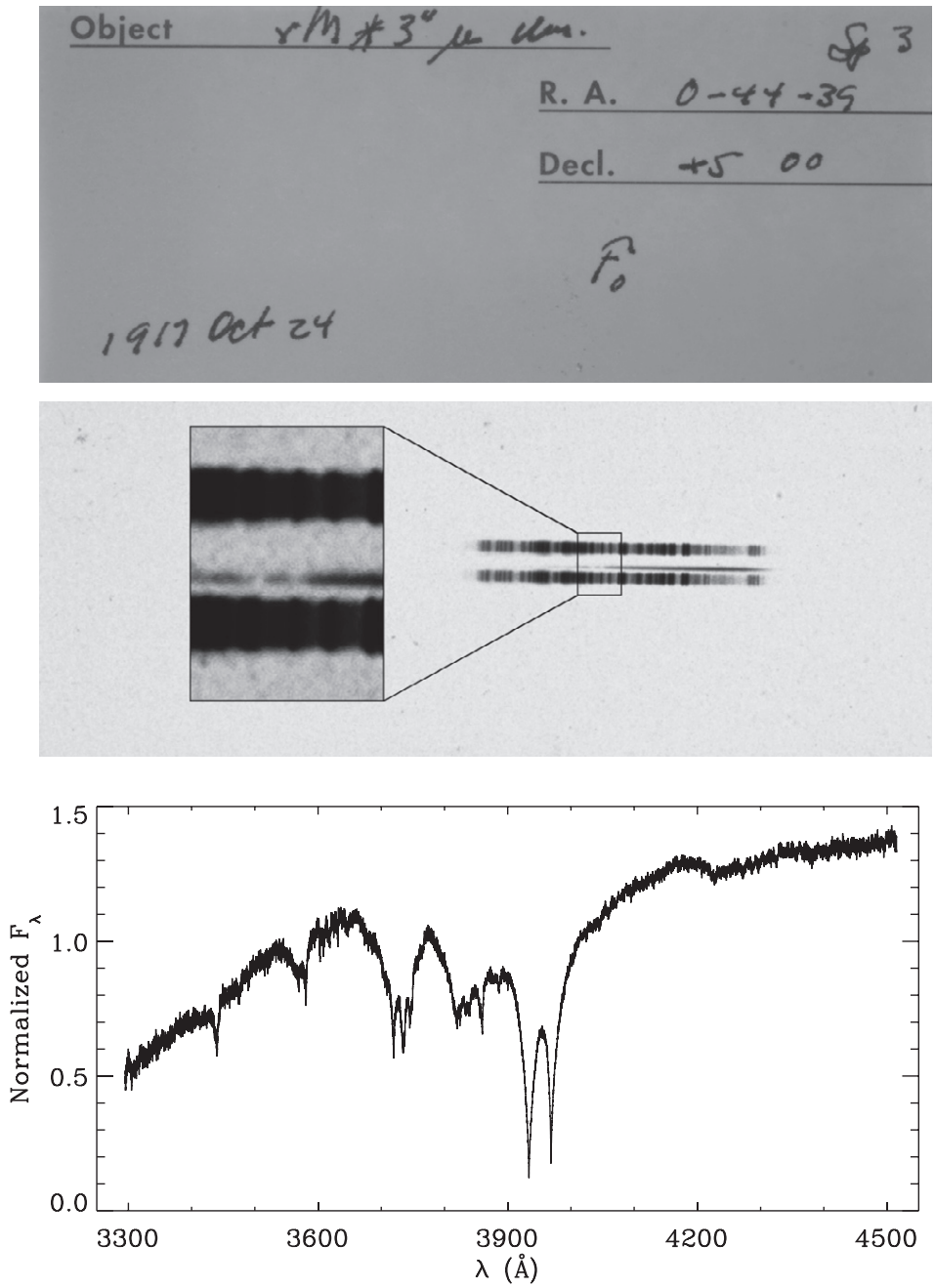

Figure 1.12: A spectrum of vMa 2, the prototypical metal-enriched white dwarf. Upper and middle panel: The 1917 photographic plate spectrum of vMa 2 (van Maanen, 1917). The box highlights the strong Ca II H and K Fraunhofer lines, which are relatively easy to see in the century old spectrum. Lower panel: An unpublished optical spectrum of vMa 2 taken with UVES on the Very Large Telescope (VLT). All salient features are absorption due to Fe, Mg, or Ca. Figure and panel descriptions reproduced from (Farihi, 2016).

dwarf, where the planetary bodies are orbiting at increased radii, and possibly becoming dynamically unstable.

It is thought that asteroids in these remnant planetary systems will be perturbed onto highly eccentric orbits (eccentricity, $e > 0.98$) (Veras et al., 2014b), bringing them close enough to the white dwarf to reach the tidal disruption radius. A number of theoretical studies show evidence that such scattering of asteroids (Frewen and Hansen, 2014; Mustill et al., 2018), and even exo-moons (Payne et al., 2016, 2017) onto star-grazing orbits around white dwarfs is possible (also see Veras 2016 and references therein). In addition, the presence of a wide binary companion to a white dwarf can destabilise a remnant planetary system (Bonsor and Veras, 2015).

Once the scattered planetesimal enters the tidal disruption radius, it will be ripped apart by tidal forces and form a broken ring of debris that orbits the white dwarf (Fig. 1.13 & 1.14). Poynting-Robertson drag due to radiation from the white dwarf will shrink the highly eccentric debris ring into a circular disc within the tidal disruption radius on a time-scale dependant on the size of the particles (Guess, 1962; Veras et al., 2015), resulting in the observationally detected dusty and gaseous debris discs (see Fig. 1.1, discussed in Section 1.6), from which the material is then accreted onto the white dwarf. The orbital periods of the material in the disc are typically in the range $\simeq$0.5–10 hrs.

While the debris is being accreted, the metals build up in the atmosphere of the white dwarf. By modelling the various elements detected in the photosphere of the white dwarf, the composition of the accreted body can be determined and the basic principles of this process are discussed in the next section.

1.5 Measuring the bulk abundances of accreted planetesimals

The metals detected in DxZ white dwarfs will sink out of the atmospheres on the diffusion time-scale, t_Z, which is dependant on the temperature and composition of the atmosphere (see Section 1.2.3). For a hydrogen-dominated atmosphere, the white dwarf is likely to have a small or no convection zone, which means that t_Z is simply the time it takes for the material to sink out of the observable atmosphere. White dwarfs with a helium-dominated atmosphere, however, usually have substantial convection zones which mix the material in the atmosphere. For this case, t_Z is the time it takes the material to diffuse out of the bottom of the convection zone, which is usually orders of magnitude longer than the sinking time in a radiative atmosphere (Paquette et al., 1986; Koester, 2009).

Following Jura and Young (2014), for the mass, $M_*(Z)$, of element, Z, in the white dwarf outer layer we can write

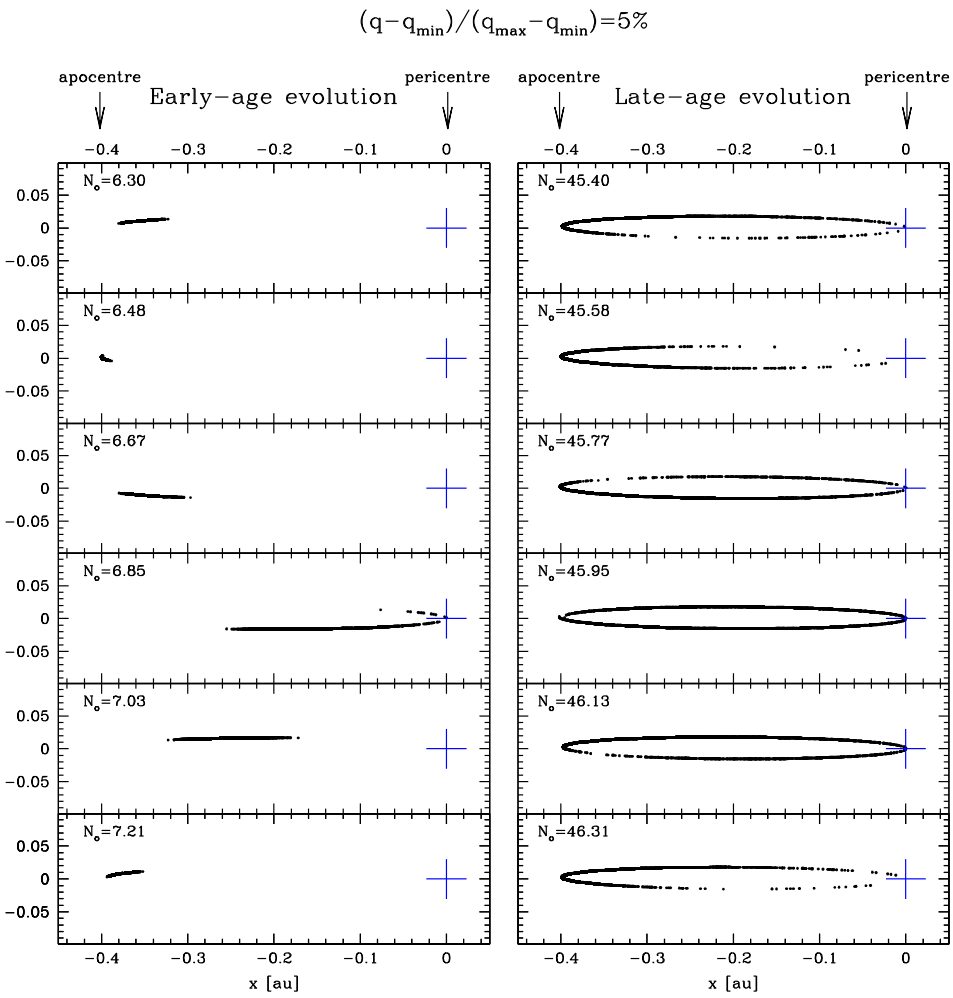

Figure 1.13: A simulation of the orbit of a broken ring of debris produced when a 'rubble pile' on a highly eccentric orbit ($e > 0.98$) is disrupted by a white dwarf. N_O denotes the number of orbits at the time each snapshot is taken. Over time the ring fills out, producing a complete debris ring. Reproduced from Veras et al. (2014b).

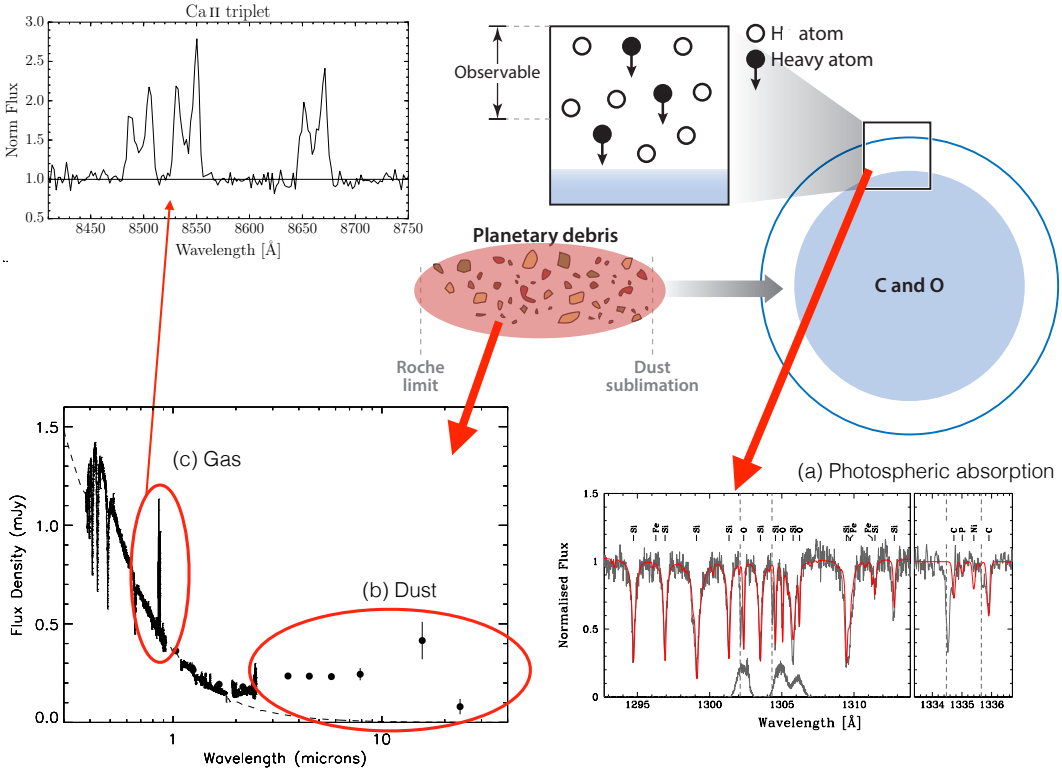

Figure 1.14: Schematic diagram of a white dwarf accreting from a planetary debris disc, adapted from Jura and Young (2014), illustrating the main observational techniques used to identify signatures of planetary systems around white dwarfs. The easiest sign to detect planetary material is the metal pollution of the white dwarf atmosphere, that imprints absorption lines in its spectrum (see (a), reproduced from Gänsicke et al. 2012, see also Figure 1.15). Such metal contamination is found at 25 - 50 % of white dwarfs (Zuckerman et al., 2010; Koester et al., 2014). This material is accreted from a debris disc, and around 40 systems show evidence for these discs as infra-red excess emission above the white dwarf flux (see (b), reproduced from Brinkworth et al. 2009). Seven published debris discs also have an observable gaseous component, most notably seen via emission from the 8600 Å Ca II triplet. (see (c)).

$$\frac{\mathrm{d}M_*(Z)}{\mathrm{d}t} = -\frac{M_*(Z)}{t_Z} + \dot{M}_\mathrm{P}(Z), \tag{1.4}$$

which equates the rate of change of $M_*(Z)$ to the rate at which the element is diffusing out of the outer layer, $-M_*(Z)/t_Z$ and the accretion rate of element Z from the planetesimal (P), $\dot{M}_\mathrm{P}(Z)$. Under the assumption that $M_*(Z) = 0$ at $t = 0$, the solution to Equation 1.4 is

$$M_*(Z) = \mathrm{e}^{-\frac{t}{t_Z}} \int_0^t \mathrm{e}^{\frac{t}{t_Z}} \dot{M}_\mathrm{P}(Z)\mathrm{d}t'. \tag{1.5}$$

This can be solved in two regimes described by Koester (2009); the steady state and early-phase accretion solutions (these solutions assume that no elements are present due to radiative levitation, an assumption that is true for the majority of remnant planetary systems that show metals, as well as all of the systems analysed in this Thesis). Koester (2009) suggest that the steady state is reached when $\mathrm{t} \simeq 5\,t_Z$, at which point $\mathrm{d}M_*(Z)/\mathrm{d}t$ goes to zero, and Equation 1.4 reduces to

$$M_*(Z) \simeq \dot{M}_\mathrm{P}(Z) t_Z, \tag{1.6}$$

assuming $\dot{M}_\mathrm{P}(Z)$ is constant. Assuming steady-state accretion, and, if we know the diffusion time-scale of element Z, and how much is in the outer layer of the white dwarf, we can calculate the accretion rate of that element. These accretion rates, determined for all detected elements can be used to calculate the abundance ratios of elements that made up the planetesimal. Given two elements, Z_k and Z_j, the abundance ratio is simply given by the ratio of the relevant accretion rates,

$$\frac{\dot{M}_\mathrm{P}(Z_\mathrm{j})}{\dot{M}_\mathrm{P}(Z_\mathrm{k})} = \frac{M_*(Z_\mathrm{j})}{M_*(Z_\mathrm{k})} \frac{t_{Z_\mathrm{k}}}{t_{Z_\mathrm{j}}}. \tag{1.7}$$

For the early-phase solution, we assume that $t \ll t_Z$ and $\dot{M}_\mathrm{P}(Z)$ is constant, and equation 1.5 can be written as

$$M_*(Z) \simeq \dot{M}_\mathrm{P}(Z) t. \tag{1.8}$$

Equation 1.8 is similar to Equation 1.6, although it depends on the total accretion time, rather than on the diffusion time for the element being accreted. As with the steady state solution, we can determine abundance ratios,

$$\frac{\dot{M}_\mathrm{P}(Z_j)}{\dot{M}_\mathrm{P}(Z_\mathrm{k})} = \frac{M_*(Z_\mathrm{j})}{M_*(Z_\mathrm{k})}, \tag{1.9}$$

which depend only on the mass of the two elements in the atmosphere.

Hydrogen-dominated DA white dwarfs have diffusion time-scales on the order of a few days to years, which increase as the white dwarf cools (see Section 1.2.3). In contrast, fully mixed, helium-dominated DB white dwarfs have t_Z at the base of their deep convection zones on the order of 10,000 years which dominates the diffusion process. The short diffusion time-scales for DA white dwarfs are a great boon to the study of planetary systems around white dwarfs, as the detection of metal pollution implies ongoing accretion.

The short diffusion time-scales for DA white dwarfs also allow the relatively safe assumption that the accretion is in steady state with the diffusion, and accurate accretion rates can therefore be determined. However, this assumption is not true for the longer diffusion time-scales at DB white dwarfs. Instead, we can use the total mass of metals contained in the convection zone to estimate a lower limit on the mass of the parent body that has been accreted by a DB white dwarf using Equation 1.8.

To obtain an abundance of an element, Z, in the atmosphere of the white dwarf (a required input needed for Equations 1.7 & 1.9), modelling of the atmospheric lines are required. Figure 1.15 shows such a model, where the individual lines from each element are carefully modelled. Free parameters in such a fit are the white dwarf effective temperature and surface gravity, and the individual abundances of all detected elements.

Using Equations 1.7 & 1.9, one can now determine the abundance ratios, and therefore the composition of the disrupted planetesimal. The majority of planetesimals analysed so far have a composition compatible with that of 'bulk Earth' Allègre et al. 2001, which is dominated by four elements, O, Mg, Si and Fe, making up 90 % of its mass. Compositions measured for planetesimals accreted by white dwarfs show that the same four elements typically make up more than 85 % of the disrupted bodies by mass (Gänsicke et al., 2012; Jura and Young, 2014). However, there are also a number of systems that deviate from this pattern, and I discuss a subset of the variety of planetesimals below.

1.5.1 A large variety in the composition of accreted bodies

Differentiated bodies

There is significant evidence that white dwarfs are accreting material from differentiated bodies. Core-like material is dominated predominately by Fe and Ni, and core-like bodies can be produced by either collisional events or stripping of the crust and mantle of a planet (Melis et al., 2011; Gänsicke et al., 2012). The converse to this is Fe-poor, crust-like material which is dominated by elements such as Al, Ca and Ti (Melis and Dufour, 2017).

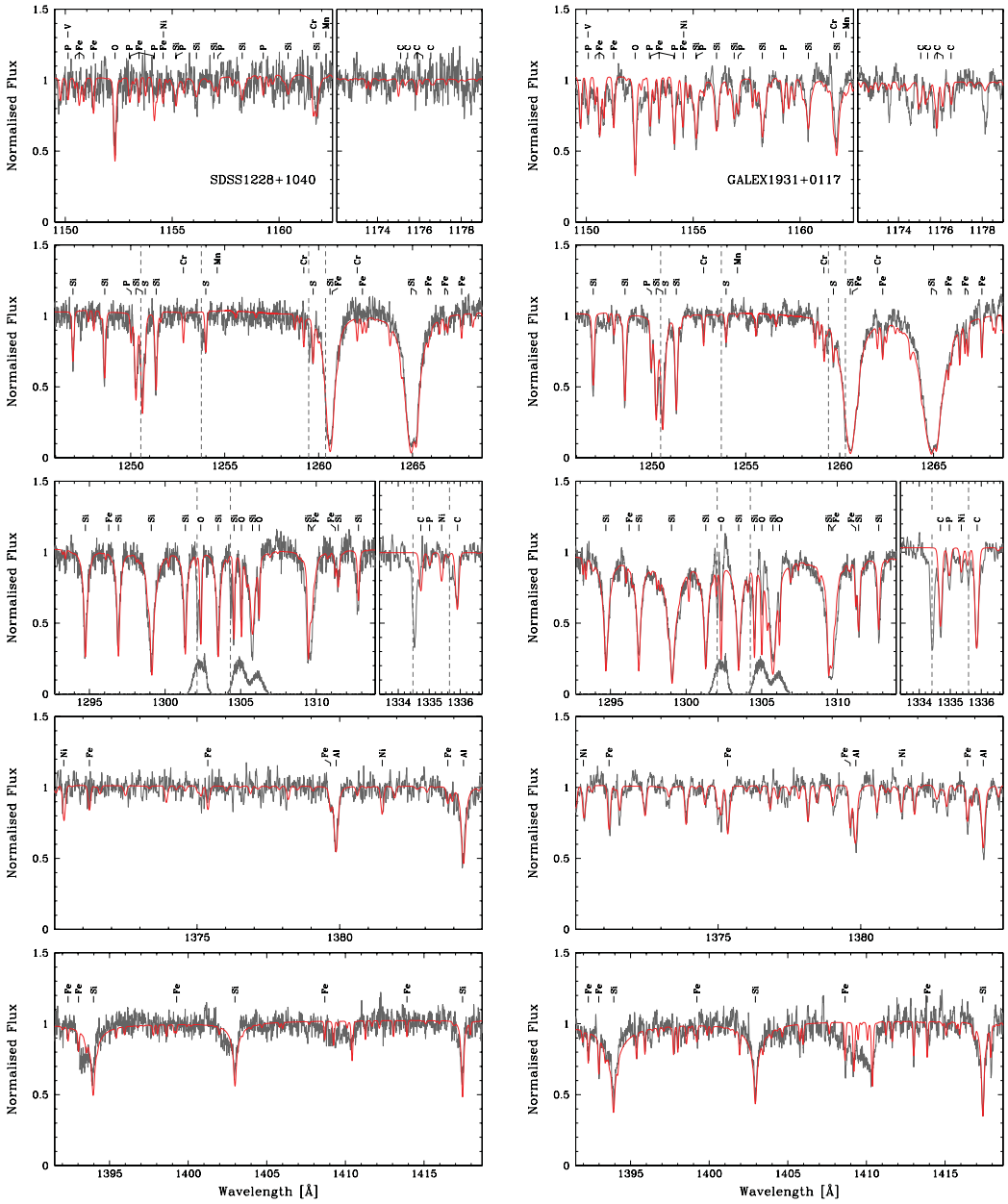

Figure 1.15: *Hubble Space Telescope* (*HST*) spectra of SDSS J1228+1040 and GALEX 1931+0117 (grey) obtained with the Cosmic Origins Spectrograph (COS). The spectra of these two white dwarfs contain a plethora of metal lines that are reproduced well by model spectra (red). The elements responsible for the strongest absorption lines are labelled, and interstellar absorption lines (not resulting from the system) are indicated by dashed grey lines. Reproduced from Gänsicke et al. (2012).

Water rich bodies

When water is accreted by a white dwarf, the H_2O molecules are unbound into hydrogen and oxygen. While oxygen can be detected in the atmosphere of a white dwarf demonstrating, the presence of accreted hydrogen is impossible for white dwarfs with a hydrogen-dominated atmosphere (DAs). For white dwarfs with a helium-dominated atmosphere (DBs), hydrogen can build up over multiple accretion events (Jura and Xu, 2010; Veras et al., 2014a; Raddi et al., 2015; Gentile Fusillo et al., 2017), or already be present in the form of primordial hydrogen (Koester and Kepler, 2015), and so the detection of hydrogen in the atmosphere of a DB cannot unambiguously be associated with the accretion of water. Moreover, oxygen is a dominant building block of rocky materials such as silicates, or volatiles such as CO and CO_2, which also makes it more difficult to determine the abundance of water in the parent planetesimal.

One can probe for an 'excess' of oxygen by calculating the number of O atoms locked in compounds such as FeO, CaO, or SiO_2. After accounting for all possible oxygen-compounds that could have been constituents of the accreted planetesimal (based on the detected metal species), any excess O can be attributed to water. This method has been applied to a number of white dwarfs so far (Farihi et al., 2013; Raddi et al., 2015), and an example of the O excess at GD 61 is shown in Figure 1.16.

As mentioned above, a second method that can be used to indirectly study the accretion of water at white dwarfs is the presence of hydrogen in the atmospheres of DB white dwarfs (Jura and Xu, 2010). There is evidence that a subset of white dwarfs with mixed hydrogen and helium atmospheres (DAB/DBAs) are formed via the accretion of multiple water-rich bodies (Raddi et al., 2015). While O sinks out of the convection zone on the diffusion time-scale, hydrogen, the lightest element, will remain in the convective zone, and there is an observed correlation showing that the metal-polluted helium white dwarfs are more likely to also contain hydrogen in their atmospheres than their non-polluted counterparts (Gentile Fusillo et al., 2017)

A Kuiper-belt-like object

Xu et al. (2017) reported the composition of an extrasolar Kuiper-belt-like object accreted by the white dwarf WD 1425+540. The inferred abundances of this planetesimal are rich in volatile elements including carbon, oxygen, and the first detection of nitrogen accreted into the atmosphere of a white dwarf. The composition of the planetesimal is close to that of Halley's comet, and it is thought that it was perturbed from an exo-Kuiper-belt by the white dwarf's wide binary companion.

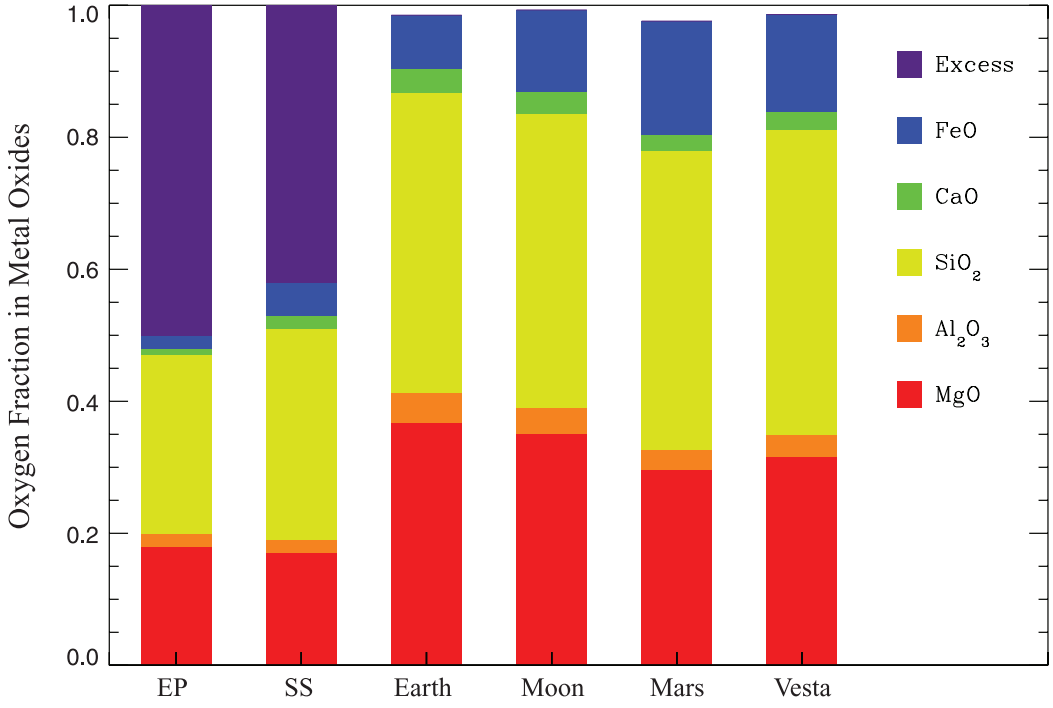

Figure 1.16: The excess oxygen in the atmosphere of GD 61 after accounting for the oxygen accreted in the form of minerals. The early-phase (EP, material has not had time to sink out of the atmosphere) and steady-state (SS, accretion and diffusion out of the atmosphere are in equilibrium) solutions are shown for GD 61, alongside the make-up of bodies in the solar-system. Figure reproduced from Farihi et al. (2013).

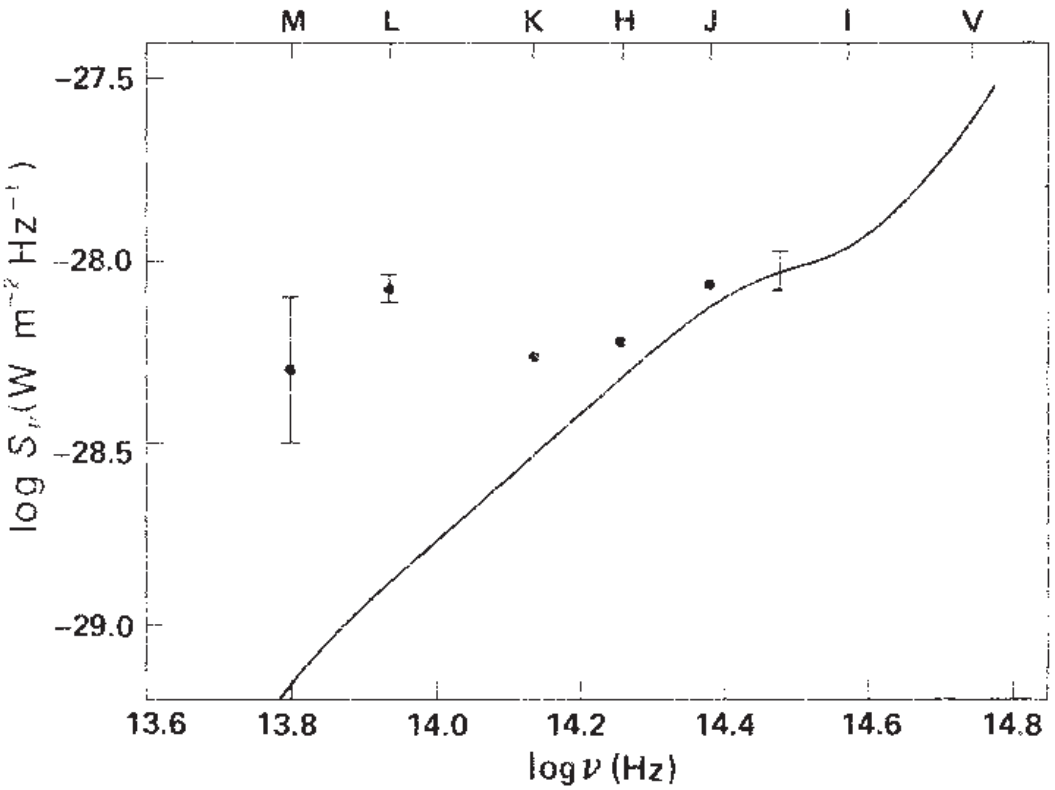

Figure 1.17: The infrared excess (points) over the white dwarf continuum (line) at G29–38. Figure reproduced from Zuckerman and Becklin (1987), identifying the first planetary debris disc at a white dwarf.

1.6 Debris discs

1.6.1 Dusty debris discs

G29–38 was discovered by Zuckerman and Becklin (1987) as the first white dwarf to host a debris disc via the detection of an infrared excess above the white dwarf continuum (Figure 1.17). Initially Zuckerman and Becklin (1987) interpreted this infrared excess as emission from a brown dwarf companion, however, the pulsations of the host white dwarf at G29–38 allowed Graham et al. (1990) to infer the presence of a dusty ring of debris, rather than a binary companion (Zuckerman and Becklin 1987 also suggested a dusty ring as a possible secondary explanation). The discovery of metal pollution of the white dwarf atmosphere was further evidence that the white dwarf is accreting from a circumstellar source (Koester et al., 1997).

Jura (2003) proposed that the infrared excess at G29–38 results from circumstellar dust produced by a tidally disrupted asteroid that entered the Roche radius of the white dwarf, and modelled the infrared excess as reradiated emission from an opaque flat ring of

dust. As described above, the perturbation and subsequent disruption of a planetesimal is now the canonical scenario for the production of a debris disc, and the model outlined by Jura (2003) is used to characterise dusty debris discs at white dwarfs. Since the discovery of G29–38, around 40 white dwarfs have been found to display an infrared excess (Jura et al., 2007; von Hippel et al., 2007; Farihi et al., 2008; Jura et al., 2009; Debes et al., 2011a,b; Brinkworth et al., 2012; Bergfors et al., 2014; Rocchetto et al., 2015; Dennihy et al., 2016; Farihi, 2016).

Studies of large samples have shown that $1-3$ % of white dwarfs host an observable dusty disc (Farihi et al., 2009; Steele et al., 2011; Girven et al., 2012; Rocchetto et al., 2015), which is surprisingly low, given that (i) 25 - 50 % of white dwarfs are metal polluted by circumstellar material (Zuckerman et al., 2010; Koester et al., 2014), and (ii) for most polluted white dwarfs (hydrogen-dominated DAs) the estimated lifetime of the discs ($\simeq 10^4 - 10^6$ yr, see Section 1.6.1) far exceeds the period for which metals diffuse through the atmosphere of the white dwarf (Girven et al., 2012) and therefore these stars must be currently accreting from a circumstellar reservoir. The deficiency of dusty disc detections has been attributed to multiple effects, one of which is that the emission from some debris discs is simply below the detection threshold. This has been hypothesised as the majority of systems with observed debris discs have moderate to high accretion rates (Rocchetto et al., 2015), and these systems may only be detected as they have the brightest discs. One way to decrease the emission from a dusty disc below the detection threshold is to reduce its surface area, e.g. having only a very narrow ring. While debris discs at white dwarfs are currently modelled as an opaque (optically thick) flat ring of dust, other scenarios have been put forward that could explain their apparant dearth, e.g., debris discs which are either optically thin, or purely gaseous Bonsor et al. (2017).

The observations obtained by infrared space observatories, primarily *Spitzer* (Werner et al., 2004) and *WISE* (Wright et al., 2010) have been instrumental for the detections of dusty discs, but the majority of these observations are only photometric. While this is sufficient for the detection of debris discs and estimating their inner and outer radii, characterising the mineralogical composition requires spectroscopic observations.

Reach et al. (2005, 2009) obtained infrared spectroscopy of G29–38 which exhibits a strong excess continuum emission superimposed with an additional silicate feature (Figure 1.18). They fitted the spectrum with a composite dust model, which provided the first mineralogical study of an exo-planetary body at a white dwarf. The ability to obtain spectroscopic observations in the infrared ceased when *Spitzer* ran out of cryogenic coolant and its spectroscopic instruments could no longer function, and will only return when the *James Webb Space Telescope* (*JWST*) is launched and operational (Gardner et al., 2006).

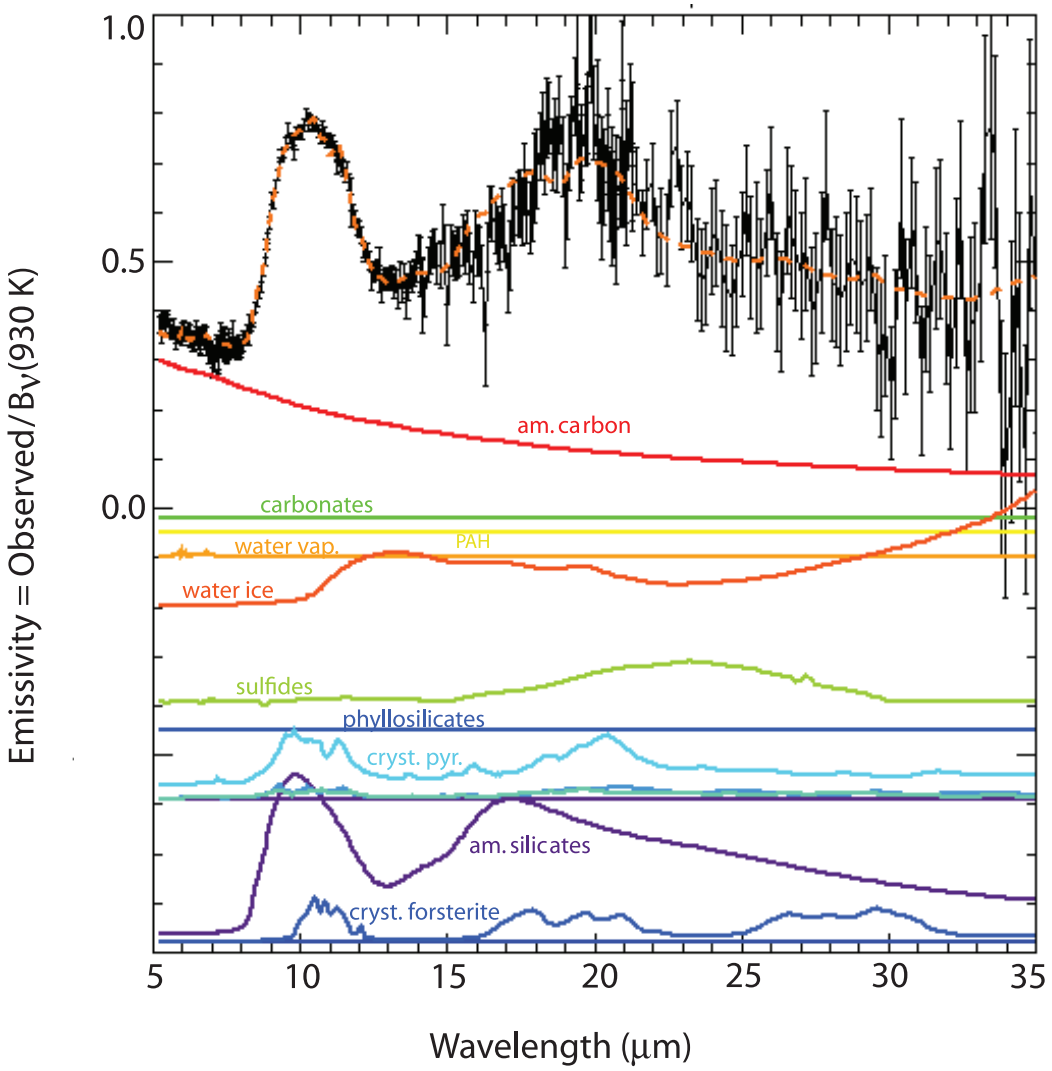

Figure 1.18: Spectroscopic observations of the infrared excess at G29–38 (black) along with a dust model fit (orange dashed line). The components of the dust are also shown individually, and are offset for clarity. The strongest spectroscopic feature is from silicate dust. Figure reproduced from Reach et al. (2009).

Lifetime of debris discs

With the number of debris discs discovered in the dozens, these systems can be analysed in a more statistical approach, and one example of such a study is the lifetime of the discs. Girven et al. (2012) developed a simple method for determining the lifetime of debris discs by combining the steady-state accretion rates obtained from DA white dwarfs with the lower limit on the mass accreted by DB white dwarfs, represented by

$$t_{\rm disc} \sim \frac{\langle M_Z \rangle_{\rm DBZ,disc}}{\langle {\rm d}M_Z/{\rm d}t \rangle_{\rm DAZ,disc}}, \tag{1.10}$$

where $\langle M_Z \rangle_{\rm DBZ,disc}$ is the average mass accreted by DBZ white dwarfs with a detected dusty disc, and $\langle {\rm d}M_Z/{\rm d}t \rangle_{\rm DAZ,disc}$ is the average accretion rate onto DAZ white dwarfs with a detected dusty disc. From this, Girven et al. (2012) calculated a disc lifetime of $\log(t_{\rm disc}[{\rm yr}]) = 5.6 \pm 1.1$ (3×10^4 yr to 5×10^6 yr). The large range of the possible lifetimes is due the spread of accreted masses and accretion rates seen at white dwarfs, and also assumes that: (i) the lifetime of the disc is shorter than the diffusion time-scale for DB white dwarfs, and (ii) that the metals in the convection zones of DB white dwarfs used in this calculation originate from a single accretion event. It is none the less a valuable first attempt at empirically estimating the lifetime of debris discs at white dwarfs (see also Jura 2008).

Debris disc variability

While debris discs are highly dynamical, there is little recorded variability in the infrared excess seen at white dwarfs. Xu and Jura (2014) discovered variability of the disc at WD 0959–0200, where the luminosity of the dusty debris decreased substantially in less than 300 days. This drop in flux was attributed to an increase in the inner radius of the debris disc. The authors proposed two hypotheses for the increase in radius, (i) a recent planetesimal impact onto the disc could cause a gradual decrease of luminosity of the disc (Jura, 2008), and (ii) an instability at the inner edge of the disc due to the presence of a gaseous component to the debris disc (see Section 1.6.2), where runaway accretion leads to a dramatic increase in the accretion rate, fed by the material at the inner edge of the dusty debris disc (Rafikov and Garmilla, 2012; Metzger et al., 2012).

More recently, Xu et al. (2018) and Farihi et al. (2018) discovered variability at three debris disc systems: G29-38 & SDSS J1228+1040, and GD 56 respectively. While SDSS J1228+1040 shows a similar decrease in luminosity to SDSS J0959–0200, observations of the disc around G29-38 revealed an increase in the infrared flux from the 10 μm silicate feature, and the disc at GD 56 appears to brighten and dim over a time-scale of 11.2 years. These observations suggest that there are different mechanisms generating the diverse variability seen at these discs (Xu et al., 2018).

1.6.2 Gaseous debris discs

A subset of debris discs around white dwarfs are known to host a gaseous component that can reveal insight into the dynamics and size of the disc via optical spectroscopy. Gänsicke et al. (2006) discovered the first gaseous disc around the white dwarf SDSS J1228+1040. The double-peaked emission profiles of the 8600 Å Ca II triplet (see Figure 1.14, (c)) are indicative of a flat, gaseous disc with particles on Keplerian orbits (Horne and Marsh, 1986), and can be used to determine the geometric extent of the disc. The two halves of the profile account for material moving towards (blue-shifted in wavelength) and away (red-shifted in wavelength) from the observer. The inner radius of the disc can be determined from the maximum velocity, i.e. the point at which the emission drops to the continuum level, and the outer radius can be estimated from the peak separation in the double peaked profile (Horne and Marsh 1986, see Fig. 2.9). The Ca II triplet profiles from the gaseous disc at SDSS J1228+1040 were used to demonstrate that the material orbits the white dwarf within the tidal disruption radius ($\simeq 1\,R_{\odot}$).

Soon after the discovery of SDSS J1228+1040, two more gaseous discs were discovered (Gänsicke et al., 2007, 2008), with additional systems uncovered throughout the years for a total of seven[2] gaseous debris discs (Gänsicke, 2011; Farihi et al., 2012; Melis et al., 2012; Wilson et al., 2014).

All known gaseous debris discs were discovered via their Ca II triplet emission, but there are signs of additional emission lines at these systems, e.g. Fe II at 5169Å in SDSS J1228+1040 (Gänsicke et al., 2006).

Variability of the Calcium triplet

A number of observations have demonstrated that the Ca II triplet varies, both in morphology and strength. Gänsicke et al. (2008) first identified changes in the morphology of the Ca II triplet at SDSS J0845+2257, where the red-shifted (rightmost) peak of each of the emission profiles dropped in strength between two observations obtained four years apart (Figure 1.19). More recently, Wilson et al. (2015) discussed the long-term variability of the Ca II triplet at SDSS J0845+2257 (Figure 1.20) over ten years of continued monitoring. The spectroscopic observations showed evidence of the peaks of the profiles changing in relative strength, with the blue-shifted (leftmost) peak becoming the dominant peak. This inversion of strength between the two peaks in the Ca II triplet profiles has also been seen in SDSS J1228+1040 (Melis et al., 2010).

[2]The Ca II triplet profiles detected at SDSS J114404.74+052951.6 by Guo et al. (2015) have recently been identified as emission from a brown dwarf companion, and hence this star is removed from the list of white dwarfs with gaseous debris discs (Wilson, private communication).

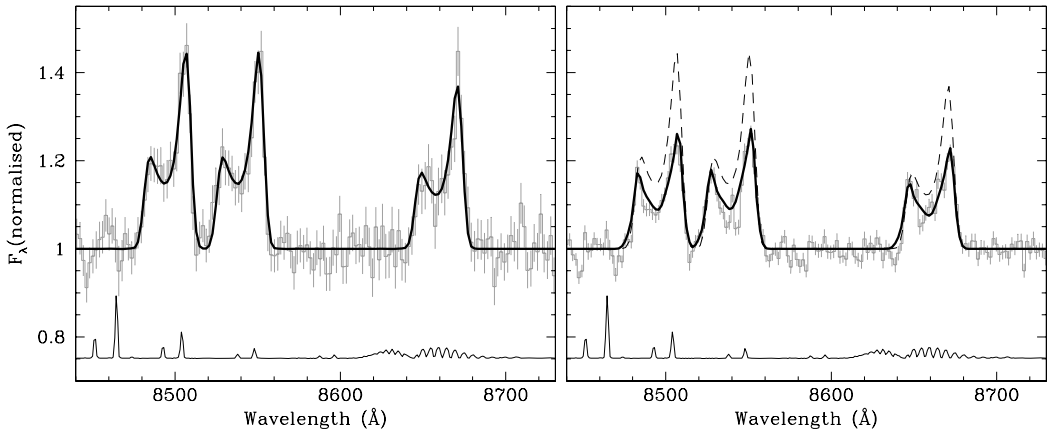

Figure 1.19: Comparison of the Ca II triplet profiles of SDSS J0845+2257 obtained in 2004 December (left-hand panel) and 2008 January (right-hand panel). A representative, normalised sky spectrum is also shown in both panels, offset by -0.3 for clarity. Reproduced from Gänsicke et al. (2008).

In addition, there is evidence of the Ca II triplet dramatically changing in strength, which was seen at SDSS J1617+1620 (Figure 1.21, Wilson et al. 2014). The system was originally identified from a spectrum obtained in 2008 by the SDSS (Gänsicke, 2011), however a previous spectrum taken in 2006 shows no sign of the Ca II emission. After 2008, the emission profile showed a steady decline in strength until it disappeared, and it is thought that additional material is impacting the disc, generating gas that is slowly accreted by the white dwarf.

1.6.3 Modelling the structure and evolution of debris discs

Modelling the structure of debris discs with both a dusty and gaseous component is not trivial, and multiple theories have been suggested to explain both the generation and emission of gaseous debris discs at white dwarfs. The general model for a gaseous debris disc is shown in Fig. 1.22, where the disc contains a dusty component which is flat and is bound by its inner and outer radius, the former defined by the sublimation point at which dust is sufficiently heated by the white dwarf to sublimate into a gaseous form (Bochkarev and Rafikov, 2011; Rafikov, 2011a,b; Rafikov and Garmilla, 2012; Metzger et al., 2012). The dust in the disc moves towards the sublimation point due to Poynting-Robertson drag (Guess, 1962), which is the loss of angular momentum of a particle orbiting a host body due to the radiation emitted by the host.

There are two main models that have been proposed to explain the presence of gaseous components to debris discs, (i) a feedback loop due to angular momentum transfer (Metzger et al., 2012), and (ii) a collisional cascade of large bodies that grind down and/or

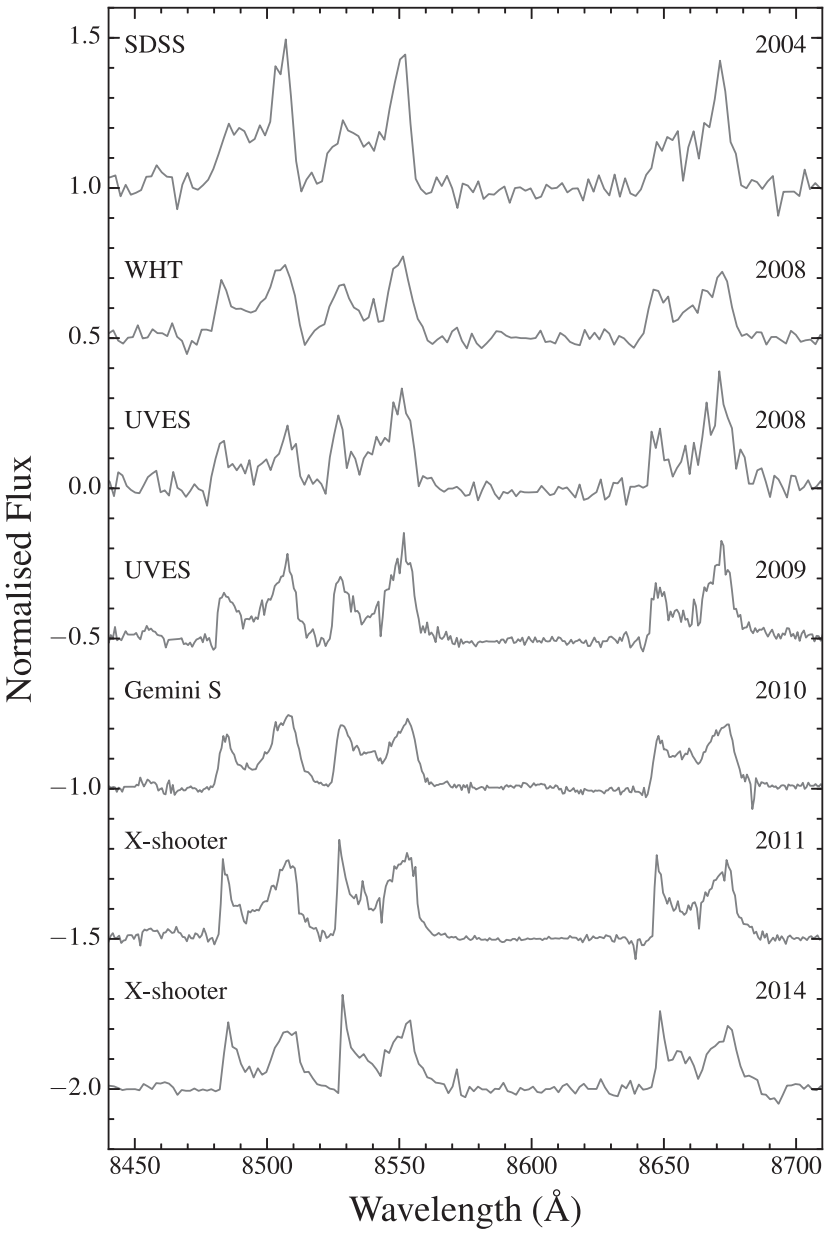

Figure 1.20: Spectra of the Ca II triplet at SDSS J0845+2257 obtained over ten years on various telescopes showcasing the morphological variability of the Ca II emission. Reproduced from Wilson et al. (2015).

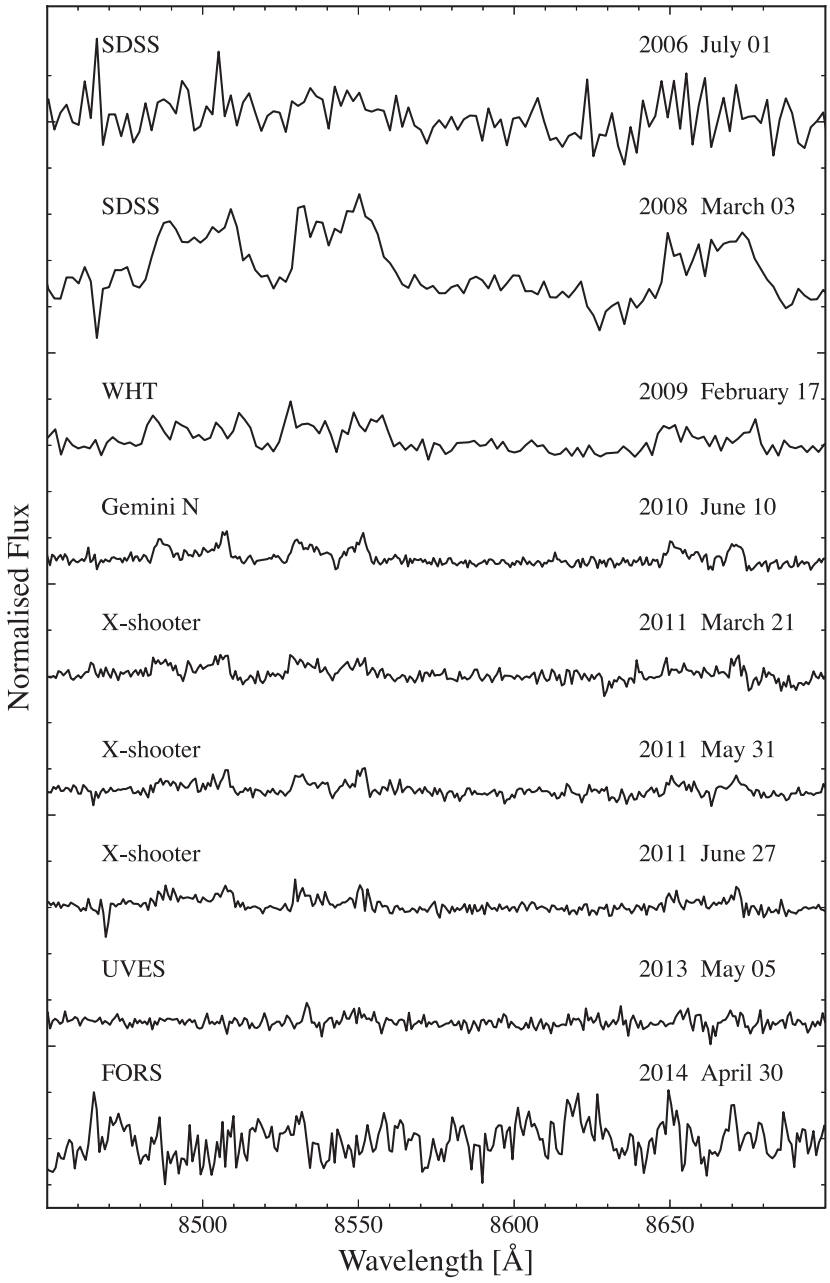

Figure 1.21: Spectra of the Ca II triplet at SDSS J1617+1620 obtained over eight years on various telescopes showcasing the transient nature of the Ca II emission. Reproduced from Wilson et al. (2014).

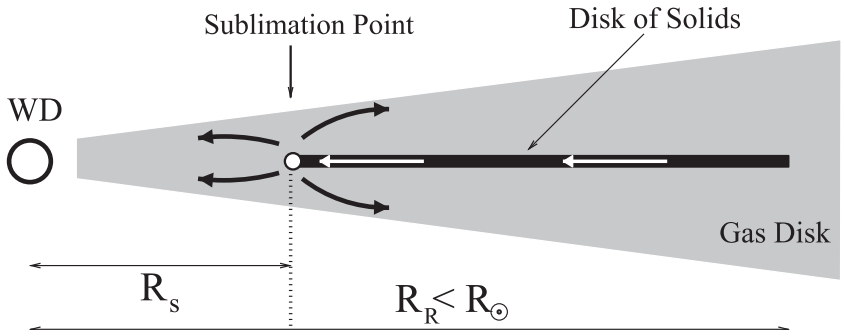

Figure 1.22: The model structure of a debris disc with a dusty and gaseous component, with the sublimation radius, R_s, noted. The white arrow show the movement of dust through the disc, whereas the black arrows show the movement of gas generated at the sublimation point. Adapted from Metzger et al. (2012).

vaporise to produce the gaseous and dusty debris disc (Kenyon and Bromley, 2017a,b), which are discussed in more detail below.

Gas production through a feedback loop

When the dust in the disc loses enough angular momentum to reach the sublimation radius, it will turn into gas and spread out due to angular momentum conservation, with some gas moving towards the white dwarf and some outward into the region the dusty disc occupies. The gas that moves into the dusty debris region will have a slower orbital velocity than the dust, and generate drag, slowing down the dust grains and bringing them into the sublimation radius at a faster rate. This leads to a runaway accretion process, as gas generated from drag-induced accretion is produced faster than it can be removed by viscous diffusion (Rafikov, 2011b). If this model is correct, then it would suggest that the systems showing gas emission are those in a runaway accretion phase, and the other debris discs host a significantly weaker, undetectable gaseous component (Metzger et al., 2012).

Gas production through a collisional cascade

Kenyon and Bromley (2017a) proposed a model where debris discs are generated by solid bodies of radius r_0 injected discretely into a narrow annulus near the tidal disruption radius of the white dwarf at a mass rate $\dot{M}_0$. These bodies will undergo a collisional cascade, where they are ground from sizes up to $\simeq$ 100-300 km down to $\simeq 1\,\mu$m dust grains (Kenyon and Bromley, 2017a). Any particles smaller than 1 μm are assumed to be vapourised and feed a gaseous disc (Kenyon and Bromley, 2017b). In this model, the gas mass and gas accretion rate either remain constant for small r_0 (≤ 10 km), or fluctuate between high and low states for large r_0, with the duration of high states dependant on the value of $\dot{M}_0$.

Physical origin of the emission lines from the gaseous disc

For the gaseous debris discs to generate the observed Ca II triplet emission, they need to be heated to several 1000 K (Melis et al., 2010). Two main mechanisms have been suggested to heat the gas to such temperatures; (i) photoionisation, and (ii) viscous heating. Debris discs are subject to the intense ultraviolet radiation from their white dwarf host, which will photoionise the gas (Melis et al., 2010; Kinnear, 2011). The gas heats up as it (a) absorbs the ultraviolet photons, and (b) cools inefficiently as it is optically thin. Hartmann et al. (2011) produced Non-LTE (Local thermal equilibrium) models of gaseous debris discs, which generate energy through viscous heating. However, heating the disc viscously would require accretion rates far in excess of what is observed.

1.7 The transiting debris around WD1145+017

No planets have been confirmed around white dwarfs so far, but the extensive work and data described above provides compelling evidence for their existence. However, the strongest evidence for planetary material around a white dwarf are the highly dynamical transits observed at the white dwarf WD 1145+017 (Berg et al., 1992). The transits were discovered by Vanderburg et al. (2015) with the *Kepler* K2 mission (Howell et al., 2014) via a collection of transits seen on periods clustering around 4.5 hr.

The ground based follow-up photometric observations of WD 1145+017 was obtained with a much higher cadence than the *Kepler* data (down to 5 seconds compared with the 30 min cadence of *Kepler*), revealing complex transit events (Figure 1.23) that vary in shape, size, duration, and phase on time-scales of several orbital cycles (Gänsicke et al., 2016; Rappaport et al., 2016). Theoretical work on WD 1145+027 has given constraints on the system parameters (Veras et al., 2016; Gurri et al., 2017), as well as the possible structure of the bodies orbiting the white dwarf. The bodies are also likely differentiated, allowing occasional mass loss from their mantles (Veras et al., 2017). It is thought that the complex transit events are generated by dusty debris that is ejected from the bodies, which is supported by the variable shape and depths of the transits.

Spectroscopic observations of WD 1145+017 show broad absorption from circumstellar gaseous material in orbit around the host white dwarf (Xu et al., 2016). As with the photometric observations, variability in the spectroscopic features have been observed (Redfield et al., 2017)

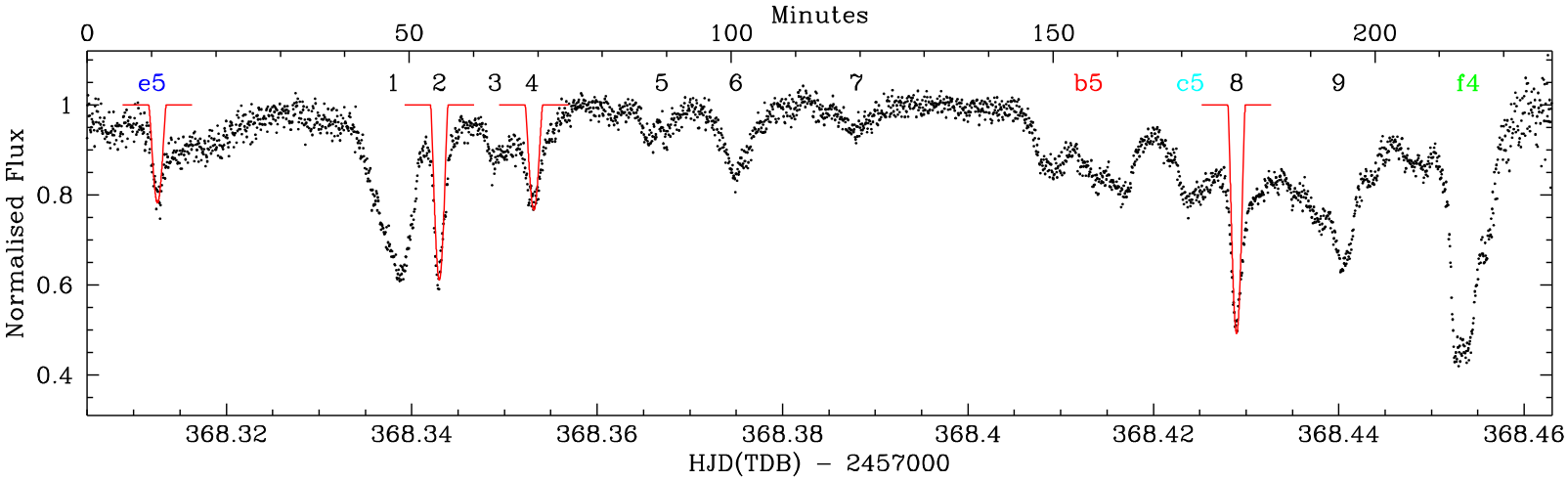

Figure 1.23: High-speed photometry of WD 1145+017 depicting the complex structure of the transiting events that vary in shape, depth, and duration. Reproduced from Gänsicke et al. (2016).

1.8 Thesis layout

In this thesis I will present my research on gaseous debris discs at white dwarfs. Chapter 2 discusses: (i) the methods used to reduce photometric and spectroscopic data present through the Thesis, and (ii) the key analysis tools to interpret the results. Chapters 3 and 4 explore the long term variability of gaseous debris discs at white dwarfs by investigating the evolution of the Ca II triplet of the discs in two systems, SDSS J1043+0855 and SDSS J1228+1040. While both of these systems share a common evolution, SDSS J1228+1040 is brighter, and has more extensive time-resolved spectroscopy, which allowed me to generate the first image of a debris disc using Doppler tomography, which models the disc as a fixed intensity pattern that precesses on a period of $\simeq 27$ yr. In Chapter 5, I present the discovery of short term spectroscopic variability of the gaseous debris disc in SDSS J1228+1040 on a period of 2 hr, which I interpret as the signature of a planetesimal orbiting within the debris disc. The final science chapter of this Thesis, Chapter 6, explores the occurrence rate of gaseous debris discs at white dwarfs, which has so far been heavily skewed by observational biases. I finally conclude my results in Chapter 7, and discuss future prospects for the study of gaseous debris discs.

Chapter 2

Methodology

The dominant source of information we receive from the Universe to detect and study astronomical sources is electromagnetic radiation, and as observers we have built many facilities to characterise light. Measuring the brightness of an astronomical object is generally known as photometry, whereas dispersing the light to analyse its wavelength dependant brightness is known as spectroscopy. These are the two main ways we study electromagnetic radiation, and I introduce these techniques below.

2.1 Photometry

Imaging is the simplest way to view the Universe, and it allows one to measure the brightness of an object. Imaging can be used to simply measure the position of an astronomical object (accurate position tracking of astronomical sources is known as astrometry), which has been performed by humans for millennia, or to characterise the brightness of a source through the method of photometry. Multiple observations of a source can be put together as a light-curve, measuring brightness variability, which allows astronomers to detect transiting exoplanets or debris around stars.

It is often useful to isolate a small section of a star's spectral energy distribution, and filters are used as they only transmit certain wavelengths of the light emitted by the star. Figure 2.1 shows the spectral response of the filters used for the Sloan Digital Sky Survey (SDSS), which clearly divide the optical component of the electromagnetic spectrum into five distinct bands. By comparing the light received from a source in different bands, many astrophysical properties can be determined which are discussed in Section 2.1.1.

However, the observations made using telescopes usually contain artefacts and systematic uncertainties which require additional calibration images to be obtained to correct the science image. These calibration steps are described below:

Bias frames: A bias frame is an image taken with zero exposure time, and is a measure of two factors: (i) the noise generated from the process of reading the photons recorded by the detector into a digital format, and (ii) the additional offset added by the readout process to circumvent negative counts. Many bias frames are obtained and averaged to create a "master bias", which is then subtracted from the science image.

Flat field: Any detector has variations in the sensitivity of the pixels in their ability to detect the intensity of light. To correct for this, "flat fields" are taken to determine the sensitivity of each pixel, and are usually images of a uniform illumination of the detector. To achieve this, an image of either the sky during twilight is taken, or a flat field screen is lit up in the dome of a telescope to illuminate the detector. A number of flat field images are taken, averaged, normalised, and then divided out of the science image so every pixel has the same effective sensitivity.

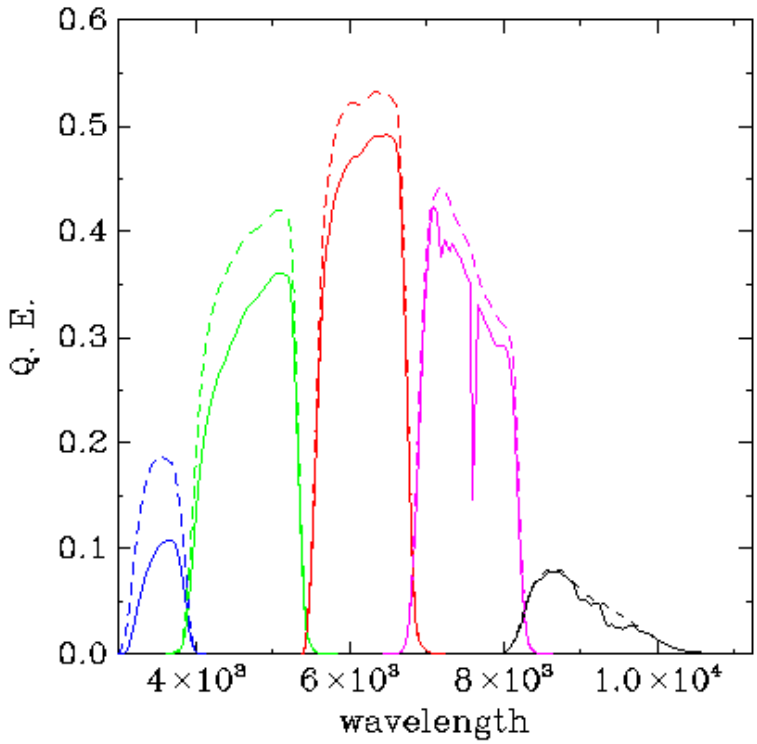

Figure 2.1: The spectral response (or QE) curves for the five filters used by the Sloan Digital Sky Survey (SDSS) at the 2.5 m telescope located at the Apache Point Observatory in New Mexico (Gunn et al., 2006). The transmission curves for the filters u, g, r, i, and z are shown in blue, green, red, pink, and black respectively, illustrating the broad range of the electromagnetic spectrum each filter can view. The solid lines give the response functions including all effects from the atmosphere to the detector, whereas the dashed lines do not include the atmosphere (Doi et al., 2010). Image obtained from http://classic.sdss.org/dr7/instruments/imager/ on 2017 - 10 - 21.

The process of bias subtraction and flat field correction is shown for an ULTRACAM Sloan g band image of SDSS J122859.93+104032.9 in Fig. 2.2. The images before and after correction are shown in the bottom left and bottom right panels of Fig 2.2 respectively. To determine the flux observed from a particular source, some additional steps are required:

Sky/Background subtraction: If the observations have been taken from the ground, then they also record emission from the atmosphere. To measure the number of counts from the source, the excess light due to the inherent brightness of the sky needs to be taken into account. Fig. 2.3 is an enlarged image of the box in Fig. 2.2, and shows an example set of apertures that can be used to determine the counts from the star and the sky (within the white circle), and counts from the sky alone (red annulus). By correcting for the differing area of the two regions, one can subtract the estimated sky counts from the region containing source and sky counts to calculate the total number of counts from the source. If there is any other background emission that affects the detector evenly, then this can also be removed in the same way.

Flux calibration - Standard star observations: The detector reads the brightness of each pixel in counts, and a conversion must be done to convert from counts to units of brightness, i.e. flux. To determine this conversion, an image of a "photometric standard star" must be taken. Photometric standard stars have a well known brightness, which can be used to determine the flux per count rate (counts divided by exposure time) for the set-up used to obtain the observations, and determine the flux of the science image.

2.1.1 Photometric methods

Colour diagrams

Using the SDSS filters as an example, if a target is observed with the g and r filters, then a 'colour' for that target could be determined, which in astronomy is the difference in brightness between two filters. The $g-r$ colour allows us to determine whether one star is 'bluer' or 'redder' than another, which gives an indication of their relative temperatures and a simple measure of which is hotter or colder. By using multiple colours, a colour-colour diagram can be generated as a tool to distinguish between different types of sources, e.g. quasars, main sequence stars and white dwarfs.

Another application of filter-based photometry is employed when observing clusters of stars, which are assumed to (i) have formed at the same time, and (ii) all be at the same distance from the Earth (i.e. their apparent magnitudes can be used in place of absolute magnitude). By observing all of these stars in a given filter, their relative brightness, or luminosities can be compared. If this is used in conjunction with another filter, then one

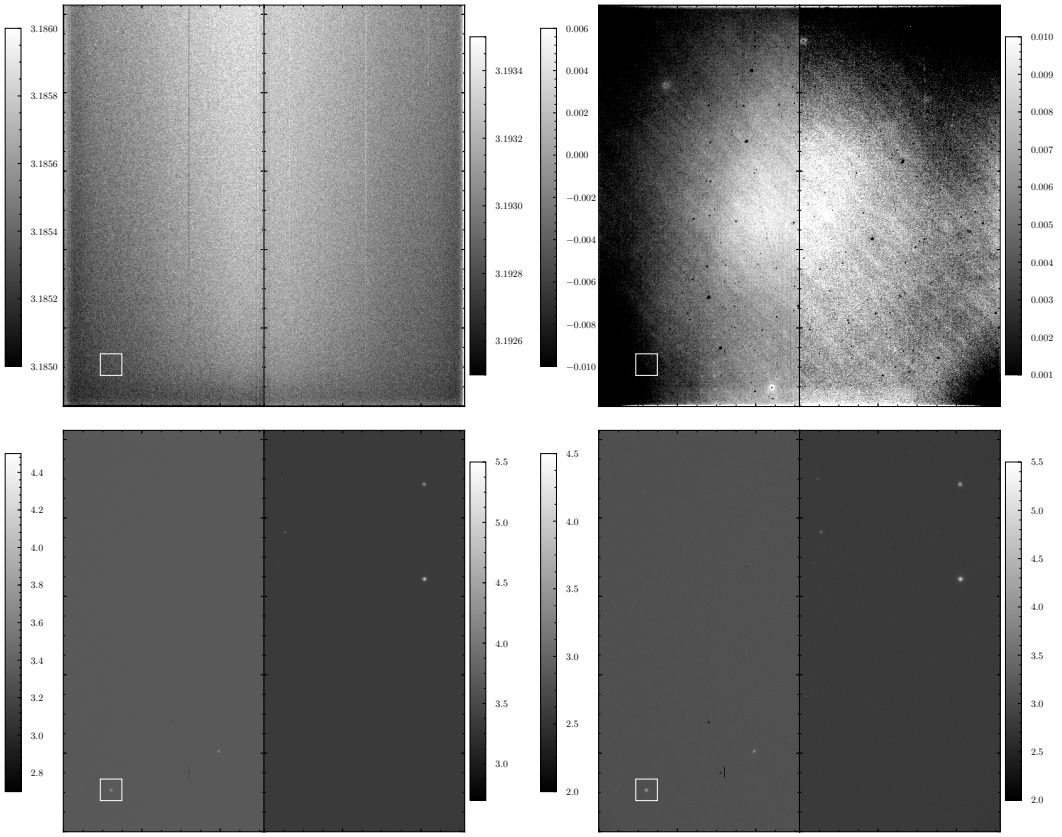

Figure 2.2: The reduction process is shown for a Sloan g' band image obtained with ULTRACAM on the WHT. The CCDs used in the ULTRACAM detector have two readout channels, and so each image is separated into two halves. The four panels show frames at various stages of the calibration of a photometric image: a bias frame (top left), a flat frame (top right), the observed image (bottom left), and the final image after correcting (bottom right), which has been bias subtracted and flat field corrected. A greyscale bar is given for each half of the images, representing $\log_{10}$(counts) (normalised counts in the case of the flat field image).

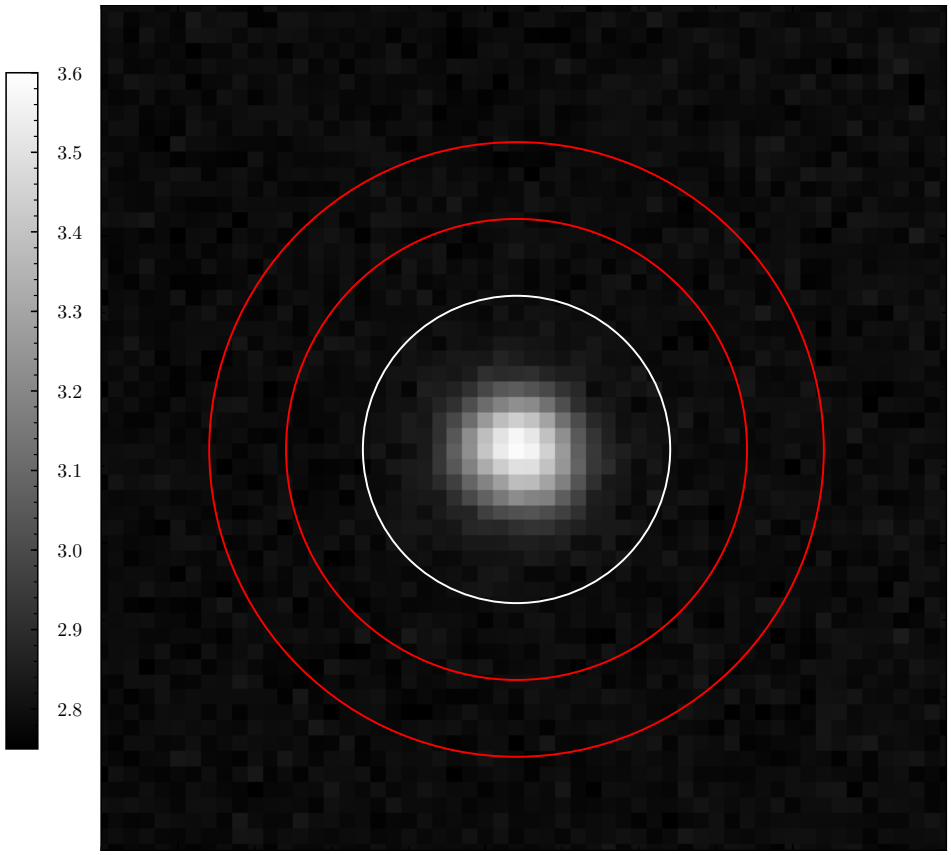

Figure 2.3: The region enclosed by the white square in the bottom right panel of Fig. 2.2 is shown here with several apertures. The white aperture defines the region of flux from the star (here, SDSS J122859.93+104032.9), and the two red apertures define the annulus in which the sky counts are estimated.

can also determine the stars' colours, and therefore their relative temperatures. Plots of luminosity versus temperature are known as Hertzsprung-Russell diagrams, and have allowed astronomers to study the evolution of stars by observing a large number of stars at different phases of evolution. They are also used to illustrate the evolution of a single star throughout its lifetime, such as Figure 1.2.

Differential photometry

As mentioned above, a major use of photometry is to obtain light-curves of systems to determine their variability over time, and is commonly done using differential photometry. For these observations, a photometric standard star is not required, only a non-variable "comparison star." The variations between each exposure, such as changing air-mass or cloud variability, are captured by both the science target and the comparison star, and by dividing the brightness of the target by that of the comparison, these effects are removed, leaving only the variability of the target (see Figure 1.23 for an example of a light curve obtained from differential photometry).

2.2 Spectroscopy

Spectroscopy is a powerful technique that disperses observed photons to investigate wavelength dependant features of thermal or atomic processes (an example ultraviolet spectrum of SDSS J1228+1040 is shown in Fig. 1.15). While this radiation can be produced in a wavelength-continuous manner, e.g. blackbody radiation, electron transitions between atomic energy levels (bound-bound transitions) must produce or absorb photons with discrete wavelengths, generating emission or absorption features in the spectrum of an object. These features are critical tools in determining fundamental astrophysical properties, such as the velocity of a star or material in an accretion disc (see Section 2.2.2), or the magnetic field which the emitting or absorbing particles are subject to. However, to be able to observe such features, the light from the source must be passed through a device called a spectrograph.

Figure 2.4 shows the schematic of a simple spectrograph that is used to disperse the electromagnetic radiation of an astronomical source onto a detector to produce a spectrum. The light reflected from the telescope is focused through the slit of the spectrograph, which is usually positioned at the focal plane of the telescope. The light diverges and is reflected by a collimating mirror creating a parallel beam. The beam of light is then reflected and dispersed by a grating, which reflects light with a wavelength-dependent angle. The dispersed light rays are then focused by the camera mirror onto the detector. As the focal point

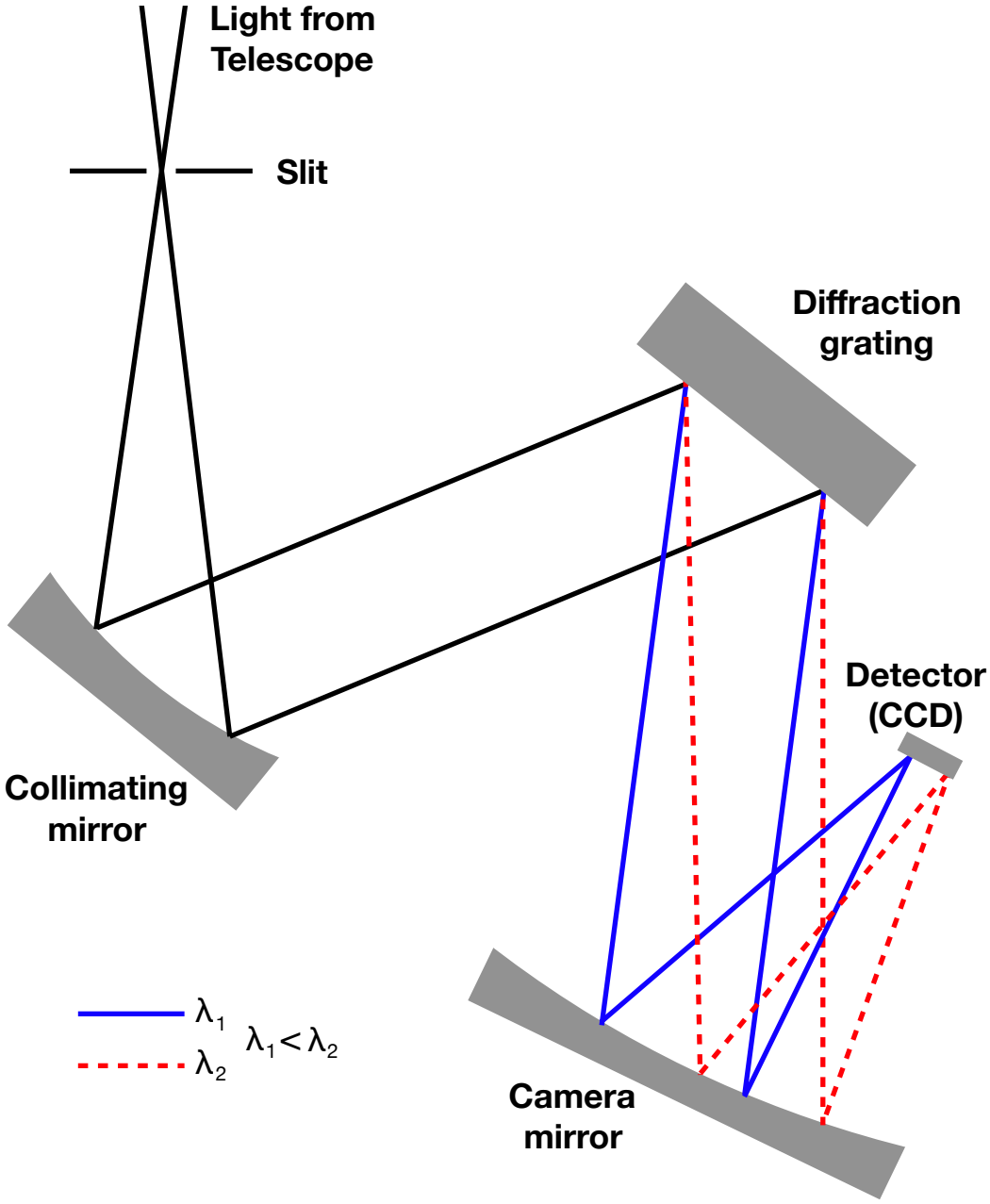

Figure 2.4: Schematic of a spectrograph.

of the camera mirror is dependant on the angle of incidence (and therefore wavelength), the spectrum of the source is spread across the detector as an image.

While the raw image can be used to quickly identify prominent features (see Fig. 1.12), it must be calibrated before any precise analysis can be done. These calibration steps are discussed below, a number of which are similar to those in the photometric method (see Section 2.1):

Bias frames: Bias frames used for spectroscopy are taken in the same way as with photometric data. An example bias frame is shown in Fig. 2.5 (a).

Flat field: The flat field obtained for a spectrum is similar to the flat field obtained for a photometric observation, except that the wavelength-dependant sensitivity of the detector and the grating also needs to be accounted for. To do this a flat field lamp is used to uniformly illuminate the slit of the spectrograph. The resulting image is then normalised to the continuum of the flat field lamp spectrum, and finally divided out of the science spectrum so every pixel has the same effective sensitivity. An example spectrum flat field is shown in Fig. 2.5 (e).

Sky subtraction: As with photometry, ground based spectroscopy is affected by emission (and absorption, see Section 2.2) from the atmosphere. These sky emission lines contaminate the observed science spectrum, and usually need to be subtracted out before the observations can be analysed. This is for spectroscopy using a slit, done by using the sky emission spectrum obtained on the same CCD as the science spectrum. For fibre-based spectroscopy, an additional spectrum of a blank position in the sky is required. Once a sky spectrum is obtained, this can be subtracted from the science spectrum.

Wavelength calibration - Arc lamp observations: The spectrum of the astronomical source is dispersed in wavelength over the pixels of the detector. Changes in the set up, e.g. telescope position or dispersion grating angle means that there is never a constant pixel-to-wavelength conversion, and thus arc lamp spectra are required. Arc lamps produce light via an electric arc generated by electron transitions in different materials used in the arc lamp, e.g. Copper and Neon (CuNe). These transitions are at very specific, well known wavelengths that can then be used to map a wavelength scale to the pixel scale on the detector. Once this is done, the spectrum can be wavelength calibrated. An example for an arc lamp exposure is shown in Fig. 2.5 (d).

Flux calibration - Standard star observations: The detector used to observe astronomical sources measure the flux in counts, which is wavelength dependant due to the varying efficiency in the interactions of light with the components in the spectrograph (including the detector itself). To convert from counts to flux, one must know the absolute response function of the spectrograph, and this is obtained by observing “standard stars." These stars are well modelled, often with accurate distances, and can be used to determine

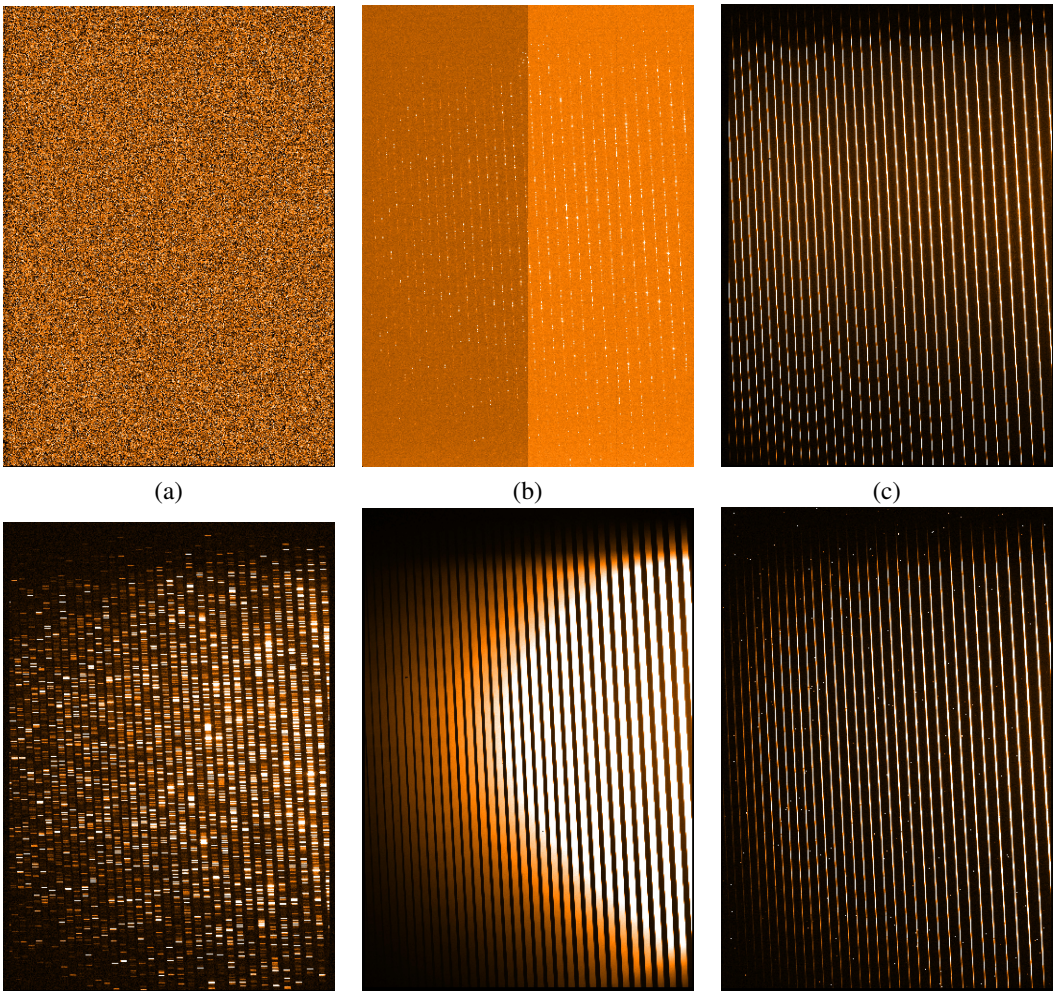

Figure 2.5: (a) a raw bias frame; (b) a raw format check frame; (c) a raw order definition frame; (d) a raw arc lamp frame; (e) a raw flatfield frame; (f) a raw standard star frame for the UVES detector. Figure taken from the UVES pipeline manual version 22.17 from http://www.eso.org/sci/software/pipelines/, accessed [2018-07-06].

the wavelength dependant transmission/absorption of the spectrograph, and to determine the count-to-flux conversion needed. A flux calibrated spectrum can then be simply obtained by dividing out the response function. An example standard star observation is shown in Fig. 2.5 (f).

Telluric correction : A major issue with ground-based astronomy is that light is absorbed as it travels through the Earth's atmosphere to our detectors. Absorption lines that arise in spectroscopic observations due to absorption in the Earth's atmosphere are called telluric features, and the major contributing compounds are water vapour, molecular oxygen, carbon dioxide and methane. The two main ways of removing telluric features in spectra are to either model them (Smette et al., 2015), or to use empirical, i.e. observed 'telluric standard templates.' These templates are produced by observing standard stars, and then carefully modelling and dividing out the stellar spectrum leaving just the telluric component.

The method I have used in my thesis to correct telluric features in X-shooter VIS arm spectra (see Section 2.2.1) is based on a library of 152 empirical telluric transmission spectra from Chen et al. (2014). Each template includes the normalised telluric absorption features over the wavelength range 5300 – 10200 Å (Figure 2.6). The atmospheric contamination does not affect this entire range and hence I initially split the templates into seven smaller regions which are corrected for independently. First, the observed spectrum is continuum normalised, and then each of the seven regions are fitted to all 152 templates with two free parameters; a wavelength shift (for telescope flexure) and the strength of the telluric features (which varies with the atmospheric conditions between different observations). The best-fitting template is then used to correct a given region. An X-shooter spectrum of SDSS J1228+1040 is shown in Figure 2.7, before and after dividing by the normalised telluric templates. The insets of Figure 2.7 reveal some of the regions affected by tellurics in more detail, illustrating the excellent success of this method.

2.2.1 UVES and X-Shooter: Echelle spectrographs

All of the spectroscopic data I have corrected from their raw form to a reduced spectrum were observed with two instruments: X-shooter (Vernet et al., 2011) and the Ultraviolet and Visual Echelle Spectrograph (UVES, Dekker et al. 2000) which are both on the ESO Very Large Telescope (VLT). To perform these reductions, I used the `REFLEX` reduction workflow[1] using the standard settings (see Section 2.2 for more information on the reduction methods used) and optimizing the slit integration limits (Freudling et al., 2013). Other spectroscopic observations I have analysed in this thesis were either reduced by collaborators or obtained calibrated from scientific archives (e.g. SDSS spectra).

[1]documentation and software for `REFLEX` can be obtained from http://www.eso.org/sci/software/reflex/.

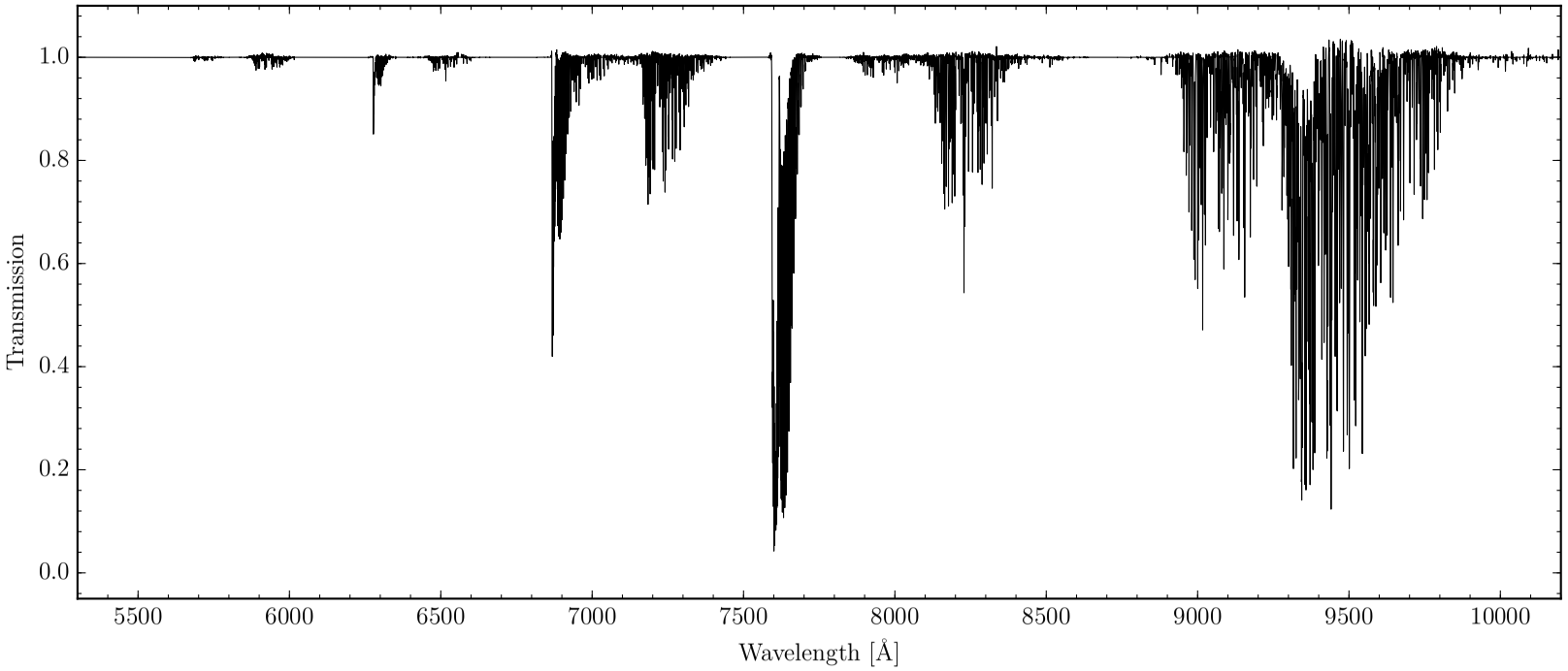

Figure 2.6: An empirical telluric transmission template from the X-Shooter Spectral Library (Chen et al., 2014).

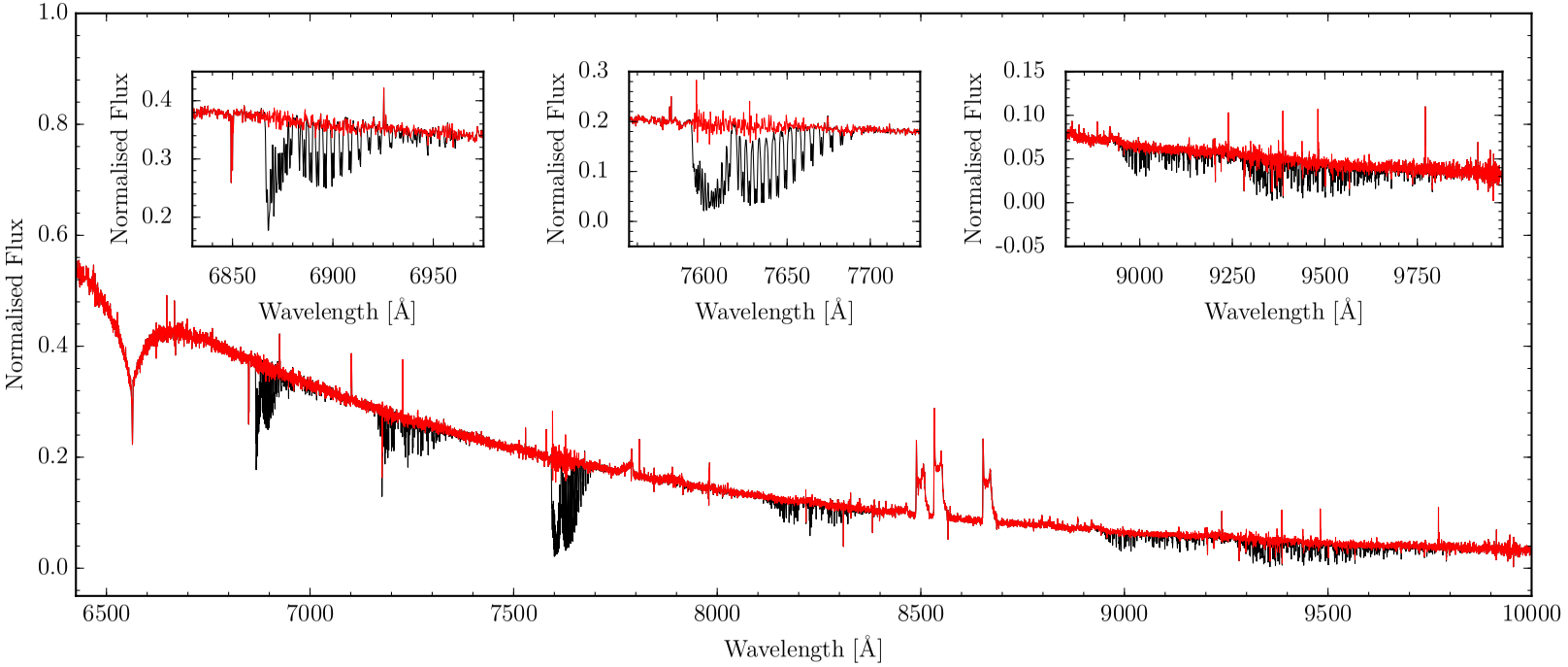

Figure 2.7: An example of a telluric corrected X-shooter spectrum of SDSS J1228+1040 (red) compared to the uncorrected sprectum (black). The insets show regions that are more heavily affected by telluric contamination.

Echelle spectrographs

Both UVES and X-Shooter are echelle spectrographs, an example of which is shown in Fig. 2.8. Echelle spectrographs spread the exposed light over multiple rows, or 'orders' on the detector, which allows a more efficient use of the two-dimensional collecting area to improve wavelength coverage and/or resolution. To achieve this, the light is dispersed using an echelle grating, which is designed to be efficient at high incident angles and therefore high order diffraction. This leads to high resolution spectra, but also significant order overlap (for example, the fifth order diffraction of a 600 Å photon will overlap with the sixth order diffraction of a 500 Å photon, $n\lambda = 5 \times 600\text{Å} = 6 \times 500\text{Å}$). This is resolved by the use of a cross disperser, which disperses the light orthogonally to the dispersion direction of the echelle grating to produce a 2D array of order-separated spectral trails, which can be clearly seen on the UVES detector in Figs. 2.5 (d), (e), and (f). The calibration of an echelle spectrum is largely similar to that of a standard spectrum. However, sometimes there are instrument specific differences, such as relating to the position of the orders on the UVES detector, which are described below:

Format check frame: This is an optional image taken on the detector to provide an initial "guess" solution for the spectral order format, and is shown in Fig. 2.5 (b) for the UVES detector.

Order definition frame: To precisely identify the position of the orders, an order definition frame is obtained by taking an exposure through a narrow slit which is illuminated by a continuum lamp, resulting in a high S/N frame. An example of this is shown in Fig. 2.5 (c).

UVES

UVES is a high resolution (R > 40 000) spectrograph on the VLT, that splits the light entering the telescope to blue and red arms (Dekker et al., 2000). The light in the blue arm is directed onto a single detector, whereas the light directed into the red arm is split over two detectors. The central wavelength of the two arms can be adjusted to study different regions in the optical spectral range. However, one must be careful when defining the central wavelength of the red arm, as there is a small gap (~0.96 mm) between the two detectors which results in gap in the wavelength coverage. If the region of interest (e.g. the Ca II triplet) is chosen to sit at the central wavelength, it may fall in this gap and not be observed.

X-Shooter

The most important region of the spectrum to observe in gaseous debris discs is in fact the Ca II triplet emission region around 8600 Å. However, the large wavelength range of

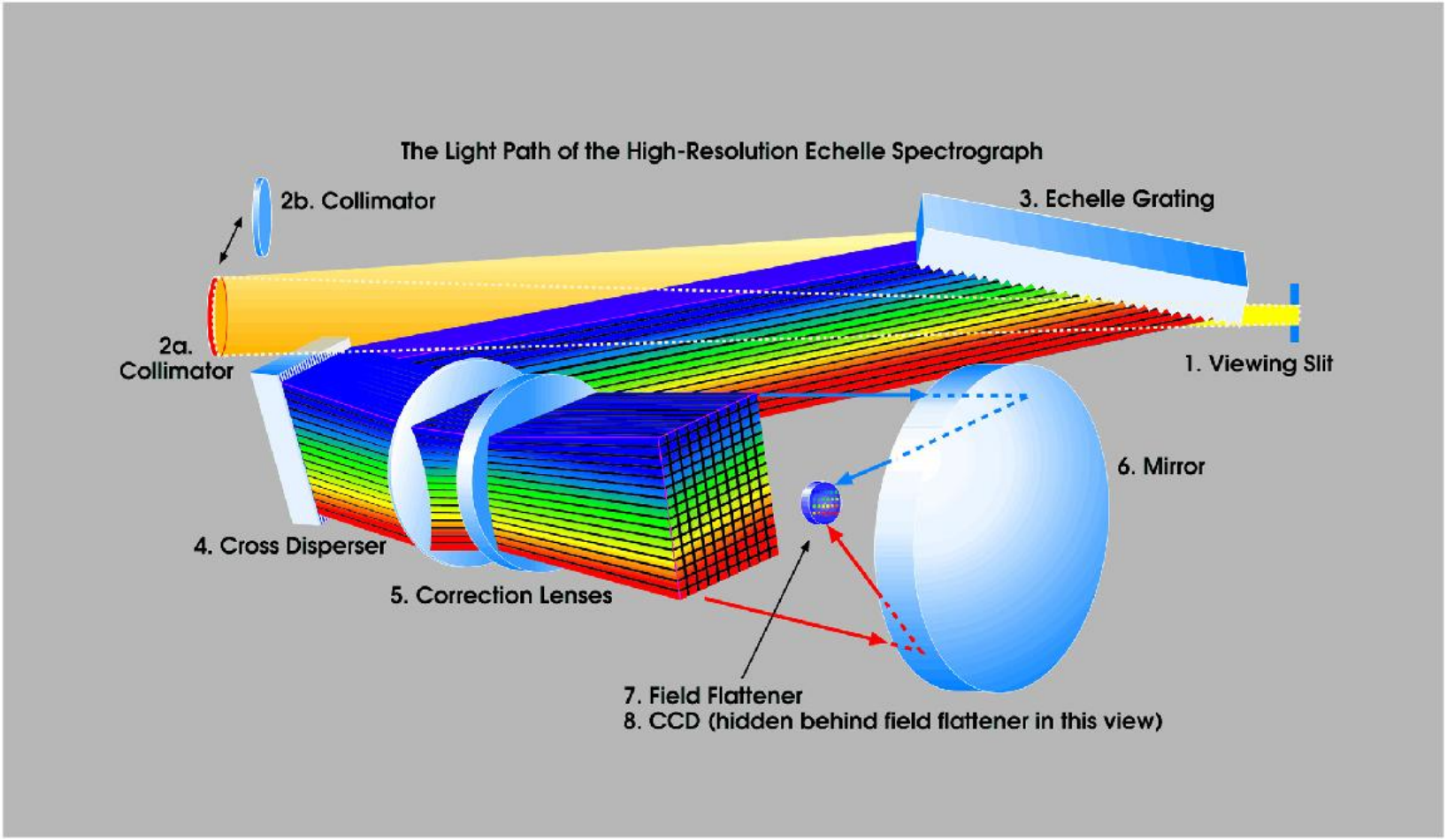

Figure 2.8: Schematic of an echelle spectrograph. The light is dispersed in two spatial directions, allowing for a more efficient use of the detector's collecting area compared to a standard spectrograph which only disperses in one spatial direction (see Fig. 2.4). Image obtained from https://www2.keck.hawaii.edu/inst/hires/ on [2018-11-06].

X-Shooter along with its intermediate resolution allows one to investigate the accretion of metals and the fundamental properties of the white dwarf (e.g. temperature, mass) along with the gaseous material.

X-Shooter is a single-target, intermediate-resolution (R ∼ 4000–17 000) spectrograph with three channels that covers a fixed spectral range from 3000 Å to 25 000 Å, and is mounted on the VLT (Vernet et al., 2011). The light is split using two dichroics into three channels that process different wavelength regions of the spectrum, and are named the UVB (3000 – 5500 Å), VIS (5300 – 10 500 Å), and NIR (9800 – 25 000 Å) channels (or arms).

The resolution of the X-Shooter instrument is lower than that of UVES, however it covers a larger wavelength range in a single observation and can achieve a sufficient signal-to-noise ratio with shorter exposures. As such, we have preferentially chosen X-Shooter to observe gaseous debris discs where possible. While debris disc systems show an infrared excess from the dusty disc, this is not usually detected in the NIR arm as the excess only begins to become apparent around ≃ 22 000 Å. Therefore, we do not analyse this region.

2.2.2 Spectroscopic methods

Velocity transformations

Spectroscopic features such as absorption or emission lines provide powerful tools to measure the velocity of the emitting source of light with respect to the observer. The radial velocity, v can simply be found using the Doppler shift equation

$$\frac{v}{c} = \frac{\lambda_o - \lambda_r}{\lambda_r}, \tag{2.1}$$

where c is the speed of light, and λ_o and λ_r are the observed and rest wavelengths of the feature respectively. (Radial) velocity measurements are used in a variety of ways, such as determining the radial velocity of a star by measuring the position of a photospheric absorption feature relative to the rest wavelength of that feature. Another useful application is analysing the velocity profile from the emission of a specific ion in an accretion disc (Figure 2.9), to infer information about the geometric structure of the disc.

Equivalent width calculations

When an emission or absorption profile is detected in a spectrum, it is often useful to compare this to either time-resolved spectra of the same system or to other systems with similar features. A good quantitative measure of the strength of a spectroscopic feature is the Equivalent Width (EW), which is independent of (i) the resolution of the instrument used to collect the spectrum, and (ii) the specific shape of the line. The EW, W_λ, measured between

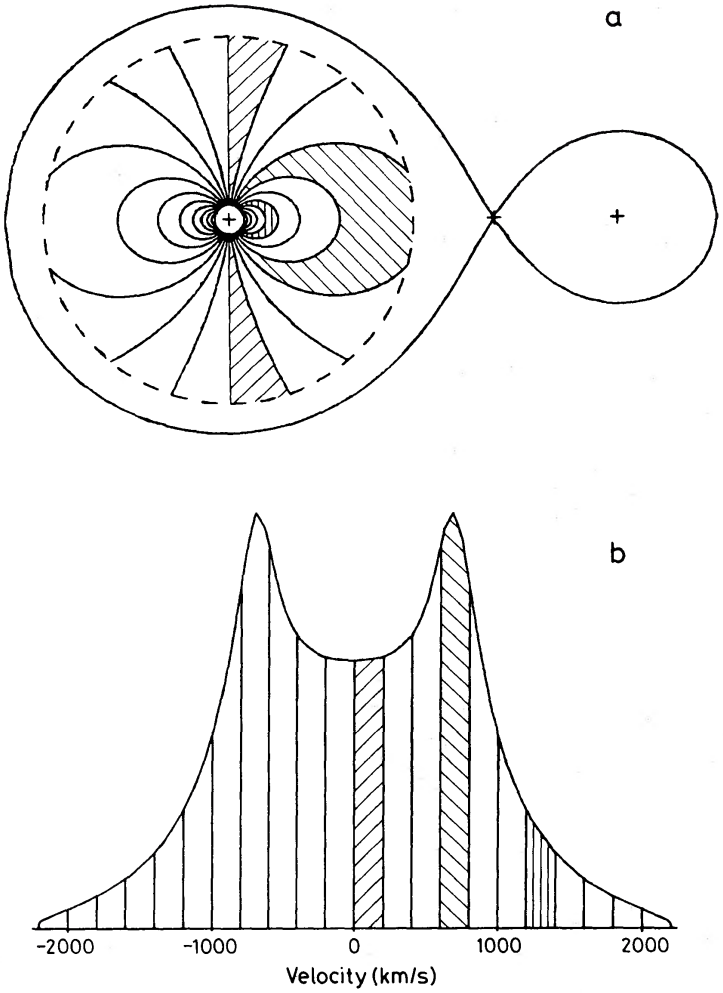

Figure 2.9: (a) An accretion disc in a binary system, bounded by the dashed circle. Assuming the disc rotates clockwise and is observed from below (i.e. the bottom of the page), the observer will detect a radial velocity profile shown in (b). The light that generates the double peaks in the radial velocity profile are dominated by the material in the outer regions of the disc (top-left to bottom-right diagonal striped region). Moving radially inwards, particles orbit at higher radial velocities, and the gas near the inner edge dominates the structure of the wings in the radial velocity profile (vertically striped region). Reproduced from Horne and Marsh (1986).

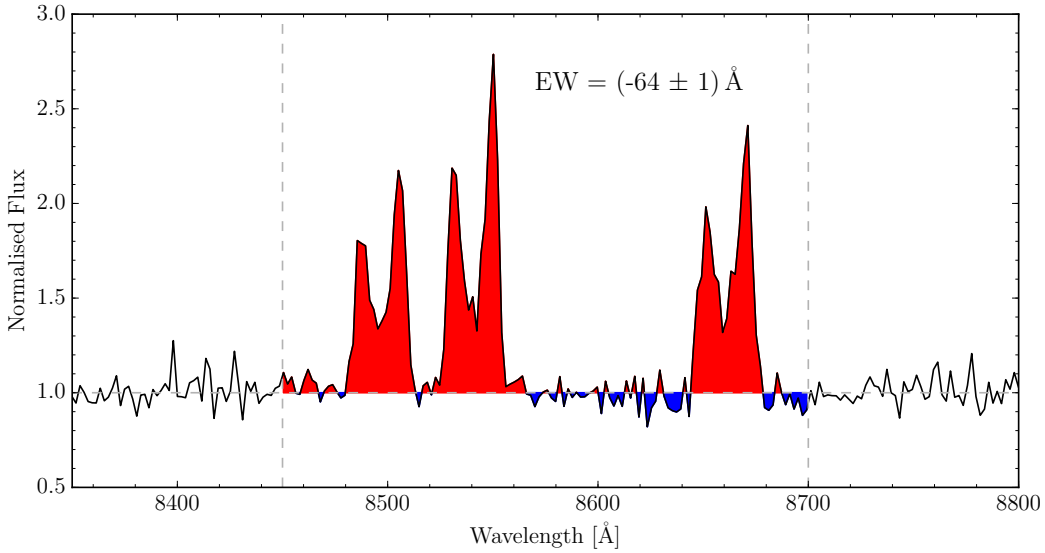

Figure 2.10: The emission profiles of the Ca II triplet in the SDSS spectrum of SDSS J1228+1040. Regions of emission and absorption with respect to the continuum (dashed horizontal line) are highlighted red and blue, respectively, illustrating the area that is considered in an equivalent width calculation between 8450 Å and 8700 Å (indicated by the vertical dashed lines).

wavelengths a and b, is defined as

$$W_\lambda = \int_a^b \left(1 - \frac{F_\lambda}{F_\mathrm{o}}\right) d\lambda = \int_a^b (1 - F_{\lambda,\mathrm{norm}})\, d\lambda, \tag{2.2}$$

where F_λ is the flux in the spectrum, and F_o is the continuum flux outside the line. The ratio of fluxes can be combined as the continuum normalised flux, $F_{\lambda,\mathrm{norm}}$, as illustrated for SDSS J1228+1040 in Figure 2.10. The integrals in Equation 2.2 have units of length, and the area of the emitting or absorbing region is equivalent to the width of a rectangle with the height of one dimensionless unit (see Figure 2.11 for a visualisation), which gives rise to the name "equivalent width." EW measurements are often used to determine the presence of variability in a system, such as the diminishing strength of the emission from the Ca II triplet seen at SDSS J1617+1620 (Wilson et al., 2014).

Doppler tomography

In my analysis of gaseous debris discs, an important tool I have used is Doppler tomography. Doppler tomography is commonly employed to deduce the structure of discs in accreting binary systems (Marsh and Horne 1988; Steeghs and Stehle 1999, see Marsh 2001 for a review). Doppler tomography produces a fixed intensity map (or Doppler map) in velocity

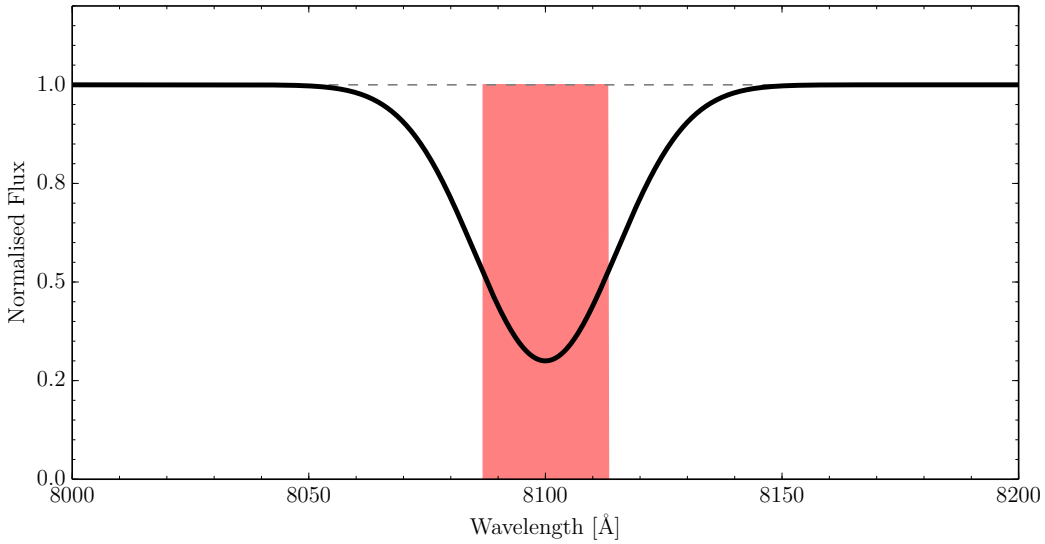

Figure 2.11: A visual representation of the equvialent width (EW). The shaded red region is equal to the area of the absorption feature (black) below the dashed line. As the rectangle has a height of one dimensionless unit, its area can be described by its width, also known as the EW.

space that, for a given period of rotation, best replicates the observed line profiles across all available epochs under the following axioms (Marsh, 2001): (1) All points on the disc are equally visible at all times, (2) The flux from any point fixed in the rotating frame is constant in time, (3) All motion is parallel to the orbital plane, (4) The intrinsic width of the profile from any point is negligible.

To produce a Doppler map of a given emission feature (e.g. the Ca II 8600 Å triplet, or H α), there are a number of inputs required: (i) a continuum normalised spectrum of the emission feature(s) for each epoch, (ii) a list of MJDs corresponding to each epoch, (iii) the central wavelength of the feature(s), (iv) the systemic velocity of the system, and (v) if there are multiple features, the intrinsic strength of each emission profile. Once these inputs are collected, a Doppler map can be produced, usually using one of two methods: maximum entropy regularisation (Horne, 1985), or filtered back-projection (Marsh, 2005). The later of these two techniques enables a more intuitive view of how Doppler tomography works and will be used here to give a basic description of the method. Filtered back-project is also used for computed tomography scans (CT-scans) in the medical industry (Smith, 1997).

Fig. 2.12 visually explains the process of filtered back-projection, showing an image generated using only three different viewing angles, and one using many (effectively infinite) viewing angles which reproduces the original image perfectly (with no added noise, Smith 1997). Similarly for Doppler tomography, as the number of phase-independent spec-

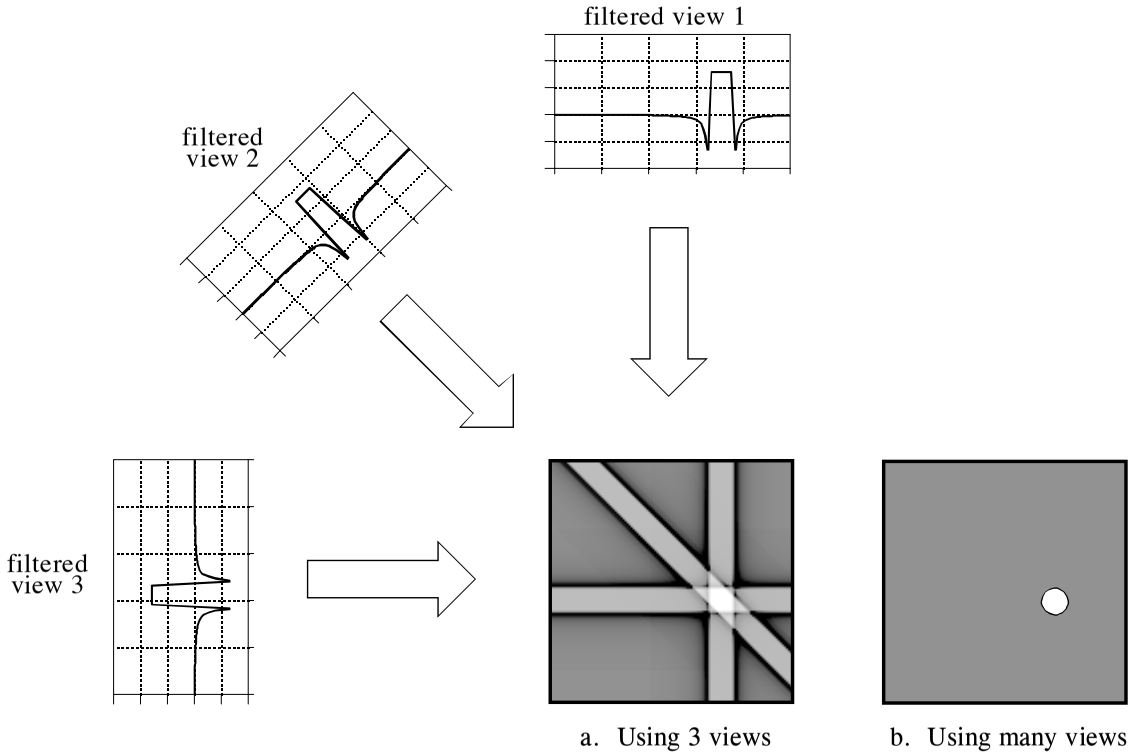

Figure 2.12: A noiseless example of the filtered back-projection method used in computed tomography. As the number of viewing angles increases, the image quality also increases until it matches the input image. Reproduced from Smith (1997).

tra obtained for a system increases so will the quality of the image until it is limited by either noise, or artefacts induced by violations of the axioms of Doppler tomography. Figs. 3–8 from Marsh and Horne (1988) reveal how various factors such as S/N, variable flux (breaking axiom 2), or incomplete sampling can affect a Doppler map. As with other techniques used to fit data, higher S/N spectra will be weighted higher than poorer quality observations. This effect is also seen when the observations have inhomogeneous coverage. If several spectra are taken in a small phase range, it will effectively be weighted higher than other, less intensely covered phase ranges.

An example Doppler map of an accretion disc with a bright spot on the outer edge of the disc is shown in Fig. 2.13. The Doppler map can also be used to reproduce an emission line profile for a given epoch by reducing the 2D intensity map in velocity space to a 1D intensity distribution in the velocity projected along the corresponding line of sight (see the emission profiles in Fig. 2.13). While it may be tempting to convert Doppler maps to co-ordinate space, they are best left in velocity space as the conversion is non-unique. In producing a co-ordinate space map, some assumptions have to be made about the physical structure of the disc. One simple example is that the eccentricity, e of the disc cannot be easily determined from the map, especially if e is dependent on the semi-major axis a.

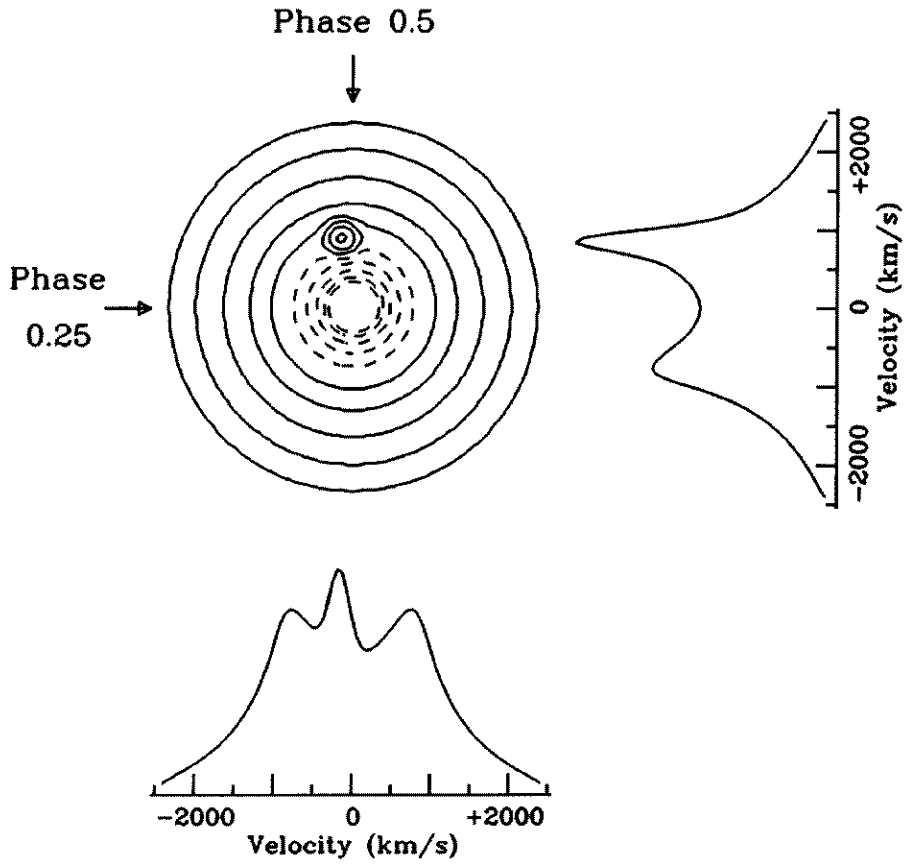

Figure 2.13: An example Doppler map of an accretion disc with a bright spot on the outer edge of the disc. Material in the outer edge of the disc is orbiting slowest, and as such it appears on the inner edge of the Doppler map of the disc. The two profiles shown are observations taken at phase 0.25 and phase 0.5, and show how one can go from the map to a specific spectrum. Reproduced from Marsh (2001).

Chapter 3

Another one grinds the dust: variability of the planetary debris disc at the white dwarf SDSS J104341.53+085558.2

3.1 Introduction

In this chapter, I investigate the variability of the gaseous disc around SDSS J1043+0855. The gaseous debris disc around SDSS J1043+0855 was discovered by Gänsicke et al. (2007) via the detection of Ca II triplet emission. An infrared excess was detected by Melis et al. (2010) and Brinkworth et al. (2012), confirming the presence of a dusty disc in SDSS J1043+0855. I show here the nine years of optical spectroscopy of the metal-polluted white dwarf SDSS J1043+0855, which presents morphological variations of the line profiles of the 8600 Å Ca II triplet emission from the gaseous component of its debris disc. Similar changes in the shape of the Ca II triplet have also been observed in two other systems that host a gaseous disc (SDSS J1228+1040 and SDSS J0845+2257, Wilson et al. 2015; Manser et al. 2016b), and are likely related to the same mechanism. I also report the Mg, Si, and Ca abundances of the debris detected in the photosphere of SDSS J1043+0855, place upper limits on O and Fe, and derive an accretion rate of (2.5 - 12) $\times$ 10^8 gs^{-1}, consistent with those found in other systems with detected debris discs. The Mg/Si ratio and the upper limit on the Fe/Si ratio of the accreted material broadly agree with those found for the crust of the Earth. I also review the range of variability observed among white dwarfs with planetary debris discs.

3.2 Observations

We obtained optical spectroscopy of SDSS J1043+0855 from 2003 to 2012 with several instruments: X-Shooter (Vernet et al., 2011) on the ESO Very Large Telescope (VLT); the 2.5 m Sloan Digital Sky Survey telescope (SDSS, data retrieved from DR7 and DR9, Gunn et al. 2006; Abazajian et al. 2009; Eisenstein et al. 2011; Ahn et al. 2014; Smee et al. 2013); and the Intermediate dispersion Spectrograph and Imaging System (ISIS) on the William Herschel Telescope (WHT). A log of the observations is summarised in Table 3.1. The X-Shooter data were reduced within the REFLEX [1] reduction work flow using the standard settings and optimising the slit integration limits (Freudling et al., 2013). The sky spectrum of each observation was used to determine the spectral resolution. The first ISIS spectrum of SDSS J1043+0855 was reported in Gänsicke et al. (2007), the additional ISIS spectra were obtained with a similar setup, and were reduced in the same fashion (see Farihi et al. 2012 and Wilson et al. 2014 for additional details). We removed the telluric lines present in the VIS arm of the X-Shooter spectra using the X-Shooter Spectral Library (XSL) provided by Chen et al. (2014), and applying the method outlined in Section 2.2. An example spectrum of SDSS J1043+0855 is shown in Fig. 3.1.

[1]Documentation and software for REFLEX can be obtained from http://www.eso.org/sci/software/reflex/

Table 3.1: Log of observations of SDSS J1043+0855. [a] Different exposure times for the individual X-Shooter arms (UVB / VIS). We did not use data collected by the NIR arm of X-Shooter as the signal-to-noise ratio was too poor.

Date	Telescope/Instrument	Wavelength Range [Å]	Resolution [Å]	Exposure Time [s] [a]
2003 April 05	SDSS	3800 – 9200	2.9	2900
2007 February 03	WHT/ISIS	7400 – 9200	2.0	4800
2009 February 16	WHT/ISIS	6000 – 8900	3.7	3950
2010 April 22	WHT/ISIS	8100 – 8850	1.1	7200
2011 January 29	VLT/X-Shooter	2990 – 10400	1.12	2950 / 2840
2011 May 30	VLT/X-Shooter	2990 – 10400	1.15	2950 / 2840
2012 January 03	SDSS	3602 – 10353	3.2	2702

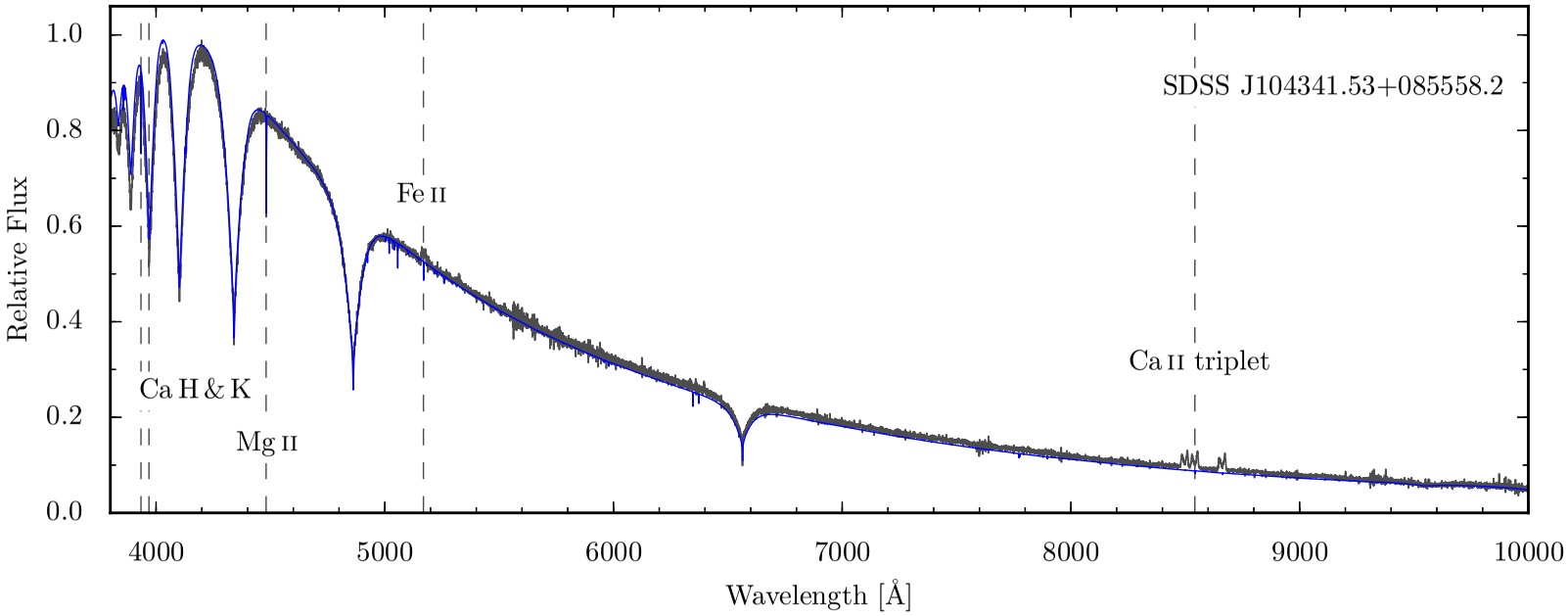

Figure 3.1: X-Shooter spectra of SDSS J1043+0855 (grey, obtained in January and May 2011) together with a model atmosphere fit (blue) using the atmospheric parameters listed in Table 3.2. The strongest emission and absorption lines have been labelled (note that the Fe II feature is in emission).

3.3 Evolution of the calcium emission profile

3.3.1 Double peaked emission from a disc

The characteristic emission profile from a gaseous disc with a radially symmetric intensity distribution and circular orbit is a symmetric, double-peaked emission profile (see Figure 1 of Horne and Marsh 1986). The width of the profile arises from the wide range of velocities projected along the line of sight and can reveal details about the structure and geometry of the gaseous disc. The largest velocities correspond to material at the inner disc radius, which can hence be determined from the full width at zero intensity, i.e. the point at which the emission drops to the continuum level, and with knowledge of the inclination, i, using $R \sin^2 i = R_{\rm obs}$, where R and $R_{\rm obs}$ denote the actual and observed radii respectively. We define the maximum red/blue-shifted velocities to represent the red/blue inner edges of the disc. The outer radius can be estimated from the peak separation in the double peaked profile.

Any departure from a radially symmetric, circular disc will manifest itself as asymmetries in the double peaked emission profile. An eccentric disc of uniform intensity, for example, would generate an asymmetric double-peaked profile if viewed along the semi-minor axis, as there is an asymmetry in the velocity distribution of the material, as well as in the total red and blue-shifted light emitted from the disc. We use this insight below to discuss the changes in the line profiles observed at SDSS J1043+0855.

3.3.2 Variation of the Calcium emission lines

The Ca II triplet in SDSS J1043+0855 changes in morphology over a time scale of nine years (Figure 3.2). All three components of the triplet vary in the same manner, and are henceforth referred to in singular.

The initial three spectra are noisy and of low resolution, showing a broad line profile. In contrast, finer features appear in the higher resolution 2010 WHT spectrum, namely a sharp red-shifted peak and a gradual drop off to blueward wavelengths, revealing a clear asymmetry in the red and blue inner edges of the disc. This asymmetry decreases in the 2011 January spectrum, and vanishes in the 2011 May spectrum. The second SDSS spectrum obtained in 2012 shows no sign of any sharp departures from symmetry, although it is of relatively low spectral resolution. In Section 3.5 we discuss the similarities, and the possible origin, of the observed variations with those seen in other systems.

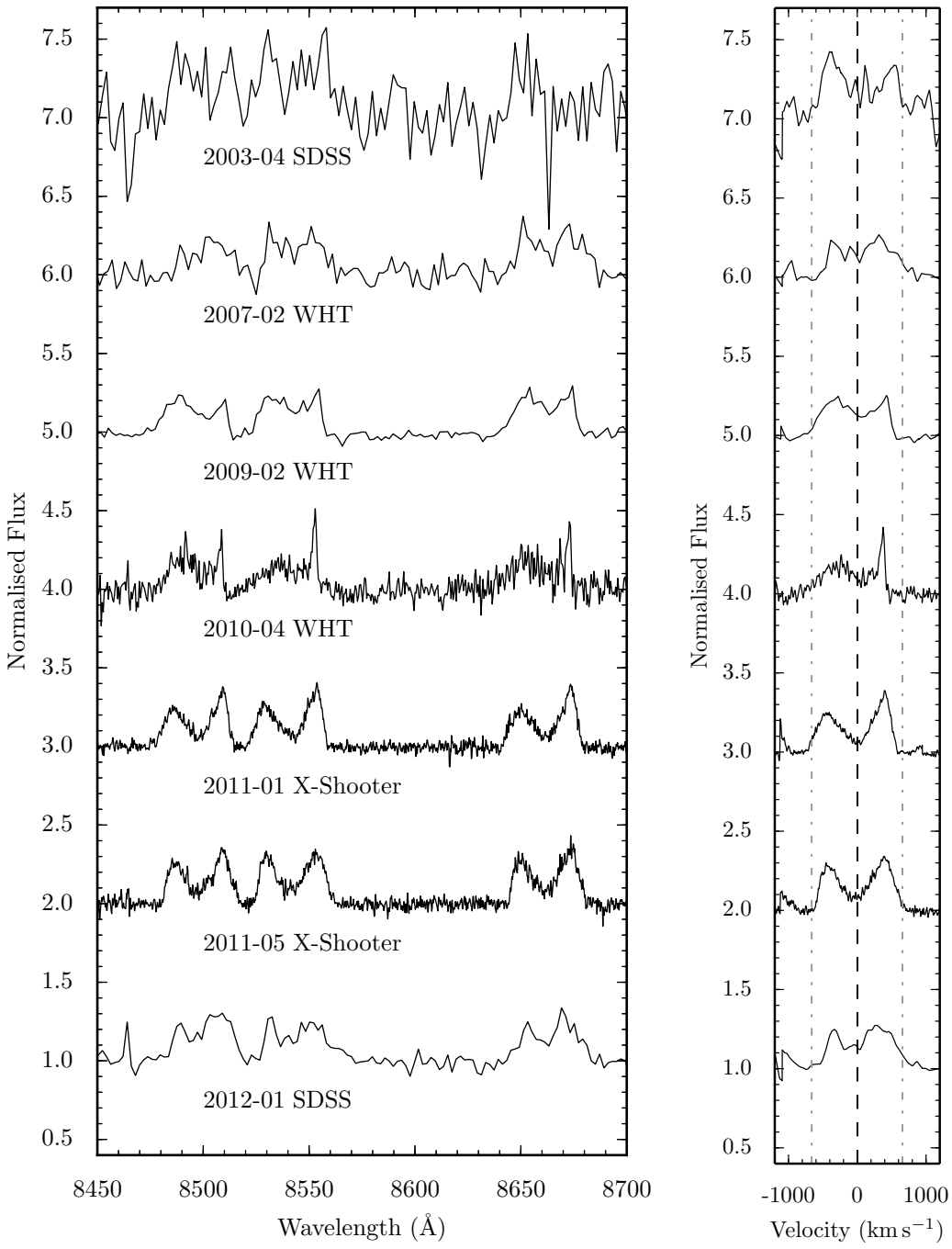

Figure 3.2: Time series spectroscopy of the Ca II triplet of SDSS J1043+0855 spanning nine years. The left panel shows the three triplet profiles in wavelength space, while the right panel depicts the average of the three profiles in the rest frame of the system in velocity space. Several artefacts are introduced in the right panel at high velocities ($< -700\,\mathrm{km\,s^{-1}}$) due to the small separation between the left and middle triple profiles. The spectra are normalised and offset in steps of one from the 2012 January observation.

3.3.3 Inclination of the disc

In the 2011 January and May spectra, the 'valley' in between the two peaks of the emission profiles almost reaches the continuum level, which suggests that the debris disc is optically thick and seen at a large inclination. Horne and Marsh (1986) have shown that in an optically thick accretion disc, line emission is more likely to escape along paths of largest velocity gradient provided by Keplerian shear flow, which is at a minimum for purely tangential or radial emission through the disc. For an observer looking through the disc at an inclination of 90° (edge on), material travelling perpendicular to the line of sight (emission in the 'valley') will be emitting along the radial direction of the disc and will be suppressed.

While the formulation described in Horne and Marsh (1986) was developed for circular orbits, it was expanded to include eccentric orbits in order to model the emission profile of SDSS J1228+1040 obtained in 2006 (Gänsicke et al., 2006), and we give additional details on this extension in Appendix A. We fit the emission profiles of the 2011 January and May spectra of SDSS J1043+0855 in the same manner (see Figure 3.3), and obtain an inclination of $i \simeq 76°$ and 72° respectively, leading to an average inclination of $i = 74°$. The statistical uncertainty obtained for the two inclinations was $\pm 0.5°$, which is likely an underestimate given the much larger range of the two measurements. Under the assumption of constant inclination, we therefore assume an uncertainty that encompasses the range of measured inclinations of $\simeq \pm 5°$.

3.4 Metal abundances in the photosphere of SDSS J1043+0855

We fitted the two SDSS spectra with DA (hydrogen dominated) white dwarf model atmospheres using the methods described in Gänsicke et al. (2012) and Koester et al. (2014), and find $T_{\rm eff} = 17879 \pm 195$ K, and $\log g = 8.124 \pm 0.033$, corresponding to $M_{\rm WD} = 0.693 \pm 0.020\,{\rm M}_\odot$ and $R_{\rm WD} = 0.0120 \pm 0.0003\,{\rm R}_\odot$ (see Table 3.2).

We note that while the atmospheric parameters derived here are consistent with previous measurements (Eisenstein et al., 2006; Gänsicke et al., 2007; Tremblay et al., 2011; Kleinman et al., 2013) the *ugriz* photometry suggests a lower effective temperature, even when allowing for the maximum reddening along the line of sight obtained from Schlafly and Finkbeiner (2011). This discrepancy is likely due to a higher amount of extinction, either by a denser patch in the interstellar medium that remains unresolved in the dust maps, or by circumstellar dust. We speculate that there could be additional dust in the system, which may not be associated with the dusty component of the debris disc at SDSS J1043+0855 (Melis et al., 2010; Brinkworth et al., 2012), and could possibly be the cause of the observed reddening.

Using the system parameters, the metal absorption lines detected in the spectra

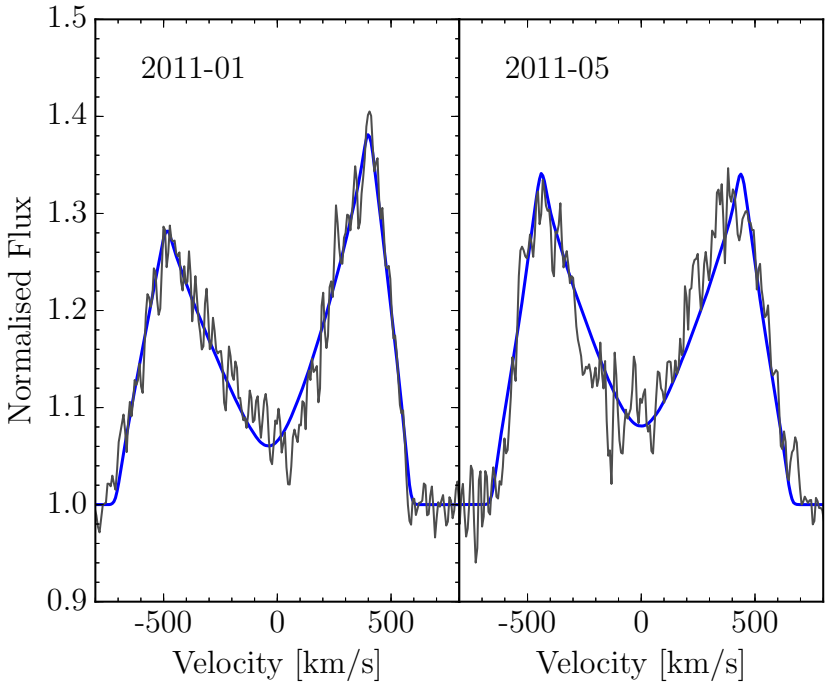

Figure 3.3: Model fit to the normalised 8542.09 Å component of the Ca II triplet for the 2011 January and May X-shooter spectra, from which we obtain an inclination of $i \simeq 74°$ for the disc at SDSS J1043+0855. The model applies the formulation described in Horne and Marsh (1986) which has been expanded to include eccentric orbits (see Appendix A for more details).

Table 3.2: Metal polluted white dwarfs with circumstellar gas detected in emission (e) or absorption (a), and evidence for photometric or spectroscopic variability (v). System parameters and accretion rates are given with errors where known. Values derived or updated in this paper are set in italics. [1] Dufour et al. (2012), [2] Wilson et al. (2015), [3] Farihi et al. (2012), [4] Xu and Jura (2014), [5] Gänsicke et al. (2007), [6] Melis et al. (2010), [7] This paper, [8] Guo et al. (2015), [9] Gänsicke et al. (2006), [10] Gänsicke et al. (2012), [11] Koester et al. (2014), [12] Manser et al. (2016b), [13] Koester et al. (2005), [14] Voss et al. (2007), [15] Melis et al. (2012), [16] Wilson et al. (2014), [17] Vennes and Kawka (2013), [18] Koester and Wilken (2006), [19] Debes et al. (2012), [20] Vanderburg et al. (2015), [21] Xu et al. (2016), [22] Dennihy et al. (2018).

Name	Type	log g ($\mathrm{cm\,s^{-2}}$)	$T_{\rm eff}$ (K)	$M_{\rm WD}$ ($\mathrm{M_\odot}$)	$\tau_{\rm cool}$ (Myr)	$\dot{M}$ ($\times 10^8\,\mathrm{g\,s^{-1}}$)	Features	ref
SDSS J0738+1835	DB	8.4 (0.2)	13950 (100)	0.841 (0.131)	477 (160)	1300	e	1
SDSS J0845+2257	DB	8.18 (0.20)	19780 (250)	*0.73 (0.11)*	*122 (44)*	160	e, v	2
SDSS J0959–0200	DA	8.06 (0.03)	13280 (20)	0.64 (0.02)	*324 (17)*	0.32	e, v	3, 4
SDSS J1043+0855	DA	*8.124 (0.033)*	*17879 (195)*	*0.693 (0.020)*	*153 (10)*	*(2.5 - 12)*	e, v	5, 6, 7
WD 1144+0529	DA	7.74 (0.03)	23027 (219)	0.49 (0.03)	21.2 (1.9)	-	e	8
SDSS J1228+1040	DA	8.150 (0.089)	20713 (281)	0.705 (0.051)	100 (5)	5.6	e, a, v	6, 9, 10, 11, 12
HE 1349–2305	DBA	8.133	18173	0.673	149.4	1.3	e, v	13, 14, 15, 22
SDSS J1617+1620	DA	8.11 (0.08)	13520 (200)	0.68 (0.05)	350 (50)	(6.4 - 7.8)	e, v	16
PG 0843+516	DA	7.902 (0.089)	22412 (304)	0.577 (0.047)	*42 (4)*	10.2	a	11
WD 1054–226	DA	8.04 (0.03)	7903 (16)	-	*1255 (92)*	-	a	17
WD 1124–293	DA	8.1	9700	0.66	*843*	1.3	a	18, 19
WD 1145+017	DB	-	15900 (500)	-	175 (75)	430	a, v	20, 21

of SDSS J1043+0855 were modelled (see Figure 3.4) to measure abundances relative to hydrogen which are given in Table 3.3, along with the diffusion time scales and accretion fluxes. The abundance by number of Mg, Ca, and an upper limit for Fe relative to Si were found to be $\log(\mathrm{Mg/Si}) = -0.64 \pm 0.21$, $\log(\mathrm{Ca/Si}) = -1.33 \pm 0.24$, and $\log(\mathrm{Fe/Si}) \leq 0.19$. From Figure 7 of Jura and Young (2014), the ratios of Mg and Fe to Si are broadly consistent with those found for the crust of the Earth, and imply the accreted object is processed rather than having a 'chondritic' composition (Zuckerman et al., 2007; Xu et al., 2013, 2014). This is also supported by the relatively low number abundance of Mg with respect to Ca, $\log(\mathrm{Mg/Ca}) = 0.70 \pm 0.25$, when compared to a sample of 60 externally polluted white dwarfs (see Figure 1 of Jura and Xu 2013). Similarly low log (Mg/Ca) ratios have also been observed at other white dwarfs that are thought to accrete crust material, such as NLTT 43806 and NLTT 19868 (Zuckerman et al., 2011; Kawka and Vennes, 2016).

We also note that the Ca K 3934 Å feature shows clear emission in the averaged, normalised X-Shooter spectra (Figure 3.4). Similar emission is seen at SDSS J1228+1040, which also revealed a difference in morphology between the Ca H & K profiles and the Ca II triplet, although the signal-to-noise of the current SDSS 1043+0855 spectra is not high enough to determine this (Manser et al., 2016b).

We estimate the total accretion rate for each element from the mass flow rates given in Table 3.3, assuming a bulk Earth composition and the respective mass fractions of each element (from Allègre et al. 2001). The resulting range from Mg, Si, and Ca, $\dot{M}_{\mathrm{Total}} = 2.5 \times 10^{8} - 1.2 \times 10^{9}\,\mathrm{gs}^{-1}$, reflects the uncertainty in the bulk abundances of the planetary debris, but agrees well with the distribution of accretion rates inferred for 19 other metal-polluted DA white dwarfs with dusty discs (Bergfors et al., 2014). For reference, the total accretion rate of SDSS J1228+1040 (where accretion fluxes for all major elements were measured from *HST*/COS ultraviolet spectra) is $5.6 \times 10^{8}\,\mathrm{g\,s}^{-1}$ (Gänsicke et al., 2012). We note that it is likely the accretion rate determined for Si is overestimated as we do not include the effects of radiative levitation in our calculations (Chayer, 2014), hve this has a negligible impact on our interpretations.

3.5 Discussion

Up until the last decade, debris discs around white dwarfs have appeared static in nature, with no significant detections of variability in the properties of the disc itself or in the strength of the absorption lines in metal polluted systems. Due to the short diffusion time scales at the majority of these systems (Koester et al., 2014), any change in the strength of the absorption lines would imply a change in the accretion rate onto the white dwarf. von Hippel and Thompson (2007) claimed changes in the equivalent width of the photospheric

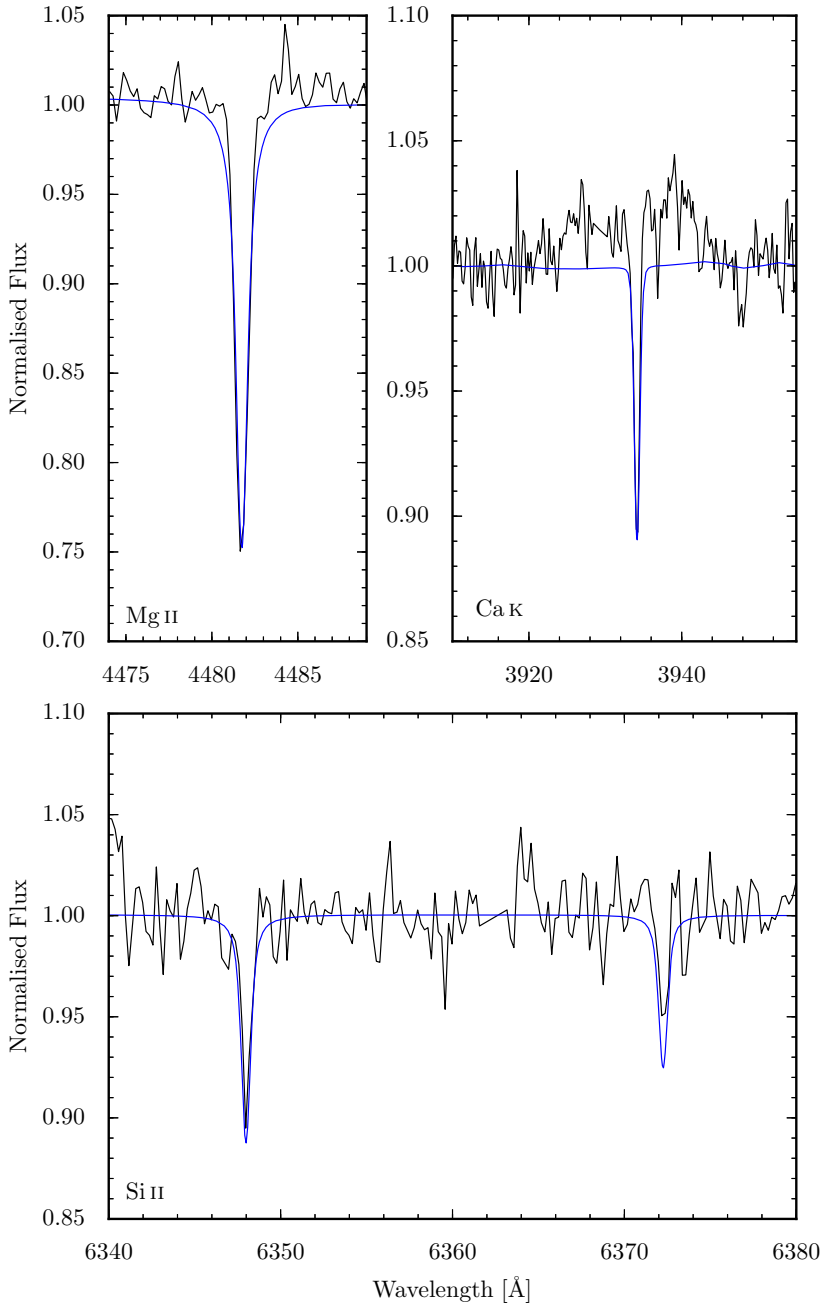

Figure 3.4: Model fits (blue) to absorption lines present in the combined X-Shooter spectra of SDSS J1043+0855 (black). The Ca K feature also contains a clearly detected emission profile from the gaseous disc.

Table 3.3: Diffusion timescales, $\tau_{\rm diff}$, and average accretion fluxes, $\dot{M}$, for the metals detected in the photosphere of SDSS J1043+0855. Photospheric abundances by number are given with respect to hydrogen. [a] We infer a total accretion rate based on the mass fluxes assuming a bulk Earth composition and the respective mass fractions for each element (from Allègre et al. 2001).

Element	log [Z/H]	$\tau_{\rm diff}$ [h]	$\dot{M}$ [g s^{-1}]	Bulk Earth mass fraction [per cent] [a]	Inferred total $\dot{M}$ [g s^{-1}]
8 O	< -4.00	65.0	$< 2.0 \times 10^{9}$	32.4	$< 6.2 \times 10^{9}$
12 Mg	-5.15 (0.15)	26.5	4.0×10^{7}	15.8	2.5×10^{8}
14 Si	-4.80 (0.15)	13.8	2.0×10^{8}	17.1	1.2×10^{9}
20 Ca	-6.00 (0.20)	18.6	1.3×10^{7}	1.6	8.0×10^{8}
26 Fe	< -4.70	11.1	$< 6.3 \times 10^{8}$	28.8	$< 2.2 \times 10^{9}$

Ca II K line over a time scale of days at GD 29–38, however additional observations obtained by Debes and López-Morales (2008) did not confirm such variation, and they concluded further data were required to determine the possible variable nature of the accretion onto the white dwarf.

In recent years, the spectroscopic monitoring of gaseous discs has revealed variability that gives us insight into their formation and dynamics. Table 3.2 lists the stellar parameters of the eight published gas disc systems. Other than SDSS J1043+0855, there are five gaseous disc systems with multi-epoch spectroscopy: SDSS J161717.04+162022.4 (Wilson et al. 2014, henceforth SDSS J1617+1620), SDSS J0845+2257 (Gänsicke et al., 2008; Wilson et al., 2015), SDSS J1228+1040 (Manser et al., 2016b), HE 1349–2305 (Dennihy et al., 2018), and SDSS J073842.56+183509.6 (Gänsicke 2011; Dufour et al. 2012, henceforth SDSS J0738+1835). The Ca II triplet observed at SDSS J0959–0200 does not have any multi-epoch spectroscopy, and is much narrower and weaker than that of the other six systems, indicating a low inclination of the disc with respect to the line of sight (Farihi et al., 2012).

SDSS J0845+2257, SDSS J1228+1040, HE 1349–2305, and SDSS J1617+1620 all show variations on a time scale of years, but follow two distinct types of evolution. In SDSS J1617+1620 the Ca II triplet emission gradually decreased in strength over a time scale of eight years while not undergoing noticeable changes in the line profile shape (Wilson et al., 2014). In contrast, the changes seen in SDSS J0845+2257, SDSS J1228+1040, and HE1349–2305 are of a morphological nature, analogous to the changes we present here for SDSS J1043+0855. Table 3.4 lists the equivalent widths (subject to systematic uncertainties related to the method used in continuum fitting, as well as the statistical uncertainties given in Table 3.4) of the Ca II emission lines in SDSS J1043+0855, which do not show any long term decay of the equivalent width of the Ca II triplet such as seen at SDSS J1617+1620. Only SDSS J0738+1835 has displayed no changes in the shape and strength of the Ca II triplet over a period of six years, although only three epochs are available, with two of them spaced only a year apart.

While the evolution of the emission from SDSS J1043+0855 appears to be remarkably similar to SDSS J1228+1040 and SDSS J0845+2257, the data have a lower signal to noise and have fewer epochs. Thus, while it is likely that the same physical mechanism is responsible for the evolution of the line profiles observed in all three systems, regular spectroscopic monitoring of all gas discs is necessary to develop a more detailed understanding of the dynamical processes present in planetary debris discs around white dwarfs.

Variability of debris discs is not only limited to the Ca II triplet line profile. The dusty disc around SDSS J0959–0200 was observed to significantly decrease in infrared flux by Xu and Jura (2014), who propose two mechanisms by which the disc could be depleted;

Table 3.4: Equivalent width measurements of the Ca II triplet in SDSS J1043+0855. The errors given here are purely statistical.

Date	Equivalent width [Å]
2003–04	-27 (3)
2007–02	-22 (1)
2009–02	-15 (1)
2010–04	-13 (1)
2011–01	-18 (1)
2011–05	-20 (1)
2012–01	-19 (1)

a recent planetesimal impact on the disc, or instability near the inner edge. We suggest an additional scenario of a vertically extended cloud of dust, generated from an asteroid colliding with a pre-existing disc (Jura, 2008). Such an optically thin cloud would temporarily add to the infrared emission of the optically thick disc, but the overall infrared emission from the system would decrease as the dust cloud settled into the disc.

In Table 3.2 we also include four additional systems where circumstellar absorption of gaseous material has been detected around the host white dwarf, including WD 1145+017, which is orbited by highly-dynamic debris, transiting the white dwarf with periods of $\simeq 4.5$ hr (Vanderburg et al., 2015; Xu et al., 2016; Gänsicke et al., 2016; Rappaport et al., 2016). WD 1145+017 is unequivocally a highly dynamical and evolving system with a planetesimal currently undergoing disruption, and also hosts circumstellar gas absorption (Xu et al., 2016). Curiously, the detection of absorption due to circumstellar gas does not correlate with the presence of Ca II triplet emission: SDSS 1228+1040 is so far the only system in which both have been detected (Gänsicke et al., 2012). We note that circumstellar gas has been detected also around a number of hot and young white dwarfs, their origin is probably diverse in nature and not unambiguously associated with evolved planetary systems (Dickinson et al., 2012; Barstow et al., 2014).

3.6 Conclusions

We report here the morphological variability of the Ca II triplet in SDSS J1043+0855 on a time scale of nine years. The evolution of the Ca II triplet reported here is similar to that of two other systems, SDSS J1228+1040 and SDSS J0845+2257.

We have also analysed the optical spectra of SDSS J1043+0855 to determine its stellar parameters and the photospheric metal abundance. The Mg/Si and (upper limit to the) Fe/Si ratios of the planetary debris that has been accreted onto the white dwarf are broadly consistent with those of the crust of the Earth.

The recent detection of the 'real time' disruption of a planetesimal at WD 1145+017, along with the dynamical evolution seen at the gaseous discs SDSS J1043+0855, SDSS J1228+1040, SDSS J1617+1620, and SDSS J0845+2257 discussed in Section 3.5 reveals that variability at planetary systems around white dwarfs is common. Additional spectroscopic and photometric monitoring of all the gaseous discs known so far is key to developing a more detailed understanding of the dynamical processes present in planetary debris discs at white dwarfs.

Chapter 4

Long term variability of the gaseous disc at SDSS J1228+1040

4.1 Introduction

Over a decade ago, Gänsicke et al. (2006) identified a gaseous disc around the white dwarf SDSS J1228+1040 via the detection of double peaked emission lines of Ca II at 8498.02 Å, 8542.09 Å, 8662.14 Å, (henceforth the Ca II triplet), which is indicative of Keplerian rotation in a flat disc (Horne and Marsh, 1986). *Spitzer* and *HST* follow-up observations detected circumstellar dust and a plethora of metallic absorption lines, respectively; strengthening the connection of the gaseous material to the presence of a remnant planetary system around this white dwarf (Brinkworth et al., 2009; Gänsicke et al., 2012). The morphology of these emission lines provided firm dynamical confirmation that the debris disc resides within the tidal disruption radius of the white dwarf.

We have been spectroscopically monitoring the white dwarf SDSS J1228+1040 for fifteen years (twelve years presented in this chapter), which shows a steady variation in the morphology of the 8600 Å Ca II triplet line profiles from the gaseous component of its debris disc. We identify additional emission lines of O I, Mg I, Mg II, Fe II and Ca II in the deep co-added spectra. These emission features (including Ca H & K) exhibit a wide range in strength and morphology with respect to each other and to the Ca II triplet, indicating different intensity distributions of these ionic species within the disc. Using Doppler tomography we show that the evolution of the Ca II triplet profile can be interpreted as the precession of a fixed emission pattern with a period in the range 24–30 years. The Ca II line profiles vary on time-scales that are broadly consistent with general relativistic precession of the debris disc.

4.2 Observations

4.2.1 The data

We obtained optical spectroscopy of SDSS J1228+1040 from 2003 to 2015 with several instruments: X-shooter (Vernet et al., 2011) and the Ultraviolet and Visual Echelle Spectrograph (UVES, Dekker et al. 2000) which are both on the ESO Very Large Telescope (VLT); the 2.5 m Sloan Digital Sky Survey telescope (SDSS, data retrieved from DR7 and DR9, Gunn et al. 2006; Abazajian et al. 2009; Eisenstein et al. 2011; Ahn et al. 2014; Smee et al. 2013); and the Intermediate dispersion Spectrograph and Imaging System (ISIS) on the William Herschel Telescope (WHT). These observations are summarised in Table 4.1. We also report the parameters of SDSS J1228+1040 in Table 4.2.The data was reduced as described in Section 6.4 and an example telluric-corrected spectrum of SDSS J1228+1040 shown in Figure 4.1.

Table 4.1: Log of observations of SDSS J1228+1040. [a] Different exposure times for the individual UVES arms (blue / red lower and upper) and X-shooter arms (UVB / VIS). [b] Observations did not cover the Ca II triplet. We did not use data collected by the NIR arm of X-shooter as the signal-to-noise ratio was too poor.

Date	Telescope/Instrument	Wavelength Range [Å]	Resolution [Å]	Total Exposure Time [s] [a]
2003 March 27	SDSS	3800 – 9200	2.7	2900
2006 June 30 - July 01	WHT/ISIS	7500 – 9200	2.0	12000
2007 April 07	VLT/UVES	3045 – 9463	0.19	11800 / 11360
2007 June 06	VLT/UVES	3758 – 9463	0.18	5900 / 5680
2007 July 09 - 10	VLT/UVES	3757 – 9463	0.18	5900 / 5680
2008 January 10	VLT/UVES	3759 – 9464	0.18	5900 / 5680
2008 April 11 [b]	VLT/UVES	3284 – 6649	0.13	11800 / 11360
2008 June 27	VLT/UVES	3758 – 9463	0.18	5900 / 5680
2008 July 19	VLT/UVES	3758 – 9463	0.18	5900 / 5680
2009 January 12 [b]	VLT/UVES	3284 – 6650	0.14	5900 / 5680
2009 February 03	VLT/UVES	3758 – 9464	0.18	5900 / 5680
2009 April 04	VLT/UVES	3282 – 9463	0.18	17700 / 17040
2010 April 27	WHT/ISIS	8100 – 8850	1.1	1800
2011 January 22	VLT/X-Shooter	2990 – 10400	1.09	2840 / 1400
2011 May 29	VLT/X-Shooter	2990 – 10400	1.14	2840 / 1400
2011 June 14	VLT/X-Shooter	2990 – 10400	1.09	2840 / 1400
2012 March 26	VLT/X-Shooter	2990 – 10400	1.11	2840 / 1400
2014 March 06	VLT/X-Shooter	2990 – 10400	1.10	1971 / 3045
2014 June 02	VLT/X-Shooter	2990 – 10400	1.09	1314 / 2030
2015 May 11	VLT/X-Shooter	2990 – 10400	1.10	2380 / 2510
2015 May 18	VLT/UVES	3732 – 9463	0.20	2980 / 2960

Table 4.2: Atmospheric parameters for SDSS J1228+1040 (from Koester et al. 2014).

$T_{\rm eff}$ [K]	log g	$M_{\rm WD}$ [$M_\odot$]	$R_{\rm WD}$ [$R_\odot$]
20713 (281)	8.150 (0.089)	0.705 (0.051)	0.01169 (0.00078)

4.2.2 Velocity corrections

The observations of the Ca II triplet were converted from wavelength to velocity space using the rest wavelengths, 8498.02 Å, 8542.09 Å, 8662.14 Å, which are corrected for the systemic velocity, i.e. the velocity along the line of sight. Gänsicke et al. (2012) calculated a velocity difference of $+57 \pm 1\,\mathrm{km\,s^{-1}}$ between the photospheric absorption lines of the white dwarf and the interstellar ultraviolet absorption lines in SDSS J1228+1040. This value combines the systemic velocity as well as the gravitational red-shift of the photospheric absorption lines at the white dwarf surface (Koester, 1987). Adopting a white dwarf mass and radius of $0.705\,M_\odot$ and $0.01169\,R_\odot$, respectively (Koester et al., 2014), we obtain a gravitational red-shift of $+38 \pm 4\,\mathrm{km\,s^{-1}}$, resulting in a systemic velocity of $+19 \pm 4\,\mathrm{km\,s^{-1}}$. This velocity is used to shift the Ca II triplet observations to the rest frame of the system as well as for Doppler Tomography discussed in Section 4.5. All the Ca II triplet observations are shown in velocity space in Figure 4.2 and we discuss the evolution of the Ca II triplet in the next section.

4.3 Evolution of the Ca II Triplet structure

4.3.1 Double peaked emission from a disc

Horne and Marsh (1986) showed that a circular gaseous disc with a radially symmetric intensity distribution orbiting a central mass will produce symmetric double-peaked emission line profiles in velocity space (See Figure 2.9), due to the range in velocities across the disc projected along the line of sight. Two properties of the physical structure of the disc, the inner and outer radii, can be easily inferred from these profiles as the Keplerian velocity increases with decreasing distance from the central object. The inner radius of the disc is determined from the maximum velocity, i.e. the point at which the emission drops to the continuum level; also known as the Full Width Zero Intensity (FWZI). We define the maximum red/blue-shifted velocities to represent the red/blue inner edges of the disc. The outer radius can be estimated from the peak separation in the double peaked profile. These observationally derived radii, $R_{\rm obs}$, relate to the true radii, R, via $R_{\rm obs} = R \sin^2 i$, where i is the inclination of the disc. This method was used by Gänsicke et al. (2006) to derive the observed inner and outer radii of SDSS J1228+1040 to be $\simeq 0.64\,R_\odot$ and $\simeq 1.2\,R_\odot$, respectively.

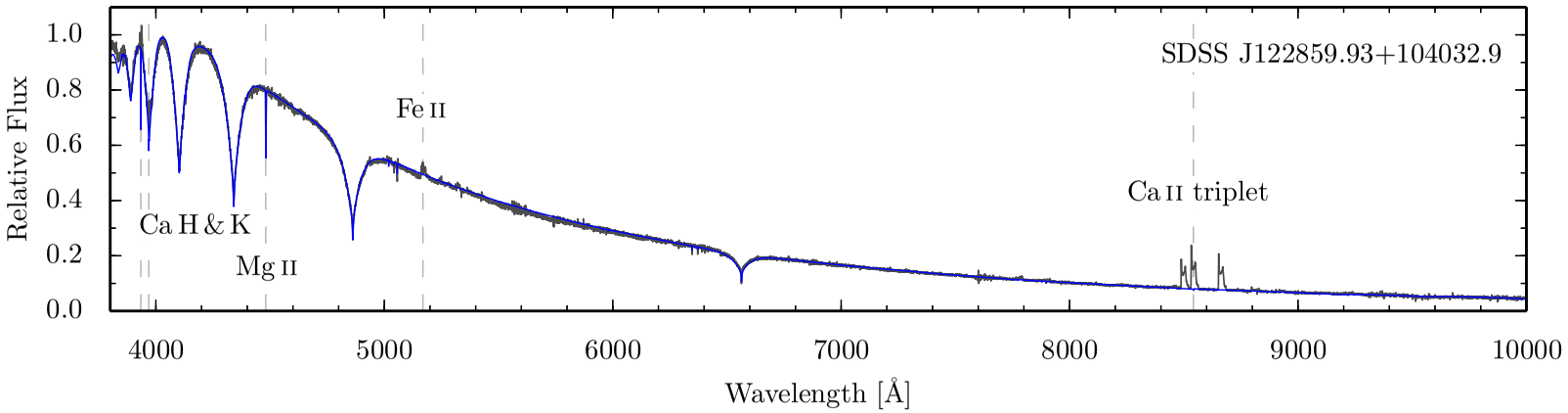

Figure 4.1: X-shooter spectra (grey) of SDSSJ 1228+1040 (obtained in January 2011) together with a model fit (blue) using the atmospheric parameters (Table 4.2). The strongest emission and absorption lines have been labelled.

A departure from the symmetric double-peaked profile can reveal information about the physical structure of the disc, as demonstrated by Steeghs and Stehle (1999) for the occurence of spiral shocks in the disc (Steeghs et al., 1997; Steeghs, 1999). An eccentric disc would generate an asymmetric double-peaked profile if viewed along the semi-minor axis, as there is an asymmetry in the amount of material emitting red- and blue-shifted light. We use this insight below to discuss the changes in the emission profiles seen in SDSS J1228+1040.

4.3.2 Variation of the calcium triplet profiles

The Ca II triplet in SDSS J1228+1040 has undergone an astonishing morphological evolution in the 12 years of observations (Figure 4.2). The three individual line profiles vary in the same manner and we therefore use the term "profile" to decribe their evolution. The initial spectra from 2003 and 2006 show a double-peaked profile indicative of a circumstellar disc with a red-dominated asymmetry. These observations were interpreted as emission from an eccentric disc with a non isotropic intensity distribution (Gänsicke et al., 2006). The maximum velocities (highest blue or red-shift) in the disc measured from the 2006 observations were found to be $\pm\,560\,\pm\,10\,\mathrm{km\,s^{-1}}$.

As the profiles evolve, there is a general smooth progression from a red-dominated asymmetry to a blue-dominated one. Throughout this evolution the morphology of the peaks also changes, with the blue-shifted peak becoming stronger and sharper. In contrast, the red-shifted peak becomes shallower and weaker and extends to higher velocities, which can be seen first in the April 2009 observations. This extension into the red is clearest in the January 2011 spectrum with a maximum extension of $+780\,\pm\,10\,\mathrm{km\,s^{-1}}$. The clear, sharp cut-off of the red wing of the profile is a sudden change compared to the more gradual evolution in shape and implies that the red-shifted inner edge of the disc has moved inwards to smaller radii (i.e. higher velocities). From 2011–2015 the red wing decreases in extent, reducing the maximum velocity to $+670\,\pm\,10\,\mathrm{km\,s^{-1}}$, accompanied by an increase in strength, showing a clear reappearance of the red peak. Overall, the profile shifts to longer wavelengths, with the blue edge moving from $-560\,\pm\,10\,\mathrm{km\,s^{-1}}$ in July 2006 to $-390\,\pm\,10\,\mathrm{km\,s^{-1}}$ in May 2015. The variation in the red and blue velocities imply an asymmetry in the inner disc edge, as a circular Keplerian orbit would produce identical red/blue velocities. In summary, the observed variations clearly show that the inner edge of the gaseous disc is not circular.

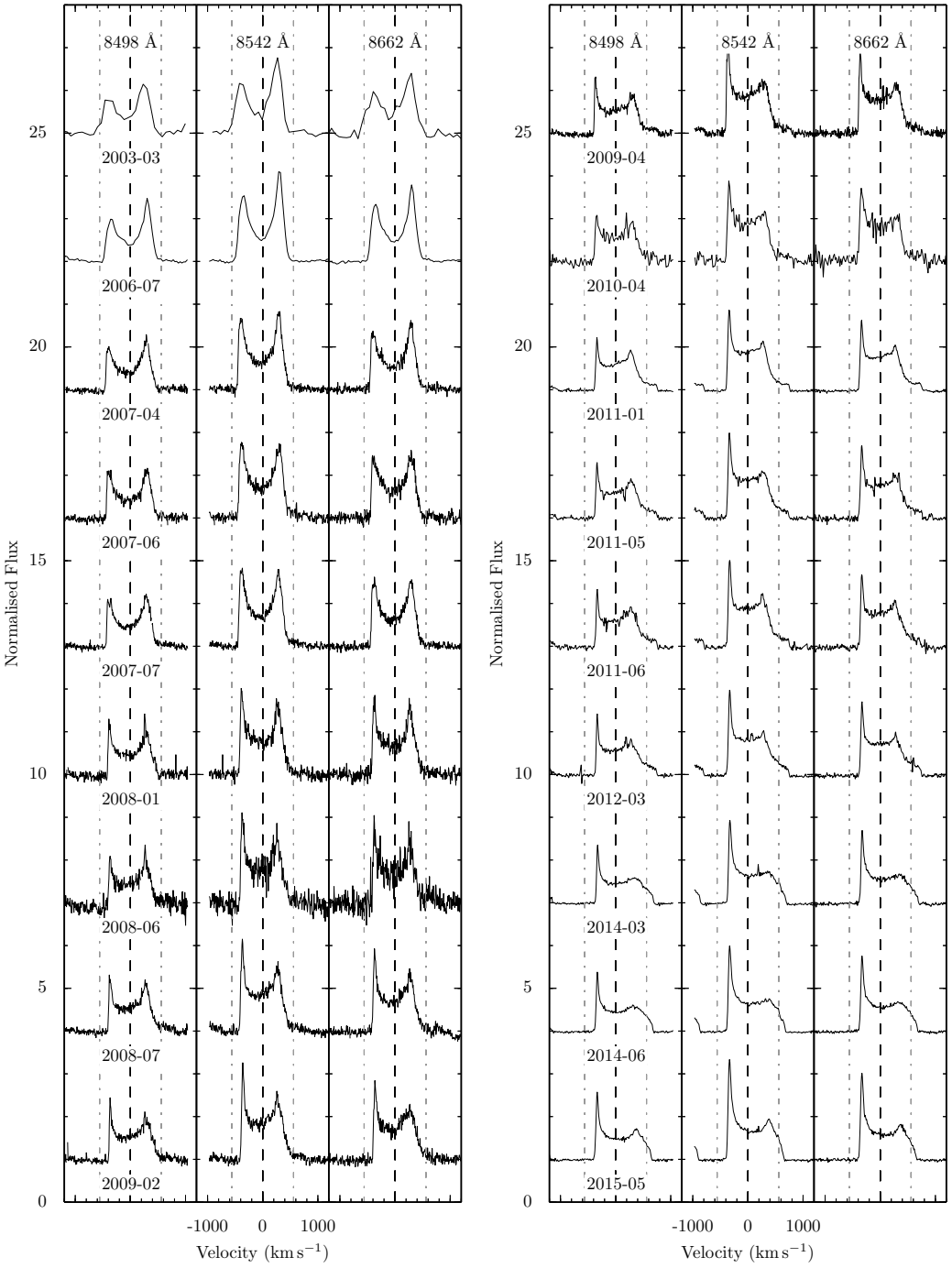

Figure 4.2: Time series of the continuum-divided Ca II triplet in SDSS J1228+1040 in velocity space. The series runs over twelve years with 18 epochs and depicts the change in the morphology of the line profiles. The dashed and dot-dashed lines indicate the minimum and maximum velocities measured from the 2006 WHT data, respectively. The 2015 May profile is averaged from the X-shooter and UVES observations collected within several days of each other. The spectra are shifted in steps of three from the 2009 February (left) and 2015 May (right) observations.

4.4 Additional Emission lines in SDSS J1228+1040

In addition to the Ca II triplet, Gänsicke et al. (2006) reported emission of Fe II 5169 / 5197 Å, however these lines were too weak to resolve the shape of their profiles. By inspecting the averaged X-shooter UVB and VIS spectral arms, we clearly detected these Fe II lines, as well as additional lines of Fe II, Ca II, Mg I, Mg II, and O I. The rest wavelengths of these lines are listed in Table 4.3, and their profiles are shown in Figure 4.3. We cannot inspect the time-resolved evolution of these lines as they are very weak and correspondingly noisy in the individual spectra.

It is evident that the four different species have distinct intensity distributions across the disc, which lead to the observed variety of line profile shapes. The sharp blue peak in the Ca II triplet is observed only in Mg I 8806 Å and Ca II 8912, 8927 Å. Rather surprisingly, the Ca H & K lines are different in shape to the Ca II triplet, with a broad profile, much weaker in strength, and no clear asymmetry in the blue edge. They do, however, possibly show an extension to the red similar to the Ca II triplet, although the signal-to-noise ratio of the individual observations makes the presence of such an extension uncertain. The O I lines at $\simeq$ 7774 and 8446 Å show a clear red-dominated asymmetric profile, which has the opposite shape of the Ca II triplet. The two emission profiles at $\sim$ 8245 (O I) and $\sim$ 9250 Å (O I and Mg II) are blended, extending over a larger wavelength range with a blurred structure.

A number of emission profiles, such as Mg II 7896 Å, show sharp absorption features. These features are the photospheric absorption lines, which is also the case at 5041 and 5056 Å, where a Si II absorption doublet punctures the continuum.

We also show for reference the *HST* spectrum (Figure 4.4) obtained by Gänsicke et al. (2012) in the far and near ultraviolet spectral range. There are far more photospheric absorption lines in the ultraviolet compared to the optical range, but only one emission line; Mg II 2800 Å, which was first noted by Hartmann et al. (2011).

As done above for the Ca II triplet, we measured the maximum red/blue velocities of the emission profiles in the optical (where possible) to determine the radial extent of the different species. The additional emission features are orders of magnitude weaker than the strength of the Ca II lines (see Table 4.4), and it is, therefore, difficult to accurately determine the maximum red and blue-shifted velocities. However, the profiles have a similar FWZI in velocity space and as such we report the average velocities of the blue-most and red-most edge of the profiles as $\simeq -400\,\mathrm{km\,s^{-1}}$ and $\simeq 800\,\mathrm{km\,s^{-1}}$, respectively, which are consistent with those obtained for the Ca II triplet in all of the X-shooter observations so far. The similarity in the maximum and minimum velocities suggests that the emitting ions share a similar location of their inner disc edges. This is interesting to note as the line profiles differ in shape, implying different intensity distributions across the disc. Estimating an outer edge

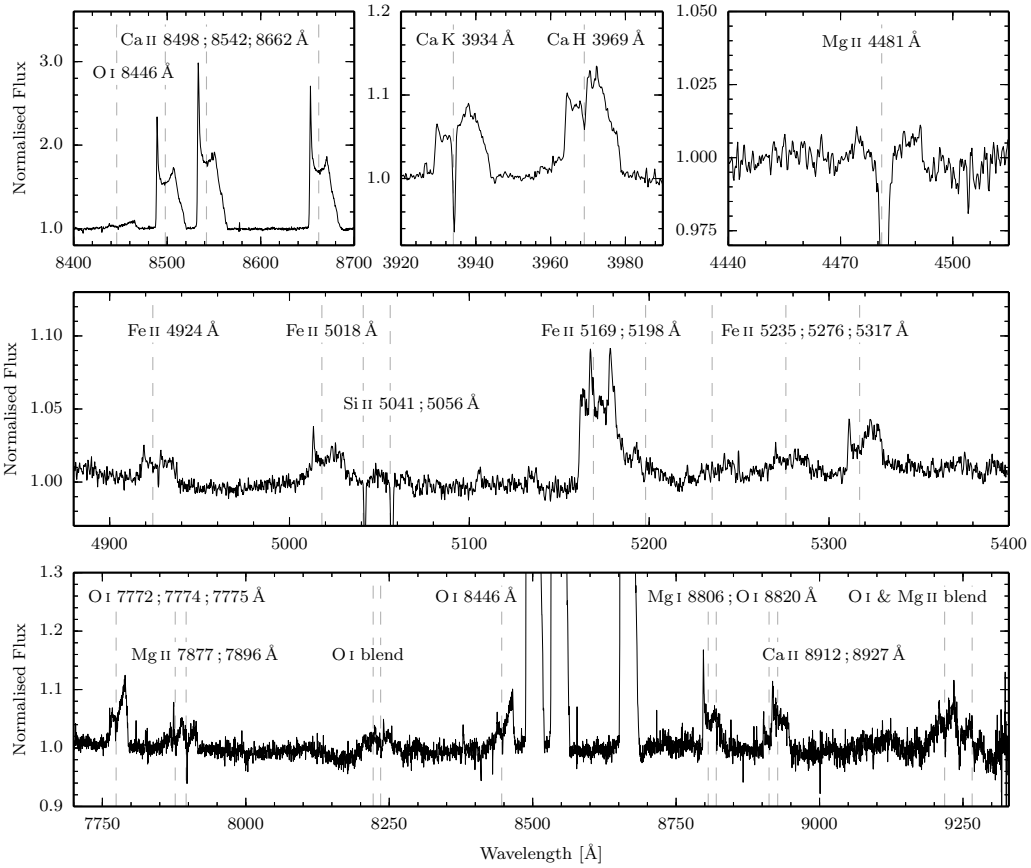

Figure 4.3: The averaged, continuum-divided X-shooter spectrum of SDSSJ 1228+1040 reveals additional emission lines with a wide range of morphologies and strengths. The bottom panel contains the Ca II triplet, which extends far off of the plot, illustrating the extremely large dynamical range of the data. The ions that contribute to each profile are labelled in each panel, with dashed lines indicating their rest wavelengths. The regions labelled as blends contain multiple lines (see Table 4.3).

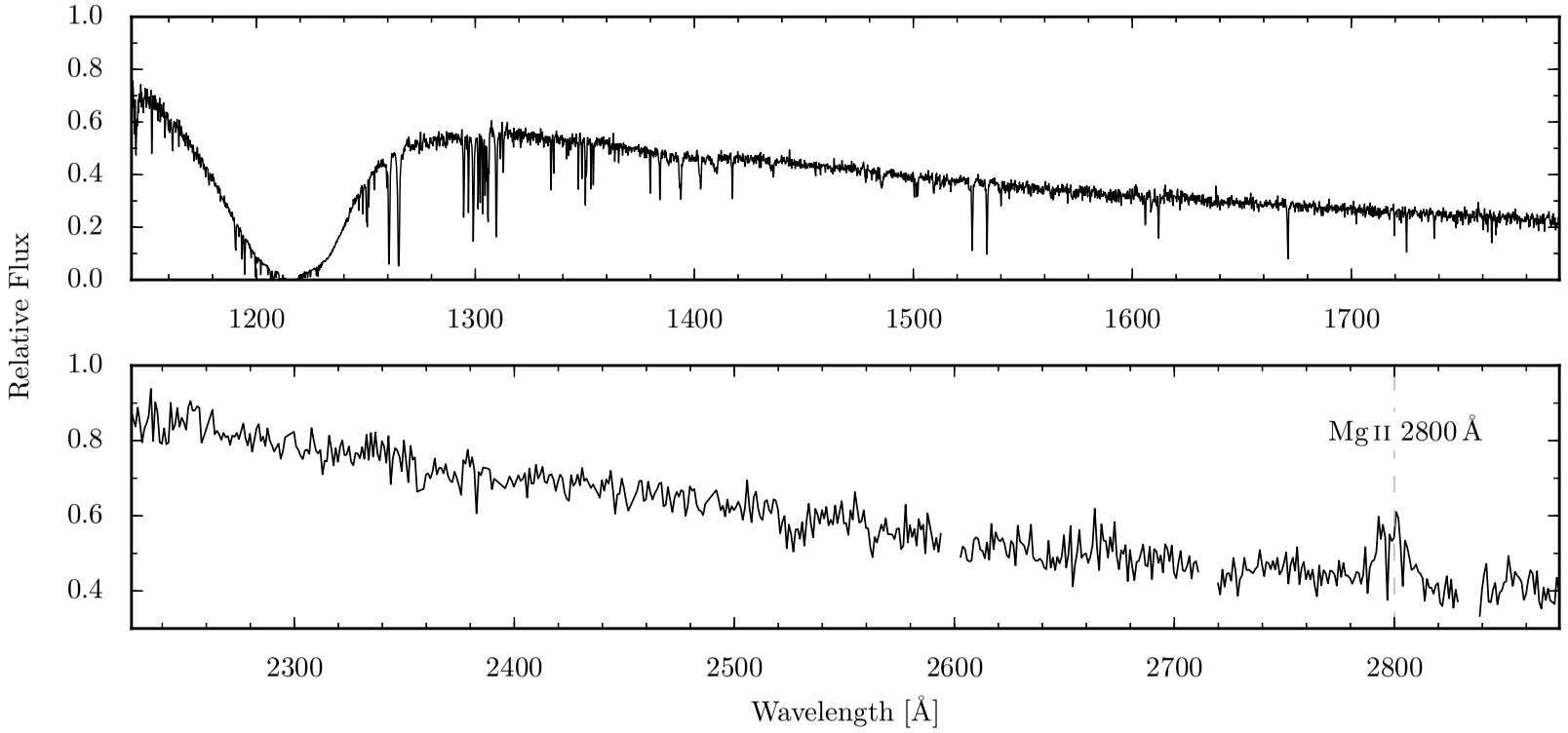

Figure 4.4: *HST* far (top) and near (bottom) ultraviolet observations of SDSS J1228+1040. The Mg II emission line is labelled.

Table 4.3: Additional emission lines detected in the average X-shooter spectrum (Figure 4.3) and the *HST* spectrum (Figure 4.4) of SDSS J1228+1040). The rest wavelengths were obtained from the NIST Atomic Spectra Database.

Ion	Vacuum wavelengths [Å]
Ca II	3933.66, 3968.47, 8498.02, 8542.09, 8662.14, 8912.07 8927.36
O I	7771.94, 7774.17, 7775.39, 8221.82, 8227.65, 8230.02, 8233.00, 8235.35, 8446.36, 8446.76, 8820.43, 9260.81, 9260.84, 9260.94, 9262.58, 9262.67, 9262.77, 9265.94, 9266.01
Mg I	8806.76
Mg II	2795.53, 2798.00, 2802.70, 4481.13, 4481.33, 7877.05, 7896.37, 8234.64, 9218.25
Fe II	4923.92, 5018.44, 5169.03, 5197.57, 5234.62, 5276.00, 5316.61, 5316.78

of the disc is much more difficult, as most of the additional emission profiles only have one clearly visible peak, and therefore a peak separation cannot be measured.

We compare the enlarged set of emission lines (Table 4.3) to the predictions from Non-Local Thermodynamic Equilibrium (NLTE) models of gaseous discs around white dwarfs (Hartmann et al., 2011). Each of the Ca and Mg lines detected in our X-shooter spectra are also present in the model of Hartmann et al. (2011), although they also predict other lines from these elements which we have not observed. These lines may lie below the detection threshold of our data, e.g. the predicted Mg I 5173 Å line is probably dominated by the emission of Fe II 5169 Å. We cannot compare our detections of Fe II or O I as these are not included in the calculations of Hartmann et al. (2011).

Hartmann et al. (2011) predict the Ca II triplet to be flanked by emission of C II 8700 Å. By comparison with the 2006 WHT spectra, the authors constrained the C abundance in the disc to less than 0.46 per cent by mass. Gänsicke et al. (2012) measured the C abundance of the debris accreted by SDSS J1228+1040 from *HST* UV spectra and found a mass fraction of 0.02 per cent, consistent with the non-detection of C emission in our deeper X-shooter spectra.

4.5 Doppler Tomography

While it is thought that the emission lines originate in a gaseous disc with an assumed Keplerian velocity field, the intensity distribution across the disc is not known. The smooth morphology variations of the Ca II triplet imply a gradual change in that distribution as viewed from Earth over the twelve years of observations, which is astonishing when com-

Table 4.4: Equivalent widths (EW) of the emission features shown in Figures 4.3 & 4.4. The Ca II triplet are set in bold.

Identifier	Central wavelength [Å]	EW (error) [Å]
Mg II	2800	-7.9 (0.4)
Ca II	3934	-0.893 (0.007)
Ca II	3969	-1.485 (0.009)
Mg II	4481	-0.061 (0.002)
Fe II	4923	-0.243 (0.007)
Fe II	5018	-0.377 (0.008)
Fe II	5185	-1.60 (0.01)
Fe II	5235	-0.220 (0.009)
Fe II	5276	-0.478 (0.009)
Fe II	5317	-0.646 (0.007)
O I	7774	-2.20 (0.02)
Mg II	7877	-0.78 (0.02)
O I	8230	-0.71 (0.03)
O I	8446	-1.50 (0.02)
Ca II	**8498**	**-16.73 (0.03)**
Ca II	**8542**	**-23.45 (0.03)**
Ca II	**8662**	**-20.76 (0.03)**
Mg I, O I	8810	-1.73 (0.03)
Ca II	8920	-1.90 (0.03)
O I, Mg II	9234	-2.64 (0.05)

pared to the orbital period of the material in the disc, which is of the order of a few hours.

One way of inducing the observed line profile variation could be the rotation (precession) of a fixed non-axisymmetric intensity structure. This has been proposed to explain some of the features observed in the emission line profiles seen at Be stars. These stars are rapidly rotating and host circumstellar material in disc structures that frequently show long term variability (Okazaki, 1991; Papaloizou et al., 1992; Okazaki, 1997). Hanuschik et al. (1995) report line profiles of Fe II 5317 Å (see their Figures 8, 14, and 15) seen in Be stars which are remarkably similar to the Ca II triplet observations of SDSS J1228+1040.

To test the hypothesis of a fixed intensity structure, we fit the Ca II triplet line profile using the method of Doppler tomography explained in Section 2.2.2. We used the 18 Ca II triplet profiles collected for SDSS J1228+1040 to produce Doppler maps with a range of trial periods spanning 24.64 years (9000 days) to 68.45 years (25000 days) with increments of 500 days. We would not expect a period much shorter than $\simeq 25$ years; otherwise the disc would have precessed $\geq 180°$, producing emission lines that are the reflection of the 2003 March observation.

Doppler maps with periods between $\sim$24–30 years ($\sim$9000–11000 days) appear very similar with only slight changes in the shape of the intensity distribution. However, for periods longer than 30 years the maps of the disc become elongated or stretched, generating discontinuous changes in velocity not expected for Keplerian orbits (examples of this are shown in Fig. 4.5). Maps with periods longer than 30 years also generate emission profiles with an additional peak in each of the components of the Ca II triplet, which are not observed here or in other systems with Ca II emission (see Section 3.5). We therefore adopt a period in between 24–30 years; 27.4 years (10000 days) and the Doppler map generated with this period is shown in Figure 4.6. We also show a trailed spectrogram generated from the Doppler map over one full 27.4 years cycle (Figure 4.7). These predictions will be compared against future spectroscopy of the Ca II triplet in SDSS J1228+1040.

The outer edge of the intensity structure corresponds to the highest velocities and hence the inner edge of the disc in coordinate space. The inner edge is clearly asymmetric, with a large dispersed region and a narrow intense strip related to the large red-shifted velocities and the sharp blue-shifted peak seen in the emission profiles, respectively.

During the 2003–2008 observations, the dispersed and narrow regions discussed above have projected velocities along the line of sight which are significantly reduced, increasing the central strength near zero velocity rather than the extremes of the profile. The dashed lines in Figure 4.6 represent circular orbits in velocity space, underlining that the Doppler image of SDSS J1228+1040 is highly non-circular, which agrees with our qualitative description of the line profiles in Section 4.3. Further, this non-circularity cannot be described well as a single eccentricity, but rather by a changing eccentricity as a function

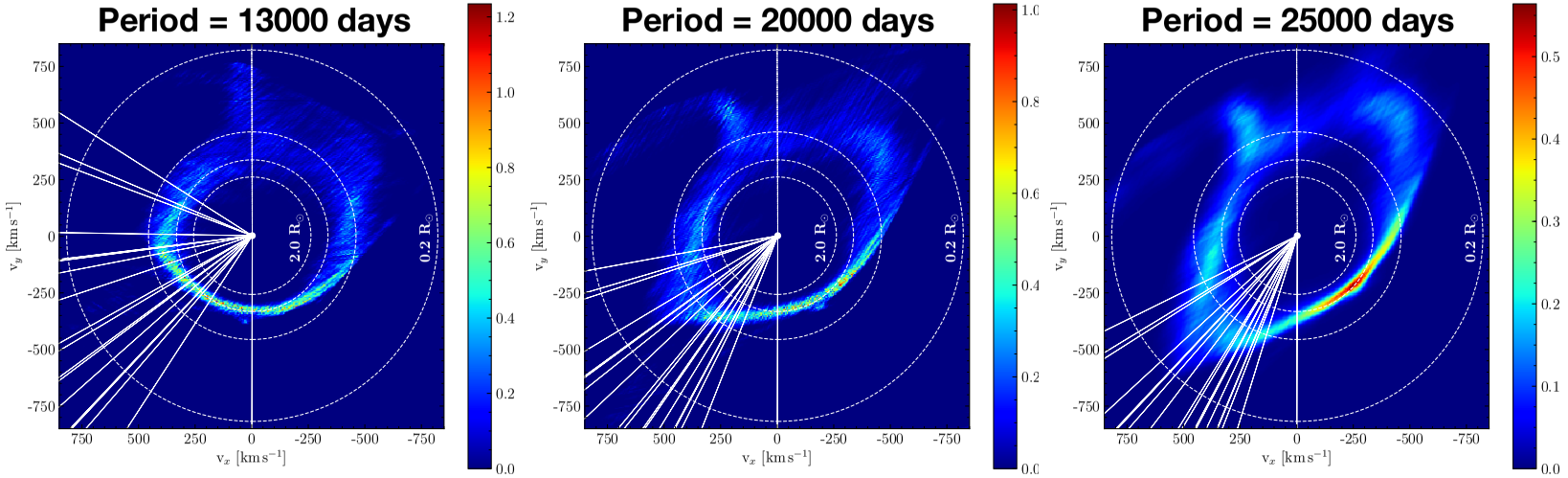

Figure 4.5: Maps similar to Fig. 4.6, but with precession periods of 13000 days (left), 20000 days (middle) and 25000 days (right), highlighting the effect going to large periods has on the Doppler maps. The line-of-sight markers (white solid lines) bunch up at higher periods, as they occupy smaller chunks of the overall precession period.

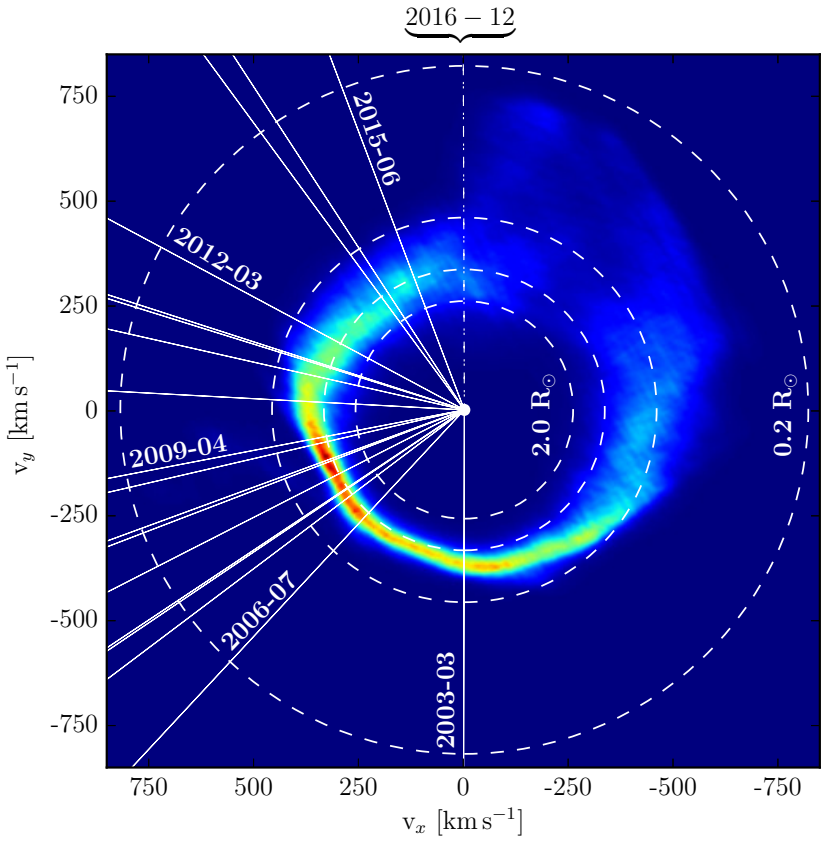

Figure 4.6: An intensity distribution in velocity space of the Ca II triplet which models the line profiles, observed in SDSS J1228+1040 obtained from Doppler tomography. The white dwarf is located at the origin of the map where the lines intersect as a solid white circle. The solid white lines represent the epoch and line of sight for each observation from March 2003 to May 2015 and the dot-dashed white line indicates when we expect the Ca II triplet to return to a morphology similar to that observed in 2003 (December 2016). The resulting profile would be a reflection of the first observation, assuming a precession period of $\simeq 27$ years. The dashed white circles indicate the location of material in a Keplerian orbit around SDSS J1228+1040, with observed orbital radii ($R \sin^2 i$) of 0.2, 0.64, 1.2 and 2 $R_\odot$, with the largest circle (highest velocities) corresponding to 0.2 $R_\odot$, and the smallest circle (lowest velocities) to 2$R_\odot$.

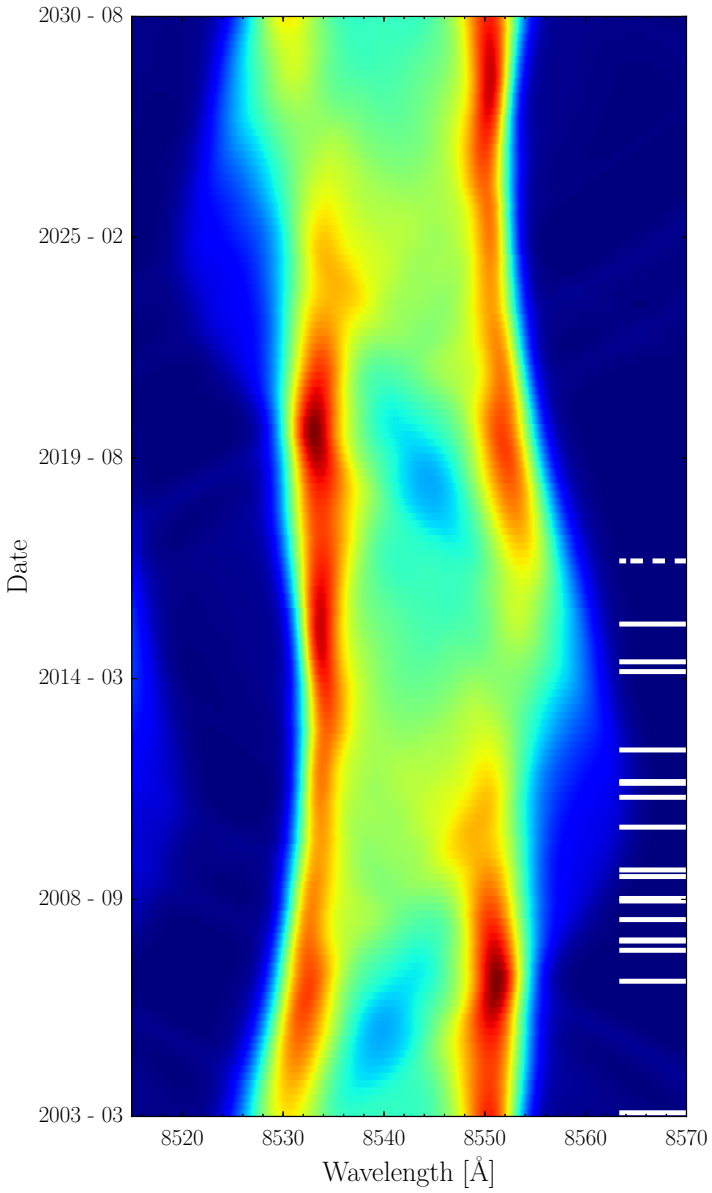

Figure 4.7: A trailed spectrogram generated from the Doppler map in Figure 4.6 over one full 27.4 years cycle. The solid and dashed white tabs indicate the position in the spectrogram where we have observed data, and the predicted halfway point respectively.

of radius.

From the Doppler map we reconstructed the emission features observed in order to check for self consistency (Figure 4.8). The line profiles generated from the Doppler map fit remarkably well for most epochs, although the sharpness of the red and blue-shifted peaks seen between 2008–2010 are not totally replicated. The inability to fully reconstruct all details of the observed emission profiles may suggest that one or more of the assumptions underlying the method of Doppler tomography required are not fulfilled in this SDSS J1228+1040, e.g. there could be additional short term variability in the system.

An additional note regarding the interpretation of the Doppler map is that it depicts only the intensity distribution of Ca II. The difference in morphology between the Ca II triplet and other ions, such as O I (see Section 4.3) suggests that these elements have different intensity distributions across the disc. Therefore Doppler maps of the emission lines of other ions in combination with that of Ca II could reveal additional information on the physical conditions (e.g. density, temperature) within the disc, if time-series spectroscopy with a sufficient signal-to-noise ratio is obtained.

4.6 A precessing disc?

We find that the data and the velocity map shown in Figure 4.6 are largely consistent with a constant non-axisymmetric intensity structure that precesses around the white dwarf, resulting in a periodically varying projection into the observed emission line profiles. The precession and the structure of the disc could be explained by several scenarios, which are not necessarily mutually exclusive:

1) We are observing a young, eccentric disc that has only recently formed from the tidal disruption of an asteroid. If only gravitational forces are considered, the asteroid is disrupted and forms a broken, highly-eccentric ring of debris around the white dwarf, the majority of which is located outside of the tidal disruption radius (Veras et al., 2014b). Adding radiation forces causes the particles in the disc to spread inwards towards the white dwarf (on time-scales determined by their size), eventually circularising (Veras et al., 2015). However, the time-scale on which a debris disc circularises is currently poorly known due to the complexity of the forces (e.g. radiation, gas drag) upon and the interactions (e.g. collisions) between the particles. If the circularisation time-scale is significantly shorter than the twelve years spanned by our observations, we would expect the asymmetry in the emission features to have evolved towards a constant, symmetric double-peaked line profile.

2) Precession due to general relativity. General relativistic effects will cause an eccentric orbit to precess over one full orbit on a period P_{ω} that is given by

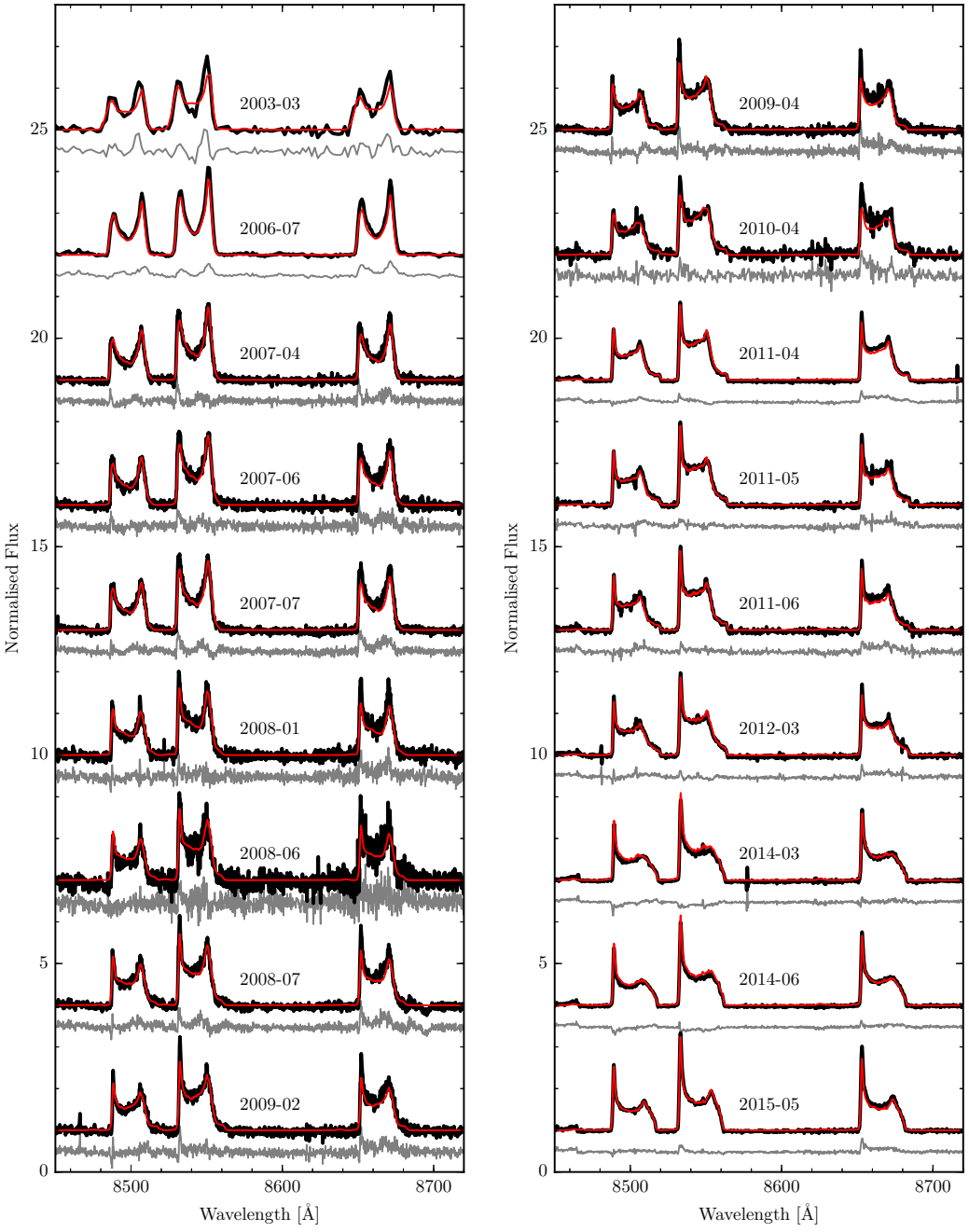

Figure 4.8: The continuum-divided Ca II triplet line profiles (black) for SDSS J1228+1040 in chronological order (as in Figure 4.2) reconstructed (red) using the Doppler map in Figure 4.6 with residuals (grey). The spectra are shifted in steps of three from the 2009 February (left) and 2015 May observations (right).

$$P_\omega \approx 84.98 \text{ yr} \left(\frac{M}{0.70\text{M}_\odot}\right)^{-3/2} \left(\frac{a}{1.00\text{R}_\odot}\right)^{5/2} \left(1 - e^2\right) \tag{4.1}$$

where M is the mass of the central star and a is the semi-major axis of the orbit (see Veras 2014 for details). In the limit of small eccentricities we can ignore the term $(1 - e^2)$. By adopting $M_{\text{wd}} = 0.7\,\text{M}_\odot$, we find precession periods of 1.54, 27.8 and 134 years for orbits with semi-major axes of 0.2, 0.64 $\text{R}_\odot$ and 1.2 $\text{R}_\odot$ respectively, i.e. the period of precession has a strong radial dependence.

General relativistic precession is intrinsic to any orbital mechanics, and furthermore the period of 27.8 years for an orbit at 0.64 $\text{R}_\odot$ is close to the period range deduced from our Doppler maps $\simeq$ 24–30 years. Therefore it is expected that general relativity should have a significant contribution to the variability observed in this system. The radial dependence of the precession period due to general relativity will cause collisions among the dust particles on different orbits, which is a possible mechanism for generating the observed gaseous component of the debris disc. These collisions would also act to dampen the eccentricity into a circular orbit, where production of gas due to general relativistic precession would eventually cease. It is worth noting that the Doppler map (inherently) does not display the radial dependence of the general relativistic precession, which may be dampened by other forces (e.g. gas pressure effects in the disc).

3) An external perturber outside the disc inducing both the eccentricity and precession. The flyby of a body orbiting on an eccentric orbit would perturb the orbits of the particles in the disc. We have performed some numerical N-body simulations to determine the effect of an external perturber on circular rings of particles located at about one Solar radius from the white dwarf. Because the asymptotic giant branch progenitor of SDSS J1228+1040 had a radius of at least 2.5–3.0 au, surviving planet-sized perturbers must now have a semimajor axis exceeding 3–11 au (see, e.g. Figure 10 of Mustill and Villaver 2012). Consequently, a perturber's current orbital period must be at least several years, which covers multiple observations from Figure 4.8, in particular during the years 2007–2008, where the observations are closely spaced. We therefore adopted a perturber semimajor axis of 5 au, with masses ($10^0 - 10^4 M_\oplus$) and eccentricities (0.990–0.998 - a realistic possibility; see Debes and Sigurdsson 2002; Veras et al. 2013; Voyatzis et al. 2013; Mustill et al. 2014; Bonsor and Veras 2015; Veras and Gänsicke 2015) in ranges that might produce an observable eccentricity change in the ring. Smaller mass perturbers would have to approach so close to the ring particles to potentially be in danger of tidally disrupting.

Each simulation contained 210 massless ring particles, and spanned one close encounter. The white dwarf mass was set at 0.705 $M_\odot$, and the particles were equally partitioned into seven rings at distances of $\{0.6, 0.7, 0.8, 0.9, 1.0, 1.1, 1.2\,R_\odot\}$. We uniformly

distributed the initial mean anomalies of the particles within each ring.

In every case changes in ring particle eccentricity occurred only within a few hours of a close encouter. During the remainder of the orbit, there was no eccentricity change. Therefore, in-between encounters (spanning several years), the geometry of the disc did not change, which is at odds with the observations from Figure 4.8. This mismatch would also hold true for perturbers with initially greater semimajor axes.

4) The disc induces its own eccentricity and precession. Statler (2001) has shown that an eccentric flat fluid disc can precess due to the pressure gradient generated within the disc. Figure 3 from Statler (2001) shows line profiles that are similar in morphology to that of SDSS J1228+1040 (see Section 4.3). In contrast to these simulations of purely fluid discs, the gaseous discs that we have observed are coupled to dust grains. Kinnear (2011) finds a typical gas mass, $M_{\rm gas}$, of $\sim 10^{19}$ g. Estimates of the dust mass, $M_{\rm dust}$, range from 10^{19} to 10^{24} g, from disc models that reproduce the observed infrared excess in systems with dusty discs (see, Jura et al. 2007; Jura 2008; Reach et al. 2009), i.e. $M_{\rm gas} \leq M_{\rm dust}$ and as such we can not assume the disc is dominated by the gaseous component. Finally, it is worth noting that Ogilvie (2001) finds that the eccentricity in a disc will dissipate on the viscous time-scale, which we estimate to be $\simeq$ 5-20 years (Section 4.6), i.e. similar to our observational baseline. Given that the eccentricity in SDSS J1228+1040 persists over this time scale, self-induction seems unlikely.

Of the different scenarios outlined above, a young eccentric disc that precesses due to general relativity appears to be the most natural scenario that can describe our observations. We would also expect this phase to be fairly short-lived, which would explain the rarity of detected gaseous debris disc components. Assuming the adopted precession period of 27.4 years, the system is expected to reach half way through the precession cycle in December 2016, i.e. we would expect a Ca II triplet morphology that is the reflection of the March 2003 observations. In the next section we discuss the variability seen in other gaseous discs around white dwarfs and the possible generation mechanisms for these systems.

4.7 Discussion

The variability of debris discs at white dwarfs is discussed in Section 3.5. The gaseous component of a debris disc will accrete onto the white dwarf, and without a sustained generation mechanism will dissipate over the viscous time-scale, which can be estimated using equation 2 from Metzger et al. (2012). The major uncertainty is the value of α, the accretion disc viscosity parameter (Shakura and Sunyaev, 1973). King et al. (2007) suggest $0.1 \leq \alpha \leq 0.4$ for a thin fully ionised disc. Given that the metallic gas is ionised to a

Table 4.5: Equivalent width measurements of the Ca II triplet in SDSS J1228+1040.

Date	Equivalent width [Å]
2003–03	-60 (7)
2006–07	-69 (2)
2007–04	-61 (2)
2007–06	-63 (2)
2007–07	-63 (2)
2008–01	-60 (2)
2008–06	-54 (2)
2008–07	-60 (2)
2009–02	-58 (2)
2009–04	-62 (2)
2010–04	-67 (1)
2011–01	-57 (1)
2011–05	-60 (1)
2011–06	-59 (1)
2012–03	-56 (1)
2014–03	-50 (1)
2014–06	-52 (1)
2015–05	-57 (1)

high degree, it is plausible to adopt this range for α, which leads to viscous time-scales of 5–20 years for a typical white dwarf mass. These time-scales match the disappearance of the Ca II lines observed in SDSS J1617+1620 discussed above.

We calculated the equivalent width of the Ca II triplet for SDSS J1228+1040 for each epoch (Table 4.5), and do not detect any significant decrease, suggesting that; 1) the gaseous discs in SDSS J1228+1040 and SDSS J0845+2257 are being sustained by ongoing gas production, and 2) there may be multiple pathways to generate a gaseous disc given that there are clear differences in the type of variability seen in these three systems and SDSS J1617+1620.

From Section 4.6, a natural scenario to explain the morphology variation is that of a young eccentric disc that precesses due to general relativity with the radial dependence of the precession period resulting in ongoing collisional gas production that ceases once the disc circularises. This scenario allows for gas generation, while not being mutually exclusive with the observations of SDSS J1617+1620, which would be better explained by a transient event such as a secondary asteroid impact onto a pre-existing, circularised disc (Jura, 2008). Such an asteroid impact would generate an initial quantity of gas that would subsequently dissipate over the viscous time-scale. A body within the disc could also induce a general relativistic precession of the gas disc, and is explored and discussed in Section 5.

The relatively short-lived transient nature of these gas generation mechanisms

also explains why there are systems with accretion rates much larger than that of SDSS J1228+1040, such as PG 0843+516 and GALEX 1931+0117, which do not show any sign of a gaseous disc (Gänsicke et al., 2012). We expect that debris discs with no detectable gaseous component are largely circularised.

4.8 Conclusions

I report the pronounced morphology changes of the Ca II triplet at SDSS J1228+1040 which we have modelled using the method of Doppler tomography. This procedure produced a non-axisymmetric intensity map in velocity space of the Ca II triplet, which we have interpreted as a precessing disc with a period in the range 24–30 years. We also detected additional emission lines in the averaged X-shooter spectra of SDSS J1228+1040, increasing the number of observed gaseous elements in this system to four. The variation in shape between the emission features of different ions is a clear indication that the intensity distribution in the disc for each ion is not the same. With time-resolved spectroscopy and sufficient signal-to-noise, Doppler tomography of the additional line profiles (such as O I 7774, 8446 Å) may reveal information about the physical properties in the disc (e.g density and temperature distributions).

The gaseous component of debris discs are a tracer of dynamical activity in these systems. Four of the five gaseous discs with time-resolved observations over time-scales of years show variability, and small-number statistics so far suggest that the dynamic variability of the gaseous discs themselves is the the norm rather than the exception.

Chapter 5

A planetesimal found orbiting within the debris disc surrounding the white dwarf SDSS J1228+1040

5.1 Introduction

There is growing evidence that gaseous debris discs are tracers for dynamical activity, from the long term variability seen at SDSS 1228+1040, SDSS 1043+0855 presented in Chapters 4 and 3, as well as SDSS 1617+1620, SDSS 0845+2257 and HE1349–2305 (Wilson et al., 2014, 2015; Dennihy et al., 2018). While gaseous discs have been monitored on a long-term basis, nobody has yet conducted an investigation into whether there is any variability on time-scales of the orbital periods within the discs ($\simeq$ hours).

In this chapter, I present short-cadence (100-200 s) observations of SDSS J1228+1040 obtained at the Gran Telescopio Canarias (GTC) which show clear variability with a period of $\simeq 2$ hours in the equivalent width and shape of the Ca II emission from the gaseous debris disc. I give several scenarios that could possibly explain the short-term variability, but argue that a planetesimal orbiting within the debris disc is the most plausible hypothesis.

5.2 Observations

SDSS J1228+1040 was observed at the 10.4 m GTC in 2017 April 20 & 21 and 2018 March 19, April 10, and May 2 using the OSIRIS spectrograph with the volume-phased holographic R2500I grating, and the data were obtained using 2×2 pixel binning and a readout speed of 200 kHz. This setup provided a wavelength range of 733–1000 nm with a spectral resolution $\simeq 0.35$ nm. We obtained a total of 519 exposures over the five nights, see Table 5.1 for full details. The majority of the observations were obtained using a 1.2 arcsec slit width, however in the second half of the 2017 April 20 night, we switched to a 0.8 arcsec slit as the weather improved, and additional calibration frames were taken as a result. The GTC observations of SDSS J1228+1040 were reduced using standard techniques discussed in Section 2.2, and we then normalised the continuum of each spectrum with a 7th-order polynomial.

Table 5.1: Log of observations.

Date	Number of exposures	Exposure time [s]	Start time [MJD]	End time [MJD]	Cycles Observed
2017–04–20	228	80	57863.85946	57864.12450	3.09
2017–04–21	131	120	57864.85940	57865.06820	2.44
2018–03–19	64	180	58196.08872	58196.24237	1.79
2018–04–10	32	180	58218.00653	58218.07959	0.85
2018–05–02	64	180	58240.90326	58241.05215	1.74

5.3 Results

5.3.1 Parameters of the white dwarf at SDSS J1228+1040

Distance Mass, and Effective Temperature

The mass and effective temperature of the white dwarf at SDSS J1228+1040 were determined by Koester et al. (2014) to be $M = 0.705 \pm 0.050\,\mathrm{M}_{\odot}$, and $T_{\mathrm{eff}} = 20713 \pm 281$ K respectively. Using a mass-radius relation, Koester et al. (2014) estimated the distance to the system using photometry in the optical and UV, as 120.9 ± 9.4 parsec and 134.2 ± 9.9 parsec, respectively. The *Gaia* Data Release 2 (Gaia Collaboration et al., 2016, 2018) reports a parallax of 7.89 ± 0.09 mas for SDSS J1228+1040 (source_id = 3904415787947492096), corresponding to a distance of 126.7 ± 1.5 parsec, which is consistent with the two distance estimates from Koester et al. (2014). Therefore we adopt the above mass.

Magnetic field strength

The non-detection of Zeeman splitting in the Balmer lines of SDSS J1228+1040 rules out magnetic fields $B \geq 1$ MG, which are detected in $\simeq 2-5\%$ of white dwarfs. The incidence of weaker fields among white dwarfs is still poorly constrained (Landstreet et al., 2012), however, fields of 70–500 kG have been detected from the splitting of metal lines in a significant fraction (three out of a sample of fourteen) of cool DAZ white dwarfs (Kawka and Vennes, 2014). If such a field were present in SDSS J1228+1040 it would certainly affect the accretion process from the disc into the stellar atmosphere, as well as possibly affecting the planetesimal. To derive an upper limit on the field strength in SDSS J1228+1040, we have compared the observed photospheric metal lines with model spectra of magnetic white dwarfs.

We computed synthetic line profiles of the line triplets of Si II at 4128–4130 Å, and of Mg II at 4481 Å and compared those to a high-resolution spectrum of SDSS J1228+1040 obtained under Program 595.C-0650(G) on 2017 March 01 with UVES on the VLT (Dekker et al., 2000). Si II and Mg II profiles were computed for a mean field modulus $\langle |B| \rangle$ (i.e. the average value of the field modulus over the observable hemisphere) ranging from zero to 50 kG. The computations were carried out using the FORTRAN code ZEEMAN (Landstreet, 1988; Bailey and Landstreet, 2013). This code requires a model atmosphere structure appropriate for the atmospheric parameters of SDSS J1228+1040 (Gänsicke et al., 2012), which was computed with the code of Koester (2010). ZEEMAN solves the LTE radiative transfer problem of photons emerging locally, as modified by a specified magnetic field, for spectral line profiles in all four Stokes parameters. The local emergent line profiles are then summed over the visible stellar disc, appropriately Doppler shifted to account for stellar

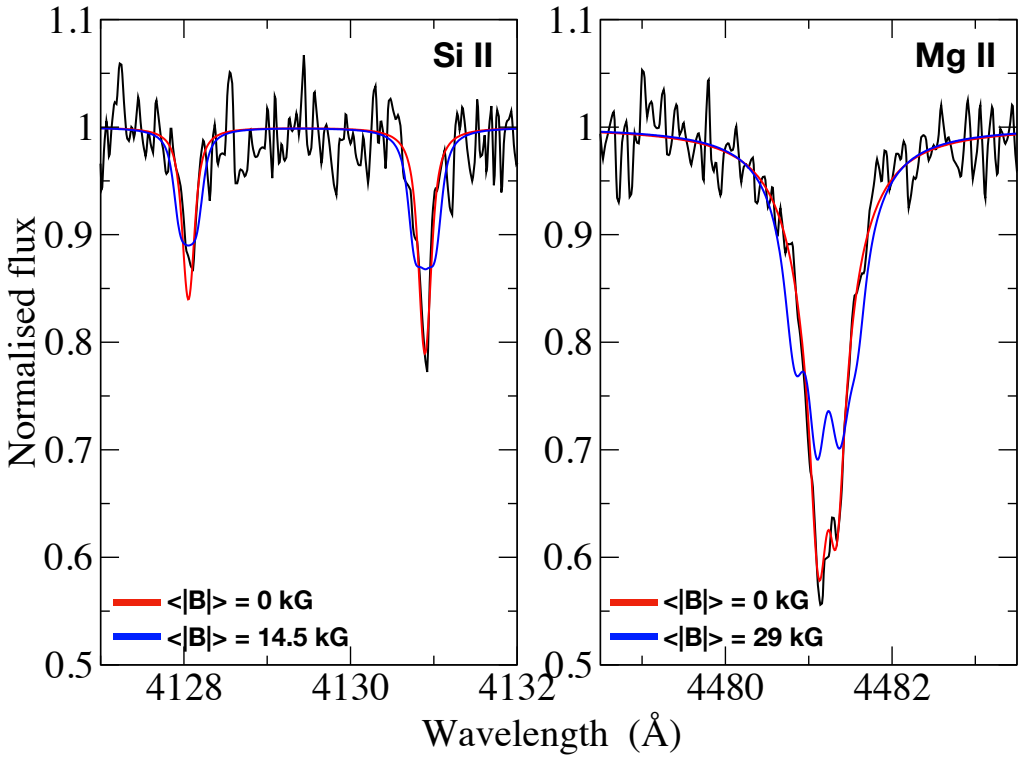

Figure 5.1: A UVES spectrum comparison of the observed line profiles (black) of Si II 4128–4131 Å and Mg II 4481 Å with computed profiles for the non-magnetic case, $\langle|B|\rangle$ = 0 kG, (red) and with profiles for which the presence of a field is clearly visible (blue). For the Mg II lines the magnetic line fit is clearly unacceptable with a field of $\langle|B|\rangle$ = 29 kG. Because the Si lines are much narrower than the blend of the two strong components of the Mg II line while, the Si II lines the fit is already very poor for a weaker field of 14.5 kG. We conclude from the Si lines that the upper limit on the field strength at SDSS J1228+1040 is $\langle|B|\rangle$ = 10–15 kG.

radial velocity, to produce a predicted set of (Stokes I) line profiles for the spectral region being studied. For SDSS J1228+1040 a dipolar field configuration, with the factor-of-two contrast between polar and equatorial field strengths of a pure dipole somewhat reduced, was assumed.

Examples of computed profiles are compared to the observed lines in Figure 5.1. It is clear, particularly from the very sharp Si II lines, that in order to escape detection, a field in SDSS J1228+1040 would have to have $\langle|B|\rangle \leq 10 - 15$ kG, a field strength close to the weakest field detected in any white dwarf (Landstreet et al., 2017).

5.3.2 Determination of the period of variability

To quantify the variability detected in the Ca II lines, we calculated the equivalent width (EW) of the three individual Ca II triplet line profiles, as well as the strength of the blue- and red-shifted sides of the profiles (Figure 5.2 & 5.3, see also Table 5.2). The EWs were calculated by integrating the flux below the line profiles in the intervals 8470 – 8520 Å, 8524 – 8568 Å, and 8640 – 8690 Å, for the left, middle, and right hand emission profiles, respectively. We split the blue- and red-shifted sections for each profile using the air-wavelengths of the Ca II profiles in the rest frame of the white dwarf which is at +19 km s^{-1} (Manser et al., 2016b). Both the EW of the profiles, as well as the ratio of flux (blue-to-red) emitted between the blue- and red-shifted sections show significant levels of variability.

Underlying the periodic signal, there are longer-term variations affecting the EW and blue-to-red ratios, both related to the observing conditions and intrinsic to the system. The blue-to-red ratio data points in Figure 5.2 show a general decrease over time, and we suspect this is due to systematic uncertainties in the continuum normalisation, which can be affected by variations in airmass, as well as in the telluric absorption features that dominate the spectrum either side of the Ca II triplet from 7500–10000 Å. However more work is needed to determine the magnitude of systematic trends. As such, we expect slow, systematic drifts in the measurements of the EWs and blue-to-red ratios. In addition, the nightly average EW measurements of the 2018 profiles in Figure 5.3 (see also Table 5.2) change more than what can be explained by variations in the continuum normalisation, revealing variability in the strength of the Ca II triplet on a time-scale of weeks to months. The amplitude of these variations is larger than that of the two-hour signal I discuss in this Chapter, and cause artifacts in both the phase-folded trailed spectrogram, and the phase-folded EW and blue-to-red ratio curves. As such, we scale the strength of the 2018 EW profiles to that of the average strength of the 2018 March 19 data for our period analysis.

Table 5.2: The average equivalent width measurements of the Ca II triplet in SDSS J1228+1040 for each night, given for each component of the Ca II triplet labeled by their zero-point air-wavelenth.

Date	8498.020 [Å]	8542.090 [Å]	8662.140 [Å]
2017–04–20	-20.11 (0.02)	-28.31 (0.02)	-25.32 (0.02)
2017–04–21	-19.70 (0.02)	-27.78 (0.02)	-24.93 (0.02)
2018–03–19	-20.66 (0.02)	-28.66 (0.02)	-24.90 (0.03)
2018–04–10	-18.26 (0.05)	-24.70 (0.04)	-21.40 (0.06)
2018–05–02	-19.13 (0.02)	-26.33 (0.02)	-22.76 (0.02)

We have analysed the EW and blue-to-red ratio curves using the MIDAS/TSA package implemented by Schwarzenberg-Czerny (1996). We combined the measurements for

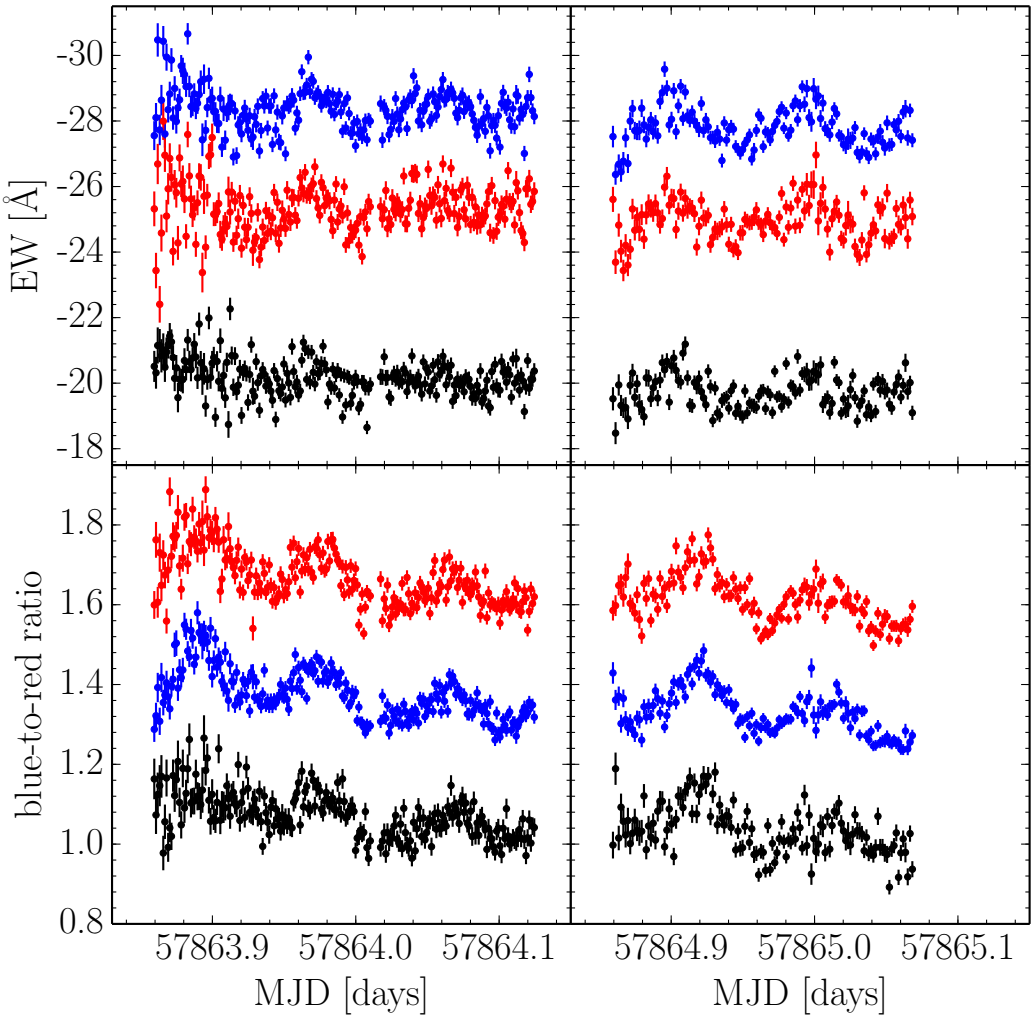

Figure 5.2: The equivalent width (EW) and blue-to-red ratio of the Ca II triplet measured from the observations taken on 2017 April 20 & 21 are shown separately for the the left (black), middle (blue) and right (red) components of the Ca II triplet as a function of Modified Julian Date (MJD). The EW and blue-to-red ratio curves are both continuum normalised. The blue-to-red ratio curves are vertically offset in steps of 0.3 from the left component of the Ca II triplet.

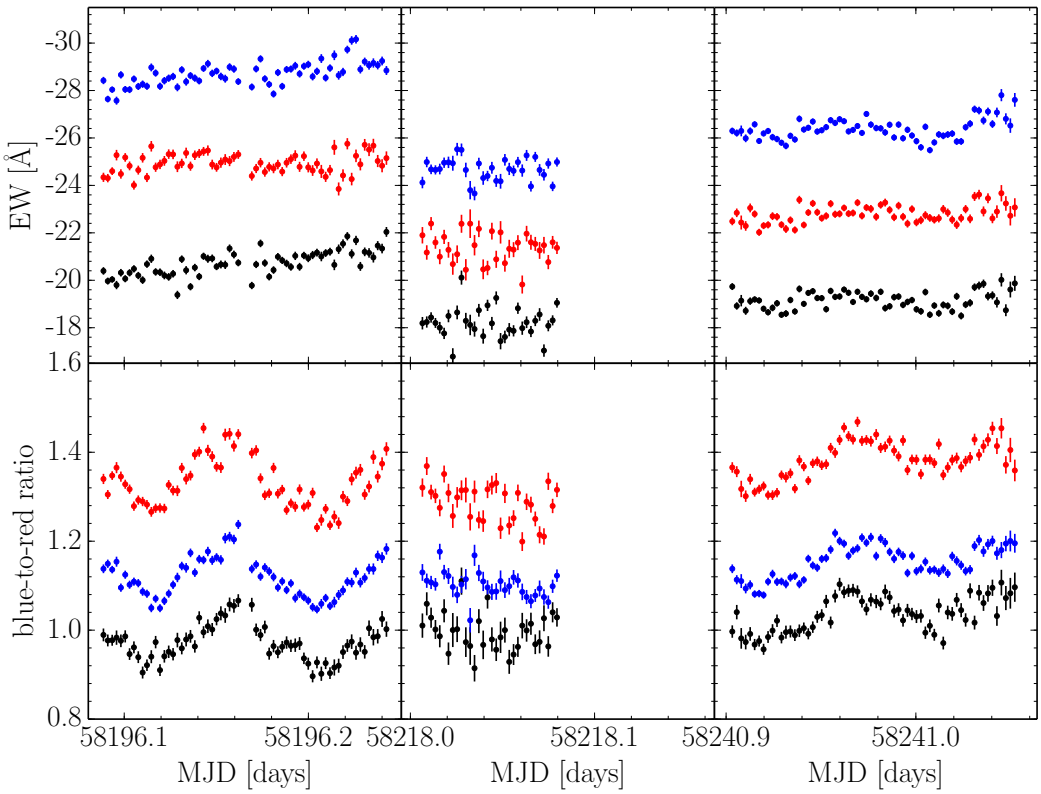

Figure 5.3: The equivalent width (EW) and blue-to-red ratio of the Ca II triplet measured from the observations taken on 2018 March 19, April 10, and May 2 are shown separately for the the left (black), middle (blue) and right (red) components of the Ca II triplet as a function of Modified Julian Date (MJD). The EW and blue-to-red ratio curves are both continuum normalised. The blue-to-red ratio curves are vertically offset in steps of 0.2 from the left component of the Ca II triplet.

the three Ca II components, and then computed discrete Fourier transforms for the two consecutive nights of data taken in 2017, and for the three nights of data taken several weeks apart in 2018 (Table 5.1).

The amplitude spectra computed from the 2017 data (Figure 5.4, left panel) show several possible period aliases separated by $1\,d^{-1}$, as it is usually the case for single-site data. We fitted sine functions to the time-series measurements to determine the uncertainties of the periods corresponding to the three strongest aliases (Table 5.3). To evaluate the likelihood of the individual aliases representing the true period of the short-term variability we ran a bootstrap simulation (Press 2002, Chapter 15.6) and found that the most likely periods measured from the variability of the equivalent widths and the blue-to-red ratios are 122.88±0.19 min (98.6%) and 123.63±0.15 min (98.0%). These two periods are consistent at the 2σ level, and folding the Ca II profiles on either of them results in equally smooth phase-folded equivalent width and blue-to-red ratio curves. We attribute the small discrepancy between the two period measurements to the systematic differences in the morphology of the equivalent width and blue-to-red ratio time-series data, and the fact that only two to three phase cycles were obtained during each of the two nights.

Table 5.3: Periods and uncertainties associated with the three strongest aliases in the amplitude spectrum computed from the 2017 equivalent width and blue-to-red ratio measurements (Figure 5.4). The likelihood of the individual aliases representing the true period of the short-period variability was assessed with a bootstrap test, and is reported in brackets.

Data	Period [min]		
2017 equivalent widths	113.21±0.20 (0.2%)	**122.88±0.19** (98.6%)	134.23±0.22 (1.2%)
2017 blue-to-red ratio	114.04±0.16 (0.0%)	**123.63±0.15** (98.0%)	135.01±0.19 (2.0%)

The 160 spectra obtained in 2018 were spaced out in three observing runs separated by ≃3 weeks each, corresponding to several hundred cycles of the Ca II variability. Given that these three sets of data only span ≃0.85 to 1.79 phase cycles, each individual set provides a period measure with an accuracy of ≃ 5% – which is insufficient to derive a unique period from the combined 2018 observations. We note that the amplitude spectrum computed from the equivalent widths is less well defined than that computed from the blue-to-red ratios, which we attribute to the variation in the nightly average of the overall Ca II equivalent width. As an initial test, we simply folded the 2018 Ca II profiles on either of the 2017 periods, which resulted in phase-folded equivalent width and red-to-blue ratio curves that are very similar to that obtained from the 2017 data.

In a final step, we computed amplitude spectra from the combined 2017 and 2018 blue-to-red ratio data, which results in strong one-day aliases superimposed with a very fine high-frequency alias structure from the week-long and year-long gaps in the time-series. The best-fit period from this data set is $P = 123.4 \pm 0.3$ min, which we adopt as the

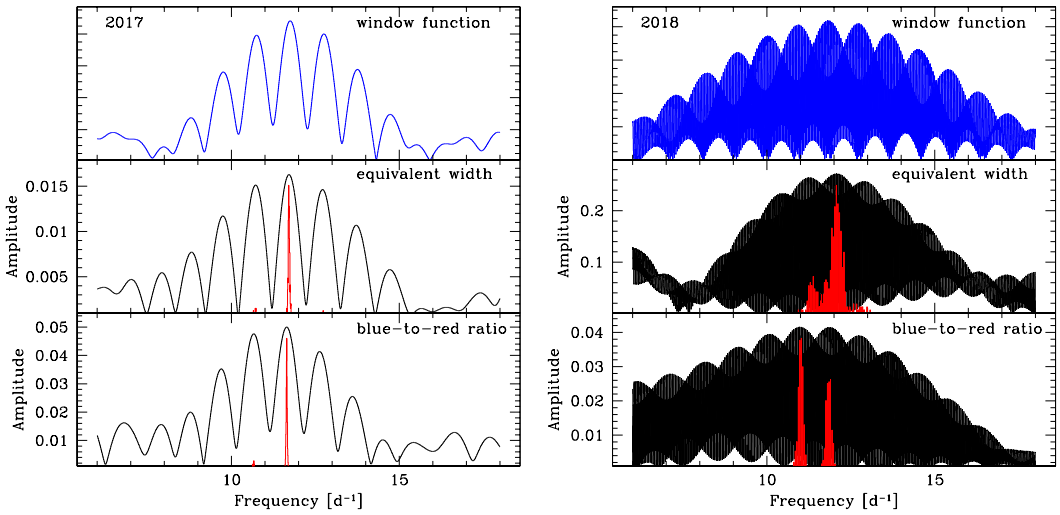

Figure 5.4: Amplitude spectra of the equivalent width and blue-to-red ratio measurements. Discrete Fourier transforms (black) were computed from the normalised equivalent widths (middle panel) and blue-to-red ratios (bottom panel) measured from the time-series spectroscopy obtained over two consecutive nights in 2017 (left) and over three nights spread out over several weeks in 2018 (right). The amplitude spectra contain the typical 1 d^{-1} alias structure for single-site time series data, which are illustrated by the window function (blue, top panel). In 2018, this pattern is superimposed by a fine-structure of aliases related to the long gaps in between the three individual observing runs (Table 5.1). The probability distribution across the different aliases was assessed using a bootstrap test, and are shown in red. Based on the larger amplitude of the blue-to-red ratio signal, and the nearly three-sigma probability (96.8%), we identify the most likely period, which we compute as a weighted average of the values derived from the equivalent widths and blue-to-red ratios, $P = 123.4 \pm 0.3$ min.

value used for the further analysis. The uncertainty was set to reflect the difference between the two periods derived above from the 2017 data, a more accurate measurement of the period will required to re-observe the system for several orbital cycles over a number of subsequent nights. The Ca II profiles for the 2017 and 2018 observations were phase-folded on this period to produce Figure 5.5. We note that we rescaled the average equivalent width of each of the spectra obtained on 2018 April 10 and 2018 May 2 to that measured from the 2018 March 19 profiles before phase folding to remove artifacts generated by the long-term variations in equivalent width.

While we are confident that we have identified the one-day alias corresponding to the true period of the Ca II variability, we note that adopting the period corresponding to either neighbouring alias changes the numerical results by a small amount, but leaves the general conclusions of the Chapter unaffected.

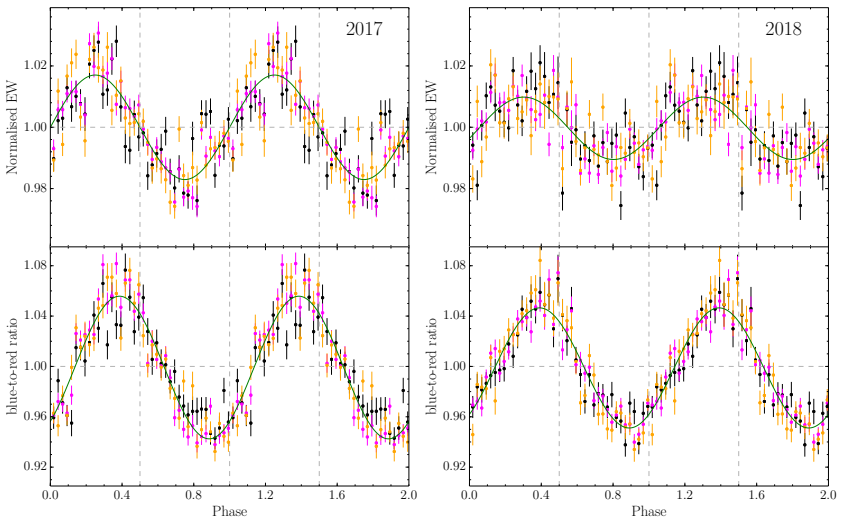

Figure 5.5: We show the equivalent width (EW, top panel) and the blue-to-red ratio (bottom panel, defined as the ratio of blue-shifted to red-shifted flux centred on the air-wavelengths of the Ca II triplet in the rest frame of the white dwarf at $+19\,\mathrm{km\,s^{-1}}$, with the mean set to 1.0) variation of the Ca II triplet emission from the gaseous debris disc around SDSS J1228+1040, phase-folded on a 123.4 min period (one cycle repeated for clarity, see supplementary material) for the 2017 (left) and 2018 (right) data sets. The EWs and blue-to-red ratios for the left, middle, and right components of the Ca II triplet are coloured in black, magenta, and orange respectively. We averaged the data over the three profiles and fitted them with a sinusoid, shown in green. The EW and the blue-to-red ratio curves are found to be offset in phase by 0.14 ± 0.01 cycles ($49^{\mathrm{o}} \pm 4^{\mathrm{o}}$) and 0.09 ± 0.01 cycles ($31^{\mathrm{o}} \pm 5^{\mathrm{o}}$) for the 2017 and 2018 profiles respectively. Phase zero for both the 2017 and 2018 data sets has been shifted such that the fit to the 2017 EW data passes through zero at zero phase, and the vertical dashed lines denote the phases 0.5, 1.0, and 1.5.

We calculated the spectrogram for the normalised Ca II triplet emission profiles phase-folded to a period of 123.4 mins (Figure 5.6, middle panels), and subtracted the averaged normalised emission profile (Figure 5.6, top panels) to produce an average-subtracted spectrogram (Figure 5.6, bottom panels, an example of this method is shown for the 2017 data at phase 0.4875 in Figure 5.7). The average-subtracted spectrogram shows a clearly detected, coherent low-amplitude ($\simeq 3\,\%$) variability in the strength and shape of the Ca II triplet with a period of 123.4 ± 0.3 min, which is clearly visible in all three components of the triplet after subtracting the average emission line profile in the five nights of observations (Figure 5.6). The detected variability has been present in the disc for $\simeq 4400$ orbital cycles, and using Kepler's third law, adopting $M = 0.705 \pm 0.050\,\mathrm{M}_{\odot}$ ($1\,\mathrm{M}_{\odot} = 1.99{\times}10^{30}$ kg) as the mass of SDSS J1228+1040 (Koester et al., 2014), the semi-major axis, a, of the orbit corresponding to the additional Ca II emission is found to be $a = 0.73 \pm 0.02\,\mathrm{R}_{\odot}$ ($1\,\mathrm{R}_{\odot} = 6.96{\times}\,10^{8}$ m).

The equivalent widths (EWs, a measure of the strength of the lines relative to the continuum) of the three Ca II triplet profiles, as well as the ratios of blue-shifted to red-shifted flux throughout the 123.4 min period are shown in Figure 5.5, illustrating the variation in the overall brightness of the emission lines, and the strong asymmetry of the velocity of the additional flux, respectively. The variable emission shown in Figure 5.6 (bottom panel) alternates (moves) from red-shifted to blue-shifted wavelengths as a function of phase. Assuming that the additional, variable emission is generated by gas in orbit around the white dwarf, this indicates that we only see the emission when it is on the far side of its orbit around the white dwarf with respect to our line of sight. This additional emitting region is obscured, either by the disc or the region itself when the material is traveling in front of the star, where we would otherwise observe the blue-shifted to red-shifted transition. We fitted sinusoids to both the EW and blue-to-red ratio data, finding them to be offset in phase by 0.14 ± 0.01 cycles and 0.09 ± 0.01 cycles in 2017 and 2018 respectively. These phase-shifts imply that the maximum EW is observed when the region emitting the additional flux is at its maximum visibility and thus furthest from us in its orbit around the white dwarf, whereas the maximum blue-shifted emission will occur up to 0.25 cycles afterwards. The smoothness of the EW and blue-to-red ratio variations, along with the extent in orbital phase ($\simeq 0.4$) of the variable emission in Figure 5.6, indicates that the emission region is extended in azimuth around the disc, rather than originating from a point source.

5.4 Possible scenarios causing the observed Ca II variability

There are several scenarios that could be generating the short-term variability we see at SDSS J1228+1040, and we discuss them below.

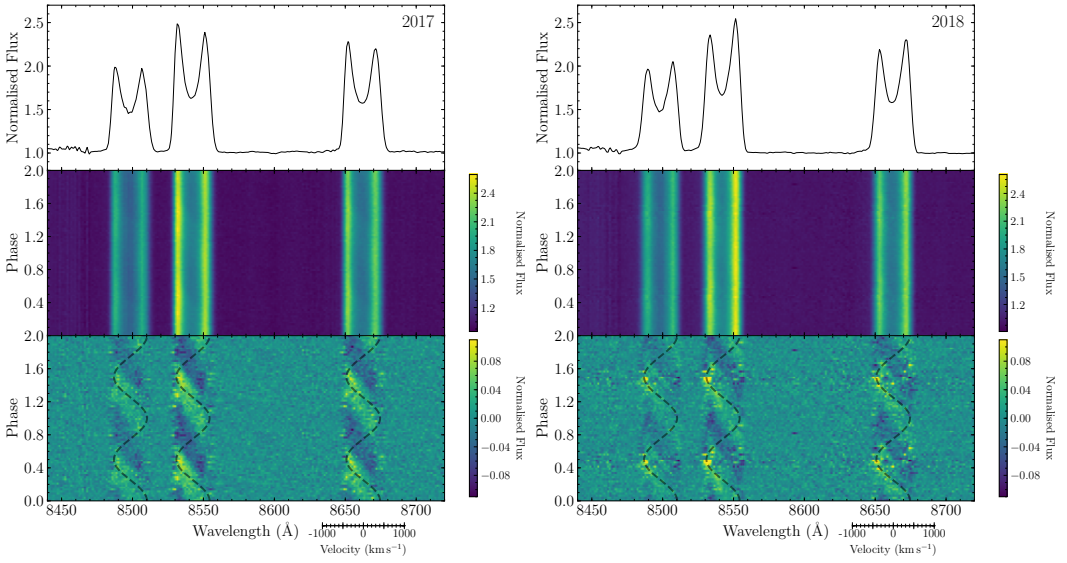

Figure 5.6: Short cadence spectroscopy of SDSS J1228+1040 was obtained with the OSIRIS spectrograph on the 10.4m Gran Telescopio Canarias on La Palma. A total of 519 spectra were taken over two nights in 2017 (left), and three nights in 2018 (right), see Table 1 for the log of the observations. The averaged, normalised spectrum of the Ca II triplet is shown in the top panel. We detected periodic variability in the equivalent width (EW) and the relative strengths of the left and right-hand sides of the profile (blue-to-red ratio, see Figure 5.5) on a 123.4 min period, on which we have phase-folded the spectra to produce the trailed-spectrogram in the middle panel (we repeat one cycle for clarity). The colour-map intensity reflects the normalised flux. Subtracting the coadded spectrum from the phase-folded trailed-spectrogram done separately for each year) clearly illustrates the variability in both flux and wavelength on the 123.4 min period in all three components of the Ca II triplet (bottom panel). The dashed curves are not fits to the data, but simply illustrate the typical S-wave trail for a point source on a circular orbit with a semi-major axis of 0.73 $R_\odot$ and an inclination of 73^o (Gänsicke et al., 2006). A velocity axis is provided for the right-most Ca II triple line profile.

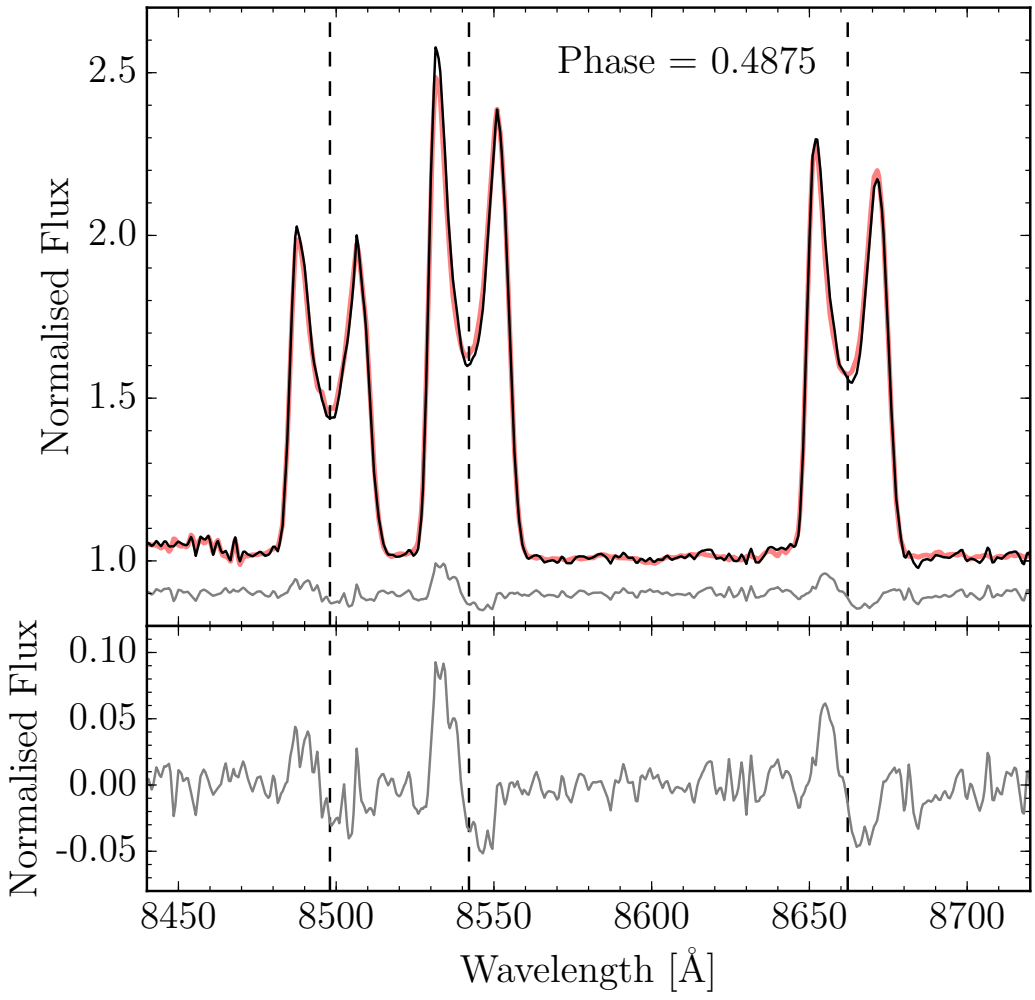

Figure 5.7: The top panel shows the average spectrum (red) for the Ca II triplet and for the phase 0.4875 (black) from the 2017 spectra (Figure 5.6, left). Subtracting the average spectrum from the averaged spectra at this phase results in the average-subtracted spectrum (grey), which has been shifted up by 0.9 for clarity. This average-subtracted spectrum is also shown enlarged in the bottom panel.

5.4.1 Stellar/Sub-stellar companion

We consider the possibility of a stellar or sub-stellar (brown dwarf or Jovian planet) in orbit around SDSS J1228+1040, where the observed variability in the Ca II triplet emission profile could be explained by the irradiated inner-hemisphere of a companion. Such emission line variability has been detected in H_α in SDSS J1557+0916, arising from a 63 M_J brown dwarf in a 136.4 min orbit with a white dwarf (Farihi et al., 2017). This system also contains a dusty debris disc polluting the white dwarf photosphere with metals.

Radial velocity measurements of the Mg II 448.1 nm line put the mass limit for any possible companion to SDSS J1228+1040 at $M_p \sin i \leq 7\,M_J$, and adopting an inclination of 73° obtained from modelling the Ca II emission line profiles (Gänsicke et al., 2006), we obtain an upper limit on the companion mass of $M_p \leq 7.3\,M_J$. More importantly, the spectrum of SDSS J1228+1040 lacks the emission of hydrogen detected in all white dwarf plus brown dwarf binaries (see also Maxted et al. 2006; Littlefair et al. 2014; Casewell et al. 2018), which is also seen in cataclysmic variables in which white dwarfs accrete from low-mass main-sequence stars (Manser and Gänsicke, 2014). We therefore confidently rule out the presence of a hydrogen-rich stellar or sub-stellar companion. Another possible analogue are AM CVn stars, a small class of binaries containing white dwarfs accreting from hydrogen-depleted degenerate companions, some of them with extreme mass ratios (Kupfer et al., 2016). However, all AM CVn stars exhibit strong emission lines of helium, which are also not detected in the spectrum of SDSS J1228+1040. Moreover, the material transferred to the white dwarfs in CVs (with hydrogen-rich donors) and AM CVn stars (with hydrogen-depleted donors) is rich in carbon and nitrogen, respectively, both of which are strongly depleted in the material accreted by SDSS J1228+1040 (Gänsicke et al., 2012). The absence of hydrogen and helium emission lines, together with the fact that the abundances of the material accreted onto the white dwarf in SDSS J1228+1040 are compatible with a rocky parent body, rules out the presence of any type of stellar or sub-stellar companion filling, or close to filling, their Roche-lobe. Finally, assuming a typical radius of a brown dwarf at $\simeq 1\,R_J$ (Laughlin, 2018), we calculate a minimum mass required for a companion to not fill its Roche-lobe at $\simeq 18\,M_J$, which is a factor two larger than our upper limit mass estimate. Therefore we exclude a brown dwarf or a Jovian planet as a possible explanation for the Ca II variability detected at SDSS J1228+1040.

5.4.2 A vortex in the disc

Dust trapping vortices have been invoked to explain non-axisymmetric structures in sub-mm observations of protoplanetary discs (Isella et al., 2013; van der Marel et al., 2013; Casassus et al., 2013; Marino et al., 2015). The origin of these structures and their conclusive

identification as vortices have not yet been determined from observations, but theoretical analyses and numerical simulations have determined some of the main properties of disc vortices. One of the most robust routes for their origin is the Rossby wave instability (RWI, Lovelace and Hohlfeld 1978; Toomre 1981; Papaloizou and Pringle 1984, 1985; Hawley 1987; Lovelace et al. 1999; Li et al. 2000), which is the form that the Kelvin-Helmholtz instability takes in Keplerian discs. The RWI is triggered by a 20 %-30 % localized axisymmetric increase in pressure, with the extra shear converted into vorticity. In numerical simulations of primordial protoplanetary discs the RWI is pervasive because this condition is easily realised at the boundaries between turbulent and quiescent zones (Varnière and Tagger, 2006; Lyra et al., 2009a; Lyra and Mac Low, 2012), at planetary gaps (Koller et al., 2003; de Val-Borro et al., 2007; Lyra et al., 2009b), and almost any transition in resistivity/viscosity (Lyra et al., 2015; Flock et al., 2017).

Vortices are known to be destroyed by the magnetoelliptic instability (MEI, Mizerski and Bajer 2009; Lyra and Klahr 2011; Faure et al. 2015), a weak (subthermal) field instability that is a generalised form of the magnetorotational instability (MRI, Balbus and Hawley 1998) in flows with elliptical streamlines (Mizerski and Lyra, 2012). This destruction happens because MEI will generate turbulence within the disc, which diminishes vortices and hinders their production (Faure et al., 2015). The MEI is a weak-field instability and should be present if the conditions for the MRI are also present. We can assess the conditions for the MRI in the disc around SDSS J1228+1040. Adopting an upper limit on the field strength of 10 kG for the white dwarf (see Section 5.3.1), the implied upper limit on the field strength in the disc is 10-100 mG. At a temperature, $T = 6000$ K and a column density, $\Sigma = 10^{-4}$ g cm^{-2} (Kinnear, 2011; Melis et al., 2010), the ratio of thermal to magnetic pressure in the disc is $\beta \sim 20 - 2000$ for a field strength of 100 mG and 10 mG respectively, and the weak-field condition is therefore satisfied. The ionisation fraction is also high, so the gas around SDSS J1228+1040 should be MRI-active. The growth rate, of MEI is exponential, and the amplification, $r_{\rm amp}$, of seed instabilities can be calculated as

$$r_{\rm amp} = e^{0.75\frac{2\pi}{P}t}, \tag{5.1}$$

where t is the length of time, and over three orbits ($t = 3P$), the amplification of MEI is $\sim 10^6$ (Lyra and Klahr, 2011; Mizerski and Lyra, 2012). From this growth rate, we can thus conclude that any vortex in this gas will be heavily unstable to the MEI and quickly destroyed. Considering these estimates and assumptions, we rule out the hypothesis that a vortex in the disc is generating the Ca II variability detected in the high-cadence GTC spectroscopy of SDSS J1228+1040.

We note that it is in principle possible to estimate the accretion rate, $\dot{M}_{\rm acc}$, onto the white dwarf due to MRI turbulence using

$$\dot{M}_{\rm acc} = \frac{3\pi\Sigma\alpha c_s^2}{\omega}, \tag{5.2}$$

where α is the viscosity parameter, $\omega = 2\pi/P$ is the angular frequency, and c_s is the sound speed given by $c_s = Tc_p(\gamma-1)$, where T is the temperature of the disc, c_p is the heat capacity at constant pressure, and γ is the adiabatic index (Shakura and Sunyaev, 1973; Lynden-Bell and Pringle, 1974). Estimates of the column density span many orders of magnitude, from $\Sigma \sim 10^{-9}$ to 0.3 g cm^{-2} (Kinnear, 2011; Melis et al., 2010; Hartmann et al., 2011). The lower limit of 10^{-9} g cm^{-2} is determined by the fact that no emission from forbidden line cooling is detected in the spectrum of SDSS J1228+1040 (Melis et al., 2010). The upper limit of 0.3 g cm^{-2} assumes that the disc is viscously heated to produce the Ca II emission (Hartmann et al., 2011), and results in an inferred accretion rate of $\sim 10^{17}$ g s^{-1}, which is many orders of magnitudes above the highest accretion rate observed in any debris-accreting white dwarf (Bergfors et al., 2014). We consider this upper limit as totally physically unrealistic. Adopting, as an example, $\Sigma = 10^{-4}$ g cm^{-2}, and $T = 6000$ K, which was determined from a photo-ionisation model for the Ca II triplet emission (Kinnear, 2011), $P = 123.4$ min, and $\alpha = 0.25$ (an estimate obtained from the disappearing gaseous debris disc around the white dwarf SDSS J1617+1620, Wilson et al. 2014), we estimate an accretion of $\dot{M}_{\rm acc} = 4 \times 10^{10}$g s^{-1}. We conclude that for a value of $\Sigma \simeq 10^{-6}$ g cm^{-2}, consistent with the current estimates of the column density, MRI turbulence would result in an accretion rate that is broadly consistent with the accretion rate derived from modelling the photospheric metal abundances, 5.6×10^{8}g s^{-1} (Gänsicke et al., 2012).

5.4.3 Photoelectric instability

Another possibility for the origin of the brightness asymmetry in the gas disc at SDSS J1228+1040 is the photoelectric instability (PEI, Klahr and Lin 2005, 2001; Besla and Wu 2007; Lyra and Kuchner 2013), which works in the following cycle as follows: (i) electrons are ejected off dust grains by ionising radiation, (ii) the superthermal electrons heat up the gas via collisions, (iii) dust grains move toward the high pressure gas, (iv) more dust leads to more photoelectric ionisations, releasing more heat, and a further increase in the dust concentration, resulting in a positive feedback. Lyra and Kuchner (2013) modeled the photoelectric instability in 2D and 3D, finding that it results in rings and arcs in both gas and dust. Richert et al. (2018) recently included radiation pressure in the model, finding a variety of other structures, including spirals and large eddies.

Although the PEI was originally proposed for gaseous debris discs around pre-main-sequence and main-sequence stars, the process should occur in any optically thin disc of gas and dust illuminated by a photo-ionising source. Systems with a high gas-to-dust ratio (~ 1)

are ideal for hosting PEI, though we note that in dust-dominated discs the PEI should also be present, albeit only in nonlinear form (see Fig 1i of Lyra and Kuchner 2013).

The two sets of time-resolved spectroscopy show that the two-hour variability in the Ca II line is present in SDSS J1228+1040 over at least 4000 orbits, whereas the longest simulations of PEI did not go beyond 400 orbits (Richert et al., 2018). To assess if the photoelectric instability could result in structures in the disc that are sufficiently long-lived to explain the observed variability, we simulated a disc using the Pencil Code for 2000 orbits, and scrutinised the time evolution of these structures. The low bolometric luminosity of white dwarfs renders radiation pressure unimportant, so the model of Lyra and Kuchner (2013) which we apply here is more applicable than that of Richert et al. (2018). We estimated the aspect ratio of the disc to be $\simeq 10^{-3}$, assuming a disc radius of $\simeq a$, and a disc scale height $H \simeq 4.3 \times 10^{-3}\,\mathrm{R}_\odot$ calculated using Equation 12 from Melis et al. (2010) with a stellar mass $M_* = 0.705\,\mathrm{M}_\odot$, and a distance from the star $D = 0.73\,\mathrm{R}_\odot$. From this, we conclude that the disc is flat and can be treated in 2D.

The PEI model is calculated in cylindrical coordinates, in 2D in the disc midplane, with radial range $r = [0.4, 2.5] R_\odot$ and full 2π coverage in azimuth. The resolution is $L_r \times L_\phi = 256 \times 256$. We added 500 000 Lagrangian particles to this grid to represent the dust component. Dust and gas interact through drag forces. The equations of motion are those of Lyra and Kuchner (2013)

$$\frac{\partial \Sigma_g}{\partial t} = -(\boldsymbol{u}\cdot\boldsymbol{\nabla})\,\Sigma_g - \Sigma_g \boldsymbol{\nabla}\cdot\boldsymbol{u}, \tag{5.3}$$

$$\frac{\partial \boldsymbol{u}}{\partial t} = -(\boldsymbol{u}\cdot\boldsymbol{\nabla})\,\boldsymbol{u} - \frac{1}{\Sigma_g}\boldsymbol{\nabla} P - \boldsymbol{\nabla}\Phi - \frac{\Sigma_d}{\Sigma_g} f_d, \tag{5.4}$$

$$P = c_V\,(\gamma - 1)\,T_0 \Sigma_0^{-1} \Sigma_g \Sigma_d + \Sigma_g c_b^2, \tag{5.5}$$

$$\frac{d\boldsymbol{v}}{dt} = -\boldsymbol{\nabla}\Phi + f_d, \tag{5.6}$$

$$f_d = -\frac{(\boldsymbol{v} - \boldsymbol{u})}{\tau_f}. \tag{5.7}$$

$$\tag{5.8}$$

In the above equations, Σ_g and Σ_d are the gas and dust density, respectively, whereas $\boldsymbol{u}$ and $\boldsymbol{v}$ are the gas and dust velocities. P is the gas pressure, Φ is the gravitational potential of the white dwarf, τ_f is the timescale of aerodynamical drag between gas and dust, and $\gamma = 1.4$ is the adiabatic index. In the equation of state (Equation 5.5), the first term embodies a simple prescription for photoelectric heating in the instantaneous thermal coupling approximation (Lyra and Kuchner, 2013), forgoing having to solve the energy equation. The second term represents a basal pressure set by other heating sources. For simplicity we keep the basal

sound speed $c_b^2 = \Theta c_s^2$ with $\Theta \equiv \text{const} = 0.5$.

The disc is started without a global pressure gradient, to prevent aerodynamical dust drift. The radial boundary condition is zero radial velocity in the inner boundary and outflow in the outer boundary, linear extrapolation in logarithm for the azimuthal velocity and density. The boundaries are padded with sponge zones, the inner one up to $r = 0.5\,\mathrm{R}_\odot$, and the outer one down to $r = 2.35\,\mathrm{R}_\odot$. Within these zones, the quantities are driven back to their initial condition, within a time $t = 0.1T_0$ where T_0 is the orbital period at the reference radius $r = 1R_\odot$. Sixth-order hyper-dissipation terms are added to the evolution equations to provide extra dissipation near the grid scale (Lyra et al., 2017). These terms are needed for numerical stability because the high-order scheme of the Pencil Code has little overall numerical dissipation (McNally et al., 2012). They are chosen to produce Reynolds numbers of order unity at the grid scale, but then drop as the sixth power of the scale at larger scales, so that they have negligible influence on the large-scale flow. Shock diffusion is added to the equations of motion, to resolve shocks to a differentiable length (Richert et al., 2015; Lyra et al., 2016; Hord et al., 2017). Extra Laplacian viscosity is added to the equations, with $\alpha = 10^{-2}$ (Shakura and Sunyaev, 1973).

An equal number particles by area is randomly distributed over the disc, with velocities set to their Keplerian value. Particles are placed between $r = [0.5, 2.4]R_\odot$ and removed from the domain if they cross these boundaries. The dust grains have Stokes number $\mathrm{St} = \tau_f \Omega = 1$, and we start them with dust-to-gas ratio $\varepsilon \equiv \Sigma_p/\Sigma_g = 1$. The backreaction of the drag force is added to the gas, conserving momentum in the system.

The upper panels of Figure 5.8 show, at every radii, the azimuthal average of the dust and gas densities vs time (upper left and upper right, respectively). The lower panels show the dust and gas density at the end of the simulation. It can be seen that the dust quickly rearranges into a series of regularly spaced arcs. We are primarily interested in checking whether any structure in the disc can remain constant in shape and location over 1000s of orbits. Rings form at $r \approx 0.7$, 1.25, and 1.75, but they are evanescent and soon disperse. A longer lived one at $r = 1.75$ is sustained until about 700 orbits. After that, the arc systems labeled A–F remain for long timescales. The system E eventually disperses at 1750 orbits, leaving systems A–D and F until the end of the simulation. It is apparent that the systems B–E all moved outwards during the course of the calculation, driven by the pressure gradient they effect on the gas. The systems A and F are more stable spatially, due to boundary conditions imposed on the computations. For either A to move inwards and F to move outwards, crossing the domain boundaries, they would need to climb pressure gradients. The fact that only the arc systems affected by boundaries retain their integrity over long timescales is a good indication that the structures produced by photoelectric instability are unlikely the origin of the variable emission we detect on a 123.4 min period.

In Figure 5.9 we shows the azimuthal power spectrum of the dust density as a function of time, broken down by azimuthal wavenumber to illustrate the time evolution of the azimuthal substructure in the arc systems A–F. Most of the power is in the $m = 0$ mode (light grey); the number of arcs is shown as the dominant azimuthal wavenumber below the $m = 0$ line. As seen, the arc systems A–E alternate between $m = 1$ (one arc) and $m = 2$, some even with $m = 3$, and no structure is long lived. The arc system F is still growing in intensity and did not achieve a steady state.

In summary, we conclude that arcs of gas generated by PEI cannot account for for the azimuthally extended emission around SDSS J1228+1040.

5.5 A planetesimal within the disc

The final possibility we consider is that a solid body is orbiting within the disc with a semi-major axis $a = 0.73\,R_{\odot}$, either interacting with the dusty component of the disc or sublimating itself to generate the detected gas. The short period of a planetesimal orbiting around SDSS J1228+1040 requires a high density or significant internal strength to avoid being disrupted by the gravity of the white dwarf, which contrasts with WD 1145+017, where the debris fragments are detected on orbits consistent with the tidal disruption radius of a rocky asteroid. Under the assumption that a body in orbit around SDSS J1228+1040 would have no internal strength and that its spin period is tidally locked to its orbital period, we calculate the minimum density needed to resist tidal disruption on a 123.4 min period as $39\,\mathrm{g\,cm^{-3}}$ for a fluid body deformed by the tidal forces using Equation 5 from Veras et al. (2017). If we assume the body has enough internal strength to retain a spherical morphology, then the minimum density required reduces to $7.7\,\mathrm{g\,cm^{-3}}$, which is comparable to the density of iron at $8\,\mathrm{g\,cm^{-3}}$ (however, the internal strength could be greater, and the density lower).

We conclude that a solid body orbiting within the disc is the most plausible hypothesis discussed in this section, and that it would need some internal strength to avoid tidal disruption. We calculate bounds on the planetesimal size below.

5.5.1 Constraints on the size of the planetesimal

We estimate lower and upper limits on the size (see Section 3.2 of Brown et al. 2017), mass and lifetime constraints on a planetesimal orbiting SDSS J1228+1040 with a semi-major axis, $a = 0.73$ R$_{\odot}$ using two different assumptions: (i) The accretion rate onto the white dwarf, $\dot{M}_{\mathrm{WD}} = 5.6{\times}10^{8}\,\mathrm{g\,s^{-1}}$ (Gänsicke et al., 2012), is generated entirely from the sublimation of the planetesimal, which would be the dominant source of gas in the system. (ii) We calculate the maximum size a body with binding forces dominated by internal strength

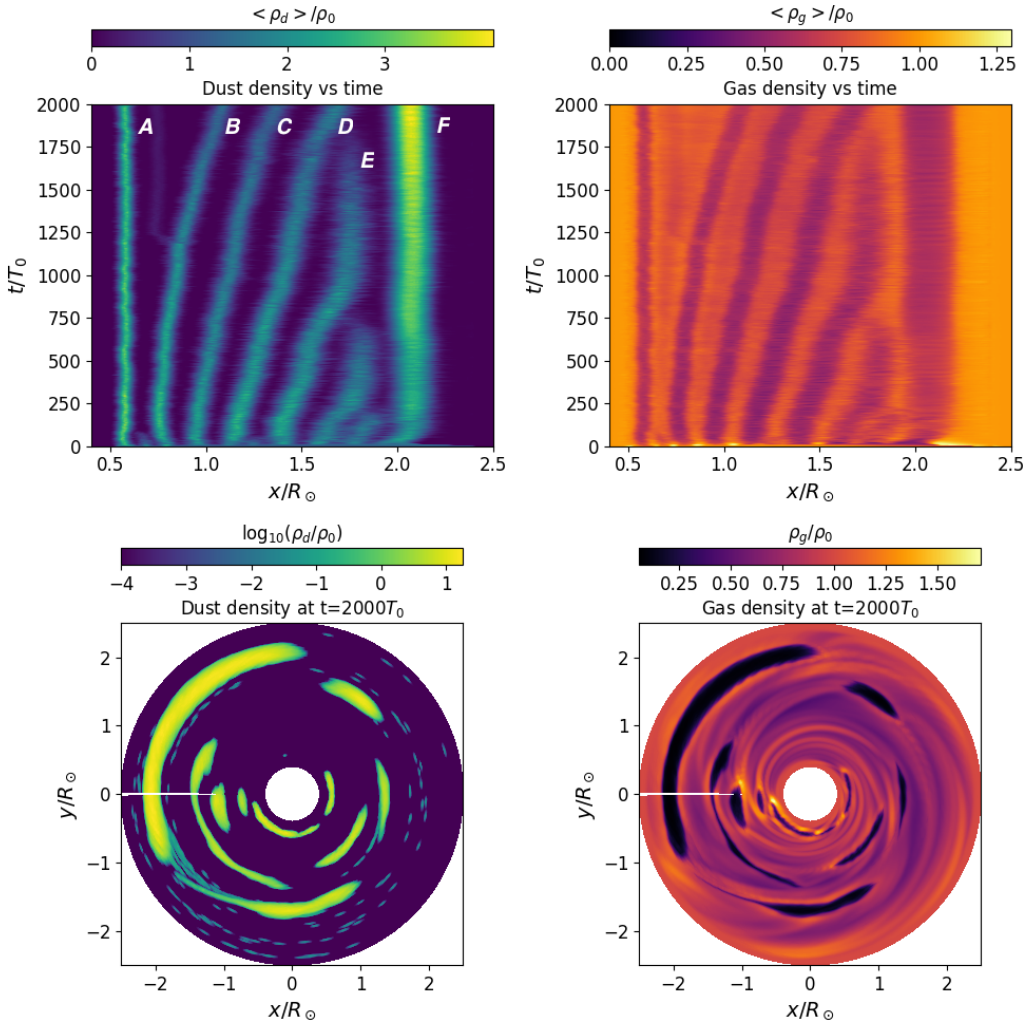

Figure 5.8: PEI model of the debris disc at SDSS J1228+1040. Upper left: Azimuthally averaged dust density vs radius and time. Some of the structure is evanescent, while five arc systems, A–D, and F, survive to the end of the simulation. Of these, the middle three significantly drift outwards. System E survived for a long time, but dispersed at around 1750 orbits. Upper right: Azimuthally averaged gas density vs radius and time. As the dust heats up the gas, the gas expands and hence the gas and density structures are anti-correlated. Hot gas with lower densities is located where the dust density is high, and cold dense is found where the dust density is low. Lower left: Dust density distribution at the end of the simulation at t = 2000 orbits. Azimuthal substructure is apparent as some orbits have more than one arc. Lower right: Gas density distribution at the end of the simulation at t = 2000 orbits.

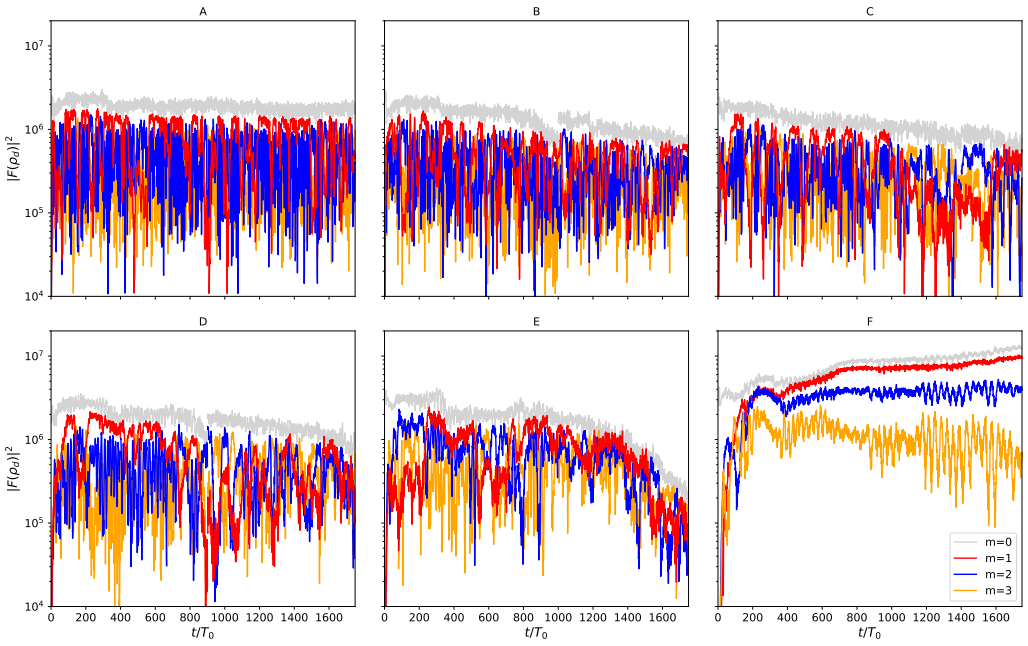

Figure 5.9: Power spectra for the PEI model of the debris disc at SDSS J1228+1040. Time series of the power spectrum of the different arc systems shown in the upper left panel of Figure 5.8, broken down by wavenumber. Most of the power is in the $m = 0$ mode, but the substructure is apparent as significant power in the other modes. It is apparent that all systems (except F) show an alternance between $m = 1$ and $m = 2$ as dominant substructure, at times even $m = 3$ in the cases of C, D and E. These modes represent the number of sub-arcs at a given radius (e.g. feature A at $\simeq 0.6\,\mathrm{R}_{odot}$ in Figure 5.8 is composed of 2-3 sub-arcs). We conclude that no structure is these arcs systems is long lived enough to explain the variability observed in the Ca II triplet. The system F results from boundary conditions and is still intensifying.

can be before being tidally disrupted. For this scenario we assume a core-like composition, e.g. iron dominated.

A lower limit from the measured accretion rate

Under the assumption that the accretion rate onto the white dwarf is equal to the rate of sublimation, $\dot{M}_{\rm sub}$ of a planetesimal, we calculated the size, s, of the object as

$$s = \frac{a}{R_{\rm WD} T^2_{\rm WD}} \left(\frac{L_{\rm vap} \dot{M}_{\rm sub}}{\sigma} \right)^{0.5}, \tag{5.9}$$

where $R_{\rm WD} = 0.01169\,{\rm R}_\odot$ and $T_{\rm WD} = 20713\,{\rm K}$ are the radius and temperature of the white dwarf respectively (Manser et al., 2016b), $L_{\rm vap} = 6.09{\times}10^4\,{\rm J\,g^{-1}}$ is the latent heat of vaporisation for iron (Dean, 1990), and σ is the Stefan-Boltzmann constant (Brown et al., 2017). This gives $s \simeq 4\,{\rm km}$, which we take as a lower limit to the size of the planetesimal, as any shielding from the debris disc would decrease the received radiation, and would require an increase in size to match the rate of accretion onto the white dwarf. A body of this size would have a mass $M_{\rm p} \simeq 10^{18}\,{\rm g}$ and a lifetime, $t \simeq 85\,{\rm yr}$, assuming that the body is sublimating at a rate equal to the accretion rate.

While these calculations assume that the planetesimal has a pure iron composition, the accreted material in the atmosphere of the white dwarf is similar to bulk Earth (Gänsicke et al., 2012). However, we note that it is possible that the solid body is the surviving core of a larger planetesimal, where the outer layers have formed the debris disc and are currently accreting onto the white dwarf. We also calculate the lower limit on size and lifetime under the assumption that the body is rocky, with a latent heat of vaporisation, $L_{\rm vap} = 8{\times}10^3\,{\rm J\,g^{-1}}$ (Brown et al., 2017), as $s \simeq 1\,{\rm km}$ and $t \simeq 1.5\,{\rm yr}$, respectively, and note that this should be considered as a strict lower limit, as the corresponding life time is only slightly exceeding the time span over which the short-term Ca II variability has been detected.

An upper limit from internal strength considerations

We discussed in the main text that an orbit with a semi-major axis of $a = 0.73\,{\rm R}_\odot$ requires that the planetesimal has some amount of internal strength, and we can hence calculate size limits for the planetesimal assuming the forces opposing tidal disruption are dominated by the internal strength. Using a range of internal strengths $S = 40$–$1000\,{\rm MPa}$ obtained from iron meteorite and iron-nickel samples (Petrovic, 2001; Slyuta, 2013), we calculate the maximum size an iron-dominated planetesimal can reach before it is tidally disrupted using,

$$s = \left(\frac{2Sa^3}{GM_{\rm WD}\rho_{\rm iron}} \right)^{0.5}, \tag{5.10}$$

where G is the gravitational constant, $M_{\rm WD} = 0.705\,{\rm M}_{\odot}$ is the mass of the white dwarf (Manser et al., 2016b), and $\rho_{\rm iron} \simeq 8\,{\rm g\,cm^{-3}}$ is the density of iron (Brown et al., 2017). This gives a range of sizes $s \simeq 60 - 600\,{\rm km}$, which corresponds to a mass range of 7×10^{21} – 7×10^{24} g. The upper end of this range is comparable to the largest asteroid in the Solar system, Ceres, with a radius of 473 km (Russell et al., 2016). Calculating the sublimation rate for bodies in this size range by rearranging Equation 5.9 results $\dot{M}_{\rm sub} \simeq 10^{11} - 10^{13}\,{\rm gs^{-1}}$, and a lifetime range of $1\,400 - 14\,000\,{\rm yr}$ respectively. These sublimation rates are significantly higher than the measured accretion rate onto the white dwarf, but shielding from the disc may reduce this.

In summary, we have shown that a planetesimal (which could be as large as Ceres) can survive within the disc for a minimum of about a century and possibly far longer. The size range we calculate, 4 - 600 km s^{-1} is in agreement with modelling of the atmospheric pollution of white dwarfs, which predicts that the pollution originates from the accretion of $\leq 35\,{\rm km}$ planetesimals (Wyatt et al., 2014). However, we note it is likely that the body is shielded somewhat by the radiation from the white dwarf, and we leave calculations regarding the heating of the planetesimal to future work.

5.6 Discussion

There are a number of open questions we briefly discuss here that warrant further investigation. (i) What is the origin of the planetesimal? It may be that the planetesimal is the differentiated iron core of a larger body that has been stripped of its crust and mantle by the tidal forces of the white dwarf. The outer layers of such a body would be less dense, and disrupt at greater semi-major axes and longer periods than those accessible to the core (Veras et al., 2017). This disrupted material would then form a disc of dusty debris around SDSS J1228+1040, leaving a stripped core-like planetesimal orbiting within it. (ii) Is the variable emission originating from interactions with the dusty disc, or from irradiation of the surface of the planetesimal? Small bodies are known to interact with discs and induce variability in spatially resolved discs, such as e.g. Daphnis and the Keeler gap in the rings around Saturn, (Porco et al., 2005; Tiscareno et al., 2007). Furthermore, a number of debris discs around main-sequence stars show evidence of second-generation gas (Dent et al., 2014). The origin of this non-primordial gas is uncertain, but it has been suggested that it could be generated by collisional vaporisation of dust (Czechowski and Mann, 2007), or collisions between comets (Zuckerman and Song, 2012). If the body is not interacting with

the disc to generate the additional gas, then the planetesimal must be producing the gas. The semi-major axis of the planetesimal, $a = 0.73\,\mathrm{R}_{\odot}$, is close enough to the star that the surface of the body may be sublimating (see supplementary material on estimates on planetesimal size and temperature), and releasing gas which contributes to the variable emission.

This emission can be modelled remarkably well as an intensity pattern, fixed in the white dwarf rest frame, that precesses on a period of $\simeq 27$ yr (Manser et al., 2016b), which is stable on a time-scale that is many orders of magnitude longer than the orbital time-scale within the disc ($\simeq$ hours). The gaseous disc has been present at SDSS 1228+1040 for at least the baseline of the observations (12 yr), implying that the planetesimal has survived in its current orbit for at least as long. A planetesimal on an eccentric orbit undergoing general relativistic apsidal precession could explain the observed precession of a fixed intensity pattern, which we explore below.

5.6.1 An eccentric orbit

We speculate that the short-term variability identified in the GTC observations is linked to the long term variability detected in the gaseous emission at SDSS J1228+1040. The morphology of the Ca II triplet emission profiles varies on a period of $\simeq 27$ yr (Manser et al., 2016b), and we suggest that a planetesimal that is subject to general relativistic precession could interact with the dust in the debris disc, generating the gaseous disc component and establishing the intensity pattern in that disc. This fixed intensity pattern observed in the gaseous disc at SDSS J1228+1040 is asymmetric, and should smear out on a few orbital time-scales, unless it is maintained in some way, such as by a planetesimal on an eccentric orbit. We calculate an eccentricity of the intensity pattern at SDSS J1228+1040 as $e \simeq 0.4$, under the assumption that the minimum and maximum velocities observed in the Doppler map (Manser et al., 2016b), are at the apastron and periastron of the orbits respectively.

We note that recent modelling of the evolution of hydrodynamical eccentric discs have shown that the observed, long-term variability could be explained by the precession of a disc due to general relativistic precession or pressure in the disc (Miranda and Rafikov, 2018). The precession period in this scenario has a strong dependence on the radius of the inner edge of the gas disc, and can explain the range of precession periods observed so far (Manser et al., 2016b; Dennihy et al., 2018). However, it is unknown whether the observed inner edge is due to a change in the density in the disc, or a change in the ionisation. Further work is needed in this area, including a mechanism to keep the gas on an eccentric orbit.

We calculate the general relativistic precession of a body as a function of eccentricity and semi-major axis in Figure 5.10. If the body in orbit around SDSS J1228+1040 is responsible for the 27 yr perioidc precession of the disc, then it would need an eccentricity of $e \simeq 0.53$. This brings the closest approach of the planetesimal to the white dwarf to

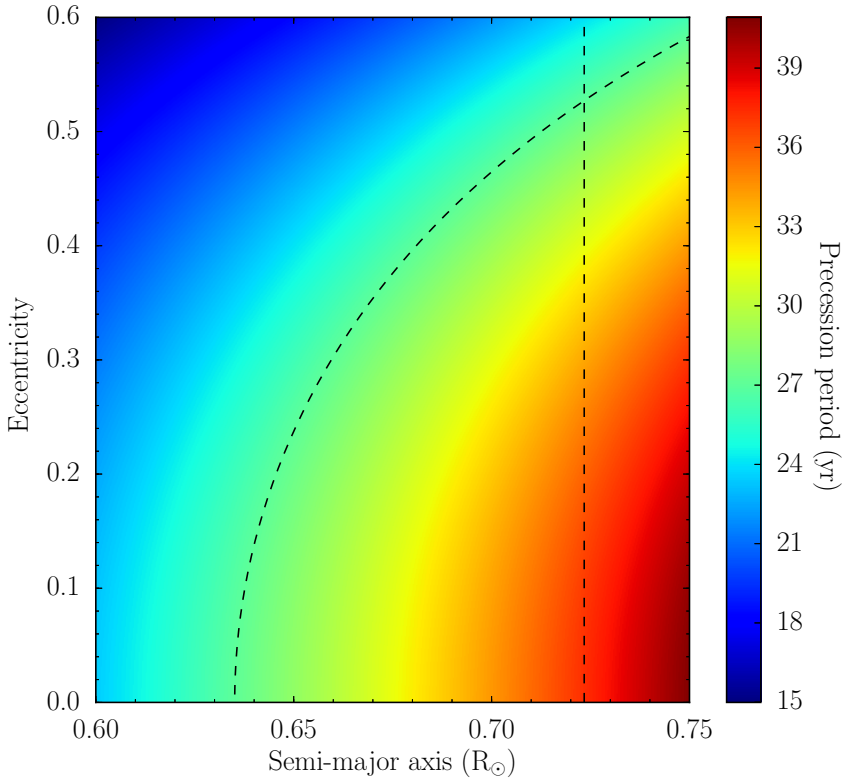

Figure 5.10: The precession period of a body due to general relativistic effects in the gravitational field of the white dwarf in SDSS J1228+1040 is plotted in colour as a function of semi-major axis and eccentricity. The straight dashed line indicates the semi-major axis $0.73\,R_\odot$ for which a body will orbit on a period of 123.4 min. The curved dashed line follows a precession period of 27 yr, which is the precession period calculated from the long-term variability in the Ca II triplet emission of the gaseous debris disc. These two curves cross at an eccentricity of $e \simeq 0.53$.

$a_c = a(1-e) = 0.34\,R_\odot$, where a is the semi-major axis. Bodies on an eccentric orbit are not tidally locked to their host star, but will enter a state of pseudosynchronisation where their spin angular velocity is approximately the orbital angular velocity at pericentre (Hut, 1981). Using Equation 42 of Hut (1981) with $e = 0.53$ returns a spin period for the body in orbit around SDSS J1228+1040 of $\simeq 40$ mins, which is roughly three times faster than the orbital period of 123.4 mins. The more rapid spin rate will increase the minimum density required to avoid tidal disruption. We recalculate this density as $13\,\mathrm{g\,cm^{-3}}$ using Equation 5 from Veras et al. (2017), with a modified constant $\mathcal{R} \simeq 3.75$ determined by re-balancing the increased tidal force with the centripetal force, against gravitational force from the planetesimal (see also Section 4.8 of Murray and Dermott 1999). Our original conclusion that the body requires significant internal strength still holds.

Using the closest approach of $0.34\,R_\odot$ to the white dwarf, we re-evaluate the constraints on the size of the planetesimal from Sections 5.5.1 and 5.5.1 as 2 km and 20 – 200 km respectively. Both of these calculations assume that the body spends all of its time at a distance of $0.34\,R_\odot$ from the white dwarf, so the size range calculated here is a conservative estimate. It should also be noted that the uncertainty in the mass of the white dwarf ($\pm 0.05\,M_\odot$), and the precession period of the gaseous debris disc (± 1 yr) will introduce an error of roughly ± 0.05 eccentricity. While this will have an effect on the value of periastron and therefore the reduced size constraints on the body, the discussion below is largely unaffected.

Below we calculate the heating and eccentric decay of a body due to induction and tidal heating, as well as heating from irradiation. We calculate these values using the planetesimal radius r_p, which is related to the size definition of the planetesimal by $s \simeq 1.65\,r_\mathrm{p}$ (see Brown et al. 2017). As such, our lower and upper bounds to the radius of the planetesimal are $r_\mathrm{p} = 1.2$–120 km.

Eccentricity damping timescale

We estimate here the time taken for a planetesimal on an eccentric orbit to decay onto a circular orbit using a linear, constant Q tidal model, where Q is a parameter that incorporates the fraction of tidal energy dissipated per orbit (usually in the range 1-100 for rocky bodies). We calculate the timescale, τ_e, for the eccentricity to dampen for this constant Q tidal model as:

$$\tau_e = \frac{e}{\dot{e}} = \frac{4}{63}\left(\frac{M_\mathrm{p}}{M_\mathrm{WD}}\right)\left(\frac{a}{r_\mathrm{p}}\right)^5\left(\frac{\tilde{\mu}Q}{n}\right), \tag{5.11}$$

where r_p is the radius of the planetesimal, n is the mean motion given by $\frac{2\pi}{P}$, and $\tilde{\mu}$ is the ratio of elastic to gravitational forces given by:

$$\tilde{\mu} = \frac{19\mu}{2\rho g_\mathrm{p} r_\mathrm{p}}, \tag{5.12}$$

where μ is the modulus of rigidity and is ~ 50 GPa for iron or rock, and, g_p is the surface gravity of the planetesimal (Murray and Dermott, 1999). Substituting the range in r_p as 1.2-120 km from Section 5.6.1, and using $Q = 10$, we obtain a range of $\tau_e = 2\text{-}2 \times 10^8$ Myr for the eccentricity to decay. This is orders of magnitude longer than the time-scale of the observations as well as the estimates for the lifetime of the planetesimal, and confirms the plausibility of a planetesimal on an eccentric orbit.

Tidal heating

The damping of an eccentric orbit due to tidal forces will also heat up the orbiting body. We calculate the power of this heating, $P_{\rm T}$, as:

$$P_{\rm T} = \frac{63}{4}\left(\frac{e^2 n}{\tilde{\mu} Q}\right)\left(\frac{r_{\rm p}}{a}\right)^5 \left(\frac{G M_{\rm WD}^2}{a}\right), \tag{5.13}$$

and for planetesimals with radii in the range 1.2–120 km, we obtain a heating due to tidal forces of 4×10^2–4×10^{16} W (Murray and Dermott, 1999). There is a strong dependence on the size of the planetesimal, and we compare these values for tidal heating to the heat received due to the radiation, $P_{\rm R}$, from the white dwarf as,

$$P_{\rm R} \simeq \pi \sigma_{\rm sb} T_{\rm eff}^4 \left(\frac{R_{\rm WD} r_{\rm p}}{a}\right)^2, \tag{5.14}$$

where $\sigma_{\rm sb}$ is the Stefan-Boltzmann constant. For the planetesimal size range above, we obtain the range in radiation power received as $\simeq 10^{13}$–10^{17} W. It is clear that tidal heating is not important for planetesimal sizes close to the lower limit, however, for sizes close to the upper limit, $r_{\rm p} = 120$ km, tidal heating contributes an additional $\simeq 40$ % than produced from the maximum radiation heating alone. Assuming tidal and radiation heating are in equilibrium with the re-radiated flux from the planetesimal, this would lead to a $\simeq 10$ % increase in the temperature of the body, which is unlikely to affect its long-term evolution on its close orbit around the white dwarf.

Induction heating

In order for magnetic induction to act, the planetesimal has to experience non-negligible anisotropic magnetic flux. In Kislyakova et al. (2017) this was caused by an anti-alignment of the stellar magnetic field with the orbital plane of the planet. Currently the relative inclination of the magnetic field and rotation axis of SDSS J1228+1040 are unconstrained, and hence magnetic induction heating of the planetesimal cannot be excluded.

We determined the upper limit on the magnetic field strength of the white dwarf at SDSS J1228+1040 in Section 5.3.1 as 10–15 kG. Assuming a dipole configuration, we calculate a conservative upper limit on the magnetic field strength at the orbital distance of the planetesimal as $B_0 \sim 0.1$ G (1×10^{-5} T).

The eddy current density, $\mathbf{J}$, induced in a homogeneous spherically symmetric conductive sphere moving through an asymmetric magnetic field with a frequency identical to the mean motion, n, can be calculated via

$$\mathbf{J}(r,\theta) = \hat{\phi}\left(\frac{-3in\sigma_{\rm con}B_0 r_{\rm p}}{2kr_{\rm p}j_1'(kr_{\rm p}) + 4j_1(kr_{\rm p})}\right) j_1(kr)\sin\theta, \tag{5.15}$$

where $\hat{\phi}$ is the unit vector in the azimuthal direction, θ is the angle of elevation, r is the radial distance measured from the center of the planetesimal, $i^2 = -1$, $\sigma_{\rm con}$ is the conductivity of the material, B_0 is the magnetic flux at the surface of the planetesimal, j_1 is the Bessel function of the first kind and j_1' is its derivative in the radial direction. Furthermore, k is the complex wavenumber, $k = (-in\sigma_{\rm con}\mu_0)^{1/2}$ (Nagel, 2018), where μ_0 is the vacuum permeability. The penetration (skin) depth, δ, of the magnetic field in the conducting sphere is given by $\delta = (2/(n\sigma_{\rm con}\mu_0))^{1/2}$, which gives the radial distance from the surface at which the field strength has dropped by a factor of $\simeq e = 2.718$.

The power dissipated in the body due to induction heating can be calculated using Ohm's law, given by,

$$P_{\rm I} = \int \sigma_{\rm con}^{-1}\mathbf{JJ}^* dV, \tag{5.16}$$

and by substituting in $\mathbf{J}$ the induction heating $P_{\rm I}$ is given by

$$P_{\rm I} = -\frac{3\pi}{2}\left(\frac{B_0}{\mu_0}\right)^2 \frac{r_{\rm p}}{\sigma_{\rm con}}\left(2 + dr_{\rm p}\frac{\sin(dr_{\rm p}) + \sinh(dr_{\rm p})}{\cos(dr_{\rm p}) - \cosh(dr_{\rm p})}\right), \tag{5.17}$$

where $d = 2/\delta$. Assuming a conductivity of iron rich materials at temperatures close to the radiative equilibrium temperature ($T_{\rm eq} \simeq 2200$ K, see Section 5.6.2) as $\sigma_{\rm con} \simeq 2\,{\rm MS\,m^{-1}}$ (Pozzo et al., 2014), we obtain $\delta \simeq 30$ m. In the range of $r_{\rm p} = 1.2$–120 km and $\sigma_{\rm con} \simeq 2\,{\rm MS\,m^{-1}}$, $dr_{\rm p} >> 1$, and Equation 5.17 can be reduced to

$$P_{\rm I} \simeq 3\pi\left(\frac{B_0}{\mu_0}\right)^2 \frac{r_{\rm p}^2}{\sigma_{\rm con}\delta}. \tag{5.18}$$

For a range of planetesimal radii 1.2– 120 km, and using $B_0 = 1\times10^{-5}$ T, $\sigma_{\rm con} = 2\,{\rm MS\,m^{-1}}$, and $\delta = 30$ m, we calculate the heating due to magnetic induction as 10^1–10^5 W. This is about 12 orders of magnitude weaker than the maximum heating of the planetesimal by irradiation from the white dwarf, and as such we neglect heating and orbital decay generated the induction heating. However a clear source of heating will come from the radiation produced by the white dwarf, which we discuss below.

5.6.2 Temperature estimate of the planetesimal

Under the assumption that the planetesimal is tidally locked to the star, we can estimate the substellar and the mean temperature over the hemisphere of the planetesimal facing the white dwarf using

$$T_{\rm eq,ss} \simeq \sqrt{\frac{R_{\rm WD}}{a}} T_{\rm eff}, \tag{5.19}$$

and,

$$\langle T_{\rm eq} \rangle \simeq 2^{-\frac{1}{4}} \sqrt{\frac{R_{\rm WD}}{a}} T_{\rm eff}, \tag{5.20}$$

respectively, where $T_{\rm eff}$ is the effective temperature of the white dwarf, a is the semi-major axis of the planetesimal's orbit, and $R_{\rm WD}$ is the radius of the white dwarf. Given $T_{\rm eff} = 20713$ K, and $R_{\rm WD} = 0.01169\,{\rm R}_{\odot}$ (Koester et al., 2014), we calculate $T_{\rm eq,ss} \simeq 2600$ K and $\langle T_{\rm eq} \rangle \simeq 2200$ K. These values are in excess of the canonical sublimation temperature of the dusty discs at white dwarfs, which is thought to be $\simeq 2000$ K (Rafikov and Garmilla, 2012). If the body is on an circular orbit and not tidally locked, then the temperature of the planetesimal will be

$$\langle T_{\rm eq} \rangle \simeq \sqrt{\frac{R_{\rm WD}}{2a}} T_{\rm eff}, \tag{5.21}$$

which results in $\langle T_{\rm eq} \rangle \simeq 1800$ K, within the expected range for the sublimation temperature of the debris disc, but higher than that of iron at $\simeq 1600$ K (Rafikov and Garmilla, 2012). However, The values calculated here are estimated upper limits, and a non-zero albedo or shielding from material in the disc could reduce the temperature of the planetesimal further. We note that for a body on an orbit with semi-major axis a, the time-averaged temperature of the body will decrease with eccentricity, e, according to Equation 16 from Méndez and Rivera-Valentín (2017). For $e = 0.53$, the decrease in the time-averaged temperature of the planetesimal is only $\simeq 2$ %, and is negligible in these calculations.

We therefore conclude that a planetesimal on an eccentric orbit could induce both the eccentricity and precession timescale seen at SDSS J1228+1040.

5.7 Conclusions

We have detected a $\simeq 2$ hour variability in the emission from the gaseous debris disc at SDSS J1228+1040 which we interpret as the signal of a planetesimal orbiting within the disc. Currently eight gaseous white dwarf debris discs are known, and long-term monitoring of three of these systems has shown similar long-term variability to SDSS 1228+1040 (Wilson et al., 2015; Manser et al., 2016a; Dennihy et al., 2018). These observations confirm that gaseous discs are key tracers of dynamical activity within the disc. If our hypothesis that these gaseous discs are generated by solid bodies on close orbits is correct, it provides a method to detect exo-planetesimals that is largely inclination-independent,

and has the potential to provide statistical insight into their properties such as their periods, sizes, and long-term stability. Future high-cadence spectroscopy of the Ca II triplet at SDSS 1228+1040 will constrain changes to the period and stability of the planetesimal.

Chapter 6

The frequency of gaseous discs at white dwarfs

6.1 Introduction

Statistics is at the heart of all scientific studies, and astronomy is no exception. Determining the prevalence of astronomical systems is critical to our understanding of the Universe. One example is the rarity of hot Jupiters, which dominated initial exo-planet detections (Wright et al., 2012).

Preliminary searches for (i) debris discs around, and (ii) photospheric pollution of white dwarfs were heavily biased, and it was only in the last decade that sufficiently large and unbiased samples were collected to calculate their occurrence (1 – 3 per cent, Farihi et al. 2009; Rocchetto et al. 2015, and 25 – 50 per cent, Zuckerman et al. 2003, 2010; Koester et al. 2014, respectively). However, the prevalence of gas discs around white dwarfs is so far unconstrained.

Models predict that all debris discs should have a gaseous component that feeds material onto the white dwarf (Rafikov, 2011b; Metzger et al., 2012), however, out of the 38 published dusty discs, only seven show gaseous emission (which co-orbits with the dust, see Table 3.2). One might be tempted to take the ratio of these two numbers ($7/38 \simeq 18\,\%$) as the fraction of debris discs that host an observable gaseous component, however this number is the result of several strong observational biases. The telescopes that are used to determine the presence of the gaseous (e.g. SDSS) and dusty (e.g. *Sptizer*) disc components have different brightness limits, and thus probe a different sample of stars. Moreover, five of the gas discs were identified via optical spectroscopy, and only then got deep Spitzer follow-up observations confirming the presence of dust, which further skews the two sample sizes. A knowledge of the occurrence rate of the gaseous components to these discs will allow constraints to be placed on the evolution of debris discs at white dwarfs (Rafikov, 2011b; Metzger et al., 2012), or the incidence of closely orbiting planetesimals at white dwarfs (Chapter 5).

In this chapter we present a statistical study of the frequency of gaseous debris discs using a magnitude limited sample of 9097 white dwarfs. We searched SDSS spectroscopy for Ca II triplet emission in this sample and determined the percentage of white dwarfs that host an observable gaseous debris disc as $0.06 \pm ^{0.03}_{0.02}$ per cent. We also present spectroscopy of the Ca II triplet region for 13 white dwarfs known to host dusty discs, where some have no prior observations of the Ca II triplet published.

6.2 Searching for gaseous debris discs in SDSS

The SDSS has been taking multi-band photometry and multi-fibre spectroscopy since 2000, using a 2.5 m telescope located at the Apache Point Observatory in New Mexico (Gunn

et al., 2006). Gentile Fusillo et al. (2015) published a list of spectroscopically identified white dwarfs selected within a colour-colour cut and colour-proper motion cut, with a magnitude limit of $g \leq 19$ using the 10th data release of SDSS (Abazajian et al., 2009; Ahn et al., 2012, 2014). We use all 8391 single white dwarfs from this sample, as well as 706 additional single white dwarfs identified in the 11th, 12th, and 13th data releases of the SDSS (Alam et al., 2015), using the same selection method as Gentile Fusillo et al. (2015), for a total of 9097 systems, with 12311 spectra ($\simeq 25$ % of white dwarfs in the sample have more than one spectrum). Figure 6.1 shows this sample of white dwarfs in the u–g vs. g-r colour-colour space, with spectral types labelled by colour. While the cuts defined by Gentile Fusillo et al. (2015) include the majority of single white dwarfs, some extreme cases are excluded, such as the cool, metal polluted white dwarfs that are found below the main-sequence in the u–g vs. g-r colour-colour space, i.e. with u–$g \geq 1$ (Koester et al., 2011; Hollands et al., 2017).

We attempted to determine the presence of gaseous emission by calculating the equivalent width (EW) of the Ca II triplet region between 8450 Å and 8700 Å, selecting systems that satisfy $\frac{-EW}{\sigma_{EW}} \geq 3$, where σ_{EW} is the error on the EW measurement (a negative EW corresponds to an emission feature). While this method was initially successful in recovering the five known gaseous debris discs in the sample, it failed to identify the subtle emission profile detected by Guo et al. (2015) at SDSS J1144+0529. Therefore we inspected the normalised Ca II triplet 8600 Å region of all 9097 stars in our sample by eye to probe for the presence of emission (an example spectrum is shown in Figure 6.2 with the Ca II triplet region highlighted as an inset). While this method is somewhat subjective, it is more powerful than using the EW measurements alone, which loses information on the shape of the emission profiles, whether all three components of the triplet are present, and suffers from residuals from the sky line subtraction. After visual inspection of entire spectroscopic sample, we recover the five known gaseous debris disc hosts in our sample, but did not find any new systems.

Figure 6.3 shows plots of EW and $\frac{-EW}{\sigma_{EW}}$ against signal-to-noise ratio (S/N) for our white dwarf sample with S/N ≤ 35. Roughly 25 % of the white dwarfs in our SDSS sample have multiple spectra, which are all (12311 spectra) included in Figure 6.3, and measurements from spectra with detected gaseous emission are shown as filled colour circles. Non-detections of gaseous emission in spectra are indicated by coloured arrows for SDSS J1617+1620 and SDSS J1144+0529, both of which have two SDSS spectra. SDSS J1617+1620 was initially observed to have Ca II triplet emission, which has subsequently fallen below detection limits (Wilson et al., 2014). The emission seen in the second spectrum of SDSS J1144+0529 is from a brown dwarf companion (Wilson, private communication), rather than a gaseous disc, and the first SDSS spectrum has no detectable Ca II

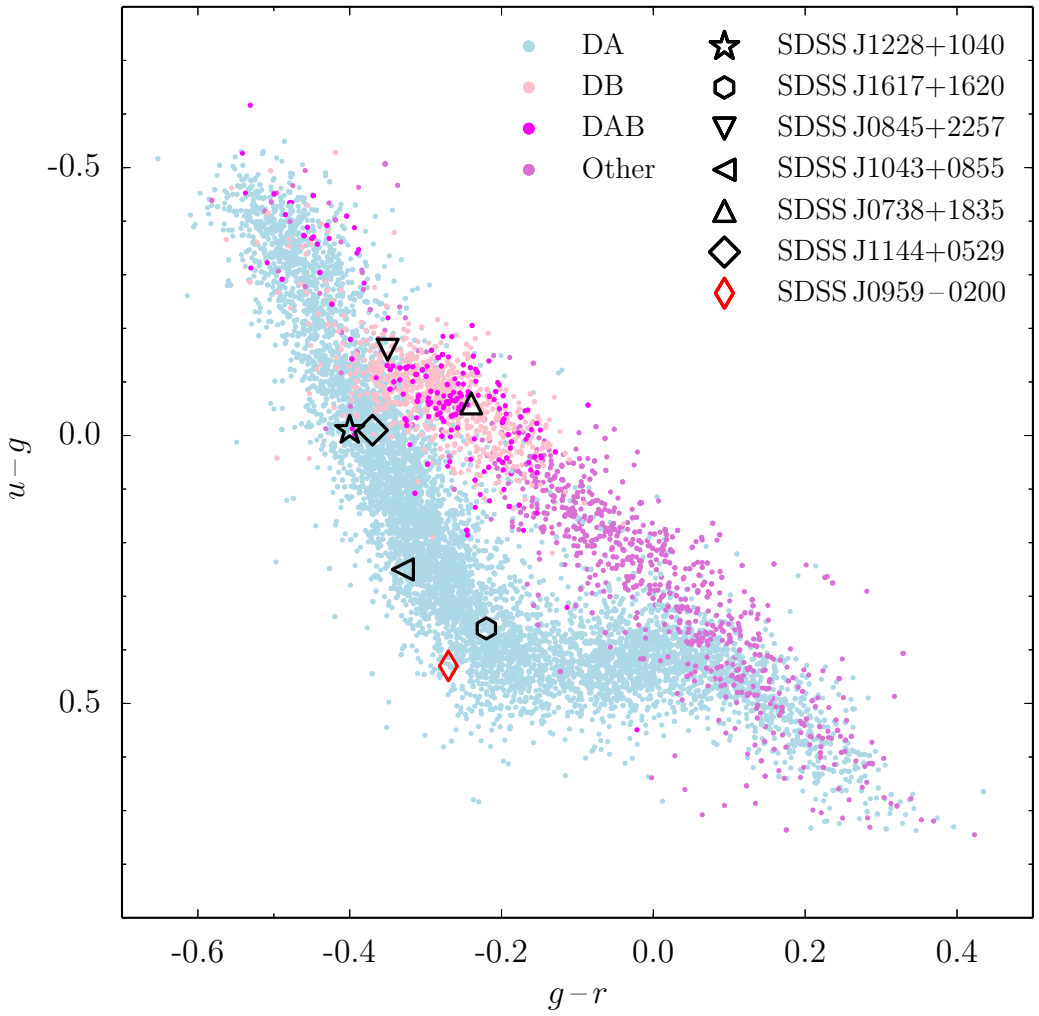

Figure 6.1: *u*–*g*, *g*–*r* colour-colour diagram of the colour and proper motion selected sample of 9097 white dwarfs from Gentile Fusillo et al. (2015). The magnitude limit of this sample is g = 19, and the main spectral types of white dwarfs labelled by colour. The five white dwarfs with a gaseous component to their debris disc contained in this sample are shown in black. SDSS J0959–0200 (Farihi et al., 2012) has no SDSS spectroscopy but is plotted for reference, as is SDSS J1144+0529, which was discovered to be a white dwarf brown dwarf binary (Wilson, private communication). The gas disc host, HE 1349–2305, is not presented here as it is not in the SDSS footprint.

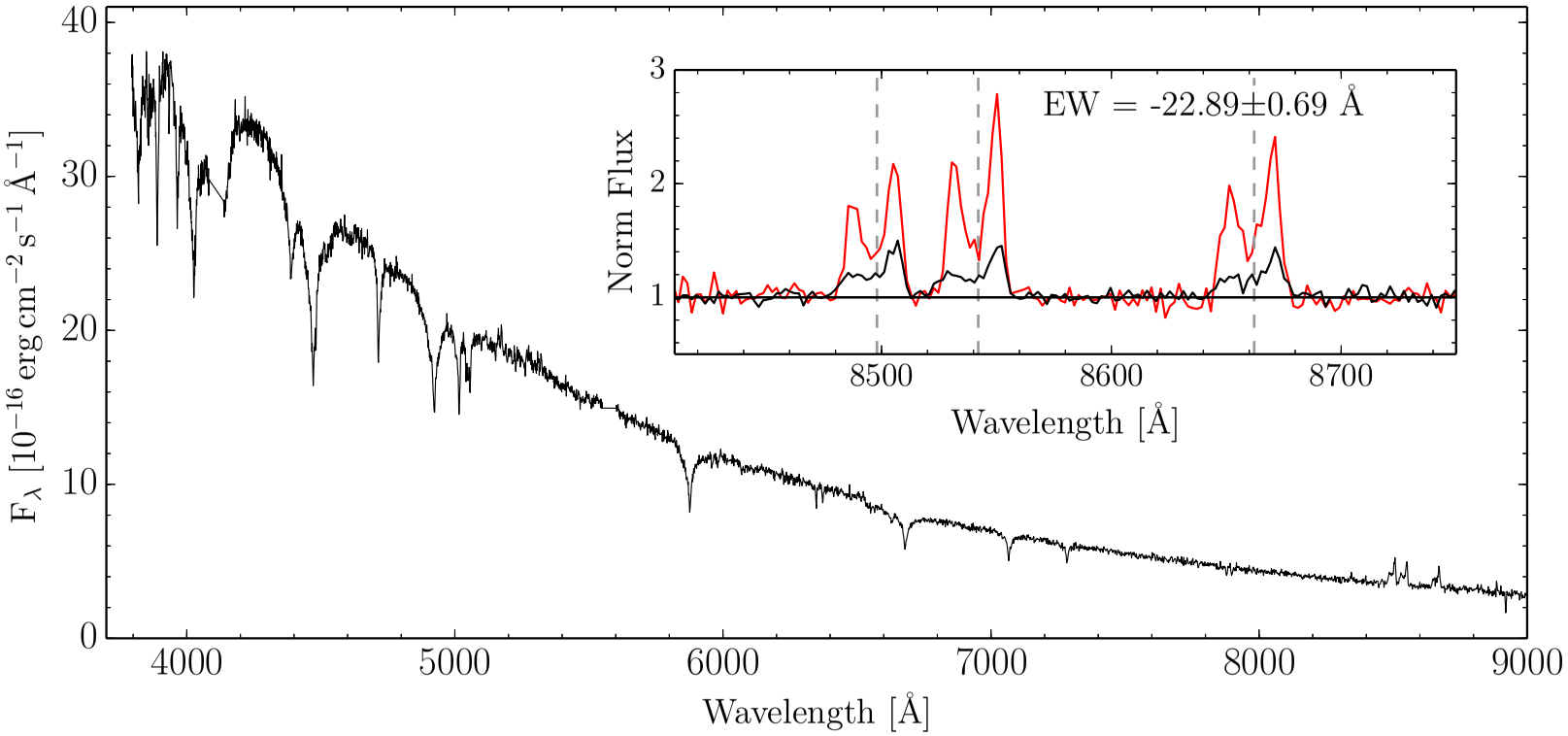

Figure 6.2: The SDSS spectrum of SDSS J084539.17+225728.0 (black) is shown as an example to illustrate our search for gas discs. The inset shows the Ca II triplet region with the rest wavelengths (dashed) marked and the combined equivalent width given. The emission profile of the prototype SDSS J122859.93+104032.9 (red) is also plotted as a comparison.

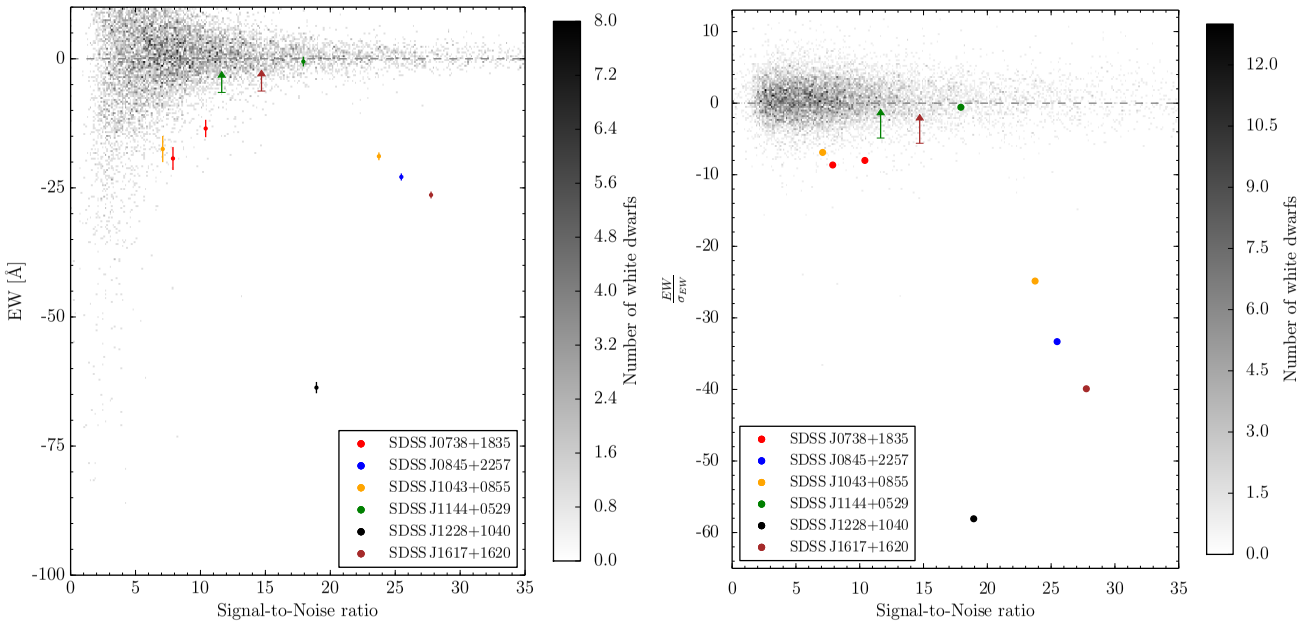

Figure 6.3: Left: A 2D density histogram for 10 695 spectra (including reobservations) from our SDSS sample of 9097 single white dwarfs, with a signal-to-noise ratio (S/N) in the Ca II region, S/N ≤ 35, and an Equivalent Width (EW), bounded by, -100 Å ≤ EW ≤ 10 Å. The dashed line lies at zero, and observations of the five known gaseous discs (in addition to SDSS J1144+0529, a white dwarf brown dwarf binary, Wilson, private communication) in the sample are marked by the coloured circles. Upper-limits on emission signifying non-detections are denoted by arrows. Right: Similar to the left panel, but showing 12005 single white dwarf spectra bounded in the y-axis by -65 $\frac{EW}{\sigma_{EW}} \leq 13$. The number of spectra shown in each panel are different due to the cuts applied to the y-axis.

triplet profiles, which is likely due to the poorer quality spectrum, and/or the radial velocity variation of the companion smearing the emission features. Four gaseous disc observations are clearly separated from the bulk of the white dwarf spectra: SDSS J1228+1040, SDSS J1043+0855, and SDSS J0845+2257, the first three of such discs discovered (Gänsicke et al., 2006, 2007, 2008).

The spread in EW values is extremely large at low S/N values due to noise (compare the left and right panels of Figure 6.3), and rapidly tightens as the S/N increases, making it easier to identify genuine emission features such as SDSS J1228+1040, SDSS J0845+2257, SDSS J1043+0845 and SDSS J1617+1620. Closer to the bulk EW distribution, it becomes more difficult to discover Ca II triplet emission such as that of SDSS J0738+1835. Within the EW distribution of spectra, noise dominates and it is possible that a number of Ca II triplet emission profiles are unidentifiable (this may be the case with the first SDSS J1617+1620, discussed above, Wilson et al. 2014). However, we conclude that it is unlikely that we have missed any strong Ca II triplet emitters such as SDSS J1228+1040, which would remain easily identifiable even at a S/N $\simeq 5$.

6.2.1 The occurrence rate of gaseous discs at white dwarfs

We find no new gaseous disc hosts in our magnitude and colour limited SDSS sample, resulting in a total of five gas discs out of 9097 systems. Using Bayes' theorem we calculate the probability distribution, $p(f|n,t)$, of determining an occurrence rate, f, of a gaseous debris disc at a white dwarf, given n detections out of t systems as

$$p(f|n,t) = \frac{p(n|f,t)p(f)}{p(n,t)}, \tag{6.1}$$

where $p(n|f,t) = f^n(1-f)^{t-n}$ is the binomial distribution, $p(f)$ is the prior distribution of f, and $p(n,t)$ is the probability distribution of detecting n gaseous disc hosts out of t white dwarfs which is a constant. We assume an uninformative prior distribution known as the Jeffreys prior (Jeffreys, 1946), which for the binomial distribution is

$$p(f) = \frac{f^{-0.5}(1-f)^{-0.5}}{B(0.5,0.5)}, \tag{6.2}$$

where B is the beta function, which when substituted in results in

$$p(f|n,t) \propto f^{n-0.5}(1-f)^{t-n-0.5}. \tag{6.3}$$

Taking the median and 1σ intervals of this probability distribution (which are independent of the proportionality constant), we find that $0.06 \pm ^{0.03}_{0.02}$ per cent of white dwarfs in this sample host a debris disc with an observable gaseous component. Given that 1-3 per cent of

white dwarfs host an observable dusty disc (Farihi et al., 2009; Rocchetto et al., 2015) we can therefore estimate that 1 - 10 per cent of dusty discs should host a gaseous component. This value is a factor of a few to an order of magnitude smaller than simply taking the ratio of known gas (7) to dust ($\simeq$ 38) discs, i.e. $\simeq$ 18 %. This is due to the fact that stars with Ca II triplet emission discovered so far in the optical are relatively faint, and the infrared emission from their dusty component is below the detection threshold of the comparatively shallow infrared surveys by *Spitzer*. Only with dedicated *Spitzer* observations were the dusty components of these discs confirmed.

6.3 Follow-up observations of dusty discs

6.4 Observations of debris discs

Out of the 38 published dusty debris discs around white dwarfs, only 23 systems have published spectroscopy of the Ca II triplet region. We obtained spectra of the Ca II triplet region for thirteen white dwarfs known to host a dust disc using the Intermediate dispersion Spectrograph and Imaging System (ISIS) on the William Herschel telescope (WHT), which are shown in Figure 6.4. The observations are summarized in Table 6.1, and were reduced by Mark Hollands using the standard procedures outlined in Section 2.2 with one exception: the spectra were not flux calibrated as the continuum flux of the Ca II triplet region is normalised to one. Our collection of thirteen white dwarf spectra contains four systems with previous Ca II triplet observations, WD 0106–328, WD 0110–565, WD 0146+187, and WD 0300–013 (Klein et al., 2010; Gentile Fusillo et al., 2017; Dennihy et al., 2017). None of these 13 white dwarfs show the characteristic emission profiles from the 8600 Å region in their spectra. We note that WD 0146+187, WD 0435+410, and WD 2326+049 show photopsheric Ca II absorption due the metal pollution of the white dwarf.

6.5 Discussion

While models predict that all debris discs host a gaseous component that is co-orbiting with the dust, and channels the accretion of material onto the white dwarf after the dusty component sublimates (see Section 1.6.3 and Figure 1.22, Rafikov 2011b; Metzger et al. 2012), I showed that less than 10 per cent of debris discs with detectable infrared excess also have observable gaseous emission. The variability seen at most of the gaseous disc systems, in conjunction with their rarity, suggests they are a short-lived dynamical phase in the lifetime of a debris disc. Apart from SDSS J1617+1620, all gaseous components to debris discs with long-term monitoring show similar morphological variations of their line

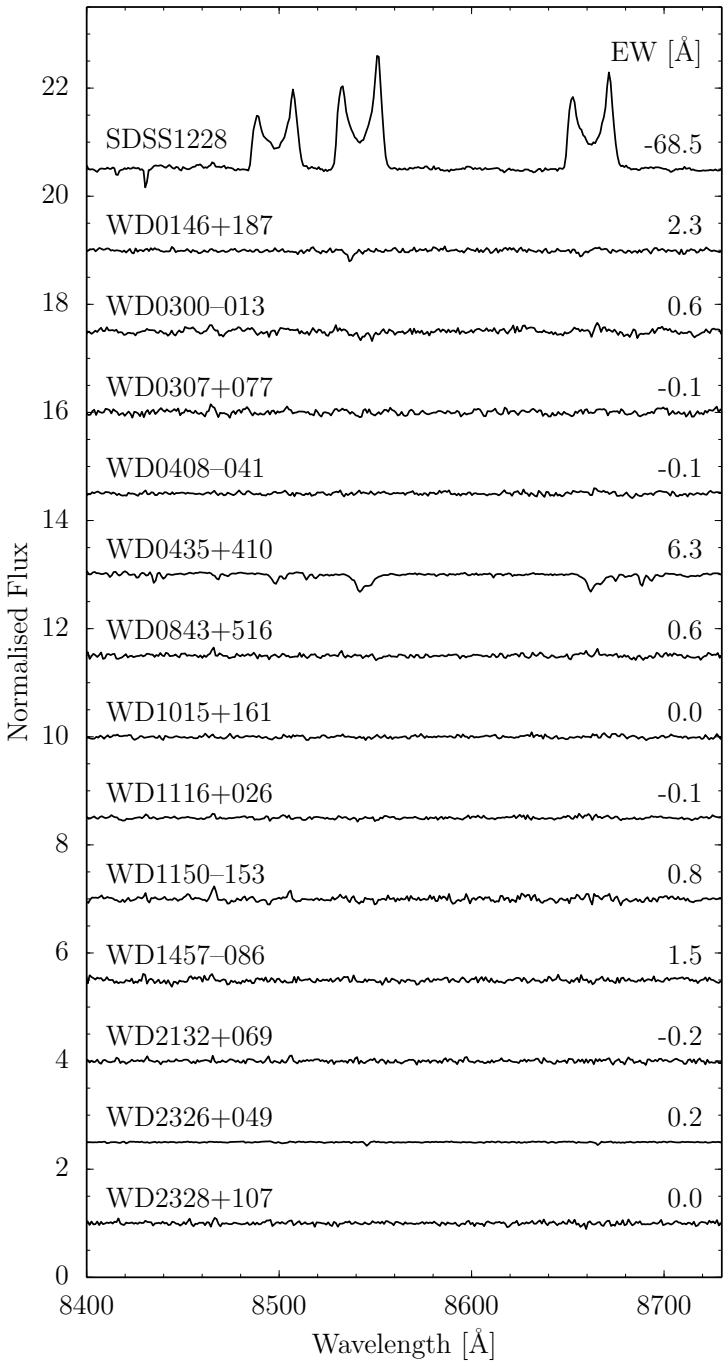

Figure 6.4: The continuum-normalised Ca II triplet region of 13 white dwarfs with a known infrared excess attributed to a dusty disc. The emission profile of SDSS J122859.93+104032.9 (SDSS1228) is included for comparison, and the equivalent widths for each profile are given. The normalised spectra are shifted by multiples of 1.5 with respect to the WD 2328+107 spectrum.

Table 6.1: Log of the WHT/ISIS observations searching for Ca II triplet emission at white dwarfs with a detected dust disc. [a] These systems already have published spectra covering the Ca II triplet region.

WD	Alternate name	Date	Exposure time [s]
0146+187[a]	GD 16	2011 - 12 - 07	4500
0300–013[a]	GD 40	2011 - 12 - 07	6600
0307+077	HS 0307+0746	2011 - 12 - 06	4500
0408–041	GD 56	2011 - 12 - 07	4200
0435+410	GD 61	2011 - 12 - 07	2700
0843+516	PG 0843+517	2011 - 12 - 06	3600
1015+161	PG 1015+161	2011 - 12 - 08	3000
1116+026	GD 133	2011 - 12 - 07	2700
1150–153	EC 11507–1519	2011 - 12 - 07	3600
1457–086	PG 1457–086	2010 - 07 - 24	2700
2132+096	HS 2132+0941	2016 - 10 - 29	1800
2326+049	G 29-38	2016 - 10 - 29	1800
2328+107	PG 2328+108	2016 - 10 - 29	1800

profiles on timescales of years to decades (Wilson et al., 2014, 2015; Manser et al., 2016b,a; Dennihy et al., 2018). The gaseous disc at SDSS J1228+1040 has been modelled as a fixed intensity pattern that slowly precesses with a period of $\simeq 27$ yr (see Section 4.5 for more information, Manser et al. 2016b). However, the emission from the disc at HE 1349–2305 evolves on a significantly more rapid timescale of $\simeq 1.4$ yr (Dennihy et al., 2018). The order-of-magnitude difference between the timescales of variability seen at these two systems is not yet understood, but points to a common underlying mechanism. Continued monitoring of the known gaseous debris discs, as well as the discovery of additional discs will allow us to study these systems in a collective manner.

Short cadence observations of the Ca II triplet at SDSS J1228+1040 show variability on a $\simeq 2$ hr period generated by a planetesimal orbiting within the Roche radius (Chapter 5). We hypothesise that this short term variability may be present in other systems that host a gaseous debris disc, which, if confirmed, would suggest that the presence of a gaseous component is an indicator of a closely orbiting planetesimal. If this hypothesis is true, it would further underline the importance of observing these targets and constraining their occurrence rates.

So far the best method for finding additional gaseous discs has been SDSS, the first large-scale multi-object spectroscopic survey. In the next decade, multiple dedicated multi-object spectroscopic surveys including DESI (DESI Collaboration et al., 2016a,b), WEAVE (Dalton et al., 2012, 2016), 4MOST (de Jong et al., 2016), and SDSS-V (all sky, Kollmeier

et al. 2017), will be starting operations, and will increase the number of observed white dwarfs from a few 10^4 to a few 10^5. This jump in the sample size will likely lead to the detection of several dozen new gaseous debris discs at white dwarfs, which are ideal systems to be followed-up in the infrared to search for a dusty disc component. White dwarfs hosting debris discs are among the most polluted from the accretion of planetesimals (Farihi, 2016), which makes them excellent systems to probe for photospheric absorption in the UV (which hosts many more lines compared with the optical, see spectra of SDSS J1228+1040 in Gänsicke et al. 2012 and Manser et al. 2016b) from metal pollution (Gänsicke et al., 2012). These systems will also be important in both (i) improving the current statistics on the occurrence rate and lifetime of debris discs and their gaseous components, and (ii) selecting targets for short-cadence observations to test the hypothesis of close-in planetesimals.

6.6 Conclusions

We have determined the occurrence rate of gaseous debris discs around white dwarfs as $0.06 \pm ^{0.03}_{0.02}$ per cent using a magnitude limited, colour-colour, colour-proper-motion limited sample of white dwarfs observed by SDSS. The ratio of observed debris discs with and without a gaseous component is significantly larger than expected from our results due to observational biases in the detections of gaseous emission and broad infrared emission. We also present the non-detection of Ca II triplet emission at 13 dusty debris disc hosts. With the advent of multiple dedicated multi-object spectroscopic surveys the number of gaseous discs observed will increase by a factor $\simeq 5$ over the next decade, and will allow further investigation into the occurrence rate and lifetime of debris discs at white dwarfs.

Chapter 7

Conclusions and future work

7.1 Conclusions

In this thesis I have studied the variability and prevalence of gaseous debris discs around metal polluted white dwarfs. The canonical pathway to produce these discs is via the disruption of a planetesimal on a highly eccentric orbit ($e > 0.98$) as it enters the Roche radius of a white dwarf. This process will form a broken ring of debris which will eventually circularise within the tidal disruption radius.

I searched a sample of 9097 single white dwarfs observed by the Sloan Digital Sky Survey and collated by (Gentile Fusillo et al., 2015) for new gaseous disc candidates but found none. With 5 confirmed gas disc hosts out of a sample of 9097 white dwarfs, I calculated the occurrence rate of these discs to white dwarfs as $0.06 \pm ^{0.03}_{0.02}$ %. This implies that only 1 – 10 % of debris discs detectable via an infrared excess around white dwarfs host an observable gaseous component. This value is a factor of a few to an order of magnitude smaller than the currently observed fraction ($\simeq 18$ %) of debris discs with a gaseous component (7) among the total number of systems with a detected infrared excess ($\simeq 38$, see Chapter 6).

My investigation into the common morphological variability of the observable gaseous debris discs strongly suggests that the presence of a gaseous component arises due to a physical phenomenon only present in a subset of discs.

I have collected and analysed observations of the Ca II triplet emission profiles of two gaseous debris discs, investigating variability that has been monitored for over a decade. In the prototypical system, SDSS J1228+1040, I modelled the variable morphology of the emission profiles remarkably well by the precession of a fixed, asymmetric intensity pattern in the disc, and produced the first image of a gaseous debris disc at a white dwarf. I also detected additional emission lines in the deep average X-shooter spectrum of SDSS J1228+1040, increasing the number of detected gaseous elements in this system to four (Ca, O, Fe, and Mg). The variation in line profile shape between the emission features of these ions is a clear indication that their intensity distributions in the disc are not the same, and this can be used to trace parameters such as the temperature and density profiles of the discs.

The second gaseous debris disc I analysed, SDSS J1043+0855, presented similar morphological variations of the gaseous emission profiles, but the quality and time-sampling of the data prevented the production of a velocity image of the disc. I have also analysed the optical spectra of SDSS J1043+0855 to determine its stellar parameters and the photospheric metal abundances. The Mg/Si and (upper limit to the) Fe/Si ratios of the planetary debris that has been accreted onto the white dwarf are broadly consistent with those of the crust of the Earth.

Long-term monitoring of the emission profiles from gaseous debris discs reveals that the majority of them share the seemingly-periodic, morphological evolution seen in the emission profiles of the gas discs around SDSS J1228+1040 and SDSS J1043+0855, and I suggest that this variability is generated by the same underlying mechanism, resulting in a fixed intensity pattern in the disc that precesses. This hypothesis is strongly supported by the recent detection of the morphological evolution of the Ca II triplet at HE 1349–2305 by Dennihy et al. (2018), who fitted a sinusoid to the velocity centroids of the profiles with a period of 1.4 yrs.

Finally, at the Gran Telescopio Canarias (GTC), I collected 519 high-cadence (100-200 s) spectra of the gaseous emission from the disc around SDSS J1228+1040, and detected variability in the shape and strength of the Ca II triplet line profiles on a $\simeq 2$ hr period. I interpret this short-term variability as the detection of a planetesimal orbiting within the debris disc, either generating gas via sublimation, or via collisions between (i) the planetesimal and the dust, or (ii) the dust grains themselves. I also hypothesise that the long-term variability, as well as the bulk of the observable gaseous emission at SDSS J1228+1040 is due to the presence of a planetesimal on an eccentric orbit, undergoing general relativistic apsidal precession and interacting with the disc. If this is confirmed, then the other six known gaseous debris discs are prime follow-up targets to search for planetesimals.

7.2 Future work

The research I have performed has helped to further develop the understanding of the debris discs that fuel the metal pollution of white dwarf atmospheres; a process which allows for the compositional analysis of planetesimals. However, the scientific potential of these discs is far from exhausted, and there are many ways, both observationally and theoretically, through which we can improve our understanding of these systems.

7.2.1 Further monitoring of the known gaseous debris discs

Long-term monitoring on the time-scale of years and decades

I currently lead several ongoing observing programs to monitor the long-term evolution of the gaseous debris discs around white dwarfs. For SDSS J1228+1040 and HE 1349–2305, obtaining additional emission profile observations will allow me to further corroborate the hypothesis of a fixed intensity pattern that precesses in the disc. For the other five gaseous debris discs (see Table 3.2), future, repeated observations of the Ca II triplet profile are needed to be able to produce Doppler maps of the gaseous emission profiles and analyse their morphological variability. Furthermore, obtaining high S/N optical spectra

of these gaseous debris discs allow us to detect additional emission profiles from different ionic transitions, as well as to analyse the metal pollution of the white dwarf photosphere.

The main feature used to study gaseous debris discs is the Ca II triplet, but as I have shown for SDSS J1228+1040, there are a plethora of additional lines that evolve in a morphologically different way to the Ca II triplet. Figure 4.3 shows these profiles, and in particular the O I emission features at 7774 Å and 8446 Å. The shape of these profiles are similar to each other, but red-shifted and blue-shifted peak strengths are flipped compared to well-studied Ca II triplet. Using the X-shooter and UVES observations of SDSS J1228+1040 presented here, as well as more recent data obtained via my monitoring campaign, I have produced a preliminary Doppler map for the O I emission profile shown in Figure 7.1. This map reveals that the emission from Ca II and O I originate from different locations in the disc.

While these Doppler maps are preliminary, one possible explanation for the difference in location of emission from different species is emission from an eccentric gas disc. As the material orbits in the disc, it will get closer and further away from the white dwarf, corresponding to a change in gas temperature due to the varying irradiation by the star. The excitation energy of the O I 7774 Å transition is a factor $\simeq 3$ higher than those of the Ca II 8600 Å triplet. This is corroborated by the Doppler maps, which show that the Ca II triplet emission appears strongest at radii greater (due to smaller orbital velocities) than the emission from O I, corresponding to a cooler region of the disc. I am also planning to produce Doppler maps for the Ca H & K emission profiles, which are the next strongest lines that we have detected (Figure 4.3).

Short-term monitoring on the time-scale of minutes and hours

With the detection of variability in the shape and strength of the Ca II triplet emission at SDSS J1228+1040 on a 2 hr period, we need to understand how consistent this variable emission is, and whether it is present in other debris disc systems.

If the planetesimal in the disc is on an eccentric orbit, then the gas generating the short-term variability should follow the same trajectory. The observed velocity profile of an eccentric orbit is more complicated than a circular one, and the shape of the profile varies as a function of the angle, α (see Figure A.1) between the line of sight of the observer, and the semi-major axis of the eccentric orbit. Due to general relativistic precession, α will change over time, and this would have an observable effect on the velocity profile of the short-term variability, which if measured would be strong evidence in support of an eccentric orbit.

By performing observations similar to those discussed in Section 5.2 on other gaseous and dusty debris discs, we will be able to investigate whether there is any correlation between: (i) the presence of a gaseous debris disc and/or long term variability and

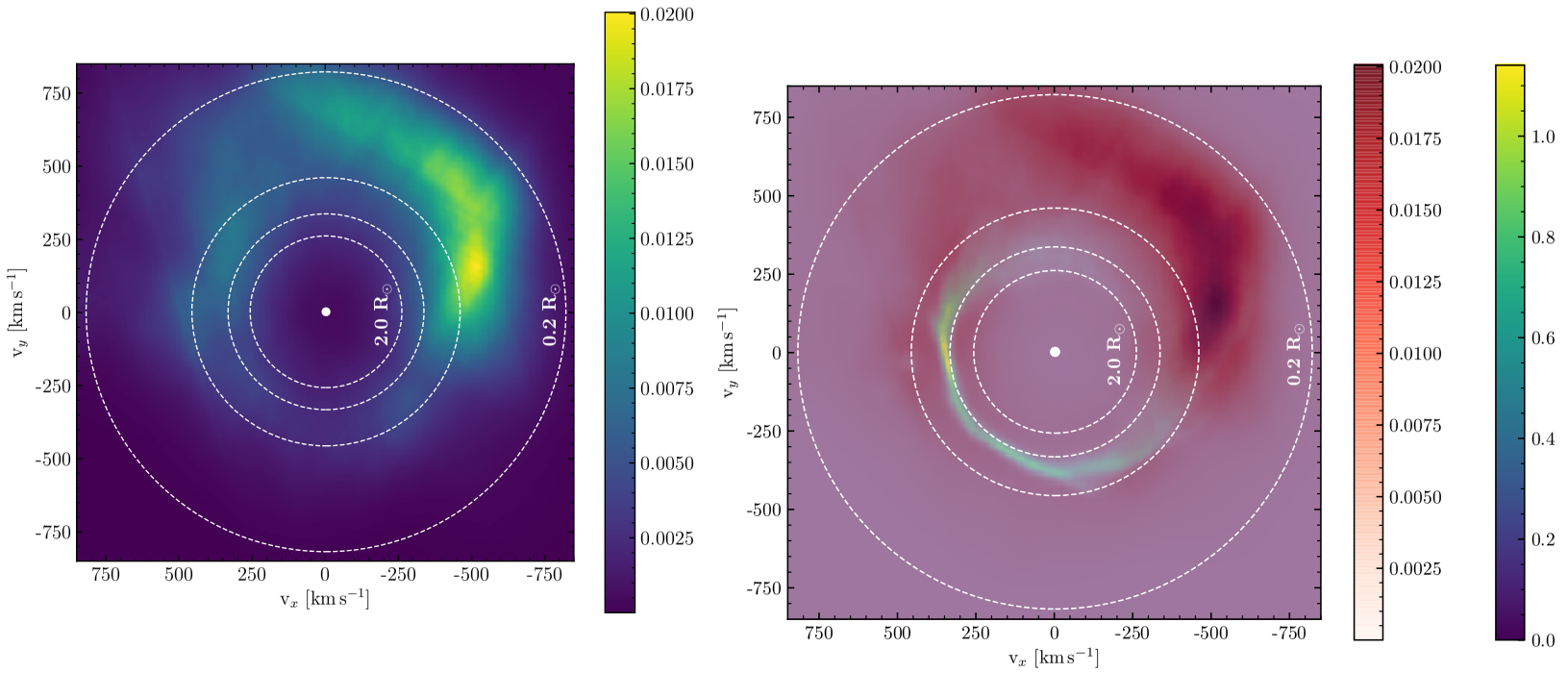

Figure 7.1: Preliminary work on mapping the various ionic species within the gaseous disc at SDSS J1228+1040. The left panel shows the Doppler map for the O I 7774 Å emission profile. The right panel shows the combination of the O I (red-black colour-map) and the Ca II triplet (yellow-blue colour-map) map of the disc (this includes additional new observations compared to the map shown in Figure 2.13). The images clearly illustrate that the emission from these two ions originates from different places in the debris disc, O I is emitted from regions closer to the white dwarf than Ca II.

the detection of a planetesimal within the debris disc, and (ii) the precession period of the variable gaseous debris discs and changes in the velocity profile of any short-term variability. If these correlations are both proven to be present at gaseous debris discs, then it would strongly suggest that these discs are powerful tracers for the presence of a planetesimal.

7.2.2 Finding additional gaseous debris discs

The clear differences in the behaviour we have observed so far, such as the order of magnitude difference between the precession periods of SDSS J1228+1040 and HE 1348-2305 ($\simeq 25$ yr vs $\simeq 1.4$ yr Manser et al. 2016b; Dennihy et al. 2018), requires us to increase the sample of gaseous debris discs in size. Only then can we begin to study gaseous debris discs in a collective, statistical manner, rather than on a case by case basis, and I discuss possible ways to increase the number of known systems below.

Multi-object spectoscopic surveys

As mentioned previously, multiple dedicated multi-object spectroscopic surveys including: DESI (DESI Collaboration et al., 2016a,b), WEAVE (Dalton et al., 2012, 2016), 4MOST (de Jong et al., 2016), and SDSS-V (Kollmeier et al., 2017) will be starting operations in the coming few years. These surveys will increase the number of observed white dwarfs from $\sim 10^4$ to $\sim 10^5$, and will ultimately lead to an order-of-magnitude increase in the number of known gaseous debris discs to $\simeq 60$.

I am currently a junior member of the DESI collaboration, working with the Milky Way Survey team, as well as the data team, to use white dwarfs as flux calibrators. I also assisted the DESI commissioning team with the prototype instrument, ProtoDESI (Fagrelius et al., 2018), which was installed on the Mayall telescope at Kitt Peak (the telescope DESI will be mounted on) to reduce technical risks for the science instrument. My work with the DESI collaboration will lead to a data set similar to, but substantially larger than, the white dwarf sample observed by SDSS, and which will be used over the coming decades.

Identifying debris disc candidates

Gentile Fusillo (2015) and Dennihy et al. (2017) have shown that cross-matching optical photometric surveys, such as SDSS, with infrared photometric surveys like WISE can be used to find candidate debris disc hosts. While the white dwarfs are dominant in the optical part of the spectrum, the excess emission from the dusty discs peaks in the infrared. Gentile Fusillo (2015) collated a sample of $\simeq 300$ white dwarf candidates with a potential infrared excesses, the majority of which are thought to be white dwarfs that host either a dusty disc, or have a low mass companion. With an occurrence rate of gaseous components to detected

dusty debris discs of 1 – 10 %, up to 3 – 30 new gaseous debris discs could be identified within this dataset alone. A large caveat to this is that the beam-width of WISE is wide, and so contamination by unrelated sources is common. Even with a false detection rate of up to 50 %, this method should still substantially increase the number of known gaseous debris discs.

7.2.3 Future theoretical studies

Prevailing models predicting the production of gas (Rafikov, 2011a; Metzger et al., 2012; Kenyon and Bromley, 2017b), and the subsequent heating of line emission from the disc (Melis et al., 2010; Kinnear, 2011; Hartmann et al., 2011) do not accurately describe current observational characteristics (see Section 1.6.3 for an overview). The temperature and density profiles of debris discs are important inputs into the current models of gaseous emission, which could be drastically improved with the Doppler maps I have produced (see Figures 4.6 & 7.1). They reveal the spatial extent and brightness distribution for emission lines of specific ions which have the potential to map the gas density and temperature in the disc. If these parameters can be constrained, then additional key physical properties of the disc, such as its gas mass can be determined, which is important for modelling gas drag on the dust and the evolution of debris discs.

At the moment, gas and dust in debris discs are modelled independently, but their interaction is likely to be important for the dynamics and evolution of the gaseous emission. The recently developed smooth particle hydrodynamics code PHANTOM (Price et al., 2017) is a potentially powerful tool to fully simulate debris discs, and I am involved in an ongoing project using this code. One of the first simulations we have attempted is the production of gaseous debris at SDSS J1228+1040 from a body that orbits in the disc. Other scenarios we plan to simulate are (i) the evolution of an eccentric, purely-gaseous disc, and (ii) the evolution of a canonical, circular debris disc (see Figure 1.22), with co-orbiting dusty and gaseous components.

Appendix A

Velocities and velocity gradients in an eccentric disc

Horne and Marsh (1986) show that line photons travelling through an optically thick disc are more likely to escape along paths of the greatest velocity gradient. We derive and list here the equations needed to calculate the radial velocity and velocity gradient at any point in an elliptical disc of constant orbital eccentricity, e and constant orientation of its semi-major axes, a. This expands the formulation for modelling emission line profiles from circular discs described by Horne and Marsh (1986). We first set up the basic components of an eccentric orbit, of which some are shown in Figure A.1.

A.1 Equations of an elliptical orbit

The polar equation for an ellipse is given as

$$r = \frac{l}{1 + e\cos\nu}, \tag{A.1}$$

where l is the semi-latus rectum, and ν is the angle measured from the point of periastron, usually called the "true anomaly". Conservation of angular momentum in a central force field means that

$$r^2\frac{\dot{\nu}}{\dot{t}} = h, \tag{A.2}$$

where h, the specific angular momentum, is constant. This therefore leads to the true anomaly as a function of time being determined by the following equation

$$\frac{ht}{l^2} = \int_0^{\nu} \frac{\dot{\nu}'}{(1 + e\cos\nu')^2}. \tag{A.3}$$

Making the substitution $z = \tan\nu/2$ and setting

$$z = \left(\frac{1+e}{1-e}\right)^{1/2}\tan\frac{E}{2}, \tag{A.4}$$

where E is the eccentric anomaly (see Figure A.1), we get

$$E - e\sin E = \frac{h\left(1-e^2\right)^{3/2}}{l^2}t. \tag{A.5}$$

When $\nu = 2\pi$, we get $E = 2\pi$ and $t = P$, so then we can write

$$E - e\sin E = nt, \tag{A.6}$$

where n is the mean angular velocity and is given by

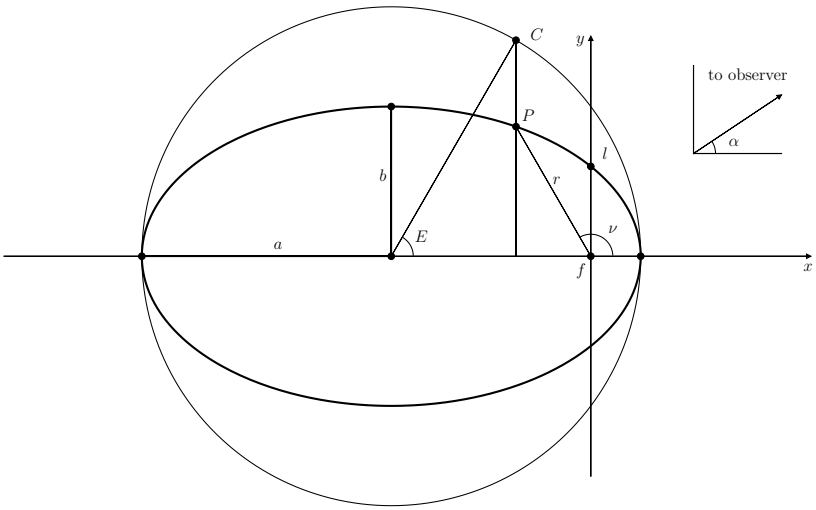

Figure A.1: An elliptical orbit of eccentricity, e, with the origin centred on the focal point, f, with semi-major and semi-minor axes a and b. A point, P, along the orbit is shown, at a radius, r, and with a true anomaly, ν. The semi-latus rectum, l, is also labelled, as is the eccentric anomaly, E, which can be constructed geometrically by putting a circle of radius, a, centred on the ellipse, and drawing a line perpendicular to the major axis through any point (P, here) on the ellipse. The angle, α, to an observer is also shown, taken to be zero when the observer is looking along the x-axis from the positive side, and increases in the anti-clockwise direction.

$$n = \frac{2\pi}{P} = \frac{h\left(1-e^2\right)^{3/2}}{l^2}. \tag{A.7}$$

Equation A.6 is Kepler's equation of elliptical motion and can easily be solved numerically, and the true anomaly, ν, follows from

$$\tan\frac{\nu}{2} = \left(\frac{1+e}{1-e}\right)^{1/2}\tan\frac{E}{2}. \tag{A.8}$$

E can be constructed geometrically by putting a circle radius a centred on the ellipse, and drawing a line perpendicular to the major axis through any point on the ellipse. The angle subtended by the point on the circle where the perpendicular line cuts it is E. Using this, or the above equation, one can show that

$$\cos E = \frac{e+\cos\nu}{1+e\cos\nu}. \tag{A.9}$$

Since E and ν always lie within the same range; 0 to π or π to 2π, this equation is sufficient to determine E. Related useful expressions are

$$\cos\nu = \frac{\cos E - e}{1 - e\cos E}, \tag{A.10}$$

$$\sin\nu = \frac{\sqrt{1-e^2}\sin E}{1 - e\cos E}. \tag{A.11}$$

Assuming that the ellipse is oriented with the focus at the origin and the semi-major axis parallel to the x-axis (pointing left so that the periastron lies on the positive x-axis giving the standard orientation for ν in 2D polar coordinates, see Figure A.1), then the velocity at any point is given by

$$v_x = v_r\cos\nu - v_\nu\sin\nu, \tag{A.12}$$

$$v_y = v_r\sin\nu + v_\nu\cos\nu, \tag{A.13}$$

where

$$v_r = \frac{el\sin\nu}{(1+e\cos\nu)^2}\,\dot{\nu}, \tag{A.14}$$

and

$$v_\nu = \frac{l}{1+e\cos\nu}\,\dot{\nu}, \tag{A.15}$$

where

$$\dot{\nu} = \left(\frac{1+e}{1-e}\right)^{1/2}\left(\cos^2\frac{E}{2} + \frac{1+e}{1-e}\sin^2\frac{E}{2}\right)^{-1}\dot{E}, \tag{A.16}$$

and

$$\dot{E} = \frac{n}{1-e\cos E}. \tag{A.17}$$

The equation for $\dot{\nu}$ can be reduced to

$$\dot{\nu} = \frac{\left(1-e^2\right)^{1/2}}{(1-e\cos E)^2}n, \tag{A.18}$$

or, equivalently,

$$\dot{\nu} = \frac{(1+e\cos\nu)^2}{\left(1-e^2\right)^{3/2}}n, \tag{A.19}$$

giving the following alternative expressions for the two components of velocity (radial and

azimuthal)

$$v_r = \frac{enl \sin \nu}{(1-e^2)^{3/2}}, \tag{A.20}$$

and

$$v_\nu = \frac{nl(1+e\cos\nu)}{(1-e^2)^{3/2}}. \tag{A.21}$$

We are now in a position to consider orbits and radial velocities, and their derivatives.

A.2 Velocity gradients in a confocal elliptical flow

If a point in the disc is viewed by an observer at angle α defined so that $\alpha = 0$ when looking along the positive x-axis and increasing anti-clockwise (see Figure A.1), then its radial velocity is given by

$$v_r = v_x \cos\alpha + v_y \sin\alpha. \tag{A.22}$$

Horne and Marsh (1986) showed that the velocity gradient is also required to fully model the emission profile of an accretion disc, which using the notation $v_{,x} \equiv \frac{\partial v}{\partial x}$, is given by

$$\begin{aligned} \frac{\dot{v_r}}{\dot{k}} &= v_{r,x}\cos\alpha + v_{r,y}\sin\alpha, & \text{(A.23)}\\ &= v_{x,x}\cos^2\alpha + \left(v_{x,y}+v_{y,x}\right)\cos\alpha\sin\alpha + v_{y,y}\sin^2\alpha, & \text{(A.24)} \end{aligned}$$

where dk is a line element towards the observer. From Equations A.12 & A.13, we have

$$\begin{aligned} v_{x,x} &= v_{r,x}\cos\nu - v_{\nu,x}\sin\nu - (v_r\sin\nu + v_\nu\cos\nu)\nu_{,x}, & \text{(A.25)}\\ v_{x,y} &= v_{r,y}\cos\nu - v_{\nu,y}\sin\nu - (v_r\sin\nu + v_\nu\cos\nu)\nu_{,y}, & \text{(A.26)}\\ v_{y,x} &= v_{r,x}\sin\nu + v_{\nu,x}\cos\nu + (v_r\cos\nu - v_\nu\sin\nu)\nu_{,x}, & \text{(A.27)}\\ v_{y,y} &= v_{r,y}\sin\nu + v_{\nu,y}\cos\nu + (v_r\cos\nu - v_\nu\sin\nu)\nu_{,y}. & \text{(A.28)} \end{aligned}$$

One can show that

$$\begin{aligned} \nu_{,x} &= -\frac{y}{r^2}, & \text{(A.29)}\\ \nu_{,y} &= \frac{x}{r^2}, & \text{(A.30)} \end{aligned}$$

while, using Equations A.20 & A.21 we obtain,

$$v_{r,x} = e(1-e^2)^{-3/2}[(n_{,x}l + nl_{,x})\sin\nu + nl\cos(\nu)\nu_{,x}], \tag{A.31}$$
$$v_{r,y} = e(1-e^2)^{-3/2}[(n_{,y}l + nl_{,y})\sin\nu + nl\cos(\nu)\nu_{,y}], \tag{A.32}$$
$$v_{\nu,x} = (1-e^2)^{-3/2}[(n_{,x}l + nl_{,x})(1+e\cos\nu) - enl\sin(\nu)\nu_{,x}], \tag{A.33}$$
$$v_{\nu,y} = (1-e^2)^{-3/2}[(n_{,y}l + nl_{,y})(1+e\cos\nu) - enl\sin(\nu)\nu_{,y}]. \tag{A.34}$$

From Equation A.1 we can obtain,

$$l_{,x} = r_{,x}(1+e\cos\nu) - er\sin(\nu)\nu_{,x}, \tag{A.35}$$
$$l_{,y} = r_{,y}(1+e\cos\nu) - er\sin(\nu)\nu_{,y}, \tag{A.36}$$

where

$$r_{,x} = \frac{x}{r}, \tag{A.37}$$
$$r_{,y} = \frac{y}{r}, \tag{A.38}$$

and from Kepler's third law, assuming the mass of the orbiting material to be negligible,

$$n^2 = \frac{GM}{a^3}, \tag{A.39}$$

where G is the gravitational constant and M is the mass of the host star, we finally get the last unknowns,

$$n_{,x} = -\frac{3l_{,x}n}{2l}, \tag{A.40}$$
$$n_{,y} = -\frac{3l_{,y}n}{2l}, \tag{A.41}$$

which now allows one to calculate the velocity derivatives.

Bibliography

Abazajian K.N. et al., 2009. *ApJS*, 182:543–558.

Ahn C.P. et al., 2012. *ApJS*, 203:21.

Ahn C.P. et al., 2014. *ApJ*, 211:17.

Alam S. et al., 2015. *ApJS*, 219:12.

Allègre C., Manhès G., and Lewin E., 2001. *Earth and Planetary Science Letters*, 185:49–69.

Althaus L.G. et al., 2010. *A&AR*, 18:471–566.

Bailey J.D. and Landstreet J.D., 2013. *MNRAS*, 432:1687–1694.

Balbus S.A. and Hawley J.F., 1998. *Reviews of Modern Physics*, 70:1.

Barstow M.A. et al., 2014. *MNRAS*, 440:1607–1625.

Berg C. et al., 1992. *ApJS*, 78:409–421.

Bergeron P. et al., 2011. *ApJ*, 737:28–+.

Bergfors C. et al., 2014. *MNRAS*, 444:2147–2156.

Berta-Thompson Z.K. et al., 2015. *Nat*, 527:204–207.

Besla G. and Wu Y., 2007. *ApJ*, 655:528–540.

Bochkarev K.V. and Rafikov R.R., 2011. *ApJ*, 741:36–.

Bonsor A. and Veras D., 2015. *MNRAS*, 454:53–63.

Bonsor A. et al., 2017. *MNRAS*, 468:154–164.

Borucki W.J. et al., 2010. *Science*, 327:977.

Brinkworth C.S. et al., 2009. *ApJ*, 696:1402–1406.

Brinkworth C.S. et al., 2012. *ApJ*, 750:86.

Brown J.C., Veras D., and Gänsicke B.T., 2017. *MNRAS*, 468:1575–1593.

Carroll B.W. and Ostlie D.A., 2006. *An introduction to modern astrophysics and cosmology*.

Casassus S. et al., 2013. *Nat*, 493:191–194.

Casewell S.L. et al., 2018. *MNRAS*, 476:1405–1411.

Charbonneau D. et al., 2000. *ApJ Lett.*, 529:L45–L48.

Chayer P., 2014. , 437:L95–L99.

Chayer P. and Dupuis J., 2010. 394–399.

Chen Y.P. et al., 2014. *A&A*, 565:A117.

Czechowski A. and Mann I., 2007. *ApJ*, 660:1541–1555.

Dalton G. et al., 2012. In *Ground-based and Airborne Instrumentation for Astronomy IV*, volume 8446 of , 84460P.

Dalton G. et al., 2016. In *Ground-based and Airborne Instrumentation for Astronomy VI*, volume 9908 of , 99081G.

de Jong R.S. et al., 2016. In *Ground-based and Airborne Instrumentation for Astronomy VI*, volume 9908 of , 99081O.

de Val-Borro M. et al., 2007. *A&A*, 471:1043–1055.

Dean J., 1990. *Materials and Manufacturing Processes*, 5(4):687–688.

Debes J.H. and López-Morales M., 2008. *ApJ Lett.*, 677:L43–L46.

Debes J.H. and Sigurdsson S., 2002. *ApJ*, 572:556–565.

Debes J.H., Walsh K.J., and Stark C., 2012. *ApJ*, 747:148.

Debes J.H. et al., 2011a. *ApJ*, 729:4.

Debes J.H. et al., 2011b. *ApJS*, 197:38.

Dekker H. et al., 2000. In M. Iye and A.F. Moorwood, editors, *Optical and IR Telescope Instrumentation and Detectors*, volume 4008 of *Society of Photo-Optical Instrumentation Engineers (SPIE) Conference Series*, 534–545.

Dennihy E. et al., 2016. *ApJ*, 831:31.

Dennihy E. et al., 2017. *ApJ*, 849:77.

Dennihy E. et al., 2018. *ApJ*, 854:40.

Dent W.R.F. et al., 2014. *Science*, 343:1490–1492.

DESI Collaboration et al., 2016a. *ArXiv e-prints*.

DESI Collaboration et al., 2016b. *ArXiv e-prints*.

Dickinson N.J. et al., 2012. *MNRAS*, 423:1397–1410.

Doi M. et al., 2010. *AJ*, 139:1628–1648.

Dufour P. et al., 2007. *ApJ*, 663:1291–1308.

Dufour P. et al., 2012. *ApJ*, 749:6.

Duncan M.J. and Lissauer J.J., 1998. *Icarus*, 134:303–310.

Dupuis J., Chayer P., and Hénault-Brunet V., 2010. In K. Werner and T. Rauch, editors, *American Institute of Physics Conference Series*, volume 1273 of *American Institute of Physics Conference Series*, 412–417.

Eisenstein D.J. et al., 2006. *ApJS*, 167:40–58.

Eisenstein D.J. et al., 2011. *AJ*, 142:72.

Fagrelius P. et al., 2018. *PASP*, 130(2):025005.

Farihi J., 2016. *New Astronomy Reviews*, 71:9–34.

Farihi J., Gänsicke B.T., and Koester D., 2013. *MNRAS*, 432:1955–1960.

Farihi J., Jura M., and Zuckerman B., 2009. *ApJ*, 694:805–819.

Farihi J., Parsons S.G., and Gänsicke B.T., 2017. *Nature Astronomy*, 1:0032.

Farihi J., Zuckerman B., and Becklin E.E., 2008. *ApJ*, 674:431–446.

Farihi J. et al., 2012. *MNRAS*, 421:1635–1643.

Farihi J. et al., 2018. .

Faure J. et al., 2015. *A&A*, 573:A132.

Flock M. et al., 2017. *ApJ*, 850:131.

Fontaine G. and Michaud G., 1979. *ApJ*, 231:826–840.

Fortney J.J., Marley M.S., and Barnes J.W., 2007. , 659:1661–1672.

Freudling W. et al., 2013. *A&A*, 559:A96.

Frewen S.F.N. and Hansen B.M.S., 2014. *MNRAS*, 439:2442–2458.

Gaia Collaboration et al., 2016. *A&A*, 595:A1.

Gaia Collaboration et al., 2018. *ArXiv e-prints*.

Gänsicke B.T., 2011. In S. Schuh, H. Drechsel, and U. Heber, editors, *American Institute of Physics Conference Series*, volume 1331 of *American Institute of Physics Conference Series*, 211–214.

Gänsicke B.T., Marsh T.R., and Southworth J., 2007. *MNRAS*, 380:L35–L39.

Gänsicke B.T. et al., 2006. *Science*, 314:1908–1910.

Gänsicke B.T. et al., 2008. *MNRAS*, 391:L103–L107.

Gänsicke B.T. et al., 2012. *MNRAS*, 424:333–347.

Gänsicke B.T. et al., 2016. *ApJ Lett.*, 818:L7.

Gardner J.P. et al., 2006. *Space Science Reviews*, 123(4):485–606. ISSN 1572-9672.

Gentile Fusillo N.P., 2015. *Stellar and planetary remnants in large area surveys*. Ph.D. thesis, University of Warwick.

Gentile Fusillo N.P., Gänsicke B.T., and Greiss S., 2015. *MNRAS*, 448:2260–2274.

Gentile Fusillo N.P. et al., 2017. *MNRAS*, 468:971–980.

Girven J. et al., 2012. *ApJ*, 749:154.

Graham J.R. et al., 1990. *ApJ*, 357:216–223.

Guess A.W., 1962. *ApJ*, 135:855–866.

Gunn J.E. et al., 2006. *AJ*, 131:2332–2359.

Guo J. et al., 2015. *ApJ Lett.*, 810:L17.

Gurri P., Veras D., and Gänsicke B.T., 2017. *MNRAS*, 464:321–328.

Han E. et al., 2014. *PASP*, 126:827.

Hanuschik R.W. et al., 1995. *A&A*, 300:163.

Hartmann S. et al., 2011. *A&A*, 530:A7.

Haswell C.A., 2010. *Transiting Exoplanets*.

Hawley J.F., 1987. *MNRAS*, 225:677–694.

Hollands M.A. et al., 2017. *MNRAS*, 467:4970–5000.

Hord B. et al., 2017. *ApJ*, 849:164.

Horne K., 1985. *MNRAS*, 213:129–141.

Horne K. and Marsh T.R., 1986. *MNRAS*, 218:761–773.

Howell S.B. et al., 2014. *PASP*, 126:398.

Hut P., 1981. *A&A*, 99:126–140.

Isella A. et al., 2013. *ApJ*, 775:30.

Jeffreys H., 1946. *Proceedings of the Royal Society of London Series A*, 186:453–461.

Jura M., 2003. *ApJ Lett.*, 584:L91–L94.

Jura M., 2008. *AJ*, 135:1785–1792.

Jura M., Farihi J., and Zuckerman B., 2007. *ApJ*, 663:1285–1290.

Jura M., Farihi J., and Zuckerman B., 2009. *AJ*, 137:3191–3197.

Jura M. and Xu S., 2010. *AJ*, 140:1129–1136.

Jura M. and Xu S., 2013. *ApJ*, 145:30.

Jura M. and Young E.D., 2014. *Annual Review of Earth and Planetary Sciences*, 42:45–67.

Kawka A. and Vennes S., 2014. *MNRAS*, 439:L90–L94.

Kawka A. and Vennes S., 2016. *MNRAS*, 458:325–331.

Kenyon S.J. and Bromley B.C., 2017a. *ApJ*, 844:116.

Kenyon S.J. and Bromley B.C., 2017b. *ApJ*, 850:50.

Kepler J., 1619. *Harmonices Mundi*. Linz, Austria.

King A.R., Pringle J.E., and Livio M., 2007. *MNRAS*, 376:1740–1746.

Kinnear T., 2011. *Irradiated Gaseous Discs Around White Dwarfs*. Master's thesis, University of Warwick.

Kislyakova K.G. et al., 2017. *Nature Astronomy*, 1:878–885.

Klahr H. and Lin D.N.C., 2005. *ApJ*, 632:1113–1121.

Klahr H.H. and Lin D.N.C., 2001. *ApJ*, 554:1095–1109.

Klein B. et al., 2010. *ApJ*, 709:950–962.

Kleinman S.J. et al., 2013. *ApJS*, 204:5.

Koester D., 1987. *ApJ*, 322:852–855.

Koester D., 2009. *A&A*, 498:517–525.

Koester D., 2010. *Memorie della Societa Astronomica Italiana,*, 81:921–931.

Koester D., 2013. *White Dwarf Stars*, 559.

Koester D., Gänsicke B.T., and Farihi J., 2014. *A&A*, 566:A34.

Koester D. and Kepler S.O., 2015. *A&A*, 583:A86.

Koester D., Provencal J., and Shipman H.L., 1997. *A&A*, 320:L57–L1997.

Koester D. and Wilken D., 2006. *A&A*, 453:1051–1057.

Koester D. et al., 2005. *A&A*, 432:1025–1032.

Koester D. et al., 2011. *aa*, 530:A114.

Koller J., Li H., and Lin D.N.C., 2003. *ApJ Lett.*, 596:L91–L94.

Kollmeier J.A. et al., 2017. *ArXiv e-prints*.

Kupfer T. et al., 2016. *MNRAS*, 457:1828–1841.

Landstreet J.D., 1988. *ApJ*, 326:967–987.

Landstreet J.D. et al., 2012. *A&A*, 545:A30.

Landstreet J.D. et al., 2017. *A&A*, 607:A92.

Laughlin G., 2018. *Mass-Radius Relations of Giant Planets: The Radius Anomaly and Interior Models*. Springer, Cham.

Li H. et al., 2000. *ApJ*, 533:1023–1034.

Littlefair S.P. et al., 2014. *MNRAS*, 445:2106–2115.

López-Morales M. et al., 2016. *AJ*, 152:204.

Louden T.M., 2016. *The composition and dynamics of exoplanet atmospheres*. Ph.D. thesis, University of Warwick.

Lovelace R.V.E. and Hohlfeld R.G., 1978. *ApJ*, 221:51–61.

Lovelace R.V.E. et al., 1999. *ApJ*, 513:805–810.

Lynden-Bell D. and Pringle J.E., 1974. *MNRAS*, 168:603–637.

Lyra W. and Klahr H., 2011. *A&A*, 527:A138.

Lyra W. and Kuchner M., 2013. *Nat*, 499:184–187.

Lyra W. and Mac Low M.M., 2012. *ApJ*, 756:62.

Lyra W., Turner N.J., and McNally C.P., 2015. *A&A*, 574:A10.

Lyra W. et al., 2009a. *A&A*, 497:869–888.

Lyra W. et al., 2009b. *A&A*, 493:1125–1139.

Lyra W. et al., 2016. *ApJ*, 817:102.

Lyra W. et al., 2017. *AJ*, 154:146.

Manser C.J. and Gänsicke B.T., 2014. *MNRAS*, 442:L23–L27.

Manser C.J. et al., 2016a. *MNRAS*, 462:1461–1469.

Manser C.J. et al., 2016b. *MNRAS*, 455:4467–4478.

Marino S., Perez S., and Casassus S., 2015. *ApJ Lett.*, 798:L44.

Marsh T.R., 2001. In H.M.J. Boffin, D. Steeghs, and J. Cuypers, editors, *Astrotomography, Indirect Imaging Methods in Observational Astronomy*, volume 573 of *Lecture Notes in Physics, Berlin Springer Verlag*, 1.

Marsh T.R., 2005. , 296:403–415.

Marsh T.R. and Horne K., 1988. *MNRAS*, 235:269–286.

Maxted P.F.L. et al., 2006. *Nat*, 442:543–545.

Mayor M. and Queloz D., 1995. *Nat*, 378:355–359.

McDonough W., 2000. In R. Teisseyre and E. Majewski, editors, *Earthquake Thermodynamics and Phase Transformation in the Earth's Interior*, 5–24. Elsevier Science Academic Press.

McNally C.P., Lyra W., and Passy J.C., 2012. *ApJS*, 201:18.

Melis C. and Dufour P., 2017. *ApJ*, 834:1.

Melis C. et al., 2010. *ApJ*, 722:1078–1091.

Melis C. et al., 2011. *ApJ*, 732:90.

Melis C. et al., 2012. *ApJ Lett.*, 751:L4.

Méndez A. and Rivera-Valentín E.G., 2017. *ApJ Lett.*, 837:L1.

Metzger B.D., Rafikov R.R., and Bochkarev K.V., 2012. *MNRAS*, 423:505–528.

Miranda R. and Rafikov R.R., 2018. *ArXiv e-prints*.

Mizerski K.A. and Bajer K., 2009. *Journal of Fluid Mechanics*, 632:401.

Mizerski K.A. and Lyra W., 2012. *Journal of Fluid Mechanics*, 698:358–373.

Murray C.D. and Dermott S.F., 1999. *Solar system dynamics*.

Mustill A.J., Veras D., and Villaver E., 2014. *MNRAS*, 437:1404–1419.

Mustill A.J. and Villaver E., 2012. *ApJ*, 761:121.

Mustill A.J. et al., 2018. *MNRAS*, 476:3939–3955.

Nagel J.R., 2018. *IEEE Antennas and Propagation Magazine*, 60.

Nimmo F. and Tanaka K., 2005. *Annual Review of Earth and Planetary Sciences*, 33:133–161.

Nittler L.R. et al., 2017. *ArXiv e-prints*.

Ogilvie G.I., 2001. *MNRAS*, 325:231–248.

Okazaki A.T., 1991. *PASJ*, 43:75–94.

Okazaki A.T., 1997. *A&A*, 318:548–560.

Papaloizou J.C., Savonije G.J., and Henrichs H.F., 1992. *A&A*, 265:L45–L48.

Papaloizou J.C.B. and Pringle J.E., 1984. *MNRAS*, 208:721–750.

Papaloizou J.C.B. and Pringle J.E., 1985. *MNRAS*, 213:799–820.

Paquette C. et al., 1986. *ApJS*, 61:177–195.

Pauli W., 1925. *Zeitschrift fur Physik*, 31:765–783.

Payne M.J. et al., 2016. *MNRAS*, 457:217–231.

Payne M.J. et al., 2017. *MNRAS*, 464:2557–2564.

Petrovic J.J., 2001. *Journal of Materials Science*, 36:1579–1583.

Pollacco D.L. et al., 2006. *PASP*, 118:1407–1418.

Porco C.C. et al., 2005. *Science*, 307:1226–1236.

Pozzo M. et al., 2014. *Earth and Planetary Science Letters*, 393:159–164.

Press W.H., 2002. *Numerical recipes in C++ : the art of scientific computing*. Cambridge Univ. Press, Cambridge.

Price D.J. et al., 2017. *ArXiv e-prints*.

Raddi R. et al., 2015. *MNRAS*, 450:2083–2093.

Rafikov R.R., 2011a. *ApJ Lett.*, 732:L3.

Rafikov R.R., 2011b. *MNRAS*, 416:L55–L59.

Rafikov R.R. and Garmilla J.A., 2012. *ApJ*, 760:123.

Rappaport S. et al., 2016. *MNRAS*, 458:3904–3917.

Reach W.T. et al., 2005. *ApJ Lett.*, 635:L161–L164.

Reach W.T. et al., 2009. *ApJ*, 693:697–712.

Redfield S. et al., 2017. *ApJ*, 839:42.

Richert A.J.W., Lyra W., and Kuchner M.J., 2018. *ApJ*, 856:41.

Richert A.J.W. et al., 2015. *ApJ*, 804:95.

Ricker G.R. et al., 2015. *Journal of Astronomical Telescopes, Instruments, and Systems*, 1(1):014003.

Rocchetto M. et al., 2015. *MNRAS*, 449:574–587.

Russell C.T. et al., 2016. *Science*, 353:1008–1010.

Schlafly E.F. and Finkbeiner D.P., 2011. *ApJ*, 737:103.

Schönberg M. and Chandrasekhar S., 1942. *ApJ*, 96:161.

Schwarzenberg-Czerny A., 1996. *ApJ Lett.*, 460:L107–L110.

Shakura N.I. and Sunyaev R.A., 1973. *A&A*, 24:337–355.

Sion E.M. et al., 1983. *ApJ*, 269:253–257.

Slyuta E.N., 2013. *Solar System Research*, 47:109–126.

Smee S.A. et al., 2013. *AJ*, 146:32.

Smette A. et al., 2015. *A&A*, 576:A77.

Smith S.W., 1997. *The Scientists and Engineer's Guide to Digital Signal Processing*. California Technical Pub, California.

Statler T.S., 2001. *AJ*, 122:2257–2266.

Steeghs D., 1999. *Spiral waves in accretion discs*. Ph.D. thesis, University of St.Andrews.

Steeghs D., Harlaftis E.T., and Horne K., 1997. *MNRAS*, 290:L28–L32.

Steeghs D. and Stehle R., 1999. *MNRAS*, 307:99–110.

Steele P.R. et al., 2011. *MNRAS*, 416:2768–2791.

Tiscareno M.S. et al., 2007. *Icarus*, 189:14–34.

Toomre A., 1981. In S.M. Fall and D. Lynden-Bell, editors, *Structure and Evolution of Normal Galaxies*, 111–136.

Tremblay P.E., Bergeron P., and Gianninas A., 2011. *ApJ*, 730:128.

van der Marel N. et al., 2013. *Science*, 340:1199–1202.

van Maanen A., 1917. *PASP*, 29:258–.

Vanderburg A. et al., 2015. *Nat*, 526:546–549.

Varnière P. and Tagger M., 2006. *A&A*, 446:L13–L16.

Vennes S. and Kawka A., 2013. *ApJ*, 779:70.

Veras D., 2014. *MNRAS*, 442:L71–L75.

Veras D., 2016. *Royal Society Open Science*, 3:150571.

Veras D. and Gänsicke B.T., 2015. *MNRAS*, 447:1049–1058.

Veras D., Marsh T.R., and Gänsicke B.T., 2016. *MNRAS*, 461:1413–1420.

Veras D., Shannon A., and Gänsicke B.T., 2014a. *MNRAS*, 445:4175–4185.

Veras D. et al., 2013. *MNRAS*, 431:1686–1708.

Veras D. et al., 2014b. *MNRAS*, 445:2244–2255.

Veras D. et al., 2015. *MNRAS*, 451:3453–3459.

Veras D. et al., 2017. *MNRAS*, 465:1008–1022.

Vernet J. et al., 2011. *A&A*, 536:A105.

Villaver E. and Livio M., 2007. *ApJ*, 661:1192–1201.

Villaver E. and Livio M., 2009. *ApJ Lett.*, 705:L81–L85.

von Hippel T. and Thompson S.E., 2007. *ApJ*, 661:477–481.

von Hippel T. et al., 2007. *ApJ*, 662:544–551.

Voss B. et al., 2007. *A&A*, 470:1079–1088.

Voyatzis G. et al., 2013. *MNRAS*, 430:3383–3396.

Werner M.W. et al., 2004. *ApJS*, 154:1–9.

Wheatley P.J. et al., 2018. , 475:4476–4493.

Wilson D.J. et al., 2014. *MNRAS*, 445:1878–1884.

Wilson D.J. et al., 2015. *MNRAS*, 451:3237–3248.

Wolszczan A. and Frail D.A., 1992. *Nat*, 355:145–147.

Wright E.L. et al., 2010. *AJ*, 140:1868–1881.

Wright J.T. et al., 2012. *ApJ*, 753:160.

Wyatt M.C. et al., 2014. *MNRAS*, 439:3371–3391.

Xu S. and Jura M., 2014. *ApJ Lett.*, 792:L39.

Xu S. et al., 2013. *ApJ*, 766:132.

Xu S. et al., 2014. *ApJ*, 783:79.

Xu S. et al., 2016. *ApJ Lett.*, 816:L22.

Xu S. et al., 2017. *ApJ Lett.*, 836:L7.

Xu S. et al., 2018. *ArXiv e-prints*.

Zeng L., Sasselov D.D., and Jacobsen S.B., 2016. *ApJ*, 819:127.

Zuckerman B. and Becklin E.E., 1987. *Nat*, 330:138–140.

Zuckerman B. and Song I., 2012. *ApJ*, 758:77.

Zuckerman B. et al., 2003. *ApJ*, 596:477–495.

Zuckerman B. et al., 2007. *ApJ*, 671:872–877.

Zuckerman B. et al., 2010. *ApJ*, 722:725–736.

Zuckerman B. et al., 2011. *ApJ*, 739:101–.